Test des Flash-ADCs, optimisation de la conception du détecteur et développement d'un nouveau concept de reconstruction spatiale dans l'expérience de neutrino Double Chooz pour la mesure de l'angle de mélange $\theta 13$.

Tarek Akiri

UNIVERSITÉ PARIS DIDEROT (PARIS 7)

ÉCOLE DOCTORALE 517 :
Constituants élémentaires et cosmos

THÈSE DE DOCTORAT

Pour l'obtention du titre de

DOCTEUR EN SCIENCES DE L'UNIVERSITÉ PARIS DIDEROT (PARIS 7)

présentée par

Tarek Akiri

Test des Flash-ADCs, optimisation de la conception du détecteur et développement d'un nouveau concept de reconstruction spatiale dans l'expérience d'oscillation de neutrinos Double Chooz

Soutenue le 24 septembre 2010 devant la commission d'examen composée de :

Inés	**Gil-Botella**	**Rapporteure**
Dominique	**Duchesneau**	**Examinateur**
Cécile	**Jollet**	**Examinatrice**
Éric	**Kajfasz**	**Président du jury**
Masahiro	**Kuze**	**Rapporteur**
Thierry	**Lasserre**	**Co-directeur de thèse**
Edoardo	**Mazzucato**	**Examinateur**
Alessandra	**Tonazzo**	**Directrice de thèse**

Contents

Test des Flash-ADCs, optimisation de la conception du détecteur et développement d'un nouveau concept de reconstruction spatiale dans l'expérience d'oscillation de neutrinos Double Chooz

Tarek Akiri
Laboratoire APC (CNRS) & CEA/Saclay (DSM/IRFU/SPP)

Double Chooz (DC) est une expérience d'oscillation de neutrinos auprès de réacteurs, dont la finalité est la mesure du dernier angle de mélange encore inconnu θ_{13}. Elle hérite de l'experience passée CHOOZ qui était limitée par des erreurs statistiques et systématiques à un niveau similaire d'environ 2.8%. Afin de diminuer l'erreur statistique, la masse de la cible du détecteur DC a été augmentée tandis que la réduction de l'erreur systématique est assurée par l'utilisation de deux détecteurs identiques. Un détecteur sera situé dans le voisinage des coeurs des réacteurs dans le but de contrôler le flux et le spectre des $\bar{\nu}_e$ émis alors que l'autre sera placé à l'endroit où l'effet d'oscillation maximal est attendu. Le premier est communément dénommé 'détecteur proche' par opposition au second dénommé 'détecteur lointain'. Les erreurs attendues sont 0.5% (stat.) et 0.6% (syst.) pour une ultime mesure $\sin^2 2\theta_{13} = 0.05$ ($\theta_{13} = 6.5°$) à trois écart-type après trois années de prise de données. Le démarrage du détecteur lointain est attendu pour novembre 2010 tandis que le détecteur proche sera opérationnel pour la mi-2012.
Cette thèse présente tout d'abord une contribution matérielle à l'expérience avec le test des Flash-ADCs qui constituent le coeur du système d'acquisition. Ensuite, elle présente des analyses effectuées sur des simulations Monte Carlo afin d'optimiser la conception du détecteur. Ce travail était composé d'analyses dans le but de choisir des composantes du détecteur avec la contamination radioactives qui convient, des analyses dans le but d'obtenir la meilleure résolution en énergie possible et une manière de déclencher la sauvegarde des données par le système d'acquisition la plus stable et la plus robuste possible. Les travaux sur l'optimisation du détecteur et les connaissances acquises sur les Flash-ADCs nous ont amené à envisager une nouvelle reconstruction spatiale basée sur le temps de vol des photons. Toutes ces contributions à l'expérience sont présentées en détails à travers ce manuscrit.

Flash-ADCs test, optimization of the detector design and development of a new concept of spatial reconstruction in the Double Chooz neutrino oscillation experiment

Tarek Akiri
Laboratoire APC (CNRS) & CEA/Saclay (DSM/IRFU/SPP)

Double Chooz (DC) is a reactor neutrino oscillation experiment whose purpose is the measurement of the last unknown mixing angle θ_{13}. It inherits from the past CHOOZ experiment which was limited by the statistical and systematic errors at the same extent of about 2.8%. To lower the statistical error, the DC detector target mass has been increased and a longer exposure is foreseen while the lowering of the systematic error is ensured by the use of two identical detectors. One will be located in the vicinity of the reactor cores to monitor the flux and spectrum of the $\bar{\nu}_e$ emitted whereas the other one will be located where the effect of the oscillation is expected to be maximal. They are respectively so-called 'near' and 'far' detectors. The expected errors are 0.5% (stat.) and 0.6% (syst.) for a measurement down to $\sin^2 2\theta_{13} = 0.05$ ($\theta_{13} = 6.5°$) at three standard deviations after three years of data taking. The far detector is expected for November 2010 while the near detector will be operational in mid-2012.

This thesis presents first a hardware work consisting in testing the Flash-ADCs that are the core of the main acquisition system of the experiment. Subsequently, it presents analyses performed on Monte Carlo simulations towards the optimization of the detector design. This work was composed of analyses to choose some detector components with the appropriate natural radioactivity contamination, analyses for the best achievable energy resolution and the most stable and robust way of triggering. The work on the optimization of the detector together with the acquired knowledge on the Flash-ADCs led us to envisage the possibility of a new spatial reconstruction based on the time of flight. All these contributions to the experiment are described in details throughout this manuscript.

Ce manuscrit est dédié à ma famille qui a été et demeurera, à n'en pas douter, mon soutien le plus infaillible.
Une pensée particulière va à mes parents dont l'abnégation, la pugnacité et la diligence constituent mes modèles au quotidien. Cette dédicace est un humble geste de reconnaissance envers les deux êtres qui ont forgé l'homme que je suis et sans qui, rien de ce que j'accomplis aujourd'hui ne saurait être envisageable.

أَنَا أُحِبُّكُم جَمِيعًا

Remerciements

Toutes les thèses sont certes différentes, mais elles ont en commun le fait de nous pourvoir de davantage d'outils pour affronter la vie. J'aimerais, à travers ces quelques lignes en Français (quel meilleur langage pour des remerciements ?), exprimer ma sincère gratitude envers les gens qui ont contribué, de quelque manière que ce soit, à faire de cette thèse une expérience fabuleuse.

J'aimerais en premier lieu remercier Pierre Binétruy pour m'avoir accueilli au sein de son laboratoire ainsi que pour les moyens mis à disposition des étudiants.

Ensuite, je tiens à remercier les membres du jury pour avoir gentiment accepté d'y prendre part et de s'être déplacé (parfois de loin) en ce vendredi 24 septembre. Je veux tout particulièrement remercier Inès et Kuze-san pour l'effort que cela a été de lire, de manière critique et assidue, ce manuscrit pendant vos vacances. En outre, un grand merci va à Kuze-san pour m'avoir accueilli à deux reprises au sein de son laboratoire et m'avoir fait découvrir une autre manière d'aborder la physique.

Cette thèse n'aurait probablement pas pu être réalisée sans la direction d'Alessandra que je souhaite remercier pour ses multiples relectures et corrections, ainsi que son suivi des mes travaux. Merci d'avoir été patiente avec moi et de m'avoir souvent recadré dans mon travail. Merci également à Thierry d'avoir été le co-directeur de cette thèse et d'avoir effectué des relectures critiques sur le manuscrit.

Je ne saurais certainement pas le physicien que je suis aujourdhui sans toi, Anatael (même s'il me reste un très long chemin à parcourir). Ton énergie (parfois trop !) et ta passion pour la physique sont extrêmement contagieuses. Merci de m'avoir inculqué la rigueur que demande le travail de physicien ainsi que de m'avoir fait découvrir les joies du métier de chercheur. Pour toutes les discussions

fructueuses que l'on a eues (même si trop souvent elles commençaient bien tard !!) et pour ton amitié, tu as ma plus profonde et sincère gratitude. Je regrette vivement le fait que tu n'es pas pu assister à ma soutenance.

Je veux également remercier tous les membres du laboratoire APC (personnel administratif, ingénieurs et physiciens) et plus particulièrement le groupe neutrino et les membres de l'expérience Double Chooz pour la convivialité de ces trois années passées avec vous. Merci en particulier à Didier qui m'a appris à peu près tout ce que je sais sur le VME. Merci d'avoir été patient malgré mes questions plus ou moins pertinentes. Je me sentais tout de même un peu esseulé avant les arrivées des 'jeunes' renforts, à savoir Michela puis Jaime et enfin Alberto. Merci à vous d'avoir partagé le bureau avec moi et d'avoir fortement égayé mon quotidien. Merci à Jaime d'avoir fait grandir mon goût pour l'hardware (ce qui n'était pas gagné !) et pour l'humour anglais !! Merci de m'avoir souvent aidé face aux difficultés techniques que je rencontrais, ainsi que les relectures de l'anglais. Merci également à Alberto pour ces moments passés en Grèce. Je tiens particulièrement à remercier Michela pour avoir accompagné les bons et les mauvais moments de cette thèse. Ainsi que pour m'avoir gratifié de phrases et moments de fous rires inoubliables (liste non exhaustive: URLS, hspace de 0cm, 52000 $\mu\Omega$, ...). Je n'ose imaginer ce qu'auraient été ces trois années sans vous tous.

J'aimerais également remercier les membres de l'expérience Double Chooz travaillant au CEA à Saclay. J'ai apprécié votre compagnie même si cela n'a été que trop rarement. J'ai une pensée pour Dario qui m'a fait découvrir, et immédiatement fait apprécier la physique des neutrinos et l'expérience Double Chooz. Sa pédagogie, sa patience et son talent pour la physique dont je n'ai pas pu suffisamment profiter, sont encrés en moi. Un grand merci à Thomas et Rachel pour m'avoir offert leur amitié et pour avoir partagé tant de bons moments aux meetings de collaboration et autres.

Je voudrais par ailleurs exprimer ma reconnaissance à mes amis du DEA qui sont devenus bien plus durant ces trois années de thèse: Antoine (qui arrive à passer plus d'une demi-heure croyant qu'il joue, mais non!), David (qui invente les règles au fur et à mesure du jeu, un bien bel exemple ce futur Papa!) et Guylaine (heureusement là pour nous rappeler qu'il n'y a pas que la physique. J'ai bien fait attention à l'orthographe, ne t'énerve pas ;-)), Fany (notre cuisinière de talent

qu'il ne faut surtout pas faire rigoler à table!), Seb (le bon joueur tant qu'il gagne, toujours prompt à nous redonner le sourire) et Thomas (le roi de la symétrie et de la mauvaise foi! Bon ok, j'aurais pu inclure Seb ou Toine mais vous constituez le top 3 de toute façon.). Merci encore à vous !! J'ai une pensée particulière pour toi Fany, qui m' a accompagné et activement soutenu durant deux années et demi de cette thèse. Même maintenant, je n'arrive pas à m'imaginer cette thèse sans ton soutien dans les moments les plus difficiles.

Finalement, je ne saurais conclure ces remerciements sans exprimer à nouveau toute ma reconnaissance envers ma famille. Je ne vous dis pas assez souvent combien je vous aime. Vous êtes ce qui compte le plus à mes yeux.

Chapter 1

Introduction

The neutrino was first postulated by W. Pauli in 1930 in a desperate attempt to save the principle of energy conservation. Then it was integrated to the first theory of β-decay built in 1933 by E. Fermi, and was finally discovered through the inverse β-decay in 1956 by F. Reines and C. Cowan. The hunt for the neutrino lasted for 26 years because of its elusive feature which is unique in the Standard Model (SM) that describes the elementary particles and their interactions. Being only sensitive to the weak interaction, which makes it hardly detectable, its study helped to understand the nature of the weak interaction and therefore to build the SM as explained in chapter 2.

The neutrino discovery lead astrophysicists to envisage the possibility to study the Sun's interior by detecting neutrinos produced in the fusion reactions. Meanwhile, neutrinos produced by cosmic rays interactions in the atmosphere, which was a background for proton decay experiments, were measured. Both type of experiment measured a deficit of the neutrino flux with respect to the calculations. These observations were so-called 'solar and atmospheric' anomalies. These anomalies, induced by flavor changing, are best explained by neutrino oscillations as presented in chapter 3.

The phenomenon of flavor changing was already known in the SM. It was observed in the quark sector that the strong interaction states do not correspond to the weak interaction states. The different transition amplitudes between the different generations was first parametrized by N. Cabibbo in 1963 and subsequently generalized to the CKM matrix in 1972 by M. Kobayashi and T. Maskawa to account for CP (charge-parity) symmetry violation observed in 1964 by J. Cronin et al.

In the framework of the SM, such oscillations were not possible for neutrinos. A right-handed chiral field is required to build the mixing terms while it is absent from the theory because of the observation in 1957 by M. Goldhaber et al. of a maximal parity violation by neutrinos. The restoring of this field leads to the possibility for neutrinos to have mass and thus oscillate between the propagation and interactions states linked by a matrix depending on 4 parameters. The solar and atmospheric experiments allowed the determination of 2 parameters, surprisingly found to be large compared to the quark sector, while the two last parameters will be addressed by experiments about to start. One is the mixing angle θ_{13} and the second one is the leptonic CP violation δ. It is of first importance to assess whether the value of the latter can explain the observed matter/anti-matter asymmetry of our Universe but the first step is the determination of θ_{13}. The hunt for these parameters is presented in chapter 4.

Double Chooz (DC) is a reactor neutrino oscillation experiment aiming at measuring the mixing angle θ_{13}. This angle is known to be small from past experiments, notably the CHOOZ reactor experiment. Going further requires to achieve better statistical and systematic errors. In order to fulfill these requirements, the target volume has been enlarged and two identical detectors will be employed: a near detector at about 400 m of the neutrino source to monitor it and a far one at about 1.05 km to measure the oscillation effect. The potential is to measure θ_{13} down to $\sin^2 2\theta_{13} = 0.05$ ($\theta_{13} = 6.5°$) at more than 3 standard deviations or set a limit of $\sin^2 2\theta_{13} \leq 0.03$ ($\theta_{13} \leq 5°$) at 90% C.L. (the current best limit from CHOOZ is $\sin^2 2\theta_{13} \leq 0.14$ ($\theta_{13} \leq 11°$) at 90% C.L.). The experiment is described in details in chapter 5.

To achieve the sensitivity described above, DC uses Flash-ADCs for the digitization of the signals and tries to control the backgrounds and determine as much accurately as possible the energy of the events. The use of Flash-ADCs allows to have a data acquisition system free of deadtime allowing to make a 'movie' of events in the detector. It will be particularly useful for detailed background studies. Tests have been performed on the Flash-ADC cards used in the experiment to ensure their features and their good working for the purposes of the experiment. They are presented in chapter 6.

Background suppression and energy resolution are two major challenges for the experiment. The natural radioactivity γ's are a source of background that should be kept at a low level. Therefore, all the detector components have to satisfy strict radioactivity constraints. Besides, the energy measured for a given energy deposi-

tion should be independent of the location of the deposition in the detector. DC uses two liquid scintillators whose light yield have to be the same. Moreover, the possibility to use light concentrators for a better energy resolution against non-uniformity following the energy deposition location had to be studied. Eventually, the stability of the way of triggering based on the energy was studied along with a new type of triggering and possible combinations of them. All these studies are presented in chapter 7.

Possible discriminations between signal and backgrounds could be made from the location of the energy deposition and from the scintillators time responses. Doing so requires to have an accurate spatial reconstruction that can be obtained by exploiting the Flash-ADCs capabilities. We developed a new type of spatial reconstruction based on the time of flight of photons from the location of the deposition and their detection on photomultiplicator tubes. Its full concept, performances and possible upgrades are presented in chapter 8.

Chapter 2

The neutrino, a very peculiar particle.

Particles composing the matter and their interactions are accurately described by the Standard Model of particles. Inside this model, neutrinos are very peculiar particles that allowed its building. Nowadays, they are at the origin of the first evidence of the necessity of physics beyond it with the phenomenon of neutrino oscillations.
In this chapter, we briefly review the Standard Model history and the role played by neutrinos. Then we focus on the formalism of neutrino oscillations which implies a mass for neutrinos, while they are massless in the Standard Model. Finally we present the experimental methods to measure the neutrino mass and especially the neutrinoless double β-decay that is a unique probe of the possible Majorana nature of neutrinos.

2.1 Neutrinos and the Standard Model

2.1.1 The Standard Model of particles in short

The Standard Model (SM) describes the strong, electromagnetic and weak interactions of the known elementary particles where interactions are represented by the exchange of mediator particles. The strong interaction is the force responsible of the binding between protons and neutrons in an atom nucleus and also of the cohesion of quarks composing these particles. This interaction is very peculiar

since its coupling constant increases as a function of the distance between the two interacting particles[1] but shows an asymptotic freedom when the distance is of the order of the atom radius ($\sim 10^{-15}$ m). The electromagnetic interaction is the force responsible of the binding of electrons to the nucleus in an atom. It corresponds to the exchange of photons between the protons that are electrically charged and the electron. The weak interaction is a force felt by all particles but its coupling constant is small compared to the previous forces because its mediators are massive implying a short range interaction.

The SM is a renormalizable gauge theory based on the quantum field theory that merges the quantum mechanic and the restricted relativity. The symmetry group that describes the interactions is $SU(3)_C \times SU(2)_L \times U(1)_Y$[2]. The first term is the gauge group of the strong interaction mediated by 8 massless gluons (g). The theory behind is called quantum chromodynamics (QCD) and it can be decoupled from the other interactions. The second and third terms correspond respectively to the weak and electromagnetic interactions. The unification of these two interactions leads to the electroweak interaction mediated by bosons[3] of spin 1: three massive ones for the weak force ($W^{\pm}$, Z^0) and a massless one (the photon γ) for the electromagnetic force.

The elementary particles are fermions[4] of spin 1/2 that are divided into two categories: quarks and leptons. Quarks are sensitive to all interactions unlike leptons that are sensitive only to the electroweak interaction. Among the leptons, it should be remarked that neutrinos are neutral and thereby only subject to the weak force resulting in a small cross-section responsible of their elusive nature. Their interactions are through charge current with the exchange of $W^{\pm}$ or through neutral current and the exchange of Z^0. There exists three generations where the two last generations are replica of the first generation with a higher mass. In the case of neutrinos, it is the electron neutrino ν_e associated to the electron (e^-), electron neutrino ν_μ associated to the muon (μ^-) and tau neutrino ν_τ associated to the tau (τ^-). The table 2.1 summarizes the particles of the SM and their properties.

[1] The mediator of the strong interaction is 'colored' what means that it is charged for the strong interaction and therefore it interacts as well. This self coupling of the mediator is responsible of the increasing coupling constant with the distance.

[2] U stands for a unitary matrix, S means that the determinant of the matrix is equal to 1 and in brackets we find the dimension of the matrix (N means N×N). C is the 'strong charge' and means color, L means left-handed (the weak interaction violates parity) and Y weak hypercharge (together with the isospin I_3 that is the 'weak charge', it gives the electric charge through the Gell-Mann-Nishijima relation: $Q = I_3 + Y/2$.

[3] The spin s is an integer.

[4] The spin s is a half-integer.

This panorama has to be completed by the Higgs boson of spin 0 that gives rise to mass terms for the elementary particles and massive bosons through the Higgs mechanism. The discovery of this particle is one of the main purpose of the experiments taking place at the Large Hadron Collider (LHC) in Switzerland. Among the elementary particles, only neutrinos are massless according to experimental results[5]. The SM model describes accurately the experimental observations but it is nevertheless believed that it is an effective theory at low energy since the strong and electroweak interactions are not yet merged and the gravitation is totally absent[6]. Tests have been performed to look for new physics unsuccessfully except for the establishment of the phenomena of neutrino oscillation described in section 2.2.

2.1.2 The neutrino history in brief

The neutrino discovery

The neutrino[7] was first postulated by W. Pauli in 1930 in a desperate attempt to save the principle of energy conservation. β-decay was thought to be a 2-body decay corresponding to a well defined energy for the e^- emitted but the spectrum was found to be continuous what matched a situation with another particle in the final state. In 1934, E. Fermi built the first theory of the weak interaction including the neutrino [1]. In this theory, it is possible to detect neutrinos through the inverse β-decay: $\bar{\nu} + p \rightarrow n + e^+$. This reaction was used by F. Reines and C. L. Cowan in 1956 to detect for the first time neutrinos. They used 4200 l of liquid scintillator placed in the vicinity of the Savannah River nuclear power plant in South Carolina (USA) and found an event rate compatible with 3 per hour. They confirmed the neutrino small cross-section responsible of their elusive character [2]. This neutrino was identified to be of electron type $\bar{\nu}_e$ thanks to the experiment of L. Lederman *et al.* in 1962.

Parity non-conservation

In 1956, T.D. Lee and C.N. Yang made a review of the experimental informations and showed that there were no evidences for parity conservation in the weak interaction [3]. To check if parity is conserved, in 1957, C.S. Wu and her colleagues

[5] See the Goldhaber experiment (see section 2.1.2)

[6] At the energies accessible with the current technology, the gravitational interaction is negligible.

[7] The neutrino was first called neutron but was renamed in 1933 to neutrino by E. Fermi after the discovery of the neutron in 1932 by J. Chadwick.

		Particle	Mass	Charge
Fermions s=1/2	Quarks	u	1.5-4 MeV	2/3
		d	4-8 MeV	-1/3
		c	1.15-1.35 GeV	2/3
		s	80-130 MeV	-1/3
		t	174.3 ± 5.1 GeV	2/3
		b	4.1-4.4 GeV	-1/3
	Leptons	e^-	511 MeV	-1
		ν_e	<15 eV	0
		μ^-	105.65 MeV	-1
		ν_μ	< 190 keV	0
		τ^-	1.777 GeV	-1
		ν_τ	< 18.2 MeV	0
Bosons s=1	Interaction mediators	g	0	0
		$W^\pm$	80.412 ± 0.042 GeV	±1
		Z^0	91.1875 ± 0.0023 GeV	0
		γ	0	0
	Higgs	H	>115 GeV	0

Table 2.1: Summary of the elementary particles of the SM, the force carriers and the Higgs. Mass and charge of each component are given. Quarks does not exist as free particles, the indicated masses are the input parameters in QCD. The neutrino masses are derived from weak decays kinematics. The corresponding antiparticles of the elementary particles that have the same mass but opposite charge are as well elementary particles.

decided to look at the β-decay of polarized ^{60}Co nuclei [4]. A ^{60}Co sample was cooled (0.003 K) and placed in a solenoid (2.3 T) so that the ^{60}Co angular momentum of 5 is aligned with the magnetic field direction. The parity operator reverses the particles momenta while leaving the angular momenta and especially the spin unchanged. Thus, if parity is conserved, electrons should be emitted isotropically in the ^{60}Co sample rest frame.
A detector was placed above the ^{60}Co sample to detect electrons. As can be seen

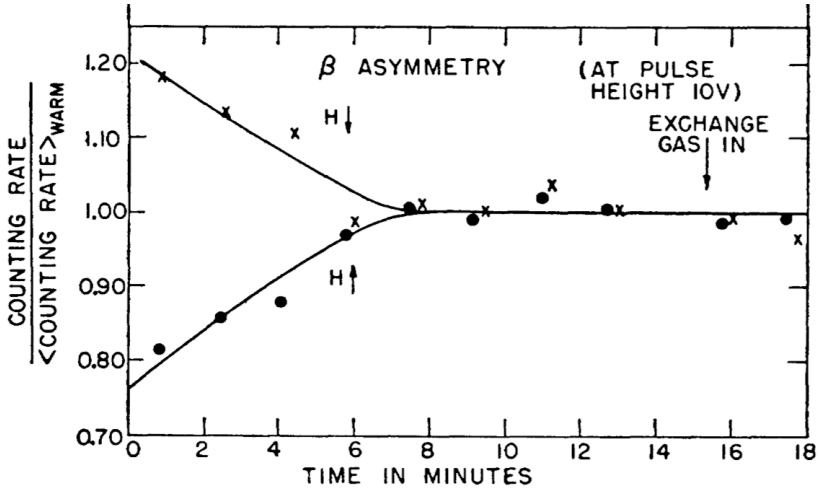

Figure 2.1: Counting rate over counting rate mean value when the ^{60}Co sample is warm as a function of time [4]. One can see that electrons are preferentially emitted in the opposite direction of the magnetic field indicating parity violation.

on figure 2.1, it was found that the electrons were preferentially emitted in the opposite direction of the magnetic field, even when it was reversed. It was a strong indication that parity is violated by the weak interaction leading to the V-A structure of the weak interaction where V stands for vector and A for axial vector, with A remaining unaffected under the parity operator on the contrary of the V part. The observations of Wu *et al.* were later confirmed on β^+ emitters [5] and even more beautifully demonstrated by Goldhaber *et al.* in 1958 that moreover determined the neutrino helicity. The helicity being defined as the projection of the angular momentum $\vec{S}$ on the momentum $\vec{P}$:

$$h = \frac{\vec{S} \,.\, \vec{P}}{|\vec{S}|\ |\vec{P}|} \tag{2.1}$$

The parity operator reverses the momentum but not the angular momentum and thus helicity should change sign under the application of parity operator.

Measurement of the neutrino helicity

The Goldhaber experiment is one of the most ingenious experiment. It proved that neutrinos have negative helicity and that the parity is maximally violated by the weak interaction. M. Goldhaber and its coworkers [6, 7] used ^{152}Eu that, after capturing an orbital electron, decays into a neutrino and ^{152}Sm* which subsequently decays to ^{152}Sm and a γ:

$$\begin{array}{ccccccc} J=0 & & s=1/2 & & J=1 & & s=1/2 \\ {}^{152}\mathrm{Eu} & + & e^- & \rightarrow & {}^{152}\mathrm{Sm}^* & + & \nu_e \\ & & & & \downarrow & & \\ \gamma & + & {}^{152}\mathrm{Sm} & \leftarrow & {}^{152}\mathrm{Sm}^* & & \\ s=1 & & J=0 & & J=1 & & \end{array} \tag{2.2}$$

Since ^{152}Eu has an angular momentum (J) equal to zero, the neutrino spin and the ^{152}Sm* angular momentum should have opposite orientations following the e$^-$ spin orientation. Furthermore, the ^{152}Sm* decays into ^{152}Sm that has J=0 and a γ that should thus have a spin aligned with the angular momentum of ^{152}Sm*. The helicity of the γ is the same as the ^{152}Sm* that should then be the same as the neutrino since they have both opposite momenta and angular momenta. Hence measuring the γ helicity gives the neutrino helicity. As shown in equation 2.1, to measure the helicity, one has to determine the particle momentum and its polarization. It was respectively achieved through resonance[8] and the utilization of a magnet. It has been found that the neutrino has only a negative helicity leading to a neutrino mass set to zero in the Standard Model.

The second generation of neutrino

In 1962, L. Lederman, M. Schwartz and J. Steinberger found that neutrinos from π^- decays are related to muons showing the existence of two generations: (e$^-$, ν_e) and (μ^-, ν_μ). π's were accelerated towards a detector at Brookhaven National Laboratory (USA) made of spark chambers. From the π decay in flight arose a muon and a neutrino with the muon being stopped by a beam dump before decay.

[8]The resonance is achieved when the emitted γ can be reabsorbed on ^{152}Sm. However some energy is lost in the recoil during the decay and in the possible reabsorption process. The doppler shift can recover this energy loss only if the neutrino is emitted in a precise direction allowing the neutrino momentum determination [7].

Measurements of charged current neutrino interactions in coincidence with the beam yielded 29 muons and 6 electrons with the 6 electrons being compatible with the background expectations [8]. It was therefore the discovery of the ν_μ.

Discovery and study of electroweak currents at CERN

From the observations, theorists attempted to build a satisfactory theory of weak interaction. Several problems arose and were solved leading around 1973 to a viable renormalizable gauge theory predicting, in addition to the mediators of charged current (the so-called $W^\pm$), the existence of neutral current mediated by a massive boson called Z^0. The Gargamelle experiment was a large bubble chamber cylinder operated under a 2 T magnetic field located at the European center for nuclear research (CERN) in Geneva (Switzerland). Alternatively neutrinos and antineutrinos were sent using the super proton synchrotron to the detector and their interaction happened either on electrons or nuclei. In the case of neutral current, the signature would be respectively a unique scattered electron or hadrons. The excitement for neutral current began with the observation of an isolated scattered electron in an antineutrino run [9]. In 1973, the experiment claimed the observation of 102 neutral current events. In 1974, it was shown that they have a flat spatial distribution on the contrary of the background giving strong confidence in the result and thereby in the recently elaborated theory of weak interaction [10]. Besides, the experiments could do the first measurement of $\sin^2\theta_W$ that is a parameter of the SM.
The W and Z bosons were discovered in 1983 by UA1 (and subsequently UA2) experiment [11] at the super proton synchrotron accelerator (SPS), a protons-antiprotons collider at CERN. In 1990s, the Large Electron Positron collider (LEP and later LEP2) studied the properties of Z and W with high statistic positron-electron collisions allowing precise knowledge of the energy in the center of mass. The W resonance was first found in the neutrino channel thanks to the missing energy and the Z resonance allowed the determination of the number of generations.

Number of neutrino generations

The Z is neutral and thus its decay modes are in a fermion and the associated antifermion. Hadrons and leptons could be detected except neutrinos that however contributes to the Z width. The number of neutrino species N_ν is inferred through [12]:

$$N_\nu = \frac{\Gamma_{inv}}{\Gamma_l}\left(\frac{\Gamma_l}{\Gamma_\nu}\right)_{SM} = 2.9840 \pm 0.0082 \tag{2.3}$$

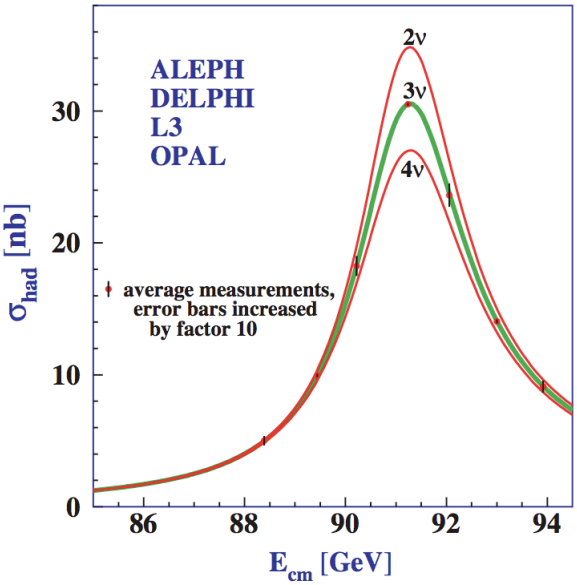

Figure 2.2: Measurements of the hadron production cross-section around the Z^0 resonance. It is best fitted by the existence of three neutrino species [12].

where Γ_{inv} is the total Z width minus the individual widths, Γ_l is a lepton flavor contribution to the width[9] and Γ_ν is the theoretical contribution of one neutrino flavor. The ratio $\left(\frac{\Gamma_l}{\Gamma_\nu}\right)_{SM}$ is used to reduce the uncertainty.
As can be observed on figure 2.2, the Z width was found to be best fitted by three neutrino flavors. It has however to be noticed that it is a proof of the existence of only three species that are active[10] with a mass lower than ∼45.5 GeV corresponding to the Z mass divided by two.

The ν_τ discovery

The τ lepton was discovered at Stanford Linear Accelerator Center in USA in 1975 leading to the supposition of the ν_τ existence. τ was found to be heavy with ∼1.8 GeV, implying a travel distance of a few mm before its decay. It was therefore very difficult to reveal a ν_τ charged current interaction creating a τ. The first confirmation of its existence came from the Z width at LEP and its direct detection was brought only in 2000 by the DONUT experiment at FermiLAB (Chicago, USA) [13]. This experiment was using emulsions for a satisfactory spatial resolution and an accurate determination of the kink pattern of τ decay that is due

[9] These width measurement has the lowest uncertainty.
[10] The possibility of sterile neutrinos that do not couple to the Z boson is still possible from some oscillation experiments [65, 69].

to the high mass difference between the τ and its daughter particles.

2.2 Neutrino oscillation formalism

The last decade has brought compelling evidences in favor of neutrino oscillations (see chapter 3). This phenomenon was first envisaged by B. Pontecorvo in 1957 with neutrino to antineutrino oscillations [14] but was fully developed by Z. Maki, M. Nakagawa and S. Sakata in 1962 on the quark mixing model [15]. The phenomenon of neutrino oscillations is a quantum-mechanical effect induced by the non-correspondance of the interaction states (the lepton flavors: ν_e, ν_μ, ν_τ) with the propagation states (the mass states: ν_1, ν_2, ν_3). The matrices used to diagonalize the Yukawa coupling matrices of charged leptons and neutrinos[11] are mixed in the charged current Lagrangian to yield the Maki-Nakagawa-Sakata-Pontecorvo (MNSP) neutrino mixing matrix $U_{MNSP} = U$. The neutrino lepton flavor states $|\nu_\alpha\rangle$ are thereby related to the mass states $|\nu_i\rangle$ by U through:

$$|\nu_\alpha\rangle = \sum_k U^*_{\alpha k}|\nu_k\rangle \tag{2.5}$$

After an elapsed time t and a distance travelled L, the lepton flavor state is given by:

$$|\nu_\alpha(t,L)\rangle = \sum_k U^*_{\alpha k} e^{-i(E_k t - p_k L)}|\nu_i\rangle \tag{2.6}$$

By inverting relation 2.5, we obtain the following relation showing clearly that after its production, a neutrino is a linear superposition of the existing lepton states:

$$|\nu_\alpha(t,L)\rangle = \sum_{\beta=e,\mu,\tau}\left(\sum_k U^*_{\alpha k} e^{-i(E_k t - p_k L)} U_{\beta k}\right)|\nu_\beta\rangle \tag{2.7}$$

The probability to find neutrinos produced as α in a state β after a time t and a distance L is [16]:

$$P_{\nu_\alpha\to\nu_\beta}(t,L) = |\langle\nu_\beta|\nu_\alpha(t,L)\rangle|^2 = |\sum_k U^*_{\alpha k} e^{-i(E_k t - p_k L)} U_{\beta k}|^2 \tag{2.8}$$

[11] The leptonic charged current can be written as (from equation 2.23) [20]:

$$j^\mu = 2\bar{\nu'_L}\gamma^\mu l'_L = 2\bar{\nu_L} V_L^{\nu\dagger}\gamma^\mu V_L^{l\dagger} l'_L = 2\bar{\nu_L} U^\dagger_{PMNS}\gamma^\mu l_L \tag{2.4}$$

From the dispersion relation $E^2 = p^2 + m^2$ and the fact that neutrinos are ultra-relativistic[12] ($t \simeq L$, $p \simeq E$), we obtain[13]:

$$E_k t - p_k L \simeq (E_k - p_k)L = \frac{(E_k^2 - p_k^2)L}{E_k + p_k} \simeq \frac{m_k^2}{2E} L \tag{2.9}$$

The oscillation probability is finally given by:

$$P_{\nu_\alpha \to \nu_\beta}(t, L) = \sum_k |U_{\alpha i}|^2 |U_{\beta i}|^2 + 2\ \Re e \sum_{k>j} U^*_{\alpha i} U_{\beta i} U_{\alpha j} U^*_{\beta j} \exp\left(-i \frac{\Delta m^2_{jk} L}{2E}\right) \tag{2.10}$$

with the mass state squared difference $\Delta m^2_{jk} = m^2_k - m^2_j$.
Only the second term in this expression is oscillating as a function of the distance between the source and the detector L and the neutrino energy E. Furthermore, the dependence on the mass difference between the mass states allows to establish that an observation of the oscillation phenomenon implies that neutrinos are massive.
It is important to notice that the survival probabilities $P_{\nu_\alpha \to \nu_\alpha}$ do not depend on the U matrix phases. Moreover, in case of invariance under CPT (charge conjugation, parity and time operators), we obtain:

$$P_{\nu_\alpha \to \nu_\alpha} = P_{\bar{\nu}_\alpha \to \bar{\nu}_\alpha} \tag{2.11}$$

2.2.1 2 flavors oscillations in vacuum

For the establishment of the neutrino oscillation probability in vacuum used in the past experiments, let us consider the simplest case where it exists only two neutrino flavors: ν_e and ν_μ linked by a rotation matrix depending only on a mixing angle θ:

$$\begin{pmatrix} \nu_e \\ \nu_\mu \end{pmatrix} = \begin{pmatrix} \cos\theta & \sin\theta \\ -\sin\theta & \cos\theta \end{pmatrix} \begin{pmatrix} \nu_1 \\ \nu_2 \end{pmatrix} \tag{2.12}$$

From equation 2.10, the resulting oscillation probability is:

$$P_{\nu_\alpha \to \nu_\beta}(L) = \ \sin^2 2\theta \sin^2\left(\tfrac{\Delta m^2 L}{4E}\right) \tag{2.13}$$

[12] As it is presented in section 2.3.4, the neutrino mass is bounded below the eV. Since in experiments, the energy is above the MeV, neutrinos are relativistic.

[13] Neutrinos have been described by plane wave here for simplicity while it should be wave packet. The treatment with wave packets leads to the same formula but adds the possibility of decoherence due to different group velocities. The latter can happen only for very large travel distances what is never the case in the current neutrino oscillation experiments [17].

where Δm^2 is the mass squared difference between the mass states ν_1 and ν_2. $\sin^2 2\theta$ controls the amplitude of the oscillations whereas $\sin^2\left(\frac{\Delta m^2 L}{4E}\right)$ is the oscillating term with phase $\frac{\Delta m^2 L}{4E}$. To obtain appreciable oscillation[14], there should be a large mixing angle but also a phase so that:

$$\frac{\Delta m^2 L}{4E} \sim 1 \tag{2.14}$$

When the phase is very large compared to one, the finite energy resolution and/or the finite detector size lead to an averaged oscillation probability of about half the amplitude factor.
Past oscillation experiments have largely used the following formula where the h and c constants have been restored:

$$P_{\nu_\alpha \to \nu_\beta}(L) = \sin^2 2\theta \sin^2\left(1.27 \frac{\Delta m^2\ (\mathrm{eV}^2) L\ (\mathrm{m})}{E\ (\mathrm{MeV})}\right) \tag{2.15}$$

2.2.2 Oscillations in matter

Neutrinos traveling through matter may be coherently forward scattered by interacting with electrons and nucleons (protons and neutrons) composing the medium resulting in a modification of the neutrino oscillation probability [18]. As can be seen on figure 2.3, all neutrino flavors interact through neutral current (NC) whereas ν_e interacts as well through charged current (CC). These interactions are at the origin of the addition of potentials to the free Hamiltonian:

$$V_{CC} = \sqrt{2} G_F N_e \qquad \text{and} \qquad V_{NC} = -\frac{1}{2}\sqrt{2} G_F N_n \tag{2.16}$$

where G_F is the Fermi constant and N_e, N_n the electron and neutron densities in the medium. V_{CC} and V_{NC} are the potentials induced respectively by the CC and the NC. The NC potential is only proportional to N_n since the matter is supposed electrically neutral and the electron and proton potentials compensate.

The NC potential creates a global phase that is irrelevant since it can be absorbed by a redefinition of the states and subsequently vanishes when considering oscillation probabilities. In the two flavors case, the diagonalisation of the new

[14] Oscillations are possible because we cannot resolve the individual neutrino mass. This explains in the same time why oscillations are not possible for charged leptons.

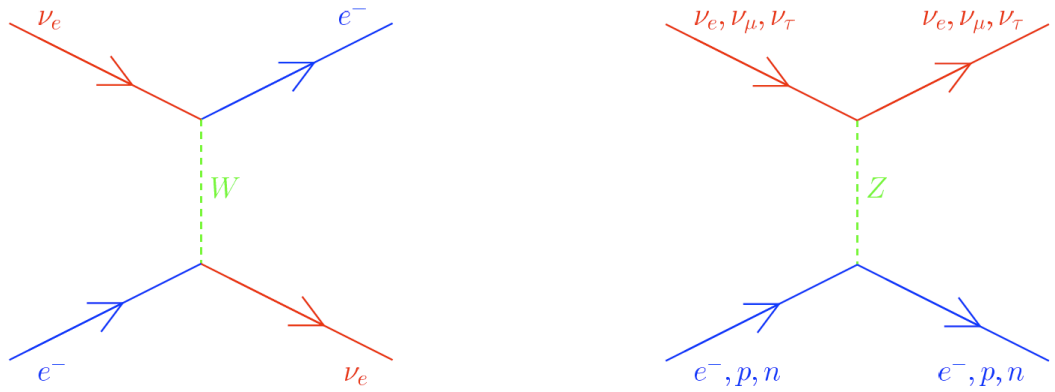

Figure 2.3: Feynman diagrams of the coherent forward elastic scattering processes that generate the CC potential V_{CC} through W exchange and the NC potential V_{NC} through Z exchange [16].

Hamiltonian yields [20]:

$$\tan 2\theta_M = \frac{\tan 2\theta}{1 - \frac{2EV_{CC}}{\Delta m^2 \cos 2\theta}}, \qquad \Delta m^2_M = \sqrt{(\Delta m^2 \cos 2\theta - 2EV_{CC})^2 + (\Delta m^2 \sin 2\theta)^2} \tag{2.17}$$

A very interesting case arises for:

$$2EV_{CC} = \Delta m^2 \cos 2\theta \tag{2.18}$$

that is the resonance condition [19]. This is the so-called MSW (Mikheev-Smirnov-Wolfenstein) effect. This effect can create maximal mixing from a mixing angle that is originally small! Moreover, it breaks the symmetry $\theta \to \pi/2 - \theta$ present in the vacuum oscillation probability formula. Indeed, as can be seen from equation 2.18, the resonance condition can be fulfilled only if $\theta < \pi/4$ because the matter potential is positive for neutrinos (negative for antineutrinos). The observation of the MSW effect in solar neutrino experiments have lead to the determination of the sign of the Δm^2 associated: $\Delta m^2_{12} > 0$.

2.2.3 Three neutrino flavors oscillations

In the case of three active neutrino flavors, the U_{PMNS} matrix depends on three mixing angles: θ_{12}, θ_{23} and θ_{13} and a CP (conjugation-parity) violation phase[15] δ. If the neutrino is a Majorana particle (particle=antiparticle, see section 2.3),

[15]This phase introduces a possible asymmetry between the oscillation probabilities of neutrinos $P_{\nu_\alpha \to \nu_\beta}$ and antineutrinos $P_{\bar{\nu}_\alpha \to \bar{\nu}_\beta}$: $P_{\nu_\alpha \to \nu_\beta} \neq P_{\bar{\nu}_\alpha \to \bar{\nu}_\beta}$.

there are two additional phases α_2 and α_3 that have no impact on the neutrino oscillation probabilities. U can be parametrized by the product of three rotation matrices and a diagonal matrix carrying the two Majorana phases:

$$U = \begin{pmatrix} 1 & & \\ & c_{23} & s_{23} \\ & -s_{23} & c_{23} \end{pmatrix} \begin{pmatrix} c_{13} & & s_{13}e^{-i\delta} \\ & 1 & \\ s_{13}e^{-i\delta} & & c_{13} \end{pmatrix} \begin{pmatrix} c_{12} & s_{12} & \\ -s_{12} & c_{12} & \\ & & 1 \end{pmatrix} \begin{pmatrix} 1 & & \\ & e^{i\alpha_2} & \\ & & e^{i\alpha_3} \end{pmatrix} \quad (2.19)$$

$$= \begin{pmatrix} c_{12}c_{13} & s_{12}c_{13} & s_{13}e^{-i\delta} \\ -s_{12}c_{23} - c_{12}s_{23}s_{13}e^{i\delta} & c_{12}c_{23} - s_{12}s_{23}s_{13}e^{i\delta} & s_{23}c_{13} \\ s_{12}s_{23} - c_{12}c_{23}s_{13}e^{i\delta} & -c_{12}s_{23} - s_{12}c_{23}s_{13}e^{i\delta} & c_{23}c_{13} \end{pmatrix} \quad (2.20)$$

where c_{ij}, s_{ij} stands respectively for $\cos\theta_{ij}$ and $\sin\theta_{ij}$.
When considering oscillation probabilities, there are three additional parameters coming from the mass squared differences between the mass states (m_1, m_2, m_3): Δm^2_{12}, Δm^2_{23} and Δm^2_{31}. However, only two of these parameters are independent since:

$$\Delta m^2_{12} + \Delta m^2_{23} + \Delta m^2_{31} = 0 \quad (2.21)$$

and consequently neutrino oscillations depends on six parameters.
As it is described in the next chapter, (θ_{12}, Δm^2_{12}) were first determined in the solar neutrino experiments and called (θ_{sol}, Δm^2_{sol}) while (θ_{32}, Δm^2_{32}) were determined in atmospheric neutrino experiments and so-called (θ_{atm}, Δm^2_{atm}).

2.3 Extension of the Standard Model

In the SM, neutrinos are massless and thus their helicity coincide with their chirality. Consequently neutrinos are left-handed chiral fields and antineutrinos are right-handed chiral fields with no possibility for a mass term construction. However neutrinos are henceforth known to undergo oscillations implying that they are massive. The minimally extended SM (meSM) restores a right-handed chiral component (left-handed chiral component) for each (anti)neutrino generation allowing the construction of a Dirac mass term and also a so-called Majorana mass term. The merging of these two mass terms can lead to the appealing see-saw mechanism explaining the smallness of the neutrino masses.

2.3.1 Dirac mass term

The meSM Higgs-lepton Yukawa Lagrangian can be written as follows [20]:

$$\mathcal{L} = -\left(\frac{v+H}{\sqrt{2}}\right)\ [\ \bar{l'_L} Y'^{l} l'_R + \bar{\nu'_L} Y'^{\nu} \nu'_R\ ]\ +\ \text{h.c.} \tag{2.22}$$

where v is Higgs vacuum expectation value and H is the Higgs boson field. $\bar{l'_L}$, $\bar{\nu'_L}$ (l'_R, ν'_R) are respectively the left-handed (right-handed) chiral charged lepton and neutrino arrays with three components. Y'^{l} and Y'^{ν} are the charged lepton and neutrino 3×3 Yukawa couplings matrices needed to preserve the gauge invariance. The Y'^{l} matrices are diagonalized through the appropriate combination of two 3×3 unitary matrices $\mathrm{V}_L^{l\dagger}$ and V_R^{l} for charged leptons, and $\mathrm{V}_L^{\nu\dagger}$ and V_R^{ν} for neutrinos:

$$\begin{aligned} V_L^{l\dagger} Y'^{l} V_R^{l} &= Y^{l} \quad \text{with } Y^{l}_{\alpha\beta} = y^{l}_{\alpha}\delta_{\alpha\beta} \quad (\alpha,\beta = 1,2,3) \\ V_L^{\nu\dagger} Y'^{\nu} V_R^{\nu} &= Y^{\nu} \quad \text{with } Y^{\nu}_{kj} = y^{\nu}_{k}\delta_{kj} \quad (k,j = 1,2,3) \end{aligned} \tag{2.23}$$

where the y coefficients are positive. Finally the Lagrangian is written as follows:

$$\mathcal{L} = -\sum_{\alpha=e,\mu,\tau} \frac{y^{l}_{\alpha} v}{\sqrt{2}} \bar{l_\alpha} l_\alpha - \sum_{k=1,2,3} \frac{y^{\nu}_{k} v}{\sqrt{2}} \bar{\nu}_k \nu_k - \sum_{\alpha=e,\mu,\tau} \frac{y^{l}_{\alpha}}{\sqrt{2}} \bar{l_\alpha} l_\alpha H - \sum_{k=1,2,3} \frac{y^{\nu}_{k}}{\sqrt{2}} \bar{\nu}_k \nu_k H \tag{2.24}$$

with $l_\alpha = l_{\alpha L} + l_{\alpha R}$ and $\nu_k = \nu_{kL} + \nu_{kR}$ the Dirac charged lepton and neutrino mass eigenstate fields.

The third and forth terms correspond to the lepton coupling to the Higgs while the two first terms correspond to the lepton masses with:

$$\begin{aligned} m_\alpha &= y^{l}_{k} v/\sqrt{2} \quad \text{with } (\alpha = e,\mu,\tau) \\ m_k &= y^{\nu}_{k} v/\sqrt{2} \quad \text{with } (k = 1,2,3) \end{aligned} \tag{2.25}$$

One has to note that the masses are proportional to v that has a fixed value of 246 GeV [21] and to the Yukawa couplings that are unknown parameters of the SM. Masses are set to the right value by choosing the Yukawa coupling accordingly to the observations. The absolute neutrino mass is not known but from our current knowledge, a coupling about 5 orders of magnitudes lower than the one of electron is needed what seems unnatural.

Besides, one can see from equation 2.24 that the meSM Higgs-lepton Yukawa La-

grangian is invariant under a global U(1) gauge transformation:

$$\begin{aligned} \nu_{kL} &\to e^{i\phi}\nu_{kL}, \qquad \nu_{kR} \to e^{i\phi}\nu_{kR}(k = 1, 2, 3) \\ l_{\alpha L} &\to e^{i\phi}l_{\alpha L}, \qquad l_{\alpha R} \to e^{i\phi}l_{\alpha R}(\alpha = e, \mu, \tau) \end{aligned} \tag{2.26}$$

leading through Noether's theorem to the conservation of the global lepton number and the individual lepton numbers. These last ones are nevertheless violated by the flavor changing due to oscillations (see section 2.2).

2.3.2 Majorana mass term

Fermion fields are described by spinors ψ that obey to the Dirac equation:

$$(i\gamma^\mu \partial^\mu - m)\psi = 0 \tag{2.27}$$

with γ^μ the 4×4 Dirac matrix and m the fermion mass.
By considering that $\psi = \psi_L + \psi_R$, the equation leads to the following relations:

$$\begin{aligned} i\gamma^\mu \partial^\mu \psi_L &= m\psi_R \\ i\gamma^\mu \partial^\mu \psi_R &= m\psi_L \end{aligned} \tag{2.28}$$

with ψ_L and ψ_R being respectively the left-handed and right-handed chiral fields that have two components. Thereby a fermion is described by a four components spinor unless being massless, depending only on two independent components and having besides helicity equal to chirality. In 1937, E. Majorana showed the possibility for fermions to build a mass term with only two components at the condition of being electrically neutral. According to the relations 2.28, he showed that the field should fulfill the following equation:

$$\psi = \psi_L + \psi_R = \psi_L + \psi_L^c \tag{2.29}$$

where $\psi_L^c = C\bar{\psi_L}^T$ is a right-handed field obtained from ψ_L through the operation of charge conjugation. One can see that $\psi^c = \psi$ showing that the fermion should not have an electric charge implying that only neutrinos can be subject to Majorana

mass term of the type[16]:

$$\mathcal{L}^{M}_{mass} = -\frac{1}{2} m_M \bar{\nu^c_L} \nu_L + h.c. \tag{2.30}$$

while it can be represented by the following in the Dirac case:

$$\mathcal{L}^{D}_{mass} = -m_D \bar{\nu_R} \nu_L + h.c. \tag{2.31}$$

since a mass term needs only both left-handed and right-handed fields.
Furthermore, one can remark from equation 2.30 that this mass Lagrangian is not invariant under the transformation in the first row of equation 2.26 leading to the violation by two units of the global lepton number. Since the interaction Lagrangian preserves the lepton number, the neutrino nature can only be investigated through processes with a 'spin flip' (change of helicity) whose amplitude are proportional to the mass, like the double β-decay without emission of neutrinos ($2\beta0\nu$) (see section 2.3.4).

2.3.3 See-saw mechanism

A general mass term can be written mixing Dirac's and Majorana's:

$$\mathcal{L}^{D+M}_{mass} = -\frac{1}{2} (\bar{\nu^c_L}, \bar{\nu_R}) \begin{pmatrix} m_L & m_D \\ m_D & m_R \end{pmatrix} \begin{pmatrix} \nu_L \\ \nu^c_R \end{pmatrix} + h.c. \tag{2.32}$$

with m_L the left-handed neutrino Majorana mass, m_R the right-handed neutrino one and m_D the Dirac mass.
The diagonalization of the mass matrix can be made with an orthogonal matrix of parameter θ:

$$\begin{pmatrix} \nu_L \\ \nu^c_R \end{pmatrix} = \begin{pmatrix} \cos\theta & \sin\theta \\ -\sin\theta & \cos\theta \end{pmatrix} \begin{pmatrix} \nu_{1L} \\ \nu_{2L} \end{pmatrix} \tag{2.33}$$

leading to:

$$\tan 2\theta = \frac{2m_D}{m_R - m_L} \quad \text{and} \quad m_{2,1} = \frac{1}{2} \left(m_L + m_R \pm \sqrt{(m_L - m_R)^2 + 4m_D^2} \right) \tag{2.34}$$

In the meSM, a mass term for the left-handed neutrino is not allowed because it implies a term with isospin equal to one while no Higgs triplet is available.

[16]The factor 1/2 avoids the double counting in the Euler-Lagrange equation

Meanwhile the right-handed neutrino is an electroweak singlet and thus its mass is not protected. The see-saw mechanism arises for $m_L = 0$ and $m_R \gg m_D$ that implies:

$$m_2 \simeq m_R, \qquad m_1 \simeq \frac{m_D^2}{m_R} \qquad \text{and} \qquad \tan\theta \simeq \frac{m_D}{m_R} \ll 1 \tag{2.35}$$

In this configuration, the 'neutrino 2' coincides with the sterile right-handed neutrino of mass m_R while the left-handed neutrino, coinciding with the 'neutrino 1', gets a mass proportional to the Dirac mass but suppressed by m_R. Since m_R can take any value, it is commonly supposed that it is related with the grand unification scale (where the coupling constant of the three interactions are similar) around the planck scale at 10^{16} eV explaining meanwhile the smallness of the neutrino mass and giving a good candidate for the dark matter with ν_R[17].

2.3.4 Neutrino mass from experiments

The absolute scale of neutrino masses has not yet been revealed by experiments. It is actively searched in β-decay experiments, $2\beta0\nu$ and in cosmology.

β-decay experiments

β^-decay is a three body decay with the emission of an electron and a $\bar{\nu}_e$:

$${}^A_Z Y \rightarrow {}^A_{Z+1} X + e^- + \bar{\nu}_e \tag{2.36}$$

The mass difference between the initial and final states gives the excess energy Q (end point) that is shared between the $\bar{\nu}_e$ and the e^- by neglecting the X atom recoil. Hence if the neutrino is massive, it affects the Q value but also the differential decay rate $\frac{dN}{dT}$ given by [22]:

$$\frac{dN}{dT} \propto (Q-T)\sqrt{(Q-T)^2 - m_{\bar{\nu}_e}^2} \tag{2.37}$$

where T is the e^- kinetic energy and $m_{\bar{\nu}_e}$ the neutrino mass.

One can see on figure 2.4 and from equation 2.37 that the effect of the neutrino mass is the most pronounced close to the end point. Consequently the β decaying isotope has to be chosen in order to have as much decay as possible in this region. This is achieved with an atom showing a small Q-value (18.57 keV) and short

[17] Our universe has been found to be composed at ~25% of matter whose nature is still unknown called dark matter.

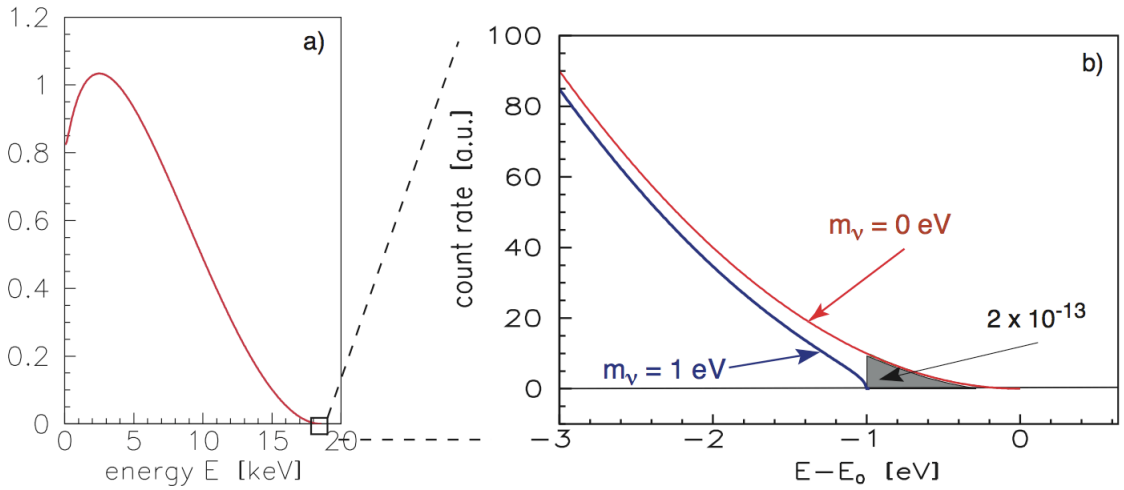

Figure 2.4: The electron energy spectrum of tritium β decay: (a) complete and (b) narrow region around end point E. The β spectrum is shown for neutrino masses of 0 and 1eV [22].

halflife time (12.3 years) as Tritium (^3H). Experimentally, electrons of the Q-value region are selected thanks to the combination of magnetic and electric fields. The past experiments Mainz [23] and Troitzk [24] measured respectively at 95% C.L.:

$$\begin{aligned} m_{\bar{\nu}_e} &< 2.3 \text{ eV} \\ m_{\bar{\nu}_e} &< 2.5 \text{ eV} \end{aligned} \tag{2.38}$$

The two collaboration have merged in an experiment with an improved sensitivity called KATRIN that will soon start and try to lower the sensitivity down to 0.2 eV at 90% [22]. It has to be noticed that these experiments give access to an effective mass given by:

$$m^2_{\bar{\nu}_e} = \sum_{k=1,2,3} |U_{ek}|^2 m_k^2 = c_{12}^2 c_{13}^2 m_1^2 + s_{12}^2 c_{13}^2 m_2^2 + s_{13}^2 m_3^2 \tag{2.39}$$

Neutrinoless double β-decay experiments

In the SM, double β-decay ($2\beta 2\nu$) is a second order electroweak transition overwhelmed by the classical β decay unless the latter is forbidden. This happens for instance to the ^{76}Ge where the β decay daughter nucleus ^{76}As has a higher energy level on the contrary of ^{76}Se (see left panel on figure 2.5) allowing the $2\beta 2\nu$ to be viewed through the spectrum of the two e^-. An interesting case is the possibility to see the neutrino emitted at the first β vertex being reabsorbed at the second β

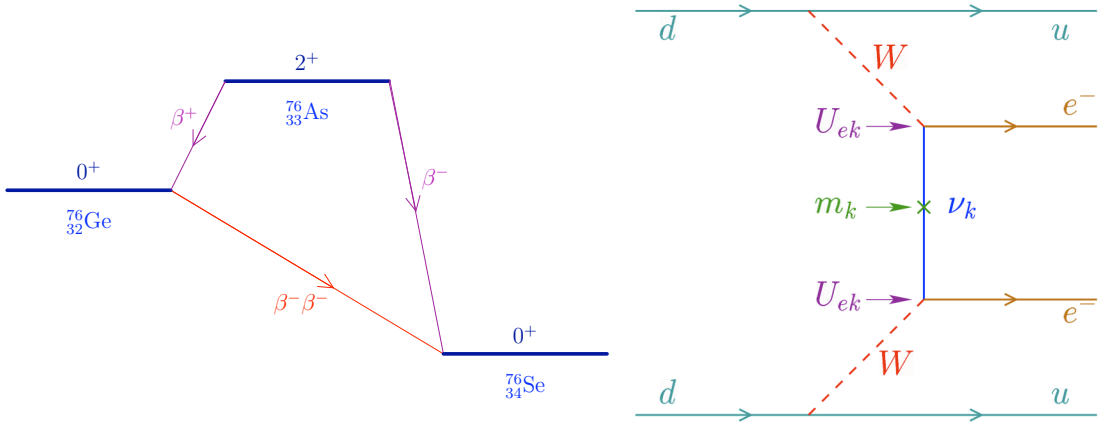

Figure 2.5: Left panel: diagram showing the ^{76}Ge, ^{76}As and ^{76}Se levels and the favorable situation of $2\beta2\nu$ for ^{76}Ge. Right panel: Feynman diagram of the $2\beta0\nu$ [25].

vertex. Let us take for instance the case of $2e^-2\bar{\nu}_e$. The antineutrino emitted at the first vertex has positive helicity while to be absorbed at the second vertex, it should be a neutrino of negative helicity. Thereby this reaction is uniquely possible for massive Majorana neutrinos[18] (right panel of figure 2.5).
The $2\beta0\nu$ halflife of a nucleus $\mathcal{N}$, $T^{0\nu}_{1/2}(\mathcal{N})$ is given by [28]:

$$\left[T^{0\nu}_{1/2}(\mathcal{N})\right]^{-1} = G^{\mathcal{N}}_{0\nu}|\mathcal{M}^{\mathcal{N}}_{0\nu}|^2|m_{2\beta}|^2 \tag{2.40}$$

where $\mathcal{M}^{\mathcal{N}}_{0\nu}$, $G^{\mathcal{N}}_{0\nu}$ are respectively the nuclear matrix element and the phase space factor, and $m_{2\beta}$ is the effective Majorana mass.
This relation implies that in addition to choosing the element with a β decay suppressed, one should look for the highest phase space factor element corresponding to the highest end point nucleus. Several experiments have been carried out with different techniques (germanium crystals, bolometers, tracking detectors) reaching a sensitivity of about $m_{2\beta} = 0.2 - 1$ eV. No signal has been observed except for a group that claimed the observation of a signal corresponding to $m^{2\beta} = 0.11 - 0.56$ eV at 95% C.L. [26] already disfavored [27]. The new generation experiments with an increased mass (for a brief review see [28]) will try to reach a sensitivity one order of magnitude better, about $m^{2\beta} = 20 - 100$ meV, checking the consistency of this signal.

[18] From equation 2.28, a Dirac particle has the two helicities only if it is massive. Furthermore, only Majorana neutrino exhibits the equality particle-antiparticle.

The effective Majorana mass implied in $2\beta0\nu$ is given by:

$$m_{2\beta}^2 = \sum_{k=1,2,3} U_{ek}^2 m_k^2 = c_{12}^2 c_{13}^2 m_1^2 + e^{i\alpha_2} s_{12}^2 c_{13}^2 m_2^2 + e^{i\alpha_3} s_{13}^2 m_3^2 \tag{2.41}$$

where α_2, α_3 are Majorana phases. Since the mass Lagrangian is no more invariant under U(1) gauge transformations, three phases of the mixing matrix can no more be absorbed by the charge current bringing in the Dirac phase (already present in the normal case) and two Majorana phases that are factorized on the right of the mixing matrix. They have no effect on the neutrino dynamic but can lead to a suppression of the effective neutrino mass.

Neutrino mass in cosmology

In the early universe, neutrinos were in equilibrium with the primordial plasma. As the universe expanded the rate of interactions decreased leading to the decoupling first of neutrinos followed by photons. The temperature of neutrinos at that time can be inferred from the photon temperature determined precisely thanks to the cosmic microwave background (CMB). From their temperature, one can deduce the present contribution to the universe energy density that is constrained by astronomical data. This constraint is transformed into a bound on the sum of the neutrino masses. Furthermore since neutrinos were relativistic at the time of decoupling, they must have suppressed the formation of small scale structures but participated to clustering on large scales resulting in changes in the matter power spectrum, The heavier the neutrino masses, the more pronounced the effect. Consequently, a constraint on the neutrinos masses can be derived from the survey of the angular matter power spectrum and particularly of large scale structures (galaxy distribution). Combining these two constraints, the cosmological bound on neutrino masses is at 95% C.L. [29]:

$$\sum_k m_k < 0.72 \text{ eV} \tag{2.42}$$

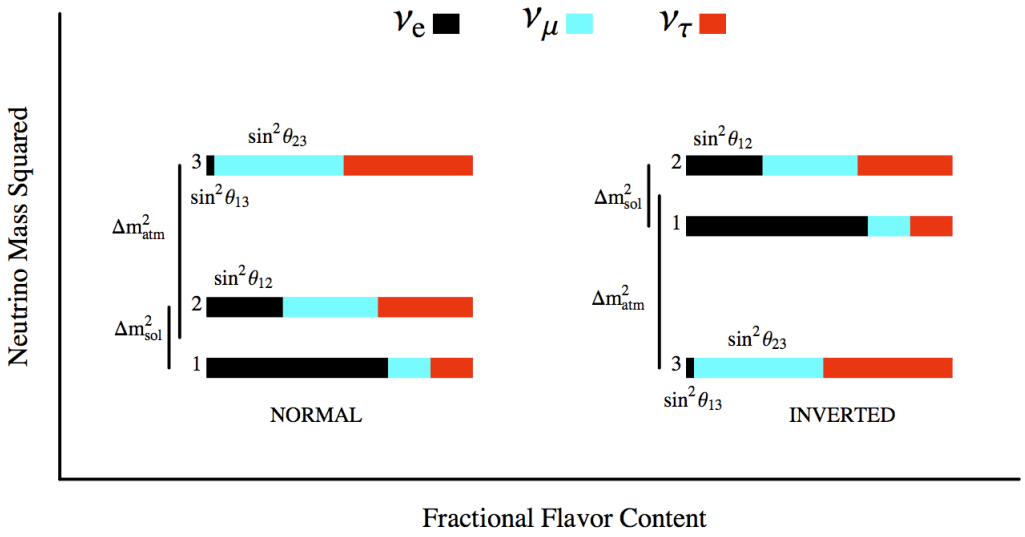

Figure 2.6: There is two possible situations for the mass hierarchy in light of the neutrino oscillation experiments, the normal and inverted hierarchies [30].

Mass hierarchy

Neutrino oscillations experiments have measured two mass squared differences (see section 3.4):

$$\Delta m^2_{sol} = \Delta m^2_{12} \simeq 7.58 \times 10^{-5}\ \text{eV}^2 \quad \text{and} \quad \Delta m^2_{atm} = |\Delta m^2_{32}| \simeq 2.43 \times 10^{-3}\ \text{eV}^2 \tag{2.43}$$

where the sign of Δm^2_{12} has been determined thanks to MSW effect on solar neutrinos. Through relation 2.21, Δm^2_{31} is given by:

$$\Delta m^2_{31} = m^2_1 - m^2_3 = \Delta m^2_{21} + \Delta m^2_{32} \simeq \Delta m^2_{atm} \tag{2.44}$$

From these observations, two possible situations arise as can be seen on figure 2.6:

- the 'normal hierarchy' (NH) where Δm^2_{32} is positive. In this situation, we have $m_3 > m_2 > m_1$. This situation seems natural since the ν_e that is essentially composed of ν_1 is lighter than the other generations mainly composed of ν_2 and ν_3.
- the 'inverted hierarchy' (IH) where Δm^2_{32} is negative. In this situation, we have $m_2 > m_1 > m_3$.

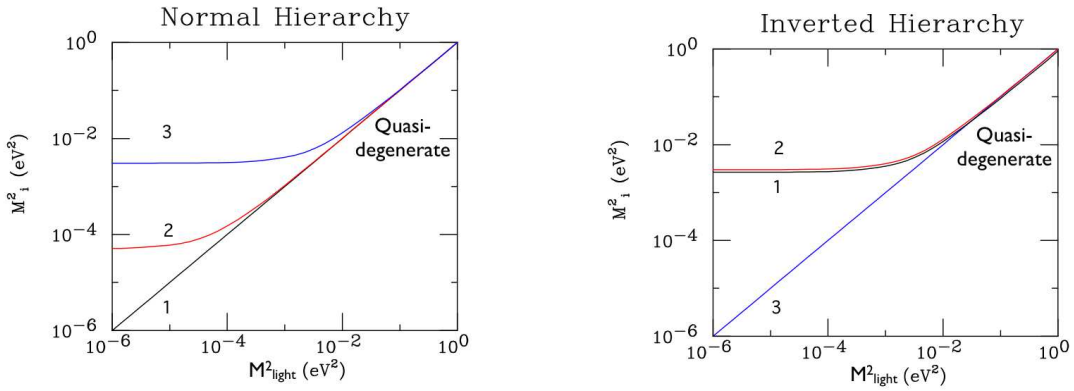

Figure 2.7: Mass value expectations as a function of the lightest mass value in the normal and inverted hierarchies [30].

The absolute mass scale is not known but one can deduce the situation to be expected as a function of the lightest mass. For the NH, the relations are:

$$\begin{aligned} m_2^2 &= m_1^2 + \Delta m_{12}^2 \simeq m_1^2 + \Delta m_{sol}^2 \\ m_3^2 &= m_1^2 - \Delta m_{31}^2 \simeq m_1^2 + \Delta m_{atm}^2 \end{aligned} \tag{2.45}$$

For the IH, we have:

$$\begin{aligned} m_1^2 &= m_3^2 + \Delta m_{31}^2 \simeq m_3^2 + \Delta m_{atm}^2 \\ m_2^2 &= m_3^2 + \Delta m_{31}^2 - \Delta m_{21}^2 \simeq m_3^2 + \Delta m_{atm}^2 \end{aligned} \tag{2.46}$$

From these relations, one can remark that the decoupling between masses can occur only for a mass of nearly $\sqrt{\Delta m_{atm}^2}$, otherwise the masses are in a 'quasi-degenerate' (QD) state. On the other hand, after this limit, in the NH case the two heaviest masses can be decoupled on the contrary of the IH case. The masses behaviour are represented on figure 2.7. The current experimental bounds on the absolute scale of neutrino masses are for now in the QD state but the new generation of experiments will soon bring informations capable of rejecting the QD case and possibly test the IH case. Indeed, the expected sensitivities of the upcoming experiments on β-decay and $2\beta0\nu$ will definitely test the QD state while cosmology experiments with possible new probes under study (weak lensing, baryon acoustic oscillations) will soon bring the most stringent bound on neutrino masses, possibly testing the IH case [31].

Chapter 3

Phenomenology of neutrino mixing

The establishment of neutrino oscillation took a long time, the first indication was observed in 1968 and the confirmation came 30 years later. This long road began with the observation of a deficit of neutrinos with respect to the solar model calculation and still the oscillations have not been fully characterized.
In this chapter, we review the experiments that led the way towards the establishment of neutrino oscillation, we consider separately the history of solar and atmospheric neutrinos experiments. Then we describe the verifications performed with man-made neutrinos: accelerator and reactor experiments. Finally, we present the conclusion of these measurements, the parameters determined and those that remain unknown.

3.1 Solar neutrino anomaly

The sun shines because of energy production by thermonuclear fusion reactions. The nuclei produced have a mass lower than the sum of the constituting nucleons one and thus the energy excess is released as photons and neutrino kinetic energy. The overall fusion reaction is:

$$4p + 2e^- \rightarrow {}^4\mathrm{He} + 2\nu_e + 26.731 \text{ MeV} \tag{3.1}$$

Two reactions happening in the core lead to this equation, they are called the pp-chain and the CNO cycle with the pp-chain being the main responsible of the

overall heat production. It is a chain of reactions initiated by the fusion of two protons whereas the CNO cycle begins with the fusion of ^{14}C with a proton up to the fusion of ^{15}N with a proton producing back ^{14}C and so forth. A 'Standard Solar Model' (SSM) [32, 33] based on these reactions, the best available physics data and fitting the observations was developed. The details of the neutrino flux expectations are displayed on figure 3.1. The sun is a very abundant source of

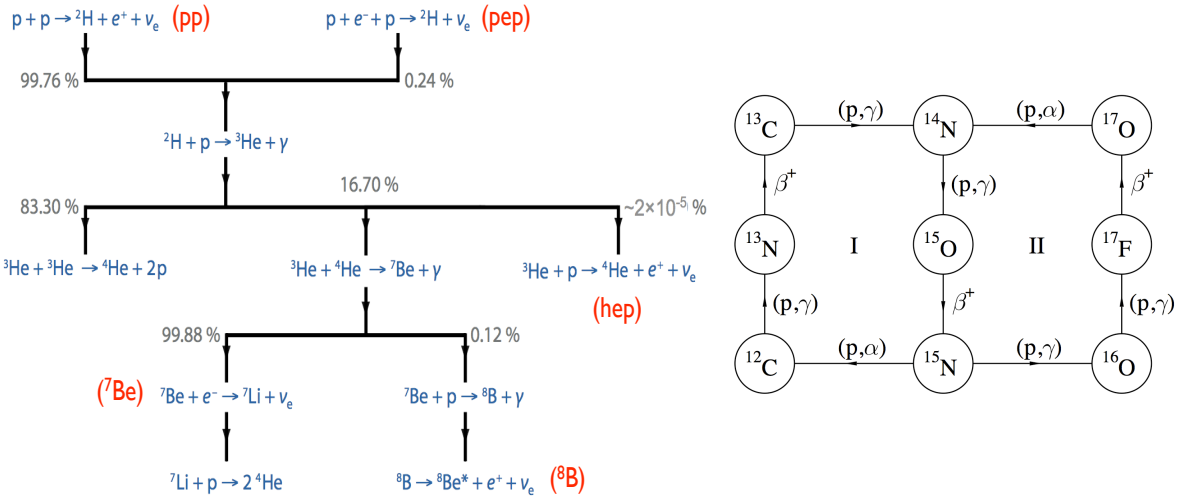

Figure 3.1: pp-chain (with the names associated to the ν_e) on left panel and CNO cycle approximated to the two main loops on right panel [34]. When producing energy, the sun produces as well electrons neutrinos.

neutrinos on Earth with 6×10^{10} $\nu/\text{cm}^2\text{s}$. The flux as a function of the energy is displayed on figure 3.2.

Several experiments were sensitive to these neutrinos as Homestake [36], GALLEX /GNO [37], SAGE [38], Kamiokande [39], Super-Kamiokande [40] and SNO [41]. They will be briefly reviewed in the following. They made measurements of the flux of solar neutrinos on Earth with different energy thresholds and compared with the expectations based on the SSM. Since the neutrinos are weakly interacting particles, they are a unique probe of the good understanding of the mechanism happening in the core of the Sun.

3.1.1 The Homestake experiment

Homestake was the first experiment built to detect the solar neutrinos, the goal was to check the validity of the SSM. The experiment was sensitive to ν_e through

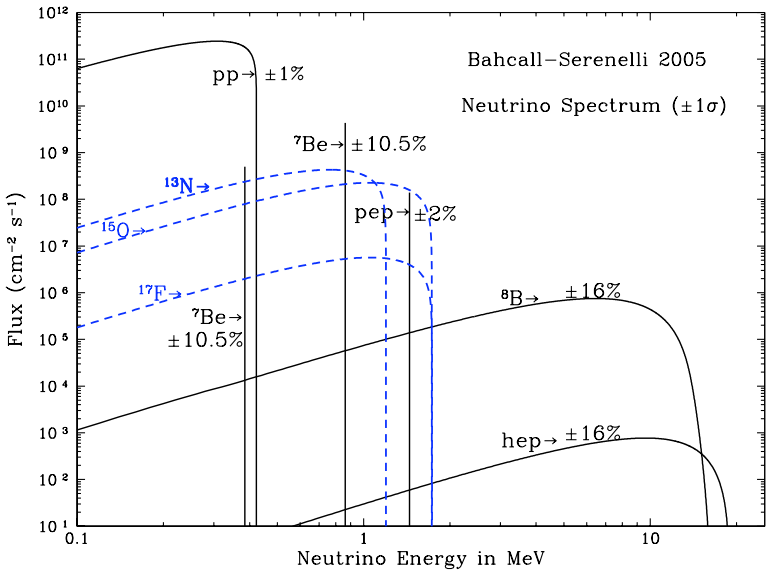

Figure 3.2: Neutrino fluxs in cm^{-2} s^{-1} MeV^{-1}(cm^{-2} s^{-1} for lines) as a function of energy for the pp-chain and the two main loops of the CNO cycle in blue. Figure taken from [35].

the following radiochemical reaction:

$$\nu_e + {}^{37}\mathrm{Cl} \rightarrow {}^{37}\mathrm{Ar} + e^- \tag{3.2}$$

that has an energy threshold E_ν^{thr}=0.814 MeV. This implied that only the high energy part of the neutrino spectrum with low flux was detectable, those called ^{7}Be and especially ^{8}B.

The experiment was built in 1965-1967 in a gold mine in South Dakota (U.S.A.) that provided a protection of 4200 m.w.e.[1] against cosmic rays. It was a cylindrical tank containing 615 tons of tetrachloroethylene (C_2Cl_4). Every two months, ^{37}Ar was extracted by chemical methods and placed in a proportional counter to count the number of atoms[2]. Using artificial Argon placed in the tank, the experiment proved that the extraction technique was working properly. The first data in 1968 indicated a flux lower than the expectations with less than 3 'Solar Neutrino Units' (SNU)[3] [42]. About 30 years later and with a highly reduced statistical error,

[1] mwe: meter water equivalent.

[2] ^{37}Ar is a noble gas that is extracted by flushing the Chlorine tank. The ^{37}Ar atoms placed in the counter capture a low orbit electron: $^{37}\mathrm{Ar} + e^- \rightarrow {}^{37}Cl + \nu_e$, yielding subsequently an Auger electron detected by the counter.

[3] 1 SNU = 10^{-36} events atoms^{-1} s^{-1}

the results were still pointing a deficit with respect to the calculations with $2.56 \pm 0.16(stat.) \pm 0.16(syst.)$ SNU (cf. fig. 3.3). Only one third of the total flux expected from SSM calculations was detected with a discrepancy of 3.3σ. The discrepancy with the expectations over the years was named 'solar anomaly' and was later confirmed by other experiments like the Gallium ones.

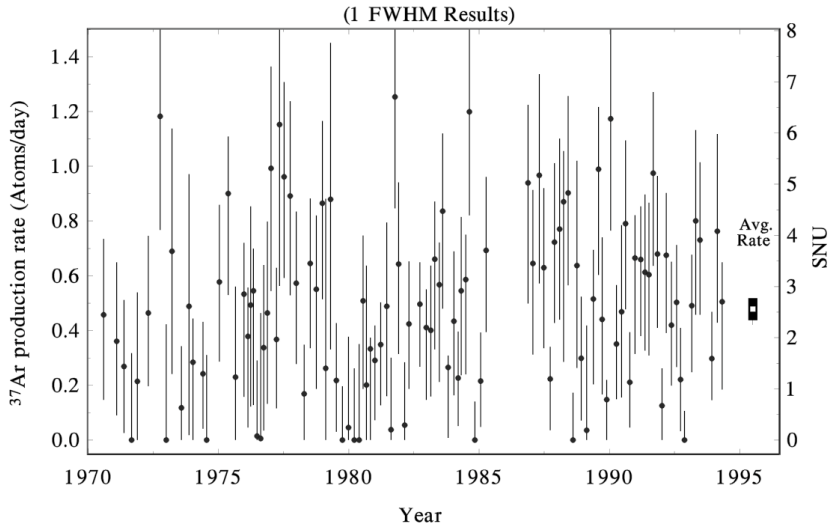

Figure 3.3: Individual results of ^{37}Ar production rate in atoms/day and the corresponding capture rate in SNU over 24 years [36]. The errors bars shown are statistical.

3.1.2 Gallium experiments

There were three experiments using Gallium to detect the solar neutrinos: GALLEX, GNO and SAGE, with GNO being an upgrade of GALLEX. They used the following radiochemical reaction:

$$\nu_e + {}^{71}\mathrm{Ga} \rightarrow {}^{71}\mathrm{Ge} + e^- \tag{3.3}$$

that has an energy threshold E_ν^{thr}=0.233 MeV. Like Homestake, these experiments were sensitive to ^{8}B and ^{7}Be neutrinos, but most notably, also to the most abundant pp neutrinos with the ratios being respectively 9%, 27% and 54%.
These experiments extracted the ^{71}Ge by chemical methods every 30 days and placed it in proportional counters to count the number of atoms[4]. The experiments

[4]The number of atoms was determined from the observed number of ^{71}Ge decays to ^{71}Ga.

used intense artificial ^{51}Cr neutrino source for calibration[5] which confirmed the good understanding of the detectors. Their measurements confirmed the solar anomaly but, unlike the Homestake experiment, the flux found was about one half of the total expected flux.

GALLEX/GNO

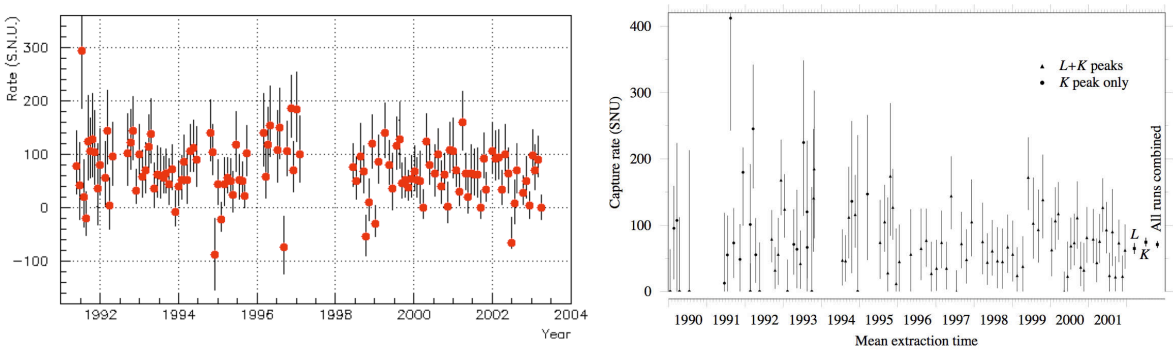

Figure 3.4: Capture rate in SNU of the individual measurements of the GALLEX/GNO (left) and SAGE experiments (right) [37, 38]. The errors bars shown are statistical.

GALLEX stands for GALLium EXperiment. It was located in the Laboratori Nazionali del Gran Sasso (LNGS) in Italy that has an overburden of 3300 mwe. The detector consisted of a 100 ton of liquid gallium chloride ($GaCl_3$-HCl) solution containing 30.3 tons of Gallium. GALLEX started in 1991 and stopped in 1997 for an upgrade of the extraction equipment. The name changed to GNO (Gallium Neutrino Observatory) when the data taking restarted in 1998 for a final stop in 2003. The capture rate was found to be $69.3 \pm 4.1(stat.) \pm 3.6(syst.)$ SNU with $>5\sigma$ deviation from the SSM expectations (cf. fig. 3.4) [37].

SAGE

The Soviet-American Gallium Experiment (SAGE) was located in the Baksan Neutrino Observatory in Russia at a depth of 4700 mwe. Measurements from 1990 to 2001 showed a capture rate of $70.8^{+6.5}_{-6.1}$ SNU (cf. fig. 3.4) [43]. New measurements performed with a reduced systematic error from 2002 to 2007 yielded a capture rate of $65.4^{+3.1}_{-3.0}(stat.)^{+2.6}_{-2.8}(syst.)$ SNU pointing out as well a $>5\sigma$ discrepancy [43].

[5]The ^{51}Cr has a Q-value of 753 keV with a typical decay time of 27.7 days making it suitable for calibration.

3.1.3 Water Čerenkov experiments

A charged particle that travels at a speed higher than the speed of light in a medium will give rise to a radiation called Čerenkov light. This light is emitted along the particle path with an opening angle depending of the refractive index of the medium and the speed of the particle. Part of the light is emitted between 300 and 600 nm making it detectable by photo-multiplicators tubes(PMTs). A detector with a good photocathode coverage allows to have an efficient track reconstruction through photons arrival time on PMTs leading to the energy determination thanks to the particle range measurement.
Kamiokande and Super-Kamiokande are water Čerenkov experiments. They are optimized for events of energy >100 MeV but they could also be sensitive to solar neutrinos through elastic scattering:

$$\nu_\alpha + e^- \rightarrow \nu_\alpha + e^- \tag{3.4}$$

where α stands for the three neutrino species: e, μ, and τ. This reaction cross section is however six times larger for electrons since charged current is also possible. This reaction has no physical energy threshold, although energy cuts are needed to reduce the backgrounds. Moreover the e^- track direction is correlated with the incoming neutrino direction allowing to reject neutrinos not correlated with the Sun-earth direction (cf. fig 3.5).

Kamiokande

Kamiokande (Kamioka Nucleon Decay Experiment) was built for the search of nucleon decay and started in 1983. It was a 3 kton water cylinder located in the Kamioka mine in Japan at a depth of 2600 mwe. In order to have a good sensitivity to solar neutrinos, the experiment was upgraded in 1986 with a a water Čerenkov veto region against cosmic rays and the detection threshold was lowered to 7.2 and then 6.7 MeV.
Kamiokande was the first experiment to detect solar neutrinos in 'real-time' allowing in 1987 the first detection of a supernovae explosion through neutrinos [44]. Measurements were performed from 1987 to 1995 resulting in a ^{8}B flux of $\Phi_{^8_B} = 2.80 \pm 0.19(stat.) \pm 0.33(syst.)) \times 10^6$ cm^{-2} s^{-1}, little less than half the expected flux from the SSM [39] with a 2.2σ discrepancy. Kamiokande was stopped in 1996 when Super-Kamiokande started.

Super-Kamiokanke

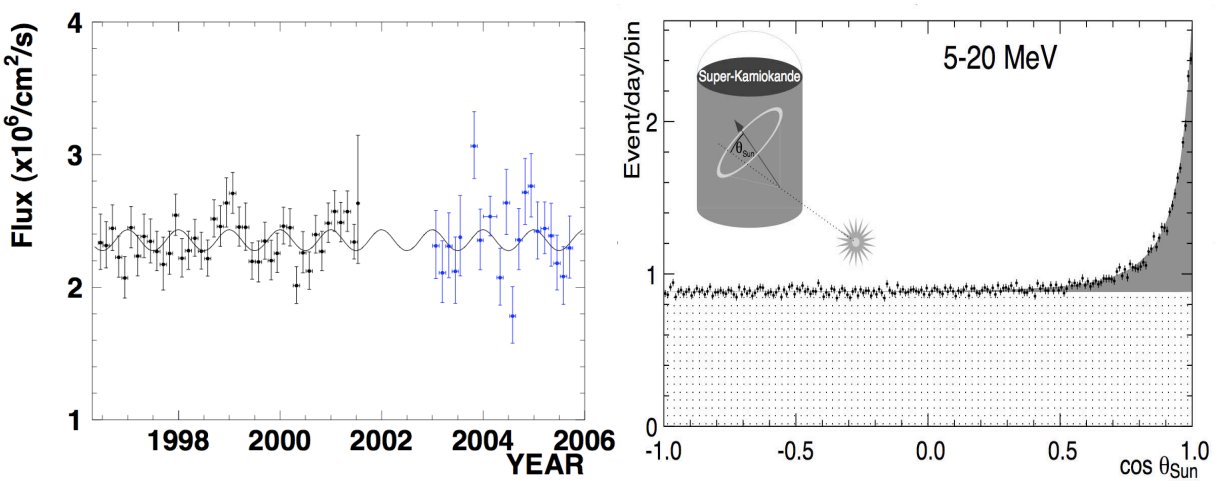

Figure 3.5: Left panel: Measured ^{8}B flux as a function of time in SK-I and SK-II [45], the errors bars shown are statistical. Right panel: number of solar neutrino candidates per bin and per day as a function of the angle between the interaction point-sun direction and the interaction point-charged lepton direction [40].

Super-Kamiokande (SK) was an improvement of the Kamionkande experiment. SK is as well located in the Kamioka mine at 500 m from the former location of Kamiokande now replaced by KamLAND (see section 3.4). The mass was enlarged to 50 kton (22.5 kton fiducial mass) and the photocathode coverage was increased from 20% to 40%. The detector is as well surrounded by an optically separated water Čerenkov veto region. SK is still running in its fourth phase.
Measurements have been published on the two first phases confirming the anomaly observed in the previous experiments. The phase I (SK-I) started in April 1996 and ended in 2001 with the implosion of half of the PMTs leading to the phase II (SK-II) with 19% coverage. The measurements gave the following ^{8}B flux: $(2.35 \pm 0.05(stat.) \pm 0.08(syst.)) \times 10^6$ cm^{-2} s^{-1} for SK-I and $(2.38 \pm 0.05(stat.)^{+0.16}_{-0.15}(syst.)) \times 10^6$ cm^{-2} s^{-1} for SK-II (cf. fig. 3.5) with respectively an energy threshold of 5 MeV and 7 MeV (cf. fig. 3.5) [40, 45]. The discrepancy with the SSM is about 2.6σ. The PMTs were replaced for SK-III and SK-IV phases currently active.

SNO

The Sudbury Neutrino Observatory (SNO) experiment has solved in 2001 the solar neutrino anomaly by showing that solar neutrinos undergo flavor transitions during their travel to the Earth [46].

The SNO detector is located in the Creighton Mine in Ontario (Canada) at a depth of 5890 mwe. It is made of 1 kton of heavy water (^2H_2O) contained in a 12 m diameter acrylic sphere surrounded by a water volume instrumented with 9456 PMTs equipped with light concentrators for a photocathode coverage of about 55%. An additional cosmic muon veto volume filled with water surrounds the inner detector. This detector was sensitive to solar neutrinos through different channels:

$$\text{CC} : \nu_e + d \rightarrow p + p + e^- \tag{3.5}$$

$$\text{NC} : \nu_\alpha + d \rightarrow \nu_\alpha + p + n \tag{3.6}$$

$$\text{ES} : \nu_\alpha + e^- \rightarrow \nu_\alpha + e^- \tag{3.7}$$

where CC stands for charged current, NC for neutral current and ES for elastic scattering.

The CC reaction has an energy threshold of 1.442 MeV whereas the NC reaction has a 2.224 MeV threshold and the ES reaction has zero physical threshold. However due to the background, a 5.5 MeV threshold was used leading the SNO experiment to be sensitive only to ^{8}B neutrinos.

The experiment had different phases corresponding to different techniques for the neutron detection in the NC reaction. This reaction was very important since it was equally sensitive to the different neutrino species. In the phase-I, from 1999 to 2001, the neutron was detected through capture on deuterium yielding a 6.25 MeV γ. In the phase-II, from 2001 to 2003, 2 kg of salt (NaCl) were dissolved in the heavy water for a quicker neutron capture (on ^{35}Cl) and better detection efficiency (γ's of 8.57 MeV). Moreover the γ's are emitted isotropically in the reaction improving the separation between e^-(CC) and n(NC).

The measurements of the ^{8}B fluxes with the three reactions for the phase-I are the following [47]:

$$\Phi_{CC} = (1.68 \pm 0.06^{+0.08}_{-0.09}) \times 10^6 \text{ cm}^{-2} \text{ s}^{-1} \tag{3.8}$$

$$\Phi_{NC} = (4.94 \pm 0.21^{+0.38}_{-0.34}) \times 10^6 \text{ cm}^{-2} \text{ s}^{-1} \tag{3.9}$$

$$\Phi_{ES} = (2.35 \pm 0.22 \pm 0.15) \times 10^6 \text{ cm}^{-2} \text{ s}^{-1} \tag{3.10}$$

The CC reaction gives access to the ν_e flux Φ_{ν_e}. The muon plus tau flux $\Phi_{\nu_{\mu,\tau}}$ is derived from the following relations:

$$\Phi_{NC} = \Phi_{\nu_e} + \Phi_{\nu_{\mu,\tau}} \qquad \text{and} \qquad \Phi_{ES} = \Phi_{\nu_e} + 0.1553 \times \Phi_{\nu_{\mu,\tau}} \tag{3.11}$$

Fgure 3.6 shows $\Phi_{\nu_{\mu,\tau}}$ as a function of Φ_{ν_e} flux the SNO measurements together with the SK ES data and with the SSM calculations. This figure clearly shows that the ν_e's change flavor on the way to Earth, resolving the solar neutrino anomaly.

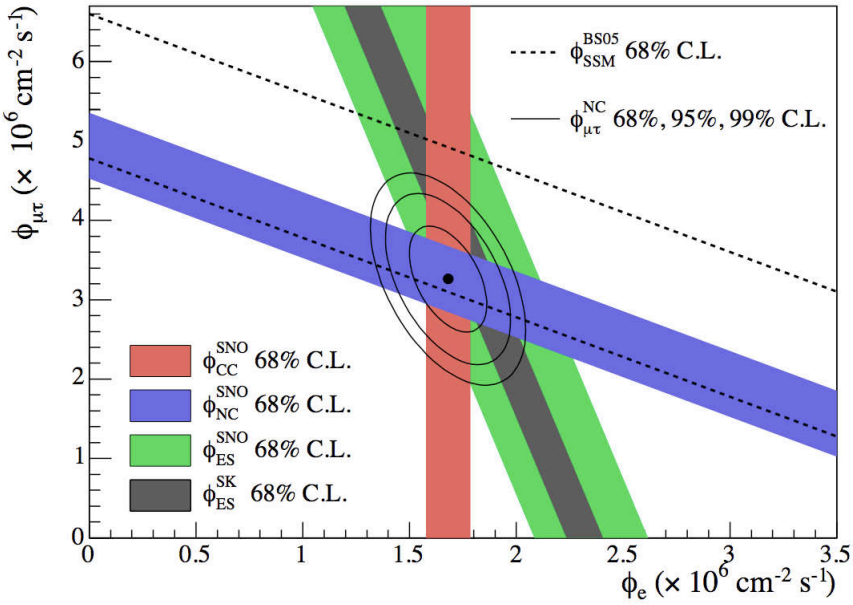

Figure 3.6: ^{8}B flux determined through the three reactions available with the SNO detector together with the SSM calculations. We can see that the measurements are compatible with the SSM calculations [41] upon neutrino oscillation.

3.1.4 Solar anomaly summary

The essence of the solar neutrino anomaly was the fact that all experiments were in disagreement with the SSM predictions but with apparent inconsistency while the SSM received a strong confirmation from helioseismology. Indeed helioseismological observations gave informations on the sound speed and the matter density in the interior of the Sun that have been found in agreement with the SSM [33]. A natural explanation was that the experiments were wrong, however they had been accurately calibrated[6] showing the correctness of the measurements. Moreover the Čerenkov experiments showed the correlation of the detected neutrinos with the Sun (cf. fig. 3.5). The anomaly seemed then due to some unknown particle physics and particularly neutrino oscillations that could accommodate the available data. The breakthrough came first in the atmospheric neutrino experiments that are

[6]Except the Homestake experiment that has nevertheless checked the good understanding of the Ar extraction.

described below. Nevertheless the most beautiful proof of the existence of neutrino flavor transitions came from SNO with its model-independent measurement (see figure 3.7). The solar deficit is nowadays interpreted in terms of $\nu_e \rightarrow \nu_\mu$ oscillations

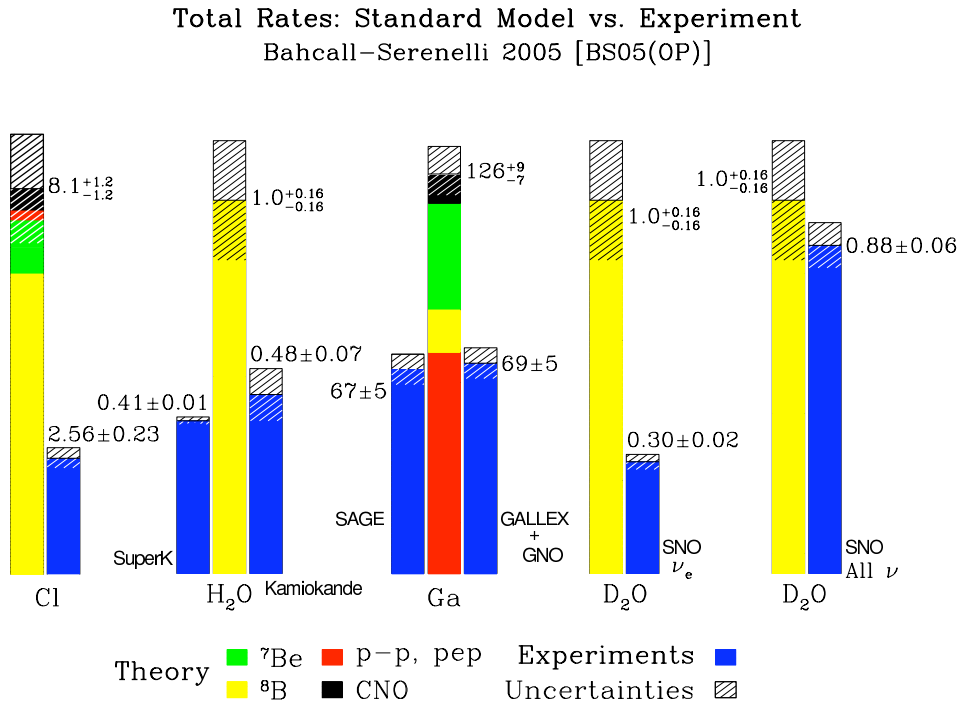

Figure 3.7: Solar neutrino measurements in SNU for Chlorine (=Homestake), H_20 (Kamiokande and SK) and Gallium (SAGE +GALLEX/GNO) experiments. The D_2O (SNO) mesurement are also shown normalized to the total expected flux. One can see that the deficit is dependent on the energy threshold while no deficit is observed when achieving a sensitivity to the three neutrino flavors. The figure is taken from [35].

but from the available experimental results, still several regions in the $\Delta m^2 - \sin^2 2\theta$ were allowed (cf. fig. 3.17). The Borexino experiment [48] that is a 100 ton fiducial mass liquid scintillator detector located in LNGS in Italy, was built in order to be sensitive to the ^{7}Be solar neutrinos in real-time (with energy measurement to select them) which can disentangle the different possible solutions since they give different survival probabilities. Data taking was foreseen for 2002 but a leakage of scintillator to the groundwater has lead to a break for 5 years. The final solution came from the KamLAND reactor experiment described in section 3.3.2 and was confirmed recently by Borexino [49].

3.2 Atmospheric neutrino anomaly

Interactions of cosmic rays (mainly protons) with nuclei of the Earth atmosphere produce hadrons. These hadrons are mainly π^-, π^+ whose decay produce $\bar{\nu}_\mu/\nu_\mu$ and subsequently $\bar{\nu}_e$,ν_μ/ν_e,$\bar{\nu}_\mu$ if the energy is low enough to allow the muon to decay before hitting the Earth through:

$$\begin{array}{lll} \pi^- \rightarrow \mu^- + \bar{\nu}_\mu & & \pi^+ \rightarrow \mu^+ + \nu_\mu \\ \downarrow & & \downarrow \\ \mu^- \rightarrow e^- + \bar{\nu}_e + \nu_\mu & & \mu^+ \rightarrow e^+ + \nu_e + \bar{\nu}_\mu \end{array} \tag{3.12}$$

The spectrum of the neutrinos goes from about 100 MeV to 10^4 GeV allowing them to be detected through charged current reactions:

$$\nu_l + N \rightarrow l^- + X \qquad \bar{\nu}_l + N \rightarrow l^+ + X \tag{3.13}$$

where l=e, μ, τ and N, X are nuclei.
The absolute flux of neutrinos suffers from uncertainty of about 20-30% so the ratio $\frac{\Phi_{\nu_\mu}+\Phi_{\bar{\nu}_\mu}}{\Phi_{\nu_e}+\Phi_{\bar{\nu}_e}}$ is commonly used. This ratio is very convenient since it should be equal to 2 at low energy[7] (see equation 3.12) with only a 5% uncertainty. Moreover, it is suited for water Čerenkov experiments that are not magnetized and therefore can not distinguish μ^-/e^- from μ^+/e^+. Nevertheless e/μ are distinguished from the Čerenkov cone pattern: due to showering and collisions, the electron ring is fuzzier than the muon-induced one. In what follows, the events will hence be denoted as μ-like and e-like events.

3.2.1 Water Čerenkov experiments

The Kamiokande and IMB (Irvine-Michigan-Brookhaven) experiments were water Čerenkov detectors (see section 3.1.3 for Kamiokande). These experiments published their results in terms of the ratio of ratios R that should be equal to 1. It is the ratio of the number of μ-like over e-like events divided by the same ratio

[7]The ratio is equal to 2 provided that the muon has time to decay before reaching the ground which means low energy pions. Moreovr, at high energy, there is more production of kaons instead of pions which shows three body decays involving the creation of ν_e.

calculated by Monte Carlo (MC):

$$R = \frac{(N_{\mu-like}/N_{e-like})_{data}}{(N_{\mu-like}/N_{e-like})_{MC}} \tag{3.14}$$

Kamiokande

In 1988, Kamiokande measured a number of sub-GeV (visible energy below 1.33 GeV) μ-like events that was 0.59 ± 0.07 of the Monte Carlo expectation while the number of e-like events was in agreement [50]. This observation was called 'atmospheric neutrino anomaly'. In the final results of the experiment, they determined the R ratio in the sub-GeV and multi-GeV (visible energy above 1.33 GeV) data separately leading to [51, 52]:

$$R_{\mu/e}^{\text{sub-GeV}} = 0.60^{+0.07}_{-0.06} \pm 0.05 \qquad R_{\mu/e}^{\text{multi-GeV}} = 0.57^{+0.08}_{-0.07} \pm 0.07 \tag{3.15}$$

IMB

These observations have been partially confirmed by the IMB experiment that was located in a salt mine in Ohio (U.S.A) providing an overburden of 1570 mwe. It was a cylinder filled with 8 kton of water observed by 2048 PMTs. The experiment took data from 1982 to 1991 and observed a consistent ratio below 1.5 GeV [53]:

$$R_{\mu/e}^{\text{sub-GeV}} = 0.54 \pm 0.05 \pm 0.11 \tag{3.16}$$

However no anomaly was found in the upward-going muon events [54] and the partially contained events above 1 GeV [55].

Super-Kamiokande

The Super-Kamiokande (SK) detector is described in section 3.1.3. Their measurement of the R ratio [56] confirmed the Kamiokande and IMB results [56]:

$$R_{\mu/e}^{\text{sub-GeV}} = 0.63 \pm 0.03 \pm 0.05 \qquad R_{\mu/e}^{\text{multi-GeV}} = 0.65 \pm 0.05 \pm 0.08 \tag{3.17}$$

Furthermore, SK brought the first clear evidence in favor of neutrino oscillations in 1998 by considering the upward/downward flux asymmetry:

$$A_{\alpha}^{up-down} = \left(\frac{U - D}{U + D}\right)_{\alpha} \tag{3.18}$$

where $\alpha = e, \mu$ and D/U are defined through the zenith angle θ_z. D corresponds to the downward-going neutrino event with $0.2 < \cos\theta_z < 1$, U corresponds to the upward-going neutrino events with $-1 < \cos\theta_z < -0.2$ that travels the Earth before reaching the detector.
Unlike the electron events, the muon events showed an asymmetry in the multi-GeV (cf. figure 3.8) considered as a $>6\sigma$ model-independent proof for muon neutrinos disappearance [57]:

$$A_e^{up-down} = -0.36 \pm 0.067 \pm 0.02 \qquad A_\mu^{up-down} = -0.296 \pm 0.048 \pm 0.01 \quad (3.19)$$

In 2004, an analysis on the events with a good resolution in energy and on the source to detector distance L (determined through the zenith angle) was performed leading to a very strong argument in favor of neutrino oscillations (cf. figure 3.8) [58] interpreted as $\nu_\mu \rightarrow \nu_\tau$ oscillations.

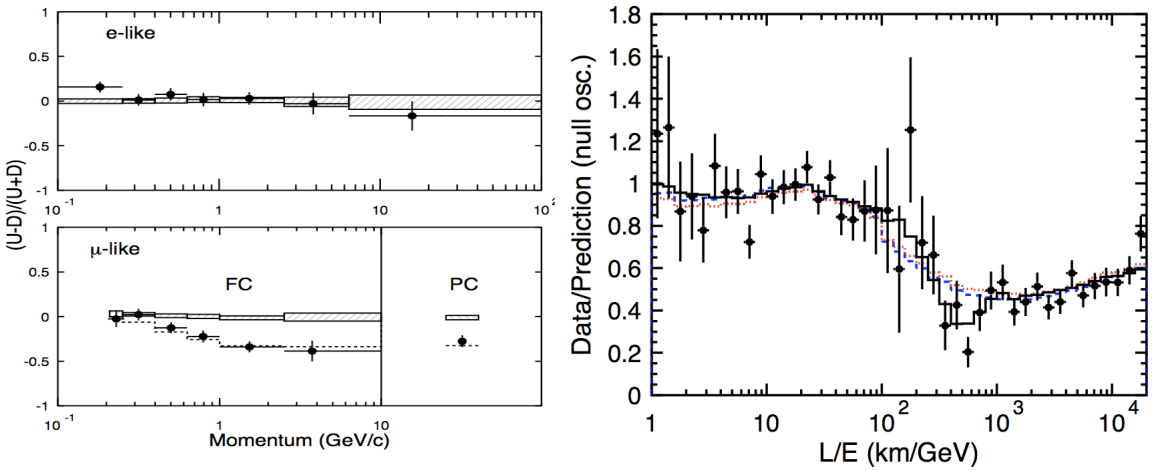

Figure 3.8: Left panel: asymmetry as a function the charged lepton momentum for e-like and μ-like events [57]. The boxes are the Monte Carlo expectations, the data are the black points with statistical error and the dotted line is the oscillation hypothesis. This indicates muon neutrino disappearance at high energy on the contrary of electron ones. Right panel: SK-I data over Monte Carlo ratio (black dots) as a function of L/E. The best fit is for the oscillation is black line [58] instead of neutrino decay (blue dashed line) and decoherence (red doted line).

3.2.2 The Soudan 2 and MACRO experiments

The Soudan 2 and MACRO (Monopole Astrophysics and Cosmic Ray Observatory) that were not based on the Čerenkov technique further confirmed the oscillation explanation in 2003.

Soudan 2

The Soudan 2 experiment was located in the Soudan mine in Minnesota (U.S.A.) at a depth of 2070 mwe. The detector was a 963 ton iron tracking calorimeter operated as a time projection chamber. The best sensitivity was obtained in events with energies above 300 and below 700 MeV. The experiment ran from 1989 to 2001 and obtained the following ratio R [59]:

$$R_{\mu/e}^{\text{sub-GeV}} = 0.69 \pm 0.10 \pm 0.06 \tag{3.20}$$

MACRO

The MACRO experiment was located in the LNGS in Italy at a depth of 3700 mwe. The detector was a large area scintillator with fine tracking granularity and time of flight measurement capabilities. Measurements of the upward through-going muons have shown a preference in favor of oscillations. MACRO considered the $A^1 = N_{low}/N_{high}$ and the $A^2 = N_{vert}/N_{horiz}$ ratios with N_{low} (N_{high}) being the events with energy below 30 GeV (above 130 GeV) and N_{vert} (N_{horiz}) being events with $\cos\theta_z \leq -0.7$ ($\cos\theta_z \geq -0.4$) [60]. The measurements are substantially lower than the expectations [60]:

$$A^1_{obs} = 0.85 \pm 0.16 \qquad A^1_{MC} = 1.50 \pm 0.25 \tag{3.21}$$

$$A^2_{obs} = 1.48 \pm 0.13 \qquad A^2_{MC} = 1.70 \pm 0.14 \tag{3.22}$$

where the errors quoted are for statistical for the measurements and systematic for the MC.

3.2.3 Atmospheric anomaly summary

The atmospheric anomaly began with the muon neutrinos deficit observation made by Kamiokande and only confirmed in the sub-GeV data by IMB. However the multi-GeV data suffer from limited statistic and moreover, the experiment had a small photocathode coverage (6%) and no outer detector to clearly disentangle the events that stopped in the detector from those who went through [61]. More problematic, the anomaly seemed to be observed only by the H_2O detectors since the two fine-grain iron calorimeter experiments using Fe as target for neutrinos

(NUSEX and Fréjus [62, 63]) saw no deficit at all[8]. This anomaly lasted for 10 years, up to the result of SK showing clearly a deficit dependence on the zenith angle at more than 6σ. The deficit was subsequently confirmed by the Soudan 2 and MACRO experiments that were using completely different detection techniques making even bigger the confidence in SK results. The atmospheric neutrino oscillation results derived from the experiments were further confirmed by the K2K and MINOS accelerator experiment described in the next section.

3.3 Validation with man-made neutrinos

Man-made neutrinos from reactors and accelerators were used since the early times to look for oscillations but they were unfortunately far from the signal region because the possible squared mass differences were believed to be of the order of the eV^2. The experiments that came later checked successfully the observed signal. We review briefly the past experiments and then in more detail those that brought confirmation of the oscillation and accurate parameter determination.

3.3.1 Accelerator experiments

Channel	Experiments
$\nu_\mu \to \nu_\mu$	CHARM
$\overset{(-)}{\nu}_\mu \to \overset{(-)}{\nu}_\mu$	CDHSW, CCFR
$\nu_\mu \to \nu_e$	BEBC, CHARM, LSND, NOMAD
$\bar{\nu}_\mu \to \bar{\nu}_e$	LAMPF-0645, LSND, KARMEN
$\overset{(-)}{\nu}_\mu \to \overset{(-)}{\nu}_e$	BNL-E776, CCFR, NuTeV
$\nu_\mu \to \nu_\tau$	FNAL-E351, CHARM, CHORUS, NOMAD
$\overset{(-)}{\nu}_\mu \to \overset{(-)}{\nu}_\tau$	CHORUS, NOMAD
$\nu_e \to \nu_\tau$	CHARM
$\overset{(-)}{\nu}_e \to \overset{(-)}{\nu}_\tau$	CCFR

Table 3.1: Summary of past accelerator experiments and their oscillation channels. See [20] and references therein.

In the years 1980's-1990's, several experiments were carried out using accelerators to produce neutrinos and look for oscillations (see table 3.1). The energy of the produced neutrinos was of the order of the GeV and therefore the experiment

[8]NUSEX had large uncertainty error whereas the Fréjus error is comparable with the Soudan 2 error. The Fréjus experiment result remains unexplained [61].

detectors that were placed at about 1 km away from the source were sensitive to $\Delta m^2 \geq 1$ eV^2. All these experiments observed no oscillations except the LSND experiment. A signal $>3\sigma$ was observed in the $\bar{\nu}_\mu \rightarrow \bar{\nu}_e$ channel [64] and a weaker one in $\nu_\mu \rightarrow \nu_e$ [65]. A large part of this signal has been rejected by the KARMEN [66] and Bugey [67] experiments nevertheless the MiniBooNE experiment was built to definitely disentangle the situation [68]. From their latest result, they observe a 3σ signal in the $\nu_\mu \rightarrow \nu_e$ channel but not in the $\bar{\nu}_\mu \rightarrow \bar{\nu}_e$ one. A misidentification of $e^{\pm}/\gamma$ could explain the observations and thus it will be checked in the coming years [69]. Other accelerator experiments that saw an oscillation signal are K2K that confirmed beautifully the SK result and later the MINOS experiment with a better accuracy. They are described below.

The K2K experiment

The KEK to Kamioka (K2K) experiment was located in Japan. ν_μ's of energy 1.0-1.5 GeV were produced in the KEK laboratory and sent to the the Super-Kamiokande (see section 3.1.3) detector located 250 km away. It was the first accelerator experiment with such a long baseline, it was indeed designed to check the SK oscillation signal. The ν_μ interactions in SK due to neutrinos from the beam were ensured through Global Positioning system (GPS). A 1 kton water tank was located at 294 m from the beam line. Its role was to measure the ν_μ interaction rate and spectrum before possible oscillations for comparison with the SK measurements. The experiment had two phases: the first one from June 1999 to July 2001 what was corresponding to the end of the SK-I phase and the second one was from January 2003 to November 2004 when half of the surviving SK PMTs were rearranged for a 19% photocathode coverage.
At the end of the year 2002, K2K reported a deficit of ν_μ events and a spectrum that was an indication for neutrino oscillation (probability of no oscillation $< 1\%$) [70]. The oscillation probability is a function of the energy at fixed baseline and the distortion induced gives strong information on the Δm^2 involved. Finally, $158^{+9.2}_{-8.6}$ events were expected in case of no oscillation while the experiment recorded 112 beam-induced ν_μ events in the fiducial volume. Moreover the shape of the recorded spectrum was distorted as can be seen of figure 3.9 leading to null-oscilation probability of 0.0015% (4.3σ) [71].
The L/E value of the experiment was nearly 5.2×10^{-3} eV^2 while the best oscillation fit was found to be 2.8×10^{-3} eV^2. Consequently the experiment was not optimized on the contrary of the MINOS experiment that came after.

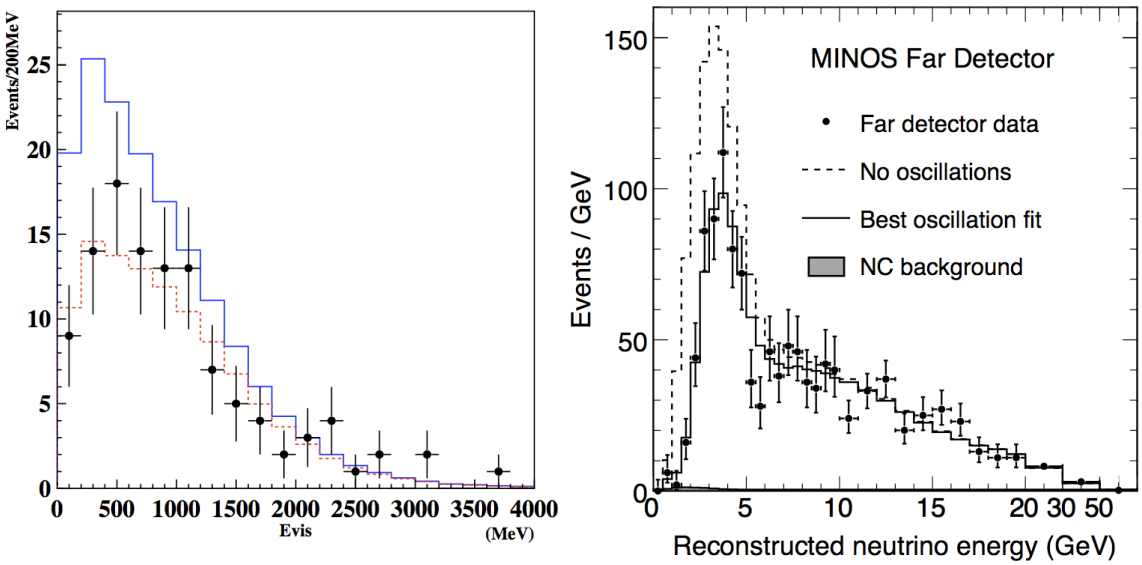

Figure 3.9: Left panel: K2K observed spectrum of the ν_μ interactions in the fiducial volume. Data are the black circles, the solid blue line is the MC expectation based of the near detector measurement and the red dashed line is the best oscillation fit [71]. Right panel: MINOS observed spectrum in the far detector. Data are the black circles (error bars are statistical), the dashed line is the no oscillation case and solid line is the best oscillation fit. The NC background contamination is also shown [72].

The MINOS experiment

The Main Injector Neutrino oscillation Search (MINOS) experiment aims at detecting a disappearance of ν_μ produced at the Neutrinos at the Main Injector (NuMI) located at FermiLAB in Chicago (USA). The neutrinos are produced with an energy of 1-3 GeV and travel from the near detector (ND) located at 1 km to the far detector (FD) 735 km away in the Soudan Mine in Minnesota (USA). Both detectors are magnetized steel-scintillator tracking calorimeters with the ND weighing 0.98 kton (103 m underground) and the FD, 5.4 kton (705 m underground).
The data taking started in May 2005 and confirmed in mid-2006 the K2K measurement (cf. fig. 3.9) [73]. The last published results in 2008 with 3.36×10^{20} p.o.t.[9] are the most accurate measurements of Δm^2_{32} and θ_{23} associated to $\nu_\mu \rightarrow \nu_\tau$ oscillations (see section 3.4). Moreover, the spectral distortion observed has excluded the neutrino decay and decoherence explanations respectively at 3.7σ and 5.7σ. The MINOS experiment have now accumulated about twice the data volume that remains to be analyzed.

[9]Protons on target.

3.3.2 Reactor experiments

In the 1970's, theoretical developments have lead to envisage neutrino oscillations and at that time, Δm^2 was believed to be rather large (of the order of the eV^2) if it exists at all. Reactor neutrino experiments with short baselines L (small source to detector distance) were very convenient. A reactor core is an abundant source of $\bar{\nu}_e$ through β^- decays occurring to the products of the fissions in the reactor cores. Their energy below 10 MeV does not allow to produce μ and τ and thus no appearance experiment can be performed. Given that $< E_{\bar{\nu}_e} >= 3$ MeV, the distance L at which an experiment is placed determines the Δm^2 value that is tested through $\Delta m^2_{tested}(\text{eV}^2) \simeq 3.7/L(m)$. Reactor experiments placed in the vicinity of the cores (L $<$ 100 m) were thus looking at small Δm^2 values (~ 0.1 eV^2) [74].
Reactor experiments used the inverse β-decay reaction to detect the $\bar{\nu}_e$:

$$\bar{\nu}_e + p \rightarrow e^+ + n \tag{3.23}$$

This reaction is remarkable since its two products give rise to a clear signature. The e^+ quickly looses its energy before it annihilates with an electron of the medium giving rise to two γ of 511 keV, this is the primary energy deposition which is related to the $\bar{\nu}_e$ energy. Meanwhile the neutron thermalizes and could be captured on hydrogen (H) yielding γ rays of 2.2 MeV, this is the secondary energy deposition. Moreover the reactor experiments used atoms like ^{6}Li, ^{3}He and Gd (Gadolinium, ^{155}Gd and ^{157}Gd) to have a better energy signature and to speed up the neutron capture thanks to their higher thermal neutron cross section.
The first reactor neutrino oscillation experiment was installed at 8.76 m of the research reactor of Laue Langevin Institute (ILL) at Grenoble in France [75]. In 1981, the experiment published their results showing no reduction of the neutrino flux which was refuting the indication found by Reines group in 1980[10] with a detector placed 11.2 m away from the Savannah River reactor [76]. Then the ILL detector was upgraded and moved to the Gösgen reactor in Switzerland. From 1981 to 1985, measurements were performed at different locations (37.9 m, 45.9 m and 64.7 m) and again no indication for oscillations was found [78]. However

[10]The Reines group experiment used the $\bar{\nu}_e$ interaction on deuterium. Therefore they had two usable reactions: the neutral current signal sensitive to all neutrino flavors which was tagged with detection of one neutron and the charged current signal sensitive only to $\bar{\nu}_e$ which was tagged with the detection of two neutrons. The one neutron and two neutron efficiencies were not well controlled which lead them to think that they obtained an indication for $\bar{\nu}_e$ 'instability'. Another experiment using the same detection procedure have observed no evidence for oscillations 18.5 m away from the Bugey reactor in 1998 [77].

at the same time, the Bugey-1 experiment[11] observed a deficit with respect to the expectations at two different distances (13.6 m and 18.3 m) [79]. The contradiction vanished after carrying out a second campaign at the same distances but with a better shielding [67]. Finally the so-called short baseline reactor neutrino oscillation experiments ended up[12] with the negative results of the Bugey-3 experiment at 15 m, 40 m and 95 m from the cores, published in 1995 [82] (cf. fig. 3.10). The

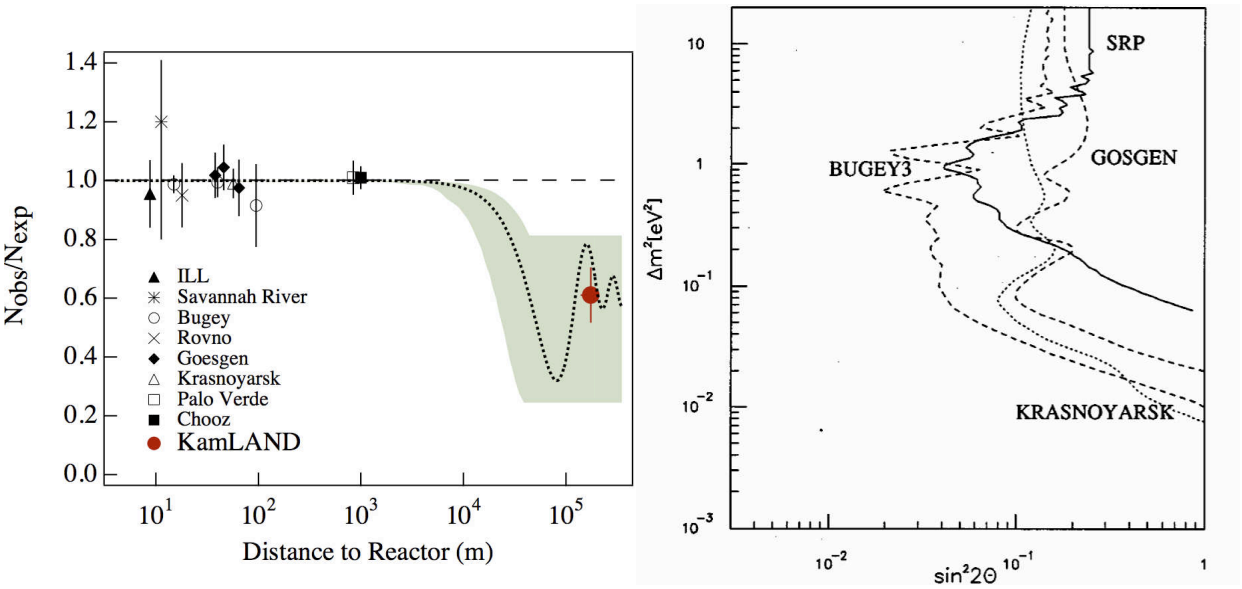

Figure 3.10: Left panel: $N_{obs}/N_{no\ osci}$ ratio for short baselines reactor neutrino experiments as well as CHOOZ, Palo Verde and KamLAND [83]. Right panel: exclusion plots obtained for the some short baseline reactor experiments [84].

latter gave the confirmation that the Pressurized Water Reactor absolute flux and spectrum are accurately modeled and it has been taken as a starting point for the so-called middle baseline experiments Palo Verde and CHOOZ, and the long baseline experiment KamLAND. The two first experiments had a detector placed at about 1 km from the reactor cores and their liquid scintillator was doped with Gd. We will review the CHOOZ experiment which was the first unsegmented reactor experiment using Gd. It had the best sensitivity to θ_{13} and has therefore strongly influenced the upcoming reactor experiments struggling for a better sensitivity

[11] From the name of the city where is located the nuclear power plant.

[12] There were 2 others short baseline reactors experiments in Ukraine at Rovno [80] and in Russia at Krasnoyarsk [81]. At Rovno the detector was 18 m away from the core and at Krasnoyarsk, which was a three reactor station, the baselines were 57 m and 231 m. The two experiments used ^{3}He proportional counters detecting only the neutron of the inverse β-decay. The Rovno experiment showed for the first time the possibility to monitor the reactor power and Krasnoyark made an analysis based on the rate comparison at the different baselines available. They both observed no depletion in the $\bar{\nu}_e$ flux.

(see section 4.1.1). Then we will briefly present the Palo Verde experiment that confirmed the CHOOZ result and finally the KamLAND experiment that confirmed that solar neutrinos do oscillate furthermore indicating a large mixing.

The CHOOZ experiment

The CHOOZ experiment took place close to the Chooz nuclear power plant, a French city in the Ardennes region in 1997-1998. The goal of this experiment was initially to try to resolve the atmospheric neutrino problem. At that time, the Kamiokande experiment observed a ν_μ/ν_e ratio lower than expected by a factor two at more than 4 σ. This could be explained either by $\nu_\mu \rightarrow \nu_e$ oscillations or $\nu_\mu \rightarrow \nu_\tau$ oscillations at the 10^{-3} eV^2 scale [85]. The experiment hence proposed to use the nuclear reactors which are an abundant source of $\bar{\nu}_e$ to disentangle the situation assuming CPT invariance. Given the energy of the reactor $\bar{\nu}_e$, a detector placed at about 1 km was sensitive to the good L/E scale (cf. fig. 3.11).

The experiment used as target liquid scintillator doped at 0.1% with natural Gd,

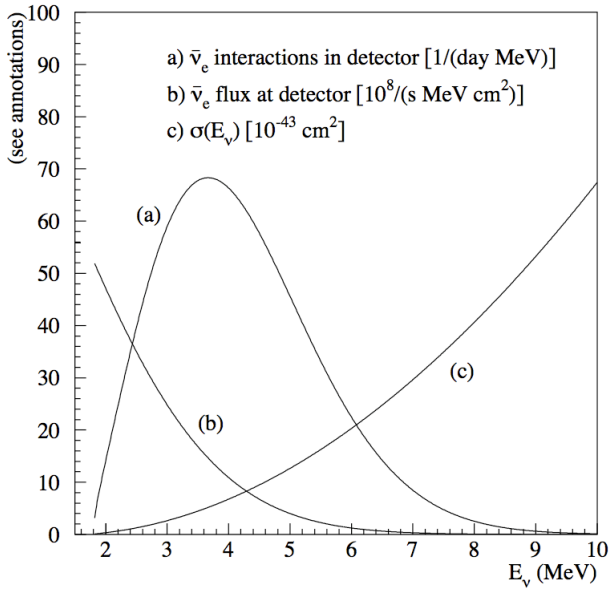

Figure 3.11: Reactor $\bar{\nu}_e$ flux, inverse β-decay cross section and $\bar{\nu}_e$ interaction spectrum at a detector based on such reaction [86].

that exhibits the highest cross section for thermal neutron, leading to a thermal neutron capture delay of typically $\tau_{Gd} \sim 30$ μs to be compared with $\tau_H \sim 180$ μs for a capture on H. Besides the capture on H yields only 2.2 MeV while it is 8 MeV for Gd well above the natural radioactivity γ background that goes up to 3 MeV. Consequently the signal selection was a primary deposition below 8 MeV followed

by secondary deposition between 6 MeV and 12 MeV in a 100 μs coincidence time window.
The CHOOZ detector was hosted in a 7 m in diameter and height cylindrical pit. It was a cylindrical steel tank of 5.5 in diameter and height surrounded by a 75 cm thick low radioactivity sand contained in an acrylic vessel and covered by 14 cm of cast iron. It was composed of three concentric volumes (cf. fig. 3.12):

- A central 5 tons neutrino target with 0.1% Gd-loaded liquid scintillator contained in transparent acrylic vessel. This was the volume for the $\bar{\nu}_e$ interaction.
- A 17 tons non Gd-loaded liquid scintillator region containing 192 8" photomultiplier tubes (PMTs). It had two purposes, the first one was to reduce the radioactivity induced by the PMTs and the second one was to contain the γ rays from the neutron capture and the positron annihilation.
- An optically separated 90 tons muon veto region. It is a also a non Gd-loaded liquid scintillator region observed by two rings of 24 8" PMTs.

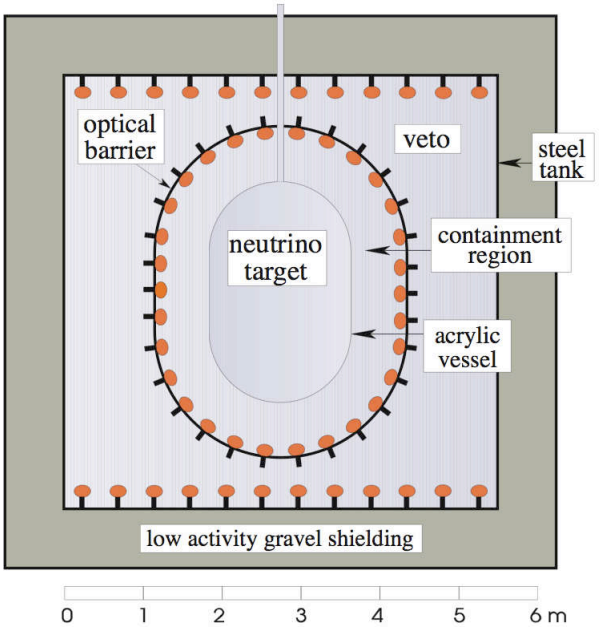

Figure 3.12: The CHOOZ experiment detector design.

In addition to the energy and time cuts, the following cuts were required to further lower the background: the primary and secondary depositions should be 30 cm

away from the PMTs support and less than 100 cm away from each other; meanwhile a neutron multiplicity equal to 1 was required[13].

Albeit the use of Gd was a great progress, it has shown some drawbacks. The Gd-complex is highly reactive and thus the Gd-loaded liquid showed a loss of transparency which lead to the end of the experiment after about one year of data (cf. fig. 3.13). Nevertheless the experiment had a unique opportunity to have both reactors OFF and periods where only one of the two reactors was functioning[14] which allowed a good measurement of the backgrounds [87, 88, 89].

The experiment observed a signal in agreement with the no oscillation expecta-

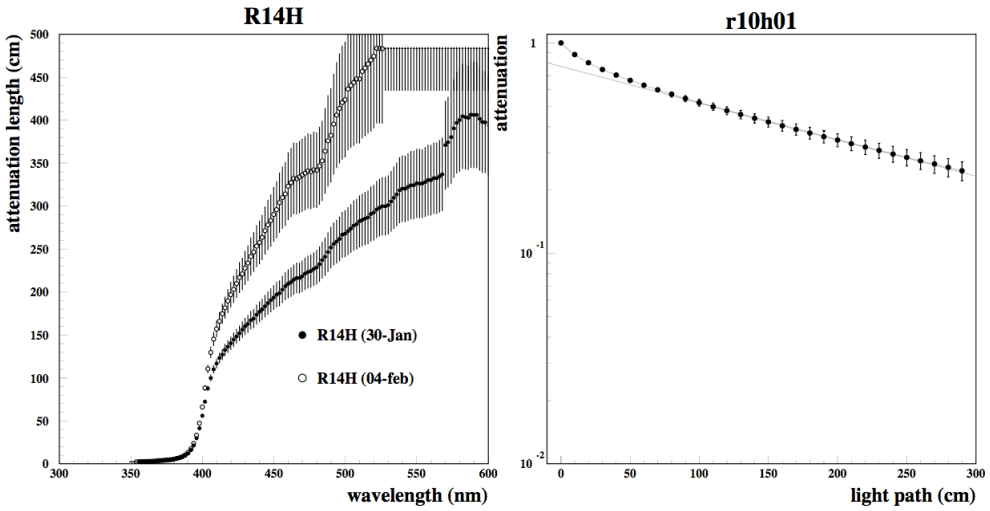

Figure 3.13: Left panel: attenuation length versus wavelength for the Gd-loaded liquid scintillator of the same type as the CHOOZ one at different aging stage. Right panel: scintillation light attenuation versus path [89]. The attenuation length decreased largely after one year of data taking, the higher the wavelength the bigger the decrease.

tions:

$$R = N_{obs}/N_{exp} = 1.01 \pm 2.8\%(stat.) \pm 2.7\%(syst.) \tag{3.24}$$

[13]Cosmic-ray muons interacting in the rock usually create more than one fast neutron. If more than one neutron is detected, this last cut allow to tag the event as a background event.

[14]When the CHOOZ experiment started, the Chooz nuclear power plant was still under construction what allowed to take reactors OFF data. The first reactor began to work in May 1997 while the second began only in August 1997 which allowed periods with only Reactor 1 running. The first one stopped for maintenance during the data taking allowing periods with only Reactor 2 working.

with N_{obs}, N_{exp} are respectively the number of events observed and expected in case of no oscillations.
Together with the SuperKamiokande experiment [90], they gave evidence for no $\nu_e \rightarrow \nu_\mu$ oscillations at the 10^{-3} eV^2 scale putting forward the $\nu_\mu \rightarrow \nu_\tau$ oscillation explanation. Despite this negative result, the experiment became famous because it was hence sensitive to $\nu_e \rightarrow \nu_\tau$ in the three flavors oscillation framework. Indeed, the $\bar{\nu}_e$ disappearance probability is written as follows:

$$P_{\bar{\nu}_e \rightarrow \bar{\nu}_e} \simeq 1 - \sin^2 2\theta_{13} \sin^2 \left(\frac{1.27 \Delta m^2_{31} L}{E_{\bar{\nu}_e}} \right) - \cos^4 \theta_{13} \sin^2 2\theta_{12} \sin^2 \left(\frac{1.27 \Delta m^2_{12} L}{E_{\bar{\nu}_e}} \right) \tag{3.25}$$

Therefore, having Δm^2_{12} of the order of 10^{-5} eV^2 scale (see section 3.4) and Δm^2_{31} of the order of 10^{-3} eV^2 scale [58], the CHOOZ experiment was only sensitive to θ_{13} since the oscillation term in Δm^2_{12} does not have time to develop (cf. eq. 3.25). The inferred constraint on θ_{13} is:

$$\sin^2(2\theta_{13}) \leq 0.14 \text{ at } 90\% \text{ C.L. with } \Delta m^2_{31} = 2.5 \times 10^{-3} \text{eV}^2 \tag{3.26}$$

which is at present the best direct constraint on this angle. The final results of the experiment are shown in figure 3.14.

The Palo Verde experiment

The Palo Verde experiment was situated near the Palo Verde nuclear power plant in Arizona (USA). This site was composed of three reactors for a total thermal power of 11 GW. However the detector that was located at 890 m from two reactors and 750 m from the other one was shielded with only 32 mwe. The detector was a 12 t fiducial mass scintillator doped with 0.1% Gd. As can be seen on figure 3.15, it was segmented in order to reduce the background with three-fold coincidence as primary deposition (e^+ plus the two annihilation γ's). Besides, every year, one of the reactor was off for 40 days allowing to deduce the background. The experiment took data from October 1998 to July 2000 and found the following ratio [91]:

$$R = N_{obs}/N_{exp} = 1.01 \pm 2.4\%(stat.) \pm 5.3\%(syst.) \tag{3.27}$$

The statistical error was better than the CHOOZ experiment but not the systematic error and thus Palo Verde was less sensitive. The result was nevertheless important since it confirmed the CHOOZ result.

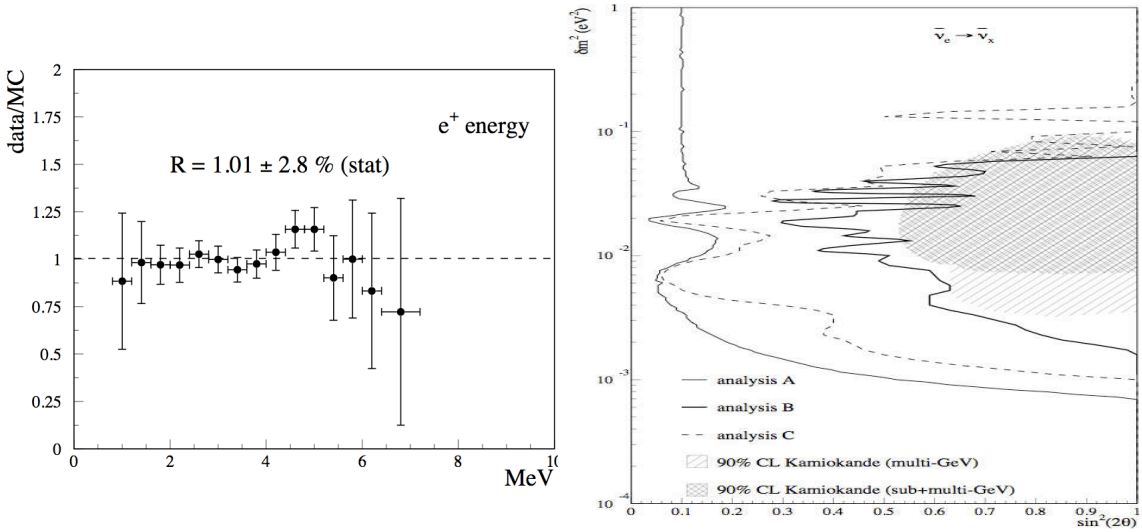

Figure 3.14: Left panel: measured over expected events per energy bin ratio. The data with the statistical error displayed is in good agreement with the null oscillation hypothesis. Right panel: exclusion contours based on the shape and normalization of the background substracted positron spectrum (analysis A), on the baseline difference between the two reactors (analysis B) and on the spectrum shape only (analysis C). All these results exclude the $\nu_\mu \rightarrow \nu_e$ oscillation explanation of the Kamiokande result [88, 89].

The KamLAND experiment

The experiments on solar neutrinos showed a deficit with respect to the calculations that could be explained by different oscillation regions in the $\sin^2\theta - \Delta m^2$ plane:

- oscillations at the 10^{-5} eV^2 scale with either a small mixing angle (SMA) or a large one (LMA). The MSW effect is large and different for these two regions.
- Or oscillations with low Δm^2 values. In these regions, the MSW effect is negligible.

The Kamioka Liquid scintillator AntiNeutrino Detector (KamLAND) was built in order to check the LMA solution and observed in 2002 a deficit at the 10^{-5} eV^2 scale [83] that was confirming this solution as the good one (assuming CPT invariance) (cf. section 3.1.4 and figure 3.17).
The KamLAND detector is located in the old Kamiokande site (see section 3.1.3). It is a 1 kton liquid scintillator detector with the purpose of detecting the $\bar{\nu}_e$ from

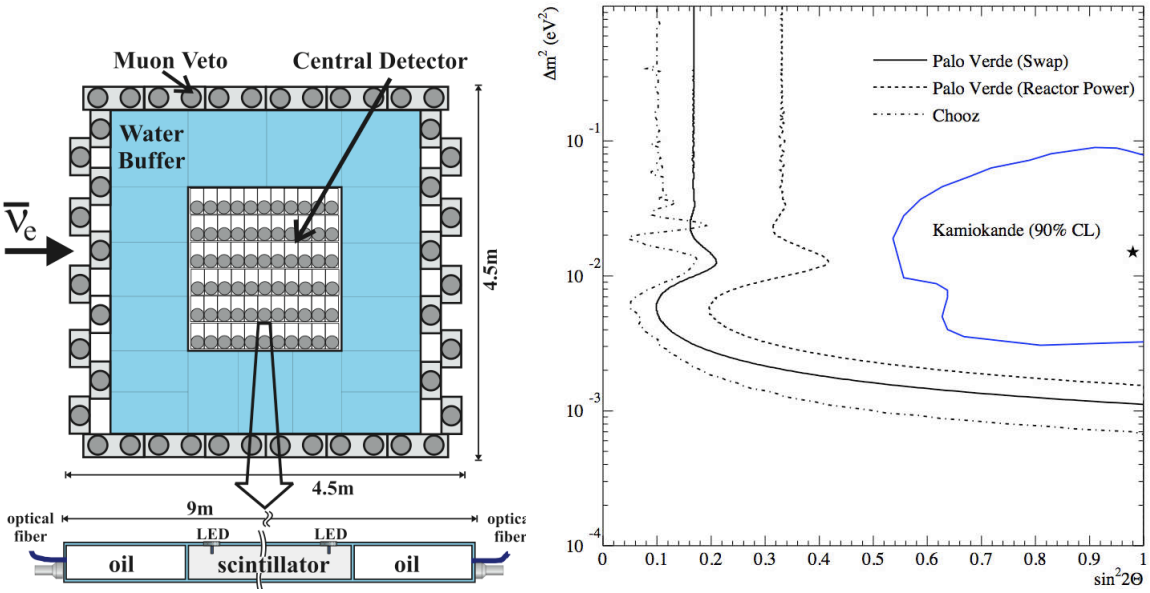

Figure 3.15: Left panel: The segmented Palo Verde detector with one cell shown in details [92]. Right panel: Final Palo Verde results in the $\Delta m^2 - \sin\theta$ plane together with the CHOOZ result [91].

the 53 nuclear power plant in Japan[15]. About 86% of the reactors contributing to the overall $\bar{\nu}_e$ flux are located between 88 km and 214 km with an average distance of 180 km. The liquid scintillator is contained in a 13 diameter spherical nylon balloon surrounded by buffer oil in a 18 diameter spherical stainless-steel containment vessel. The latter holds the 1879 PMTs for a photocathode coverage of 34% (22% for the first analysis without the 554 old Kamiokande PMTs). A cylinder filled with water surrounds the previous volumes being a Čerenkov veto against the backgrounds as cosmic-rays muons, γ rays and neutrons from the surrounding rock. The $\bar{\nu}_e$ are detected through the inverse β-decay (see equation 5.8). This reaction allows the $\bar{\nu}_e$ energy (E_ν) determination through the visible energy of the primary energy deposition E_{vis} (neglecting the neutron recoil energy):

$$E_\nu = E_{vis} + 0.782 \text{ MeV} \tag{3.28}$$

Data taking started in March 2002 and at the end of 2004, the experiment published the ratio of the observed events over the expected ones in case of no oscillation [93]:

$$R = N_{obs}/N_{exp} = 0.658 \pm 4.4\%(stat.) \pm 4.7\%(syst.) \tag{3.29}$$

[15]The detector receives a 2% contribution from reactors in South Korea and a <1% contribution from the rest of the world

that proved at about 5σ that disappearance of $\bar{\nu}_e$ was observed pushing definitely forward the LMA solution and excluding the other explanations of the solar neutrino experimental measurements. On figure 3.16 are displayed the spectrum observed and the oscillation fit to the data together with the measured to expected events ratio as a function of L/E. One can remark the clear oscillation pattern that allowed the experiment to have the best sensitivity to Δm^2_{12} associated to such oscillations (see section 3.4).

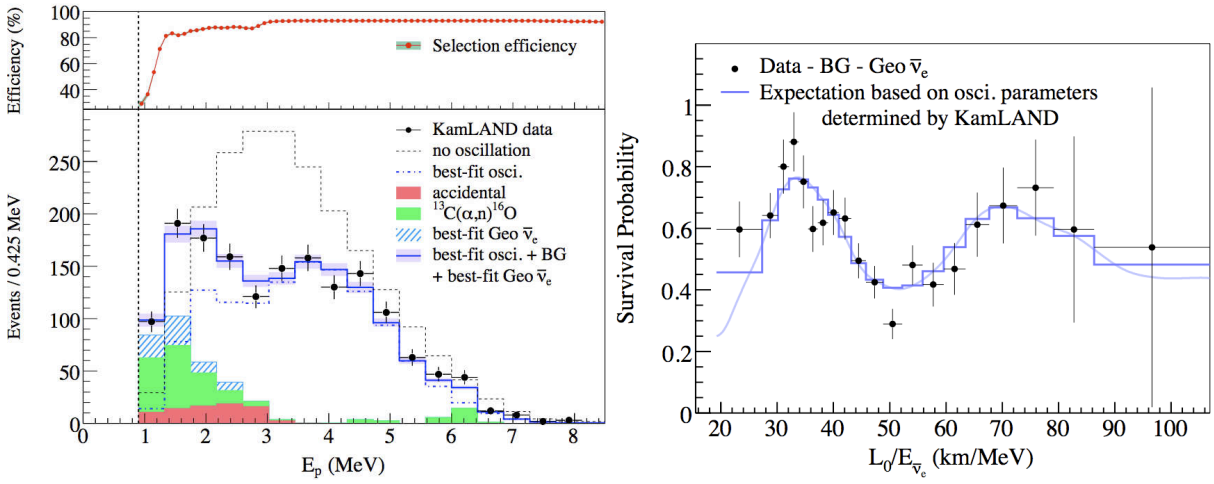

Figure 3.16: Left panel: Prompt energy spectrum of $\bar{\nu}_e$ candidates with the estimated background contribution. The best oscillation fit is shown as well. Right panel: measured to expected events ratio as a function of L_0/E where L0 is the averaged distance of the nuclear power plants. One can see the oscillation pattern [94].

3.4 Neutrino oscillation parameters

The oscillation parameters measurements are summarized on figure 3.17 in the plane $\Delta m^2 - \tan^2\theta$ (two flavor oscillations approximation).

The measurements performed on the atmospheric and accelerator experiments have shown that the oscillations observed in the 'atmospheric' sector are $\nu_\mu \rightarrow \nu_\tau$ oscillations at the 10^{-3} eV^2 scale with maximal mixing, the parameters associated are Δm^2_{32} and θ_{23} (cf. left panel of figure 3.18). The values of the parameters found are the following [72]:

$$\sin^2 2\theta_{23} > 0.9 \text{ (90\% C.L.)} \tag{3.30}$$

$$|\Delta m^2_{32}| = (2.43 \pm 0.13) \times 10^{-3} \text{ eV}^2 \tag{3.31}$$

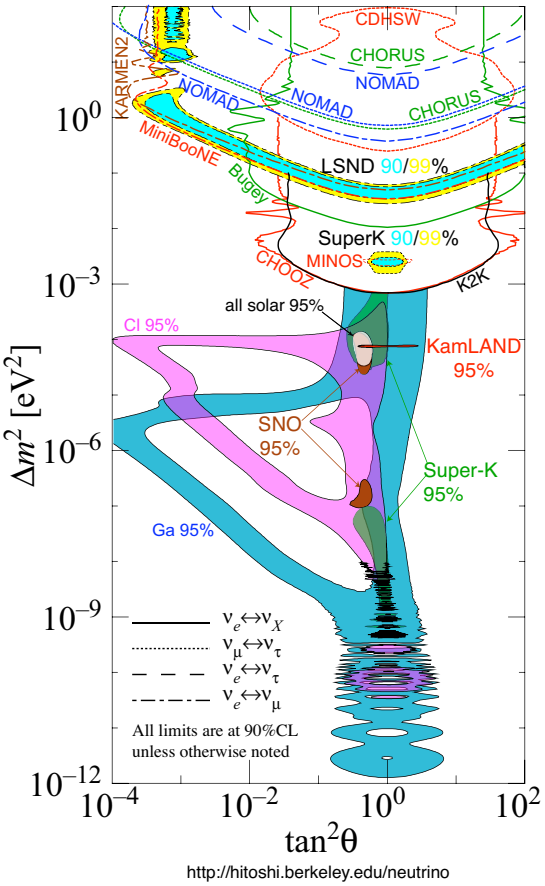

Figure 3.17: Summary of 40 years of neutrino oscillation experiments in the $\Delta m^2 - \tan^2\theta$ plane. [95]

The exact mixing value (is the mixing maximal or not?) and the sign of Δm^2_{32} are not known. Besides, no direct evidence of ν_τ appearance in a ν_μ beam has yet been observed but it should be done in the coming years by the OPERA and ICARUS experiments [96, 97]. The SK $\nu_\mu \rightarrow \nu_\tau$ oscillation explanation was confirmed by the middle baseline reactor experiments that observed no disappearance of $\bar{\nu}_e$ at this Δm^2.

The experiments on solar neutrinos showed a deficit with respect to the calculations that could be explained by different oscillation regions in the $\sin^2\theta - \Delta m^2$ plane. The Borexino experiment could have disentangled the situation through the MSW effect but the solution came from the KamLAND experiment that observed oscillations at the 10^{-5} eV^2 scale with large mixing. Solar oscillations are explained by $\nu_e \rightarrow \nu_\mu$ transitions of parameters Δm^2_{12} and θ_{12} (cf. right panel of figure 3.18).

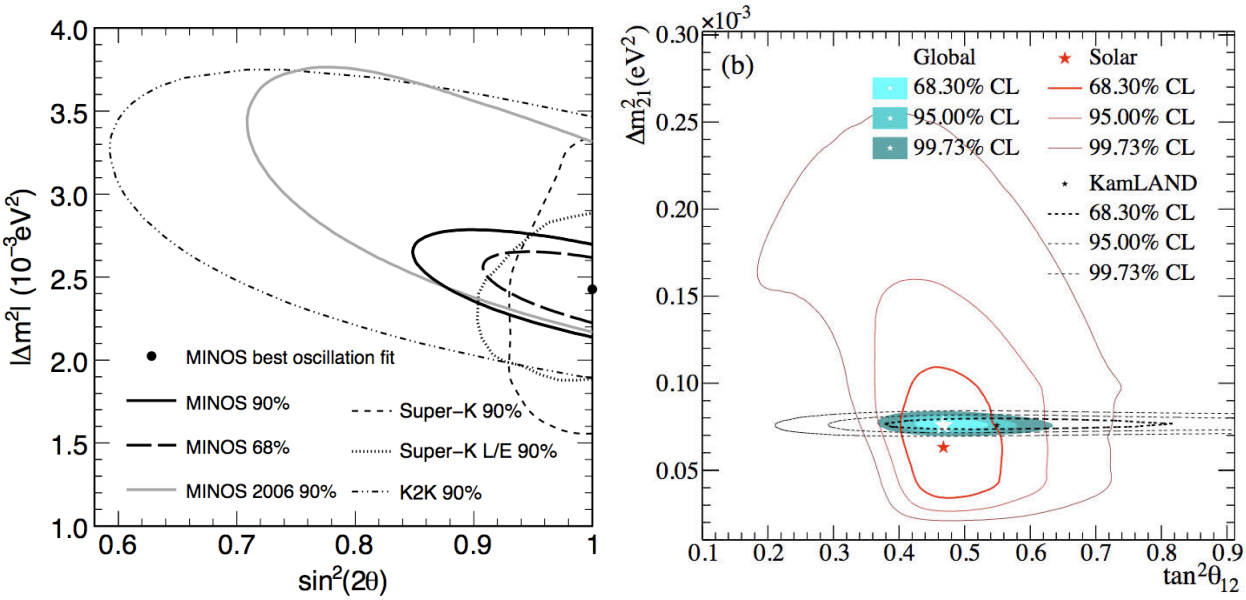

Figure 3.18: Left panel: $\nu_\mu \to \nu_\tau$ oscillation results of the SK, K2K and MINOS experiments in the $\sin^2 2\theta - \Delta m^2$ plane [72]. Right panel: $\nu_e \to \nu_\mu$ oscillation results of the available data in mid-2010 from solar experiments in the $\tan^2\theta - \Delta m^2$ plane [98]

The values of these parameters are the following [94, 98]:

$$\tan^2\theta_{12} = 0.457^{+0.040}_{-0.029} \tag{3.32}$$

$$\Delta m^2_{12} = 7.58^{+0.10}_{-0.07}(stat.) \pm 0.15(syst.) \times 10^{-5}\ \text{eV}^2 \tag{3.33}$$

The two measured mixing angle are very large, θ_{23} induces a mixing very close or equal to the maximum (>90%) and θ_{12} induces a mixing nearly >85%. This situation is very surprising compared to the CKM matrix parameters measured in the quark sector. More surprising is the last unknown mixing angle θ_{13}. Indeed as discussed in section 3.3.2, there is only a limit set by the CHOOZ experiment, confirmed by Palo Verde and more recently confirmed by MINOS in the normal hierarchy case [89, 91, 99]:

$$\sin^2 2\theta_{13} < 0.14\ (90\%\ \text{C.L.}) \tag{3.34}$$

with $\Delta m^2_{31} \simeq \Delta m^2_{32}$ due to the factor 30 in the ratio of Δm^2_{32} and Δm^2_{12}. Fits to solar, atmospheric sectors and middle baseline reactor experiments in the three flavors framework can further help to constrain θ_{13}. Except the middle baseline reactor experiments, θ_{13} appears as a subleading effect constrained by its non ob-

servation. The so-called global constraint is [100]:

$$\sin^2\theta_{13} \leq 0.035 \text{ at } 90\% \text{ C.L.} \tag{3.35}$$

with a preference for a non-zero θ_{13} value arising from the 'tension' between solar and KamLAND best fit values which are reconciled by a non-zero θ_{13} value [100]. This hint, also observed in other global analysis of neutrino oscillations data [101,

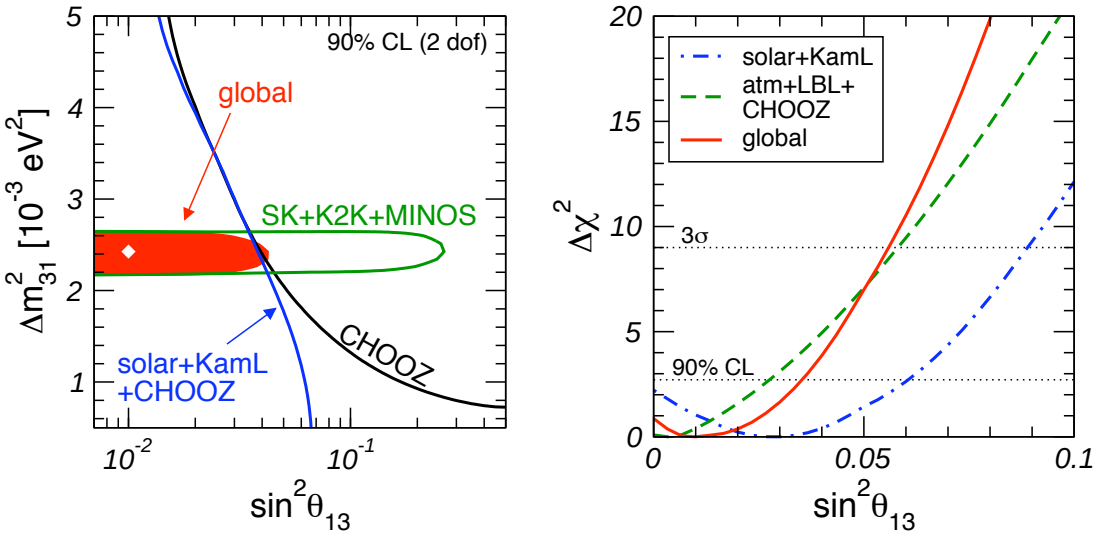

Figure 3.19: Global fit to oscillation experiments data. One can see that the solar sector's $\Delta\chi^2$ favorites a non-zero value of θ_{13} reachable by the new generation of oscillation experiments [100]

102], is reachable by the new generation of oscillation experiments described in details in the next chapter. Their purpose is to measure (or lower the bound on) the θ_{13} angle and, in the case of ν_e appearance in accelerator experiments, possibly measure as well the CP violation phase δ that appears coupled to θ_{13} and Δm^2_{31}:

$$\begin{aligned} P_{\nu_\mu\to\nu_e} &\approx \sin^2 2\theta_{13}\sin^2\theta_{23}\frac{\sin^2(A-1)\Delta}{(A-1)^2} \\ &+ \alpha\sin 2\theta_{13}\sin 2\theta_{12}\sin 2\theta_{23}\cos(\Delta+\delta)\frac{\sin A\Delta}{A}\frac{\sin(A-1)\Delta}{A-1} \\ &+ \alpha^2\sin^2 2\theta_{12}\cos^2\theta_{23}\frac{\sin^2 A\Delta}{A^2}. \end{aligned} \tag{3.36}$$

where $A \equiv \frac{2E_\nu V}{\Delta m^2_{31}}$ with $V = \sqrt{2}G_F N_e$ (N_e is the electron density), $\Delta \equiv \frac{\Delta m^2_{31} L}{4E_\nu}$ and $\alpha \equiv \frac{\Delta m^2_{21}}{\Delta m^2_{31}}$ [103].

In solar experiments, the sign of Δm^2_{12} is known thanks to the observation of

MSW effect on solar ν_e (see section 2.2.2). In the future, accelerator experiments that have long baseline could determine the Δm^2_{31} sign (see equation 3.36) and therefore disentangle between the two possible hierarchies but the first step is the determination of θ_{13}.

Chapter 4

Chasing the mixing angle θ_{13}

After the resolution of the atmospheric and solar anomalies plus the measurement of the corresponding parameters (cf. chapter 3), the next steps for neutrino oscillations experiments is to determine the values of the last unknown mixing angle θ_{13}, the leptonic CP violation phase δ and the sign of Δm^2_{31}. The θ_{13} angle is the key parameter of three neutrino oscillations and is always present in oscillation terms bringing in δ and the sign of Δm^2_{31} (see equations 2.20 and 3.36). Consequently, determining the value of θ_{13} is the goal of the new generation of neutrino oscillation experiments.
Middle baseline reactor experiments are a sensitive probe of θ_{13} as well as accelerator experiments looking at ν_e appearance in a ν_μ beam. Such experiments have already started or will do so soon. Other less constraining informations on θ_{13} are available through the interpretation of neutrino oscillations measurements in the three neutrino flavors framework. Besides supernovae could also give us informations on θ_{13}.
In this chapter, we will first review the reactor and accelerator experiments and then their complementarity. Afterwards we will present some realistic projects with a longer time scale and finally we will present the other possible but less probable measurements of θ_{13}.

4.1 Reactor neutrino experiments

Reactors are sources of $\bar{\nu}_e$ of the order of a few MeV and thereby only disappearance experiments are possible. Reactor experiments are close to the source (<2km)

making the matter effects negligible. The survival probability of $\bar{\nu}_e$ is given by equation 3.25 but can be approximated to the following equation for middle baseline experiments (cf. section 3.3.2):

$$P_{\bar{\nu}_e \to \bar{\nu}_e} \simeq 1 - \sin^2 2\theta_{13} \sin^2 \left(\frac{1.27 \Delta m^2_{31} L}{E_{\bar{\nu}_e}} \right) \tag{4.1}$$

4.1.1 Inheritance from the CHOOZ experiment

The current best sensitivity on θ_{13} is given by the CHOOZ experiment (see section 3.3.2) which was limited by both the statistical (2.8%) and systematic (2.7%) error. The new generation of reactor experiments aims at lowering these two errors by a factor ∼5.

Statistical error

The number of expected $\bar{\nu}_e$ events in a detector can be simplified as follows:

$$N_{\bar{\nu}_e} = \Phi_{\bar{\nu}_e}(\bar{\nu}_e/\mathrm{cm^2 s}) \times \sigma_p(\mathrm{cm^2}) \times n_p(\mathrm{p/ton}) \times M(\mathrm{ton}) \times T(\mathrm{s}) \times \epsilon_{det} \tag{4.2}$$

where $\Phi_{\bar{\nu}_e}$ is the $\bar{\nu}_e$ flux at the detector, σ_p is the $\bar{\nu}_e$ cross section on free proton and n_p is the estimated number of free protons per ton. M is the target mass, T is the exposure time and ϵ_{det} is the detector efficiency.
Therefore to lower the statistical error, one has to increase whichever of these parameters. The target mass can be increased easily at the cost of money while the $\bar{\nu}_e$ flux can be increased only by choosing a higher thermal power reactor complex since the far detector location is fixed around one oscillation length for better sensitivity. To increase the exposure time, one has to design long run-time and well monitored detectors with special care given to the Gd-loaded liquid scintillator as the CHOOZ experiment has demonstrated.

Systematic Error

The systematic error can be divided into two categories: the reactor-related errors and the detector-related errors. In the CHOOZ experiment, the former amounted to $\sim$ 2.2% and the latter to $\sim$ 1.5%. To lower the reactor-related errors, the solution envisaged is to perform a relative measure of the deficit of $\bar{\nu}_e$ instead of an absolute one by using a near detector to monitor the $\bar{\nu}_e$ flux. This detector is placed the closest possible to the cores to get rid of the errors related to reactors power,

the energy released per fission (∼200 MeV), the number of $\bar{\nu}_e$ per fission (∼6) and the $\bar{\nu}_e$ cross section ($\sim 10^{-44}\text{cm}^2/\text{MeV}^2$). Meanwhile using an identical detector, most of the detector related uncertainties are reduced as the chemical composition of the liquid scintillator (H/C ratio), the target mass and the H/Gd ratio. The goal is to have a systematic error below 0.6% dominated by the uncertainty on the number of free protons and the event selection cuts as can be observed in the following formula giving the ratio of the number of events in the two detectors:

$$\frac{N_f}{N_n} = \frac{P_{\bar{\nu}_e \to \bar{\nu}_e}(E, L_f)}{P_{\bar{\nu}_e \to \bar{\nu}_e}(E, L_n)} \times \left(\frac{L_n}{L_f}\right)^2 \times \left(\frac{n_{p,f}}{n_{p,n}}\right) \times \left(\frac{\epsilon_f}{\epsilon_n}\right) \tag{4.3}$$

where the index f stands for far and n for $near$. L is the distance source-detector and $P_{\bar{\nu}_e \to \bar{\nu}_e}(E, L)$ is the disappearance probability after a travel distance L for $\bar{\nu}_e$ of energy E. n_p is the number of free protons and ϵ is the $\bar{\nu}_e$ signal selection efficiency. The ratio of the probabilities $P_{\bar{\nu}_e \to \bar{\nu}_e}(E, L)$ is a function of $\sin^2(2\theta_{13})$ as can be seen in equation 4.1 and the source-detector distances are well measured assuming $\bar{\nu}_e$ coming from the barycenter of the core. Careful attention is given to n_p determination by using weight and flow rates measurements and the signal selection efficiency is characterized by calibration. The uncertainty on the signal selection is improved by diminishing the number of necessary cuts. As explained in section 3.3.2, seven cuts have been used in the CHOOZ experiment (cf. tab. 4.1) while only three cuts are foreseen for the upcoming experiments: the e^+ energy selection, the neutron energy selection and the coincidence time window criteria; the spatial cuts could be abandoned thanks to an improved detector design. Ultimately, the systematic error will depend on the extent to which the detectors have been made identical, the level at which it can be known and on the knowledge of the backgrounds. The table 4.1 summarizes the systematic errors and the expected improvements.

Backgrounds and new detector design

The CHOOZ experiment has classified the backgrounds for reactor neutrino experiments into two types: correlated and accidental backgrounds (cf. fig. 4.1).

Correlated background This background is entirely due to spallation and photonuclear processes initiated by cosmic-ray muons. When a muon interacts in the surrounding rock, it can create fast neutrons with an arbitrary energy and mean free path going towards the detection volumes (target + γ containment region). This neutron can induce in the liquid scintillators a proton recoil with enough en-

		CHOOZ	Baseline for upcoming experiments
Reactor	Power	$\sim 2\%$	negligible
	E/fission	0.6%	negligible
	$\bar{\nu}_e$/fission	0.2%	negligible
	Distances	negligible	0.1%
	Reactor tot.	$\sim 2.1\%$	0.1%
Detector efficiency	e^+ energy cut	0.8%	0.1%
	n energy cut	0.4%	0.2%
	e^+-n delay	0.4%	0.1%
	e^+-PMT wall distance	0.1%	not used
	n-PMT wall distance	0.1%	not used
	e^+-n distance	0.3%	not used
	n multiplicity	0.5%	probably not used
	Gd/H captures	1.0%	0.2%
	Detector tot.	1.5%	0.3%
# target p		0.8%	0.2%
	Total syst. error	$\sim 2.7\%$	0.4%

Table 4.1: Summary of the CHOOZ experiment systematic error and the order of magnitude of the improvements expected for the new generation of reactor experiments [104, 105]. Some errors becomes negligible (compared to others of the same type) thanks to the identical near detector whereas the spatial cuts are not used thanks to an improved detector design. It is not yet clear if the n multiplicity cut will be used or not.

ergy to mimic the primary e^+ energy deposition. If after thermalization it gets captured in the target on Gd in the coincidence time window, it is mistaken as $\bar{\nu}_e$ signal. Besides a muon entering the detection volumes can create cosmogenic isotopes by interacting with ^{12}C. The most dangerous are ^{9}Li and ^{8}He because they undergo β-n cascades with >100 ms half-life time [106, 107] that makes them hardly reducible unless using an analysis deadtime window after each muons entering the target.
The CHOOZ experiment has estimated the rate of this background to:

$$R_{correlated} = 1.01 \pm 0.1 \ d^{-1}.$$

Accidental background This background is due to random coincidences of e^+-like energy deposition followed by a neutron capture-like energy deposition in the coincidence time window. The e^+-like energy deposition is mainly faked by the radioactivity γ rays while the n capture-like energy deposition is due to a neutron

capture in the target, either from natural radioactivity or muon-induced as neutrons from muon capture on ^{12}C or spallation neutrons. This background can be estimated from the measurement of the individual rates or by inverting the selection criteria: the n capture-like energy deposition followed by the e^+-like energy deposition in the coincidence time window.
The determined accidental rate in CHOOZ was:

$$R_{accidental} = 0.42 \pm 0.05 \ d^{-1}.$$

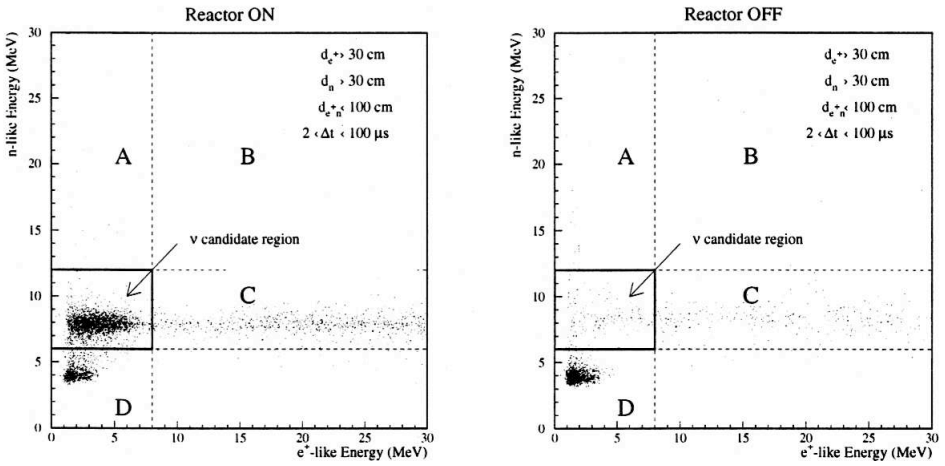

Figure 4.1: 'n-like energy' versus 'e^+-like energy' for reactor-ON (left) and reactor-OFF (right) with the selection criteria applied. It can be observed that the bigger contamination in the $\bar{\nu}_e$ region comes from spallation fast neutrons as a continuation of region C. The other non negligible component is random coincidences from natural radioactivity and untagged stopped muon.

Improvements to the CHOOZ detector design The accidental background can be reduced by using low radioactivity materials and by working in a clean environment when building the detector. However its main contribution is due to the natural radioactivity of the PMT glass and the surrounding rock. To fight against it an intermediate non scintillating region called 'buffer' has to be introduced between PMTs and the γ rays containment region. It reduces the rate of γ arriving to the detection volumes with an energy above the read-out threshold making the CHOOZ spatial cuts no more useful. It will as well reduce the mean energy of fast neutrons entering the detection volume possibly making the proton recoil undetectable and thus the induced faked $\bar{\nu}_e$ signal. The rock surrounding

the detector is an important source of radioactivity and should be as efficiently as possible reduced. An external protection with a better γ rays stopping power has to be envisaged. It will reduce accidentals but also the rate of interactions in the active veto region possibly making it useful for fast neutron studies by detecting proton recoil. The best solution against the correlated background is to go deeper underground to reduce the muon rate and therefore the correlated background.

4.1.2 Sensitivity to θ_{13}

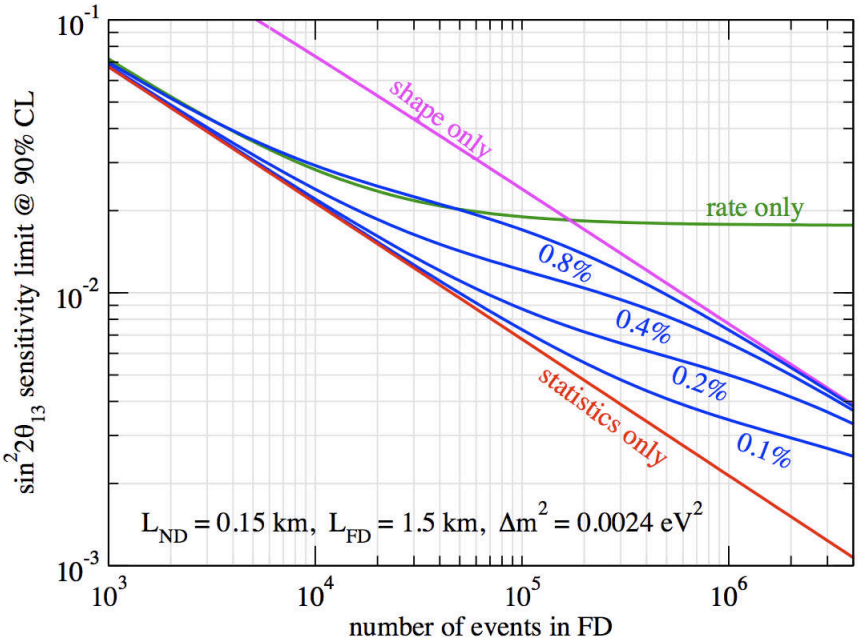

Figure 4.2: Illustration of the luminosity scaling of the $\sin^2(2\theta_{13})$ sensitivity at 90% C.L at a fictitious reactor experiment. The red curve shows the statistical limit in case of no systematic error. The blue curves are the sensitivity for different absolute normalization errors. The magenta and green curves shows respectively the sensitivity with shape only and rate only analysis, the shape only curve is idealized. Like the rate only analysis, the shape analysis reaches a plateau determined by the uncorrelated errors which is not present on this plot [103] (more details in [108, 109]).

A $\bar{\nu}_e$ disappearance due to oscillations would affect the number of $\bar{\nu}_e$ detected and their energy distribution since the oscillation effect is energy dependent. Thus two kind of analysis can be performed, respectively 'rate' analysis (cf. eq. 4.3) and 'shape' analysis (cf. fig. 3.16); they can even be combined for a more powerful test. However the shape analysis is limited by the statistics in each bin. Figure 4.2 shows the sensitivity to θ_{13} to be expected including both analysis as a function of

the number of events in a fictitious detector, here the sensitivity is the maximum value of $\sin^2(2\theta_{13})$ which is consistent with the no oscillation hypothesis at 90% C.L. We can observe the existence of three different regimes:

- 'The low statistics regime' up to $\sim 10^4$ events where the sensitivity is close to the statistical limit. This is a regime where only rate analysis can be performed. This regime extends up to a statistical error of the same order of the systematic error.
- 'The intermediate regime' from $\sim 10^4$ events up to $\sim 10^6$ events. Here the sensitivity is driven by the systematic error on the absolute normalization between the two detectors and the lack of statistics per energy bin does not allow to perform an efficient shape analysis. In this regime, both analysis can be performed with more importance given to the rate analysis.
- 'The high statistics regime' from $\sim 10^6$ events. In this regime, the accumulated statistic is sufficient to perform a shape analysis but the sensitivity is limited by the uncorrelated errors between energy bins and detectors. The latter is driven by the knowledge of the backgrounds and is an indication of the maximum potential of reactor neutrino experiments for a non-zero θ_{13} discovery. The rate analysis is no more needed.

This plot demonstrates that the upcoming reactor experiments aiming at measuring θ_{13} (being all within the intermediate regime) have to be careful with the absolute normalization systematic error because it determines when the sensitivity to $\sin^2(2\theta_{13})$ reaches a plateau, this is the most important effect to keep under control. However, the existence of the second statistical regime shows that if the detector is large enough to have a negligible statistical error per energy bin, this normalization error becomes irrelevant and the sensitivity is ultimately driven by the uncorrelated errors. Thus the use of an identical near detector is not mandatory provided that there is no bias in the signal shape and energy scale determination. The level of determination of the backgrounds at the different sites will be of first importance.

4.1.3 The upcoming experiments

Several projects aiming at measuring the θ_{13} angle at reactors were finally abandoned like Angra in Brazil, Krasnoyarsk in Russia, Diablo Canyon and Braidwood in U.S.A, and KASKA in Japan [110]. The Krasnoyarsk and Diablo Canyon

projects were quickly abandoned while the Braidwood and KASKA experiments were more detailed and advanced projects[1]. They were abandoned for financial reasons and their collaboration joined the Double Chooz (France) and Daya Bay (China) collaborations which are experiments about to start soon. Another experiment of the same type is RENO in South Korea. We will review these experiments in this section.

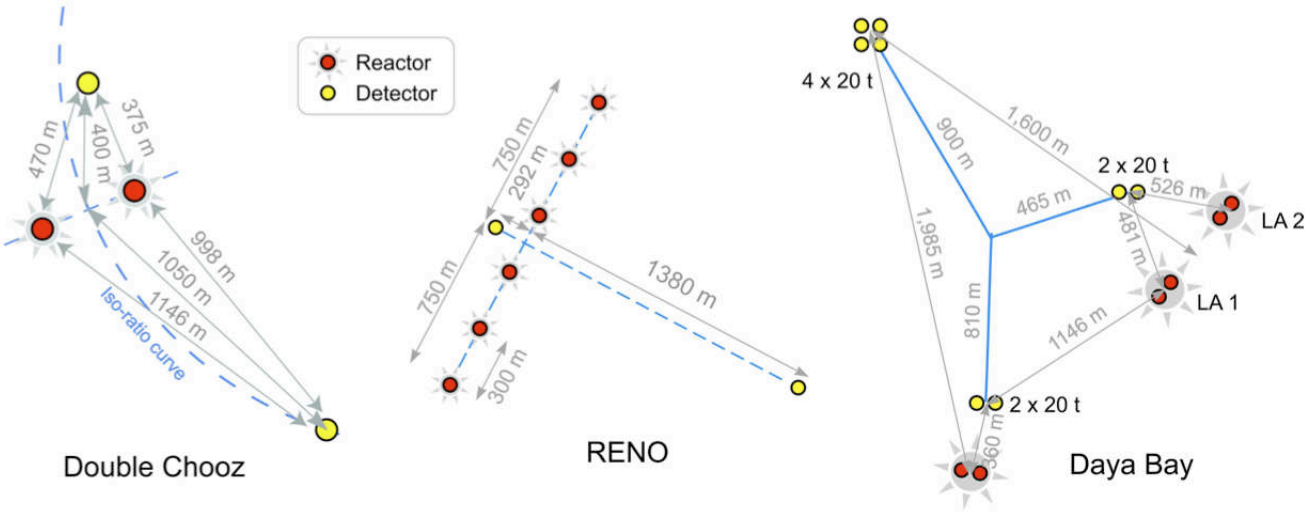

Figure 4.3: Configuration of the experimental layout of the three upcoming reactor experiments in a short time scale: Double Chooz, RENO and Daya Bay. The dashed curve is the iso-ratio line from the reactors [103].

The optimal experiment

The optimal reactor neutrino experiment would receive a high $\bar{\nu}_e$ flux, will have a far site located at the first oscillation maximum while the near site should be the closest to the cores as possible because of the uncertainty on the flux contribution from each core. Having a high $\bar{\nu}_e$ flux means a power plant with multiple reactors however the gain in statistics can be spoiled by the dependence on the power and fuel composition. Ideally the near and far detectors would present the same ratio of the fluxes received from the cores (iso-flux lines in figure 4.3). The far detector would be located at the first oscillation maximum about 1.5 km for $\Delta m^2_{13} = 2.5 \times 10^{-3}\text{eV}^2$ in order to have a sensitivity to θ_{13} less dependent on to the actual

[1] Angra was a project of a detector with a mass of the order 200 tons what would have allowed to enter the 'high statistics regime' but was recently abandoned. The construction of such a big reactor experiment is not envisaged for the time being.

Δm^2 value [111]. Furthermore the site should present a hill topology to protect efficiently the detectors from the irreducible backgrounds due to cosmic rays. The money saving has to be considered when designing the total target mass of the detectors as well as the possible reuse of underground laboratories which will not imply big civil work. All the experiments that will be described in what follows had to accommodate with these constraints.

The Double Chooz experiment

Site and Schedule Double Chooz is an international collaboration composed of institutes from Brazil, France[2], Germany, Japan, Russia, Spain, United Kingdom and United states [104]. This experiment is reviewed in details in the next chapter. The site chosen for the experiment is the former location of the CHOOZ experiment with its twin reactor cores producing up to 8.6 GW_{th}. Only one near detector will be used at 400 m away from the cores barycenter with an overburden of 120 mwe and only one far detector at 1.05 km with 300 mwe overburden (cf. fig. 4.3). Two phases are foreseen: the phase 1 which will begin in november 2010 with only the far detector running, and the phase 2 with the near detector running as well, expected for mid-2012 [112].

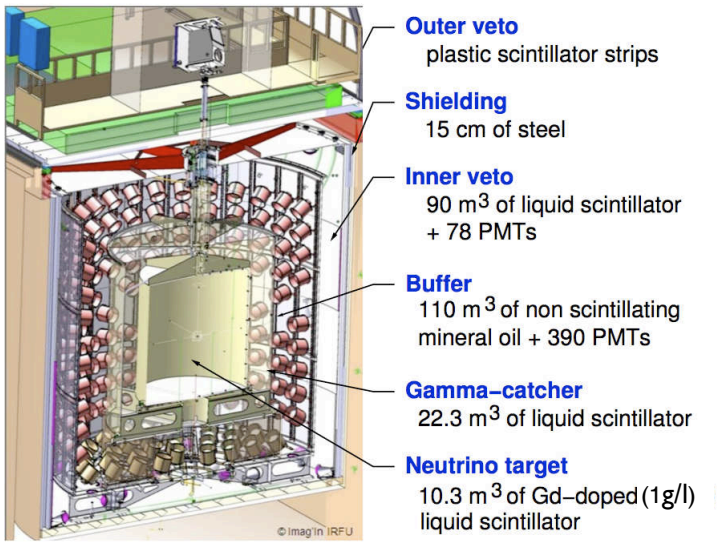

Figure 4.4: The Double Chooz design. The improvements in the design with respect to the CHOOZ experiment are the buffer region, the steel shielding and the outer muon veto.

[2]Belgium is an member institute connected to France

Detector Design and sensitivity The target will consist of of Gadolinium-loaded liquid scintillator. Its fiducial mass will be 8.3 tons. A 105 cm thick buffer zone between the PMTs and the detection volumes is foreseen to reduce significantly the radioactivity induced backgrounds as well as a 15 cm thick steel shielding enveloping the detector. To better fight against the muon induced backgrounds, segmented plastic scintillator strips coupled to wavelength shifting fibers will be placed on the top of the detector and will be extended on the edges in order to tag potential background induced by a near passing muon. This system is complementary of the Inner Veto system which is a liquid scintillator volume observed by 78 PMTs (cf. fig. 5.10). The goal of the experiment is to reach a systematic error of 0.6% with the relative measurement between the two detectors and a statistical error of 0.5% in order to have an ultimate sensitivity of $\sin^2(2\theta_{13}) = 0.03$ at 90% C.L. after three years with the two detectors running [104].

The Daya Bay experiment

Site and Schedule The Daya Bay experiment is mainly a United States-China collaboration that also include Russian, Taiwanese and Czech institutions [113]. Its name comes from the power plant that hosts the experiment. The experimental site is located near Hong Kong in the Guangdong province in China showing a mountainous topology well suited to reduce the backgrounds. The nuclear power complex is currently composed of two pairs of reactors, Daya Bay and Ling Ao-I, about 1200 m apart from each other. Another two reactors named Ling Ao-II are under construction and should be operational in 2011. Each core yields 2.9 GW_{th}, thus the site is currently 11.6 GW_{th} and will be 17.4 GW_{th} with the Ling Ao-II start.

This site requires at least 2 near detectors to monitor separately the Daya Bay and Ling Ao sites. The near detector site for the Daya Bay reactors will be located 360 m away from the cores barycenter and the one for the Ling Ao sites will be placed 481 m away from Ling Ao 1 and 526 m away from Ling Ao-II; both will have an overburden of 260 mwe. The far detector site is located at about 2 km from Daya Bay cores and at 1.6 km from the barycenter of the Ling Ao sites and present an overburden of 910 mwe (cf. fig. 4.3). The data taking is foreseen to begin in autumn 2012 with the three detector sites operational. The Daya Bay near site should be ready for spring 2011 [114].

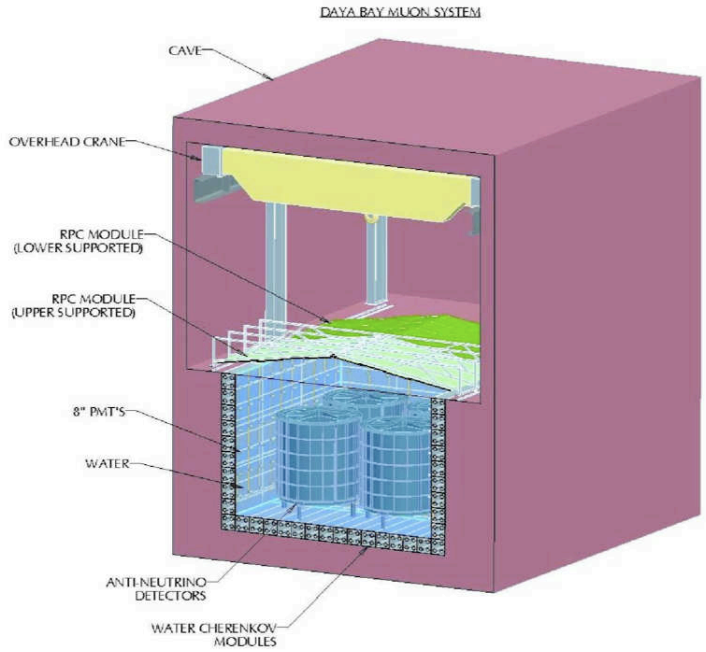

Figure 4.5: The Daya Bay muon veto system and the 4×20t detectors.

Detector Design and sensitivity The Daya Bay experiment will use 8 detectors containing each a 20 tons fiducial mass of Gd-loaded liquid scintillator. The detectors will be distributed as follows: 2 detectors at each near sites and the remaining 4 detectors at the far site. The 2 detectors at each near site will allow cross-calibration in order to reduce the systematics while the high target mass at the far site will allow to reduce significantly the statistical error. Another ambitious project is to reduce the systematics down to 0.18% (0.38% without this option) by moving the detectors on trucks to change the sites for direct performance testing. The design of the detectors is very similar to the Double Chooz one except for the detectors shielding. At each site the detectors will be submerged into a swimming pool filled with purified water giving a protection against both radiations and fast neutrons. At the bottom and the edges, the swimming pool is divided into small water-Cherenkov cells observed by four 8" PMTs at each end that will be used to tag muons together with layers of resistive-plate chambers (RPCs) (cf. fig. 4.5). The RPCs will be disposed above the detectors and extended on the edges for backgrounds studies. The buffer region is 45 cm thick and contains 192 8" PMTs as well as top and bottom reflectors. The effective photocathode coverage is below 12% and the energy resolution is 12% at 1 MeV. The expectation is to reach $\sin^2(2\theta_{13}) = 0.01$ after three years of data taking at 90% C.L. [113]

The RENO experiment

Site and Schedule The RENO experiment (Reactor Experiment for Neutrino Oscillation) is a South Korean-Russian experiment located at Yonggwang nuclear power plant in the Southwestern part of South Korea [115]. This power plant consists of 6 equally spaced reactors in a line spanning 1.5 km and yielding up to 16.4 GW_{th}. Only one near and far detector are foreseen and they will be placed on the iso-flux line from the reactors. The near detector will be located at about 290 m from the cores barycenter with an overburden of 120 mwe and the far one at 1380 m surrounded by 450 mwe (cf. fig. 4.3). The two detector sites are foreseen to be finished for december 2010 allowing the data taking to start [116].

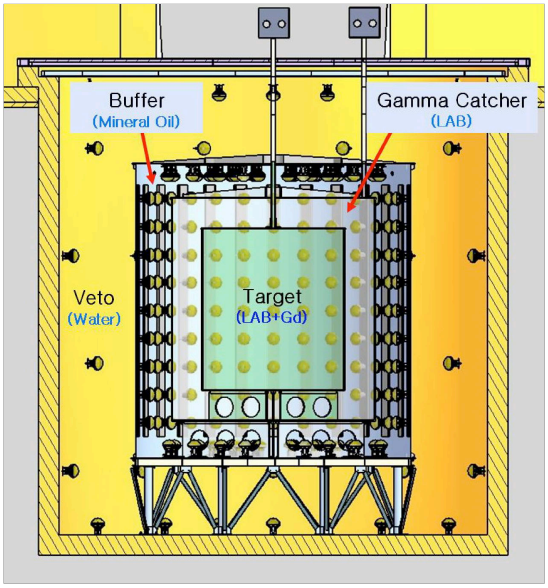

Figure 4.6: The RENO detector design. It is similar to the Double Chooz one except the muon veto made of water contained in a concrete vessel.

Detector Design and sensitivity The fiducial target mass will be 16 tons of Gd-loaded liquid scintillator contained in a 25 mm thick acrylic vessel. The design is essentially the same as Double Chooz with a notable difference for the muon veto system: it will be a 30 cm thick cylindrical concrete vessel filled with water observed by 60 10" PMTs (cf. fig. 4.6). This volume will allow to reduce significantly the rock radioactivity as well as the fast neutrons background. It will also act as a Čerenkov veto to tag muons. The buffer region is 70 cm thick and contains 342 10" PMTs for a 12.6% photocathode coverage and an energy resolution of ∼8%. The goal of the experiment is to have a systematic error of the same order of the

foreseen statistical error of 0.4% which will lead to a sensitivity of $\sin^2(2\theta_{13}) = 0.02$ at 90% C.L. after three years of running [115].

4.1.4 Reactors Discussion

The Double Chooz experiment should be the first reactor experiment to start data taking, shedding new light on the θ_{13} value but only with the far detector running. In case of no disappearance observation, the sensitivity to θ_{13} begins to saturate around 6 months after the data taking start when the RENO experiment is expected to begin. This experiment would drive the sensitivity up to the arrival of Daya Bay about one year later according to the last schedules. The ultimate systematic error of these experiments should lie below 0.6% that is very low and thus the level reached would have to be demonstrated. As regards the reactor-related error, Double Chooz with only two cores and RENO with its two detectors receiving the same ratio of the fluxes from the six cores seem in the best position compared to Daya Bay and its complicated site configuration. As regards the detection-related errors, RENO and particularly Daya Bay that have a consequent overburden should less suffer from the backgrounds whereas Double Chooz benefits from the in-situ measurements of CHOOZ. Moreover with only two cores, it is possible for Double Chooz to have data with both reactors or one of them off what is useful for background studies. Besides reactor experiments will also have to be competitive with the discovery potential of accelerator experiments.

4.2 Accelerator experiments

In the three-flavours oscillation framework, the oscillation of ν_μ into ν_e at the atmospheric Δm^2 value is a very sensitive probe for a non-zero θ_{13} (see equation 3.36). The first term of this equation is analogous to a two-flavor atmopheric oscillation probability with the ν_μ fraction involved in the process is controlled by the $\sin^2 2\theta_{23}$ factor. The third term is an oscillation perturbation due to the solar mixing angle and finally the second term is an interference term which imply the CP violation phase δ. In the case of Inverted Hierarchy (IH), $\Delta m^2_{31} < 0$ and thus $A < 0$ because $V > 0$ for neutrinos. Consequently the (A-1) factors in equation 3.36 leads to a suppression of the transition probability for the IH. It can be seen that the first term is directly proportional to $\sin^2 2\theta_{13}$ and is the main contribution if θ_{13} is large enough ($\sin^2 2\theta_{13} \geq 0.01$). Indeed the second term is suppressed by the α factor and

the third one by α^2, therefore the latter can be neglected. The second term is also dependent on θ_{13} and thus although suffering from degeneracies, an appearance of ν_e from a ν_μ source at Δm^2_{atm} would indicate a non-vanishing θ_{13}.
The known intense sources of ν_μ are either atmospheric or accelerators or solar neutrinos after oscillation. Solar neutrinos have energies below 20 MeV and a long path length that will lead to averaged oscillations. Atmospheric neutrinos span wide energy band ($0.5 - 10^2$ GeV) and path ($20 - 10^4$ km), thus the L/E value is not optimized. Moreover they are composed of all neutrino species and the amount of each flavor is not known accurately enough to seek small θ_{13} values. On the contrary, accelerators are an almost pure ν_μ or $\bar{\nu}_\mu$ source with energies that can be controlled with a minimum energy of the order of GeV implying a baseline of a few hundredth km for sensitivity to θ_{13}.
After the evidence for atmospheric neutrino oscillation (see section 3.2), long baseline accelerator experiments have been carried out in order to confirm the oscillation by looking at the ν_μ disappearance. As a by-product, they were sensitive to $\nu_\mu \rightarrow \nu_e$ oscillations and thus to θ_{13}. We will review the limits brought by such experiments: K2K and MINOS. Then we will focus on the upcoming accelerator long baseline experiments, T2K and NOνA designed to seek a non vanishing-θ_{13}. Afterwards we will briefly present three future projects: LBNE, T2HK and MEMPHYS.

4.2.1 Accelerator technology

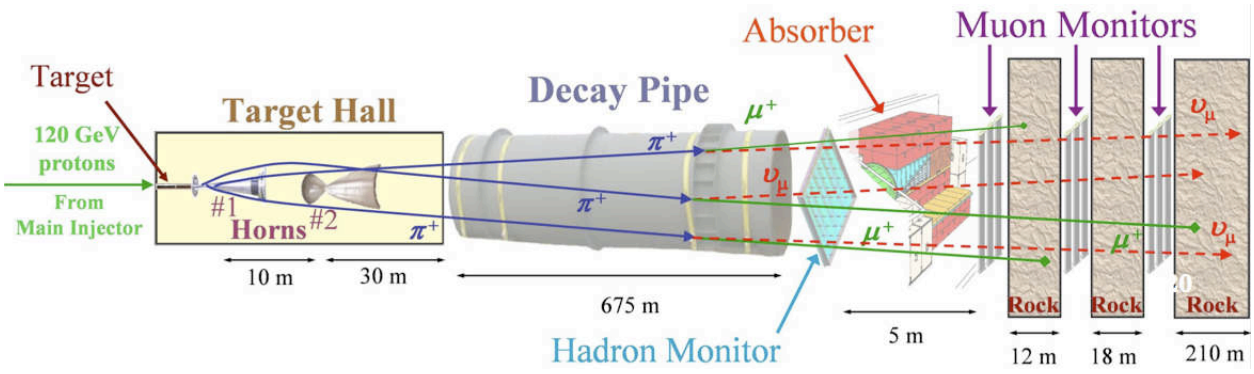

Figure 4.7: Illustration of a neutrino beam principle with the NuMI beam at FermiLab (Chicago, U.S.A) [117].

The technology used to create the neutrinos is called 'pion decay in flight' and is illustrated on figure 4.7. The principle of this technique is to accelerate protons to the desired energy and send them on a target material. The reaction that occurs

then creates pions and kaons. According to the polarity of a magnetic horn placed after the target, positively or negatively charged particles are selected. Positively charged particles give birth after decaying to ν_μ through $\pi^+, K^+ \rightarrow \mu^+ + \nu_\mu$ while a small amount of ν_e is created through $\pi^+, K^+ \rightarrow e^+ + \nu_e$ ($\sim 0.01\%$) and $K^+ \rightarrow \pi^0 + e^+ + \nu_e$ ($\sim 0.5\%$[3]). Another contamination of the beam comes from muon decay. A beam dump is placed about 100 m behind the horn in order to allow only pions and kaons to decay and to stop muons by ionization energy loss. However, about 1% of the muons do have time to decay and consequently give rise to ν_e and $\bar{\nu}_\mu$ through $\mu^+ \rightarrow e^+ + \nu_e + \bar{\nu}_\mu$. The same approach is valid for a $\bar{\nu}_\mu$ beam (the horn polarity has to be changed).

The energy of the neutrinos is related to the pions and kaons whose energy is related to the proton energy. Thus the neutrinos energy band is defined by the proton beam energy. Besides since the pion and kaon decay are two-body reactions, the neutrino energy is defined by:

$$E_\nu \simeq \left(1 - \frac{m_\mu^2}{m_{\pi,K}^2}\right) \frac{E_{\pi,K} m_{\pi,K}^2}{m_{\pi,K}^2 + E_{\pi,K}^2 \theta^2} \tag{4.4}$$

where E_ν, $E_{\pi,K}$ are respectively the neutrino and pion/kaon energies. m_μ, $m_{\pi,K}$ are the muon and pion/kaon masses, and θ is the detector angle with respect to the pion/kaon direction of flight. This equation is obtained by neglecting the neutrino mass and in the approximation of small θ. The equation indicates that the neutrino energy closely follows the pion/kaon energy, it is even directly proportional to $E_{\pi,K}$ for an on-axis detector. Hence the neutrino energy band is determined by the pion/kaon one, this is the case of the K2K, MINOS and LBNE experiments; the two first will be described in the next section. A very interesting case is when the detector is placed off-axis at the angle which minimizes the E_ν dependence to $E_{\pi,K}$: $\theta \simeq m_{\pi,K} / < E_{\pi,K} >$, giving an almost monochromatic neutrino beam [20]:

$$E_\nu \simeq \left(1 - \frac{m_\mu^2}{m_{\pi,K}^2}\right) \frac{m_{\pi,K}}{2\theta} \simeq \frac{29.79 \text{ MeV}}{\theta}. \tag{4.5}$$

The T2K and NOνA experiments that will be described in the third section will use this technique.

[3]Kaons represents typically 10% of pions with a 5% branching ratio for $K^+ \rightarrow \pi^0 + e^+ + \nu_e$.

4.2.2 K2K and MINOS

K2K [71] and MINOS [72] are experiments designed for the ν_μ disappearance measurement. The K2K experiment was built to check the oscillation evidence found by SK as well as the MINOS experiment that came later and is still running (see section 3.3.1). Albeit not optimized for ν_e appearance, they have brought constraints on θ_{13}.

The K2K experiment

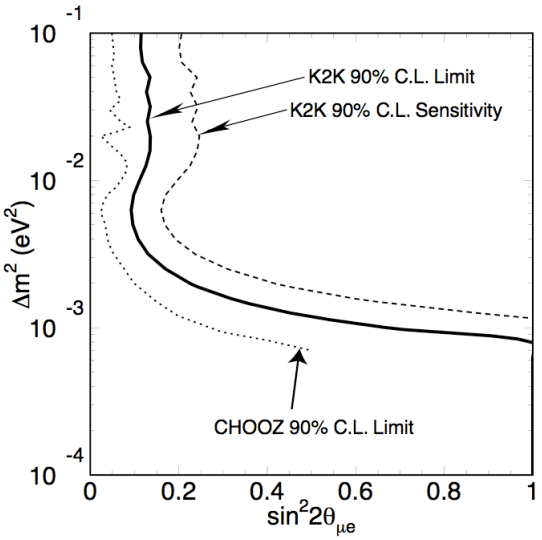

Figure 4.8: K2K confidence interval (solid line), sensitivity (dashed line) at 90 % C.L. compared to the CHOOZ results. $\sin^2 2\theta_{\mu e}$ is the amplitude of the oscillation probability, $\sin^2 2\theta_{\mu e} = \sin^2\theta_{23} \sin^2 2\theta_{13} \simeq \frac{1}{2}\sin^2 2\theta_{13}$.

The K2K experiment was the pioneering accelerator long baseline experiment looking to $\nu_\mu \rightarrow \nu_e$ transition. The ν_μ beam of mean energy 1.3 GeV was sent from the KEK laboratory to the SK detector located in the Kamioka mine at a distance of 250 km. The ν_e candidates were selected assuming charged current quasi-elastic interaction (CC-QE) that implied a single e^--like Čerenkov ring in the SK detector above 100 MeV[4]. The background was obviously due to the intrinsic ν_e contamination of the beam and misidentified ν_μ charged current interactions (CC-nonQE) but more seriously to non quasi-elastic neutral current interactions creating a π^0. If its energy is large enough, the two boosted γ from its decay can

[4]These cuts alow to reject ν_μ CC-QE events, low momentum charged pions from CC-nonQE and electrons from muon decay whose momentum is under the Čerenkov threshold.

merge to mimic the electron ring or if the energy is low, in asymmetric decay the lower energy γ can be hidden under the scattered light of the higher one. The background events were assessed by extrapolating measurements of a 1kt water Cerenkov near detector. From the data taken from June 1999 to July 2001, only one ν_e event was found where 2.4 background events were expected in case of no oscillations [118]. The limit found was $\sin^2 2\theta_{13} \leq 0.3$ at $\Delta m^2_{31} = 2.8 \times 10^{-3}\text{eV}^2$, consistent with the CHOOZ measurement (cf. fig. 4.8).

The MINOS experiment

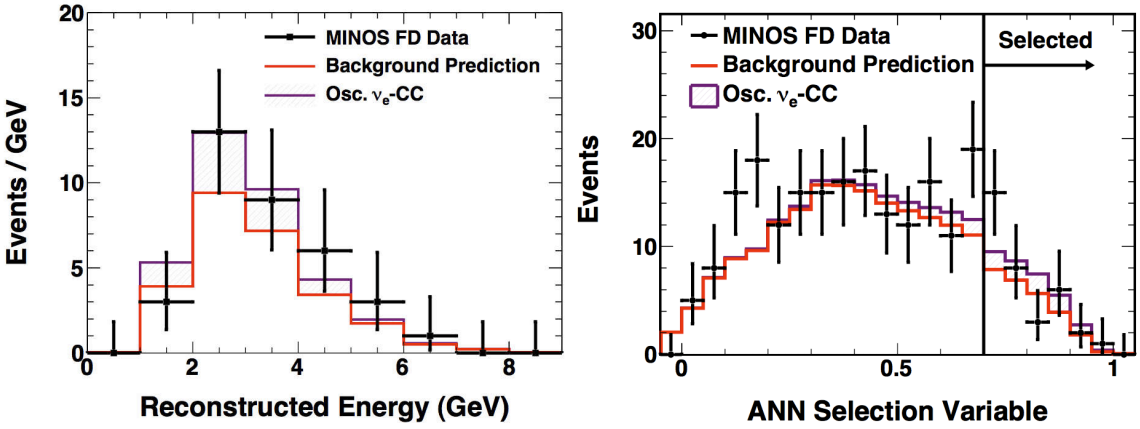

Figure 4.9: Left panel: reconstructed energy distribution of the ν_e-CC selected events between 1 and 8 GeV. Right panel: distribution of the ANN (Artificial Neural Network) selection variable and the cut applied. On both plots, the data are the black points with the statistical errors, the background prediction is in red and the required ν_e-CC excess is the oscillation hypothesis is in purple.

The MINOS experiment brought the current best value on Δm^2_{atm}: $|\Delta m^2_{atm}| = (2.43 \pm 0.13) \times 10^{-3}\text{eV}^2$ by looking at ν_μ disappearance between its near and far detectors [72]. Its neutrino beam is sent from the Fermilab NuMI facility (310 kW of beam power) with a mean energy of 3.5 GeV to the Ash River site, 735 km away. The far detector located on this site is a magnetized tracking calorimeter optimized for the ν_μ charged current (CC) interaction. Like the K2K experiment, ν_e can be detected through CC interaction with a background arising from neutral current (NC) and misidentified ν_μ CC. The experiment have observed interesting results between 1 and 8 GeV: 35 events have been selected as ν_e events while only 27±5(stat.)±2(syst.) were expected giving about 1.5 σ excess[5]. The signal

[5]From the MINOS presentation at Neutrino 2010, the excess is now 0.7σ[117].

lies in θ_{13} values just under the CHOOZ limit for all δ values and for $|\Delta m^2_{atm}| = (2.43 \pm 0.13) \times 10^{-3}\text{eV}^2$ and $\sin^2 2\theta_{23} = 1$ [119]. The NC data can also be used to look for $\nu_\mu \rightarrow \nu_e$ transition since the ν_e-CC interactions have the same event topology. An analysis has been performed in [103] on both data sets and the results have been compared. The hint for the ν_e appearance data is not confirmed by the NC data (cf. fig. 4.10). Furthermore the ν_e-CC events were selected thanks to an artificial neural network based on eleven inputs variables characterizing the longitudinal and transversal energy deposition in the detector. One can notice on figure 4.9 that the signal excess over the background depends strongly on the position of the cut. Thus it is important to wait for the analysis including the full MINOS statistics since the error bars are quite large. Indeed the full MINOS statistics is currently 7×10^{20} p.o.t.[6] while this analysis include only 3.14×10^{20} p.o.t.

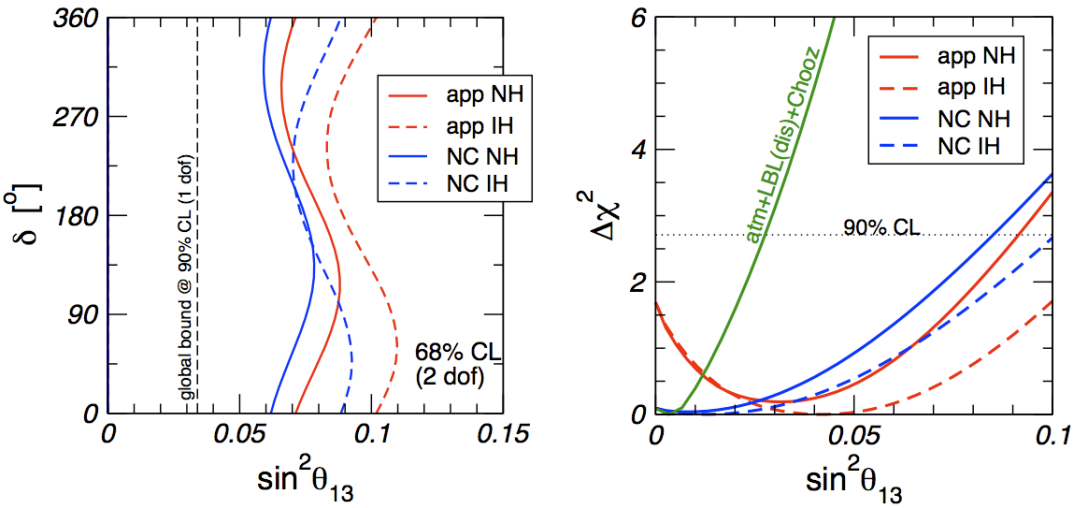

Figure 4.10: Left panel: allowed regions in the $(\sin^2\theta_{13} - \delta)$ plane at 68% C.L. for MINOS ν_e appearance and NC data. Regions are shown separately for normal (NH) and inverted (IH) neutrino mass hierarchy. The bound from global data at 90% C.L. is shown for comparison. Right panel: $\Delta\chi^2$ projection as a function of $\sin^2\theta_{13}$ for MINOS ν_e appearance and NC data, assuming NH (solid) and IH (dashed), both with respect to the common minimum, which occurs for IH. The green solid curve corresponds to the bound from CHOOZ+atmospheric+K2K+ MINOS (disappearance) data [103].

[6]Protons on target

4.2.3 T2K and NOνA

These two experiments use Super Beams, the principle is the same as described above but the beam power is increased to ∼750 kW (about twice the beam power of conventional beams) for a better statistics on the ν_e appearance. The ν_e appearance

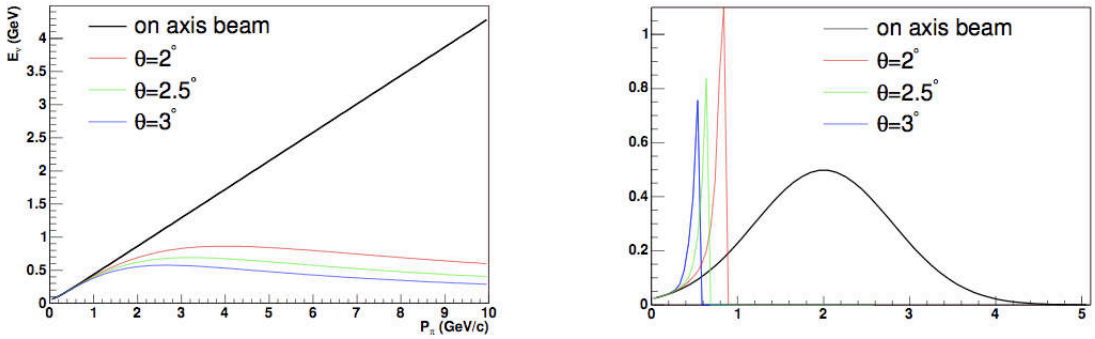

Figure 4.11: Illustration of the ν_μ energy dependance on the angle between the pion direction of flight and the detector. The right plot shows the normalized ν_μ energy distribution while the left plot shows the ν_μ energy as a function of pion momentum [120].

experiments T2K and NOνA use the off-axis technique. As shown in equation 4.5, this technique allows to have a neutrino beam energy solely depending on the angle between the pion/kaon direction of flight and the detector (cf. fig. 4.11). It has three important advantages [120, 103]:

- Although the overall neutrino flux decreases, the flux at the atmospheric L/E value is larger.
- By selecting accurately the energy, the flux of higher energy neutrinos causing most probably non quasi-elastic (non-QE) interactions that is an important source of background, is reduced.
- The intrinsic ν_e beam component is reduced by selecting only the ν_e candidates around the energy peak of the beam. Indeed, most of this background comes from the three-body decay (continuous spectrum) of muons and kaons.

The T2K experiment

The T2K (Tokai to Kamioka) experiment can be considered as an upgrade of the K2K experiment. A high intensity neutrino beam is sent from the J-PARC (Japan Proton Accelerator Research Center) facility to the SK detector located 295 km

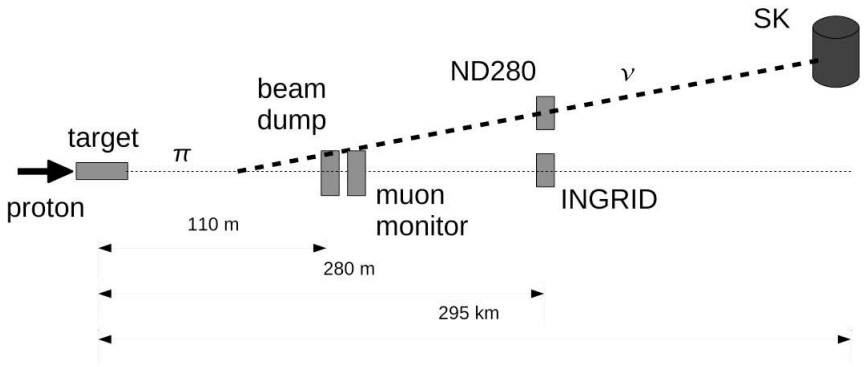

Figure 4.12: Schematic of the T2K experiment from [122].

away with a 2.5° off-axis angle. The neutrino beam has an energy peaked around 700 MeV and the nominal power expected is 750 kW. The experiment does not have currently the nominal power but expect to reach around 2017 the exposure equivalent to 5 years at nominal power [121].

The experiment has a hall at 280 m from the proton target that contains two near detectors: one on axis called INGRID and one off-axis at 2.5° called ND280 (cf. fig 4.12). The goal of the INGRID detector is to control the neutrino beam direction precisely ($<$ 1 mrad) since a deviation of the beam would change the detector angle and therefore there would be different spectral shapes in the near and far detector. The target is point-like for the SK detector but not for the near detectors and thus the extrapolation will suffer from a large uncertainty. The ND280 detector goal is not only to measure the ν_μ flux (5% accuracy) and spectrum (2% accuracy) but also to measure the ν_e contamination (<10% accuracy) and the non-QE/QE ratio (5-10% accuracy). This latter measurement is important since the cross section is poorly known in the neutrino beam energy range. This detector contains a π^0*detector* (POD) that has good capabilities for neutral current π^0 production measurement.

The experiment has detected the first neutrino event at the end of february 2010 and is currently taking data up to the scheduled shutdown in June 2010. The sensitivity is typically $\sin^2 2\theta_{13} = 0.006$ for $\Delta m^2_{31} = 2.4 \times 10^{-3}\text{eV}^2$ at 90% C.L. after five years of data taking (3.75 MW$\times$ 10^7s) without taking into account correlations nor degeneracies ($\delta = 0$ and NH). An upgrade of the experiment is foreseen with the T2HK (Tokai to HyperKamiokande [123]) where the far detector mass will be greatly enlarged ($\sim$1 Mton) and the beam power will be increased (up to 4 MW). The detector will also be off-axis. It would be possible to run with $\bar{\nu}_\mu$ and provide

a high statistics for CP violation research (right plot of figure 4.16).

The NOνA experiment

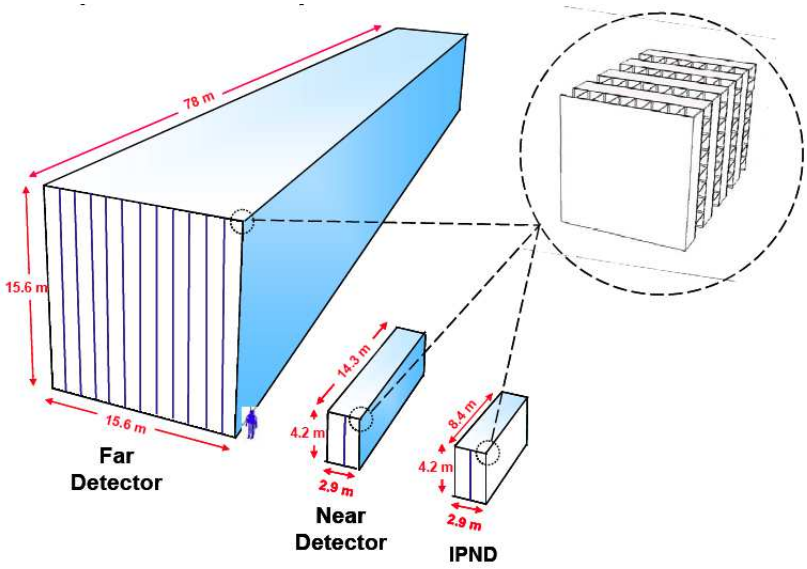

Figure 4.13: Schematic of the NOνA detectors [124].

The NOνA experiment is expected to start in 2013. It is foreseen to send neutrinos with a mean energy of 2 GeV from the NuMI facility to the Ash River site located 810 km away. The existing MINOS beam will be upgraded in order to reach a power of 700 kW. The detector will be a 15 kton segmented plastic scintillator placed 0.8° off-axis, it will be 15.7 m wide and tall, and 78 m long. The near detector will be 2.9 m wide, 4.2 m tall and 14.3 m long, and placed at the same off-axis angle as the far detector (cf. fig. 4.13). A prototype detector of 2.9 m wide, 4.2 m tall and 8.4 m long called IPND is expected soon at the surface of the NuMI building with 0.6° off-axis angle. The experiment is designed for electron neutrino appearance and with its higher energy and path to the far detector, it will be more sensitive to the matter effects and thus to the sign of Δm^2_{31}. The experiment is planned to run 3 years with ν_μ and then 3 years with $\bar{\nu}_\mu$ offering good sensitivity to CP violation measurement. The sensitivity is typically $\sin^2 2\theta_{13} = 0.007$ for $\Delta m^2_{31} = 2.4 \times 10^{-3}\text{eV}^2$ ($\delta = 0$, NH and $\sin^2 2\theta_{23} = 1$) at 90% C.L. after three years of data taking [124].

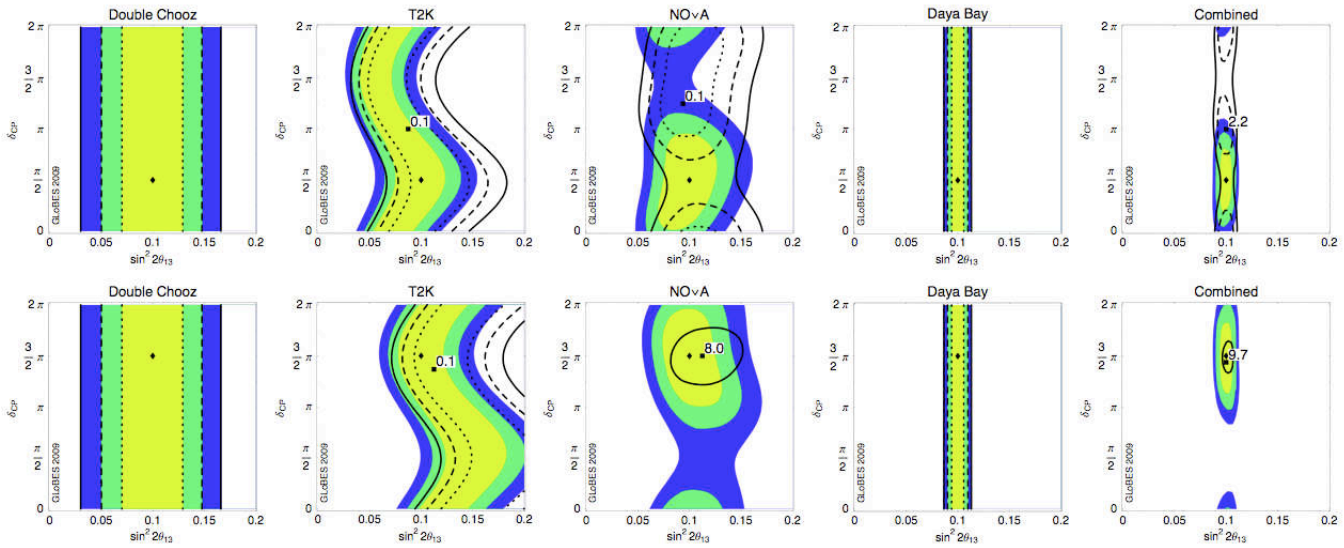

Figure 4.14: Simulated measurements by Double Chooz, T2K, NOνA, Daya Bay and all combined of $\sin^2 2\theta_{13}$ as a function of δ assuming $\sin^2 2\theta_{13} = 0.1$ and $\delta = \pi/2(3\pi/3)$ for the upper (lower) plots. The colours are 1σ, 2σ and 3σ for NH and the curves for IH. One can remark the dependence on the parameters for the accelerators and not for the reactors. An important thing is that by combining the results of accelerators and reactors, the parameter space is greatly reduced allowing a good estimation of δ [109].

4.3 Accelerators and reactors complementarity

At first glance, the accelerator and reactor experiments look concurrent since both are looking for a non-vanishing θ_{13} mixing angle but actually they are rather complementary for accurate determination not only of θ_{13} but also of the CP violation phase δ and the mass hierarchy (MH) determined by the sign of Δm^2_{31} [125].
For the time being, neutrino oscillation experiments have not been able to determine θ_{13}, δ, the sign of Δm^2_{31} and if $\sin^2 2\theta_{23}$ is maximal or not. This can lead up to eight-fold degeneracies while the degeneracy due to θ_{23} have a small impact compared to the others. A ν_e appearance in a beam of ν_μ would indicate a non-vanishing θ_{13} but could be unable to disentangle between (θ_{13}, δ) clone solutions. Even an experiment in an optimized configuration:

- L/E value optimized to reduce the (θ_{13}, δ) correlation from an ellipse to a line in the $(P_{\bar{\nu}_\mu \to \bar{\nu}_e}, P_{\nu_\mu \to \nu_e})$ plane
- run at high energy with a long baseline to get rid of the possible degeneracy due to the sign of Δm^2_{31} (however the uncertainty on the matter density will increase the uncertainty on δ).

could still suffer from degeneracies[7] [126].

The accelerator experiments will have the best θ_{13} discovery potential being however very dependent on the mass hierarchy and the δ value. A signal observation at accelerators will indicate a non-zero θ_{13} and will give a range for its value that will probably be measured by reactor experiments opening the way to the δ measurement (cf. fig. 4.14). In the case of no θ_{13} effect observation, the sensitivity is clearly driven by reactor experiments and especially Daya Bay down to $\sin^2 2\theta_{13} < 0.01$. Going further in constraining θ_{13} will require accelerator projects[8] with a large fiducial volume in order to have a sensitivity only limited by the systematic due to the intrinsic contamination of the beam (cf. fig 4.15).

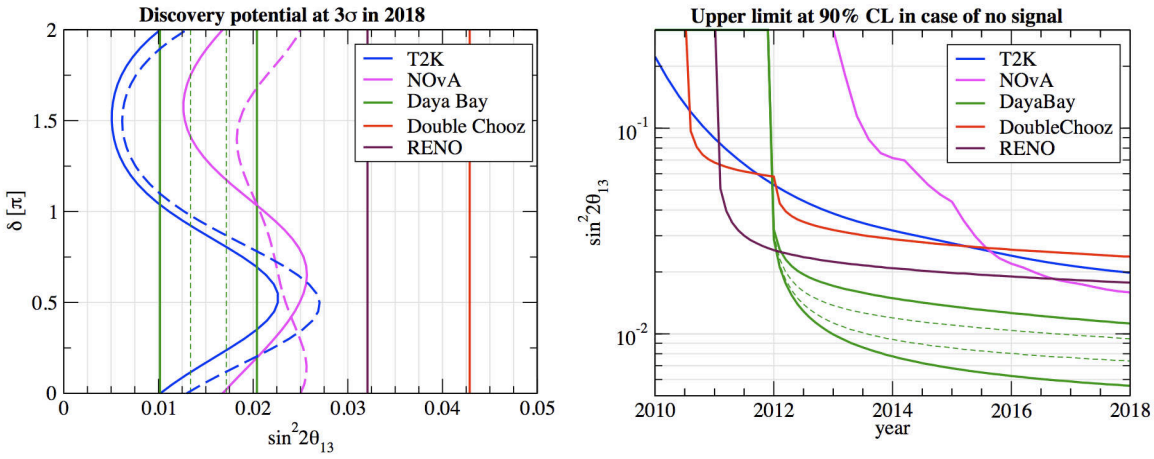

Figure 4.15: Left panel: discovery potential expected in 2018 for the five running/upcoming experiments in the plane $\sin^2 2\theta_{13}$-δ. Straight line are the reactor experiments and curved lines are the accelerator ones. Right panel: evolution of the 90% C.L. sensitivity to $\sin^2 2\theta_{13}$ as a function of time. In both plots, the several Daya Bay curves correspond to different possible systematic uncertainties [103]. The best discovery potential is for the accelerators while the best sensitivity is for the reactors experiments.

Future large fiducial mass detectors

There are three realistic far future projects that aims at studying oscillations induced by θ_{13} and according to the results of the experiments cited just previously,

[7]The degeneracies could be resolved by adding a detector at an intermediate baseline or by building an experiment with a 'magic' baseline that allow to be sensitive only to θ_{13} by causing the disappearance of the solar and interference terms [126, 127].

[8]Reactor experiments with a very large fiducial volume (M $\simeq$ 200 tons) and a different small near detector have capabilities to go further in constraining θ_{13} as the abandoned ANGRA project [128]. No project of this type is envisaged for now.

possibly the CP violation phase δ and the sign of Δm^2_{31}. The possibility to access δ and the sign of Δm^2_{31} is strongly dependent on how large θ_{13} is: if it lies just below the CHOOZ limit, it will be possible otherwise these experiments will bring the stringent limit. The three projects are LBNE, MEMPHYS and T2HK. T2HK is an upgrade of T2K and has already been presented together with it. MEMPHYS and LBNE will be briefly reviewed in what follows.

The LBNE project LBNE stands for Long Baseline Neutrino Experiment and is a project initiated by the U.S.A. The principle is to send a high intensity neutrino beam from the FermiLAB NuMI facility to on-axis underground detectors located at DUSEL (4200 mwe) in the South Dakota, 1300 km farther. This long distance allows to be very sensitive to matter effects and thus to the sign of Δm^2_{31}. Two detection techniques are envisaged: Water Čerenkov (WC) with a fiducial mass above 300 ktons or Liquid Argon Time Projection Chamber (LArTPC) with a fiducial mass above 50 ktons. It is even envisaged to have both technologies due to their complementarity. WC is the most probable technology to be used since the LArTPC one at this detector scale has not yet been proved to work. The WC detector will have to be split in several sub detectors to reach the fiducial mass goal. The project has recently been granted and is hence the most realistic project from those cited above.

The MEMPHYS project MEMPHYS stands for MEgatonne Mass PHYSics, this is a project that aims to use the Čerenkov light detection technique. The wished site for the experiment is Fréjus in the Modane underground laboratory (4800 mwe) at 130 km from CERN, in France. It could thus receive Super Beams or even β-beams[9] and have capabilities to measure θ_{13} with an unprecedented sensitivity like the T2HK project. Three cylindrical detectors of 60 m (80 m is possible for the Fréjus site) in height and 65 m in diameter are foreseen with a 30% coverage (81000 PMTs each) for a total fiducial mass of 440 kton. A 2 ton prototype of the experiment called MEMPHYNO is installed at the APC laboratory for research and development studies [131].

[9]This technique is under study, the proposal is to use boosted radioactive ions whose decay produce a pure beam of ν_e for ^{18}Ne (β^+) and $\bar{\nu}_e$ for ^{6}He (β^-) [130].

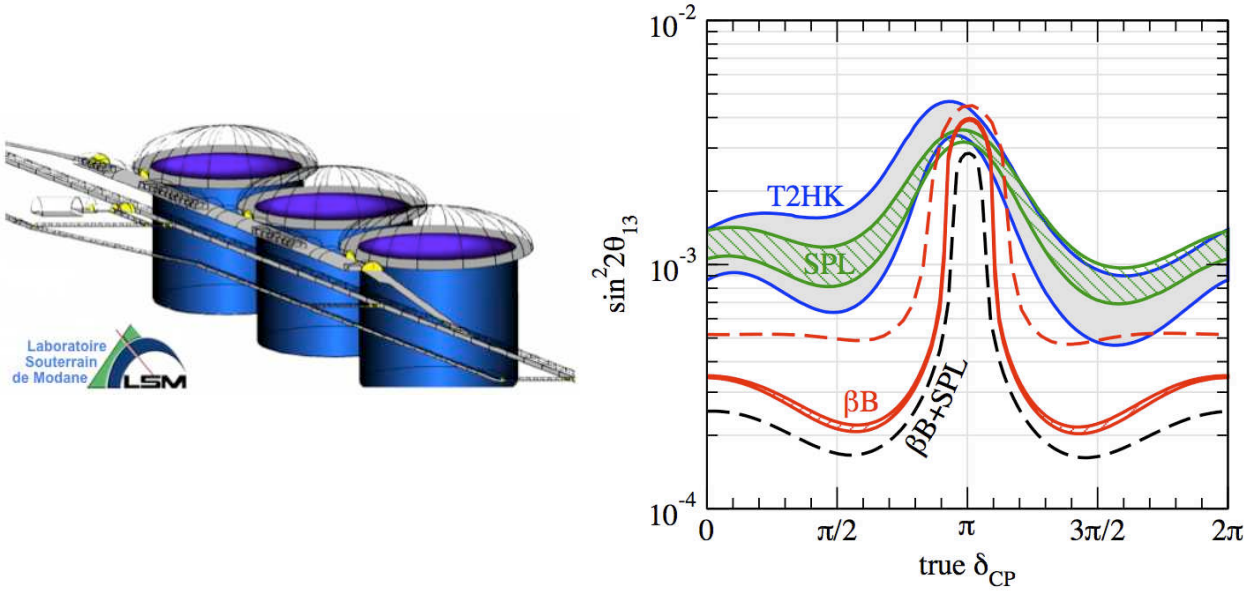

Figure 4.16: (Left) Scheme of the MEMPHYS detectors in the Fréjus site. (Right) 3σ discovery sensitivity to $\sin^2 2\theta_{13}$ for T2HK and β-beams (βB, 5 years ν_e and 5 years $\bar{\nu}_e$), Super Beams (SPL, 2 years ν_μ and 8 years $\bar{\nu}_\mu$) sent to MEMPHYS as a function of the δ_{CP} value. The width of T2HK and SPL are due to systematic error value between 2% and 5 %. The dashed dark curve is the combination of βB and SPL while the dashed red curve is the βB sensitivity for an ion decay rate divided by two [129].

4.4 Other measurements of θ_{13}

Although less sensitive or less probable, there is other ways than reactor and accelerator experiments to possibly measure θ_{13}, we will briefly review them here.

4.4.1 Atmospheric neutrinos

MSW effect in the Earth can produce large oscillation probability of atmospheric ν_μ into ν_e. For θ_{13} at the CHOOZ limit and a neutrino energy between 2 and 10 GeV, it can lead to a 40% change in the flux as can be observed on figure 4.17. The effect is the most pronounced for upward going neutrinos and thus a detection of a θ_{13} effect would be an excess of upward going electron event in the multi-GeV data. The SuperKamiokande experiment has observed no evidence for this effect [132]. The limit brought is close to the CHOOZ limit: $\sin^2\theta_{13} < 0.04$ ($\approx \sin^2 2\theta_{13} \leq 0.15$) at 90% C.L. assuming normal hierarchy.

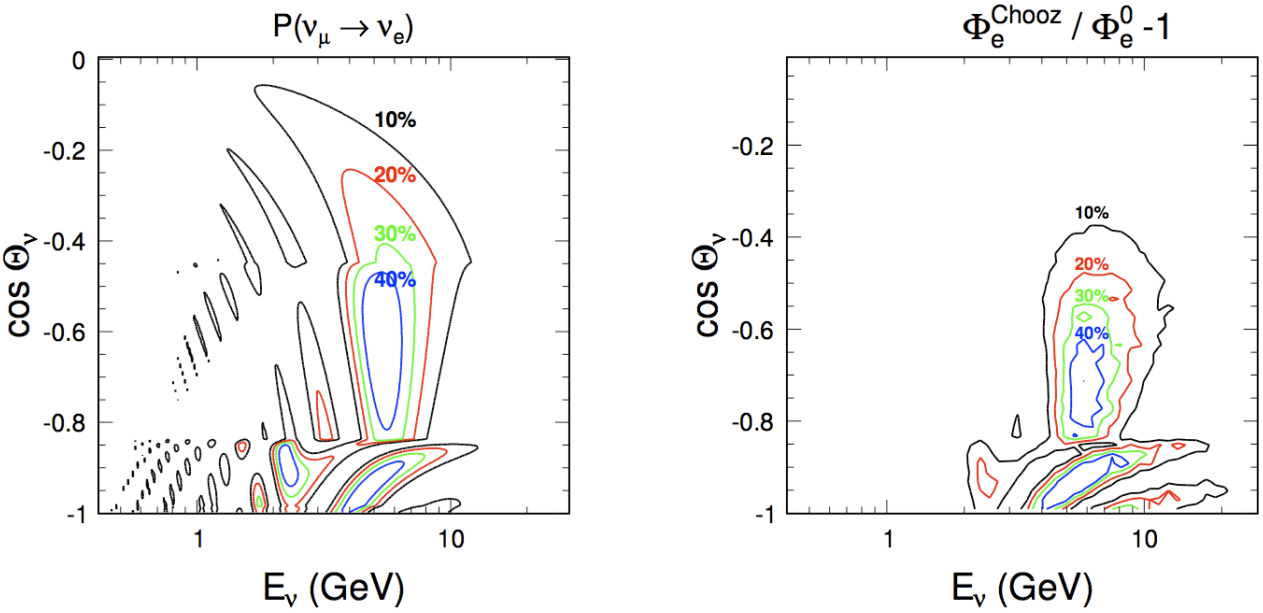

Figure 4.17: Left panel: three flavor oscillation probability $\nu_\mu \to \nu_e$ for θ_{13} at the Chooz limit under the normal hierarchy (solar and interference terms neglected). Right panel: ν_e flux ratio $\Phi_e^{Chooz}/\Phi_e^0 - 1$ for oscillations with θ_{13} at the CHOOZ limit. $\cos\Theta_\nu = 0, -1$ correspond to horizontal and vertically upward directions respectively. The atmospheric parameter chosen are $\Delta m^2_{32} = 2.1 \times 10^{-3}\text{eV}^2$ and $\sin^2 2\theta_{23} = 1$ [132].

4.4.2 Solar neutrinos

An asymmetry of the solar neutrinos oscillation probabilities during day and night can be a probe for θ_{13} thanks to the 'regeneration' effect in the Earth. Considering the Earth density as constant, the difference in the oscillation probabilities can be written as follows [133]:

$$P_N - P_D = -\frac{2EV}{\Delta m^2_{21}} \cos^6\theta_{13} \langle \cos 2\theta^m_{12} \rangle \sin^2 2\theta_{12} \sin^2 \frac{\Delta m^2_{21} L}{4E} \tag{4.6}$$

where P_D and P_N are respectively the probabilities for the day and the night. V is the matter potential of the Earth, $\langle \cos 2\theta^m_{12} \rangle$ is $\cos 2\theta_{12}$ altered by the matter effects averaged on the neutrino production point in the sun. L is the neutrino source-detector distance and E is the neutrino energy.
The asymmetry defined as:

$$A_{DN} = 2\frac{P_N - P_D}{P_N + P_D} \tag{4.7}$$

is proportional to $\cos^2\theta_{13}$ being a probe of θ_{13}. Such effect has been searched for unsuccessfully at SuperKamiokande, SNO and recently Borexino [134, 135, 136]. The measurement is limited by the statistical error.

4.4.3 Supernova neutrinos

The neutrino fluxes in a supernova explosion are dependent on θ_{13} due to the MSW effect happening inside the supernova [132, 137]. However other supernova parameters influence the fluxes making difficult to extract informations on θ_{13}. The experiments aiming at such a measurement would need to have spectral informations on the neutrinos flavours with enough statistic to disentangle between the different parameter values. Large water Čerenkov detectors are the best detectors for this measurement especially when doped with Gd for a high efficiency to inverse β-decay (Gd-doping is envisaged in the three large fiducial volume projects). The θ_{13} effect appear for $\sin^2 2\theta_{13} < 0.001$ as can be viewed on figure 4.18. Therefore a supernova explosion detection with the requirements just presented fulfilled will tell us if $\sin^2 2\theta_{13}$ is above or below this limit value possibly determining the future program for θ_{13} and δ measurements.

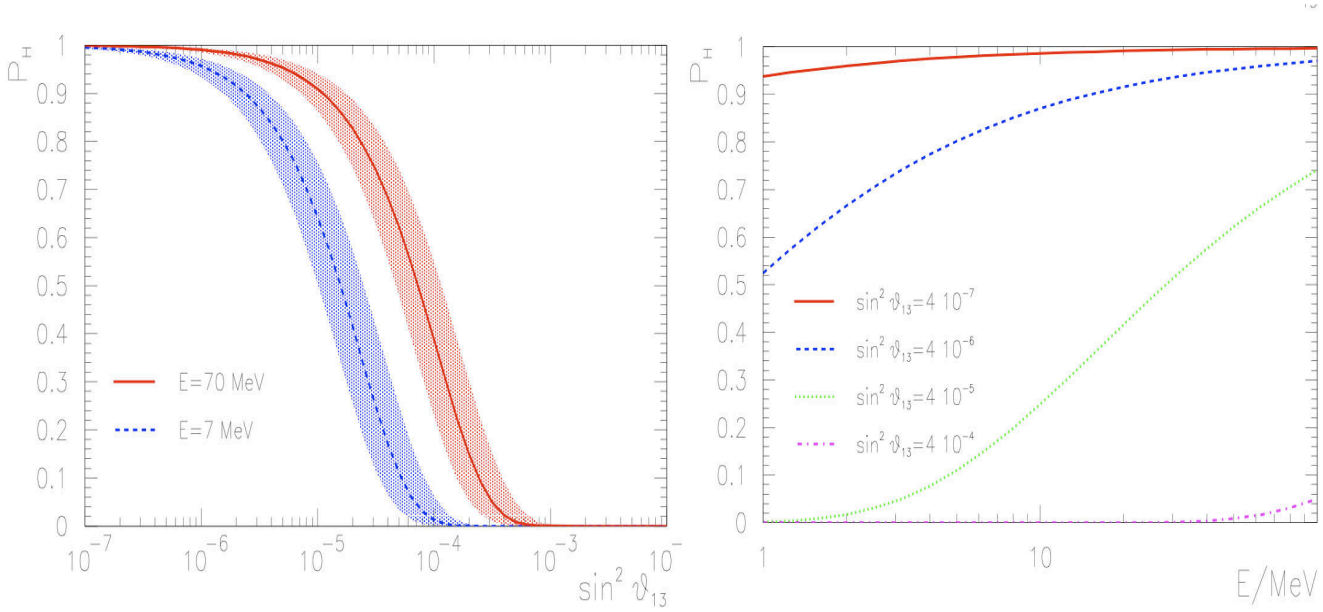

Figure 4.18: Transition probability at resonance P_H as a function of $\sin^2\theta_{13}$ for different energies (right panel) and as a function of energy for different $\sin^2\theta_{13}$ values (left panel) [137].

Chapter 5

The Double Chooz experiment

Nuclear reactors have played a crucial role in neutrino history. The neutrino was discovered by Cowan-Reines reactor experiment at Savannah River [2] and 45 years later they allowed the KamLAND experiment to solve model-independently the long standing solar neutrino problem [83]. They are still a precious source for the search for a non-zero θ_{13} as does the Double Chooz experiment.
The Double Chooz experiment is designed to measure or constrain θ_{13}. To reach this goal, it will measure $\bar{\nu}_e$ disappearance by precise comparison of flux and spectra at two detectors and at different distances from nuclear reactor cores. The site chosen is the nuclear power plant of Chooz, a town in the Ardennes in France which hosted the famous CHOOZ experiment [89]. In this chapter, we will first focus on the source of the electron antineutrinos and then on the expected sensitivity. We will also review the detector design and the far detector integration as well as the data acquisition system.

5.1 The Chooz nuclear power plant site

5.1.1 Description of the Chooz power plant

The Chooz nuclear power plant is a PWR (**P**ressurized **W**ater **R**eactor) N4 type. This is the most common type of reactor in the world whose fuel is slightly enriched uranium dioxide (UO_2) that contains 3.45% of ^{235}U while it is only 0.711% in nature[1]. The major contribution to energy production in a nuclear power plant

[1]The remnant components are ^{238}U at 99.284% and ^{233}U at 0.0058%.

comes from the fission of ^{235}U nuclei which releases a mean energy of ∼200 MeV per fission. The fission reaction is initiated by a thermal neutron and emits in turn 2 or 3 neutrons. These neutrons need to be slowed down in order to initiate a new reaction, this is why the fuel is immersed in water which acts as a moderator. However, the reaction should be prevented from a runaway, only one neutron in average should initiate a new reaction. This is the reason why the water contains boron and control rods which absorb neutrons[2]. The water present in the core at a temperature of about 280° is warmed at a temperature of 327 °C by the products loosing their kinetic energy[3] and would evaporate if its vessel, called the primary, circuit was not kept under a pressure of typically 150-160 atm. This circuit is in contact with an independent water circuit called the secondary circuit whose water is not pressurized. After the contact with the primary circuit, it evaporates and turns the turbine coupled with an alternator producing electrical energy. The yield of this thermal power transformation is ∼ 33%. Eventually the water of the secondary circuit is cooled by a third circuit which contains water coming from the Meuse river and is consequently available for a new loop of energy production. One third of the fuel needs to be changed every year.

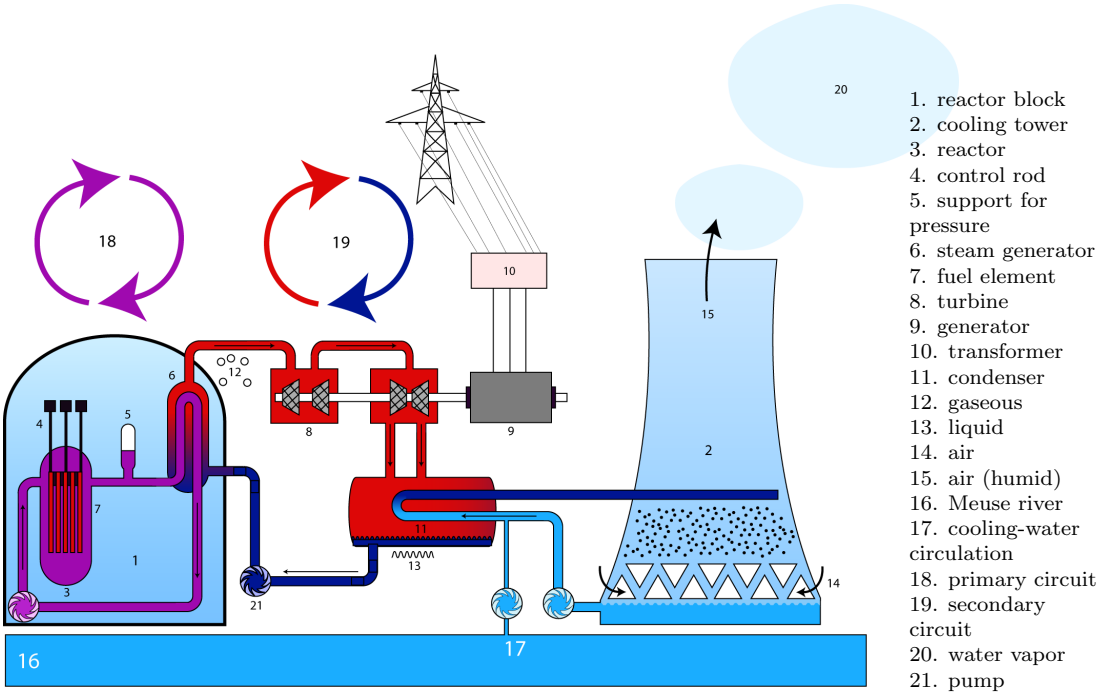

Figure 5.1: Design of a PWR reactor type.

[2]The length of the control rods immersed is adjusted for the good functioning of the reactor, it can even be completely immersed to stop the reaction in case of emergency.

[3]Mainly the 2 nuclei of the fission reaction (90%) but also γ rays, fast neutrons and β particles.

5.1.2 Production of electron antineutrinos

The fission which takes place in the reactor vessel produces lighter nuclei which are neutron rich. These nuclei then undergo β^- decays which produce electron antineutrinos. The ^{235}U fission yields about 200 MeV (cf. fig. 5.1) and 2 daughter nuclei which after 3 β^- decays on average, produces a mean number of 6 $\bar{\nu}_e$. Therefore, the number of $\bar{\nu}_e$ is correlated with the thermal power of a reactor (cf. fig. 5.2). Typically 5% of the heat produced per fission is carried away by $\bar{\nu}_e$.

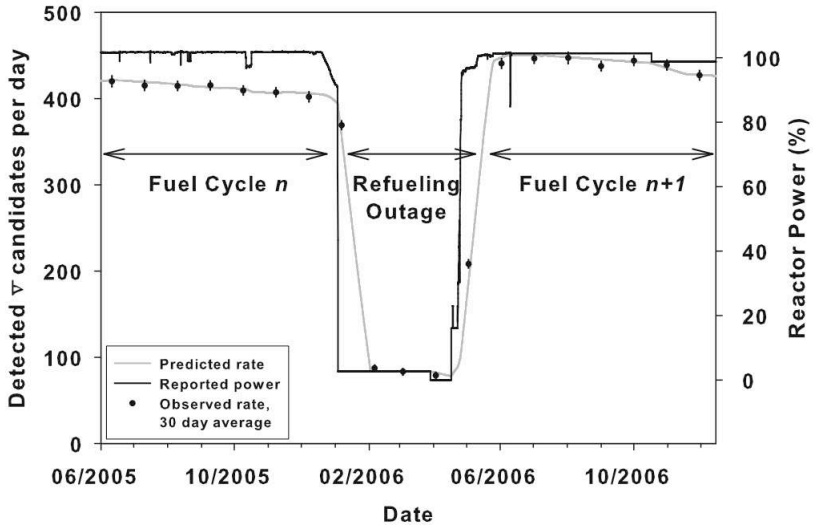

Figure 5.2: Evidence of the correlation between the number of $\bar{\nu}_e$ detected and the thermal power of the reactors at San Onofre (U.S) [138].

Though ^{235}U is the main responsible of the thermal power of a reactor it is not the only one, there are other elements which contributes notably as ^{238}U, ^{239}Pu and ^{241}Pu (cf. tab. 5.1). ^{238}U is fissile only with neutrons above 0.8 MeV but leads to the production of Plutonium through thermal neutron capture. The ^{239}Pu is produced thanks to a neutron capture by ^{238}U followed by two β^- decays:

$$\mathrm{n} + {}^{238}\mathrm{U} \rightarrow {}^{239}\mathrm{U} \rightarrow {}^{239}\mathrm{Np} \rightarrow {}^{239}\mathrm{Pu} \qquad \mathrm{T}_{1/2}({}^{239}\mathrm{Pu}) = 24110 \text{ years} \quad (5.1)$$

and the ^{241}Pu is produced by two successive neutron captures by ^{239}Pu:

$$\mathrm{n} + {}^{239}\mathrm{Pu} \rightarrow {}^{240}\mathrm{Pu}\ ,\ \mathrm{n} + {}^{240}\mathrm{Pu} \rightarrow {}^{241}\mathrm{Pu} \qquad \mathrm{T}_{1/2}({}^{241}\mathrm{Pu}) = 14.3 \text{ years} \quad (5.2)$$

All the emitted $\bar{\nu}_e$ cannot be detected since their detection occurs through the inverse β-decay reaction whose threshold is 1.8 MeV. This allows only the $\bar{\nu}_e$ from the short half-life isotopes to be detected. The isotopes with long half-life have a

	^{235}U	^{238}U	^{239}Pu	^{241}Pu
Energy per fission (MeV)	201.7 ± 0.6	205.0 ± 0.9	210.0 ± 0.9	212.4 ± 1.0
Mean energy of $\bar{\nu}_e$ (MeV)	1.46	1.56	1.32	1.44
$\bar{\nu}_e$ per fission	5.58	6.69	5.09	5.89
$\bar{\nu}_e$ per fission above 1.8 MeV	1.92 ± 0.036	2.38 ± 0.048	1.45 ± 0.030	1.83 ± 0.035
Duty cycle's beginning	60.5%	7.7%	27.2%	4.6%
Duty cycle's end	45.0%	8.3%	38.8%	7.9%

Table 5.1: Features of the 4 elements significantly involved in the $\bar{\nu}_e$ spectrum [139, 140, 141, 142].

small end point value and are consequently below the reaction threshold[4]. This fact allows the experiment not to take care of the waste fuel stored on the reactor site. In addition, the number of detectable neutrinos is reduced to $\sim 25\%$. The Chooz power plant is composed of 2 cores from the French standard N4 which can reach an electrical power of 1450 MW. Considering an efficiency of 33%, 200 MeV/fission released and 1.5 $\bar{\nu}_e$/fission emitted, the maximum rate of detectable $\bar{\nu}_e/s$ emitted by the Chooz power plant is the following:

$$N(\bar{\nu}_e/s) = \frac{2 \times 1450 \times 1.5}{33\% \times 200 \times 1.6 \cdot 10^{-19}} \approx 4 \cdot 10^{20} \tag{5.3}$$

5.1.3 Spectrum of the electron antineutrinos

As the emission of $\bar{\nu}_e$ occurs through β-decay, the possible energy for a $\bar{\nu}_e$ is a continuous distribution up to the end point (Q-value) of its parent nucleus. As mentioned in the previous section, with the ^{235}U example, there are many β^- decays occurring for the products and further these nuclei can be produced in an excited state or even capture neutrons. All the β-branches have to be summed accordingly to their yield to compute correctly the final spectrum:

$$S_{tot}(E) = \sum_{fp} Y_{fp} \sum_{b} BR_{fp_b} S_{fp_b}(Z_{fp}, Q_{fp_b}, E) \tag{5.4}$$

[4]The half-life of a given isotope is inversely proportional to the phase space available which is determined by the Q-value.

where S_{tot} is the total spectrum, Y_{fp} is the fission yield of the fission product fp, BR_{fp_b} is the branching ratio of the b branch of fp and $S_{fp_b}(Z_{fp}, Q_{fp_p}, E)$ is the spectrum of the fp branch of fp which is a function of the Q-value Q_{fp_b} and Z_{fp}[5] of the nucleus considered.

Using the Fermi theory with its corrections and the nuclear databases [143], predictions can be made on the electron and $\bar{\nu_e}$ spectra as did a Double Chooz group. The most accurate data to be compared with are the data taken by Schreckenbach group in 80's at ILL (Institut Laue-Langevin, Grenoble, France) [144, 145]. They measured the β spectra of ^{235}U, ^{239}Pu and ^{241}Pu from thermal neutron induced fissions with a high resolution electromagnetic spectrometer with negligible statistical and calibration error up to electron energies of 8 MeV[6]. The electron spectra comparison showed a discrepancy of $\pm 5\%$. Consequently it is hard to consider an accuracy better than 5% for the obtained $\bar{\nu_e}$ spectrum which is too large for the purposes of reactor neutrino experiments. This discrepancy arises from the dependence on the used nuclear databases which are known to be not exhaustive especially at high energy. Nevertheless, these computations have been used to revisit Schreckenbach's group electron-$\bar{\nu_e}$ conversion procedure. His group fitted the measured electron spectrum with 30 virtual β-branches and applied the principle of energy conservation to recover the $\bar{\nu_e}$ spectrum[7]. The Double Chooz group decided to rather fit with their 10000 physical β-branches which represent 95% of the measured electron spectrum. The remaining 5% were fitted with 5 virtual branches to get a discrepancy smaller than 1% as Schreckenbach's group required for its calculation. This technique yields a mean systematic normalization of +3% with respect to Schreckenbach's group calculation which remains after careful tests[8]. This calculation is believed to be a new reference for reactor neutrino experiments and is to be published soon [146].

[5]The electrons which are charged particles need to have enough kinetic energy to escape the coulomb barrier determined by the number of protons Z. Therefore the measured spectrum of e^- does not go through (0,0). The $\bar{\nu_e}$ spectrum which is the mirror of the electron one shows thus discontinuities at high energy.

[6]The ^{238}U spectrum has not been measured since it is not fissile with thermal neutrons (cf. equation 5.1). However, its contribution is always less than 10% to the total thermal power in REP.

[7]It is considered that all the energy is carried out by the e^- and the $\bar{\nu_e}$: $E_0 = E_{\bar{\nu_e}} + E_{e^-}$.

[8]The remaining 5% can also be fitted by allowing the decay branching ratios of the each fission product to vary although it seems less physical than some missing β branches. This technique yields the same shift of +3%. Further crosschecks have been performed, the Schreckenbach conversion procedure have been applied on an electron spectrum computed from the nuclear databases and compared to the corresponding $\bar{\nu_e}$ spectrum. A discrepancy of +3% has been found which is consistent to the one of the Double Chooz group prediction.

The technique described above predicts the reactor $\bar{\nu}_e$ spectrum at a given time

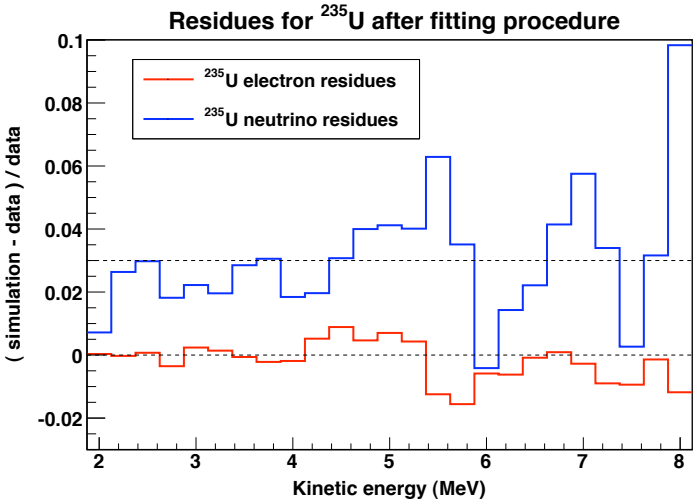

Figure 5.3: ^{235}U residues between the Schreckenbach's group measurement and the fitting procedure in red, it remains below 1% as required by Schreckenbach's group fitting procedure. In blue, ^{235}U residues between the two conversion procedures. A mean shift of +3% is observable between the 2 techniques [146].

while the fuel composition changes with time. Indeed during the reactor functioning, ^{235}U is consumed while there is creation of ^{239}Pu and ^{241}Pu and a slight decrease of the ^{238}U, this is the so-called burn-up of the fuel. This burn-up effect can be observed on figure 5.4 which shows calculations of the evolution of the contributions per element to the thermal power over a reactor duty cycle. Since the spectra of these elements are not the same (cf. fig. 5.5), it is of primary importance to model the fuel composition evolution. Other Double Chooz groups dedicated their work to predict the fuel composition at any time using the MURE (MNCP Utility for Reactor Evolution) code and DRAGON respectively [147, 148]. Many factors like the core geometry, the fuel composition at the beginning of a reactor cycle and the neutron flux and physics had to be taken into account as well as off equilibrium effects. This work is complementarity with the work detailed above can predict the $\bar{\nu}_e$ flux and spectrum as a function of the thermal power of the nuclear power plant and time. These calculations will be indispensable for the phase 1 of the experiment where only the far detector will be available[9]. This will be the dominant systematics.

[9]They are also very suited for the non proliferation studies which aims to detect any use of a civil reactor to divert plutonium for military use [138].

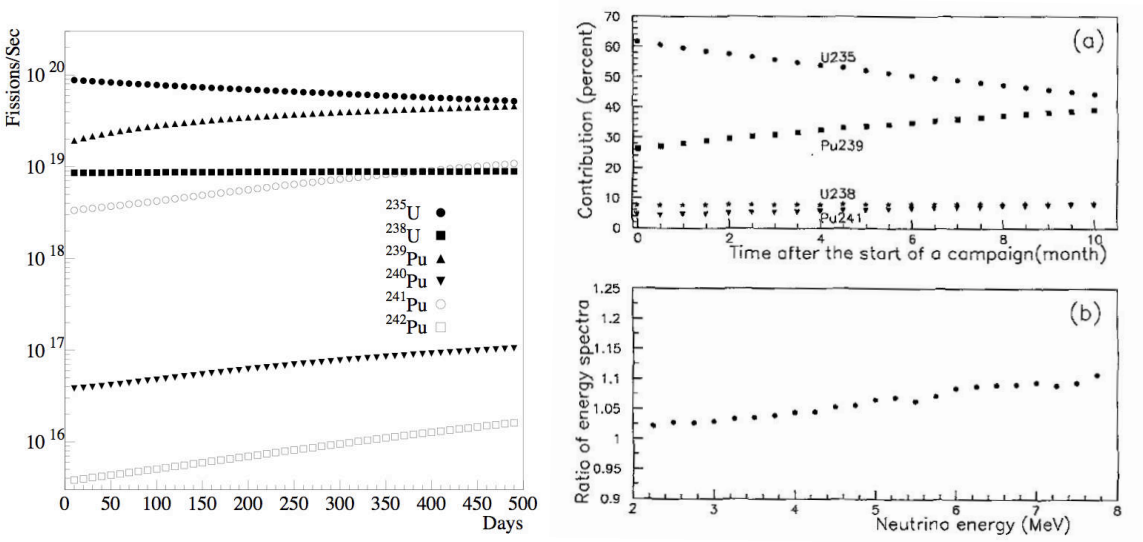

Figure 5.4: Left plot: calculation of the fuel composition evolution during a duty cycle for one of the Palo Verde reactor [86]. ^{240}Pu and ^{242}Pu contributions can be neglected since they represent less than 1% of ^{238}U.
Right plots: a) Calculated contribution per element to the energy production of the Bugey reactor. b) Ratio of the calculated $\bar{\nu}_e$ spectra at the start and the end of the Bugey reactor duty cycle [82]. An noticeable change of up to 10% can be noticed in the spectrum.

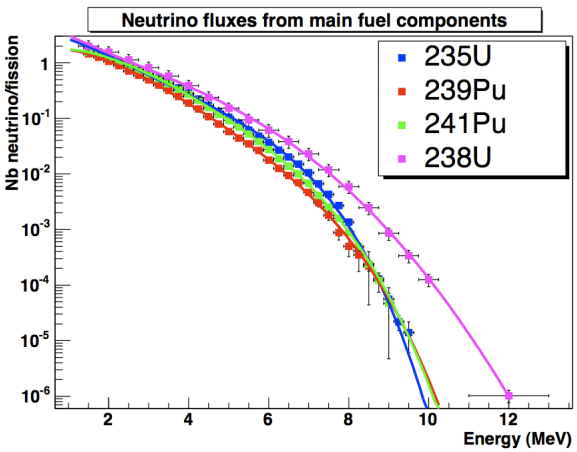

Figure 5.5: Spectrum of the 4 elements involved in the $\bar{\nu}_e$ production [139, 140]. The x axis is the energy in MeV and the y axis is the number of $\bar{\nu}_e$ per fission.

5.1.4 Detector positions

The Double Chooz experiment uses 2 identical detectors, one close to the 2 reactor cores to monitor the $\bar{\nu}_e$ flux and spectrum labeled 'near detector' and one far, in the hole of the previous CHOOZ experiment labeled 'far detector'. The sensitivity

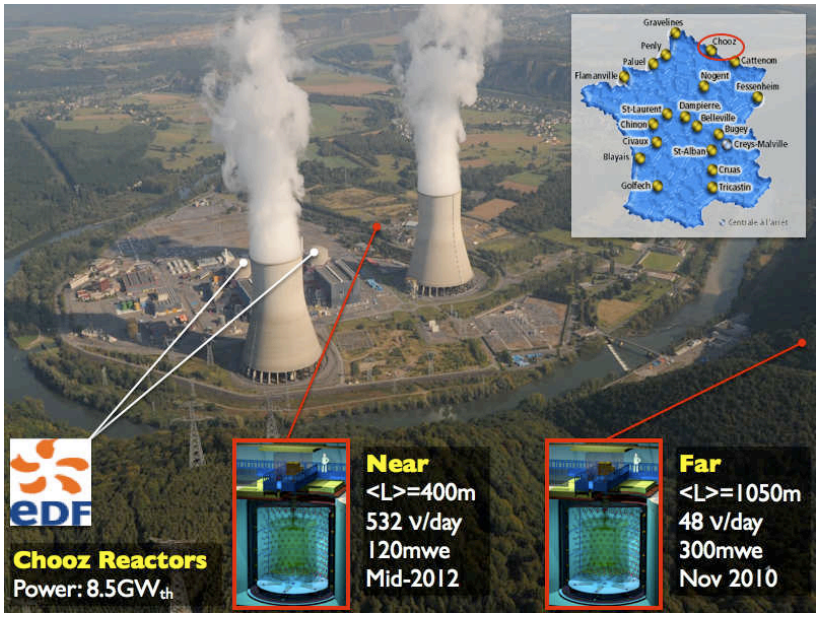

Figure 5.6: Detectors position and topology on the Chooz nuclear power plant site.

to θ_{13} is determined by the signal to background ratio which needs to be optimized. The reactor cores emit the $\bar{\nu}_e$ isotropically and thus the signal goes like $1/4\pi L^2$ (L is the distance source-detector) while the background is related to cosmic rays and so it is important to go underground to reduce its rate as well as having a clean environment to avoid natural radioactivity.
In case of no oscillation, the rate of interactions is calculated as follows:

$$N_{\bar{\nu}_e}(events/day) = \epsilon_{eff} \times \epsilon_{Gd} \times \frac{N(\bar{\nu}_e/day) \times \sigma_p(cm^2) \times n_p(protons/mm^3) \times V(mm^3)}{4\pi L^2(cm^2)} \tag{5.5}$$

where ϵ_{eff} is the detector efficiency[10]. ϵ_{Gd} is the percentage of neutron captured on Gd, N($\bar{\nu}_e/day$) is the number of detectable neutrinos emitted per day. $\sigma_p(cm^2)$ is the $\bar{\nu}_e$ cross section on free protons for a mean neutrino energy of 3 MeV and n_p is the estimated number of protons per mm^3 in DC target liquid scintillator. V is the target volume and $1/4\pi L^2$ is the solid angle factor.

$$N_{\bar{\nu}_e}(events/day) = \epsilon_{eff} \times 80\% \times \frac{4.6 \cdot 10^{25} \times 2.7 \cdot 10^{-43} \times 6.6 \cdot 10^{19} \times 1.02 \cdot 10^{10}}{4\pi L^2}$$

$$N_{\bar{\nu}_e}(events/day) = \frac{4.3 \times 10^{11}}{L^2(cm^2)} \tag{5.6}$$

[10]A dead time is induced by muons which deposit a large energy in the detector and saturate the PhotoMultiplier tubes. At second order, It is also induced by pile-up events.

assuming a detection efficiency of 90%.
The far detector is located at a mean distance of 1.05 km from the cores, close to the first minimum of $\bar{\nu}_e$ flux only due to θ_{13}. The depth and location are fixed because of the existence of the CHOOZ experiment site. Its depth is 300 m.w.e[11] giving rise to an expected muon rate of about 10 Bq in the detection volumes. It turns out that the location does not correspond to the minimum of the $\bar{\nu}_e$ flux[12] which is around 1.5 km for $< E_{\bar{\nu}_e} >= 3$ MeV and $\Delta m^2_{13} = 2.43 \times 10^{-3}$ eV^2. However, this position guarantees a higher flux, a mountain to lower the cosmic rays rate and the same flux from the 2 cores (cf. fig. 5.6 and 5.7). Considering these aspects and the savings in time and money, this location is a good compromise. With a dead time estimated to 0.5%[13], it is expected to have 48 events/day. The backgrounds are expected to be 2 per day for the accidentals and 1.6 per day for the correlated ones. The near detector will be placed at a mean distance of 400 m from the cores where almost no $\bar{\nu}_e$ will have oscillated. This distance allows to receive a large $\bar{\nu}_e$ flux and thus to stay at a rather shallow depth of 120 m.w.e which induce a rate of muons of about 50 s^{-1} in the detection volumes [149]. Estimating then the dead time to 5%, it is expected to have 532 events/day. The backgrounds are expected to be 11 per day for the accidentals and 5.2 per day for the correlated ones.

5.2 The Double Chooz detector

5.2.1 Detection principle

Reactors $\bar{\nu}_e$ have energies of the order of the MeV and hence they can be detected through elastic scattering on electrons and quasi-elastic scattering on proton or deuteron or even on a nucleus. The reaction considered for Double Chooz and most of the reactor experiments is the inverse β-decay (IBD, cf. fig. 5.8)[14]:

$$\bar{\nu}_e + p \rightarrow e^+ + n. \tag{5.7}$$

[11] Meter Water Equivalent.
[12] The location was settled when the Super-KamioKande experiment suggested oscillations at the 10^{-3} eV^2 scale with large uncertainty. It was thus better to choose a position maximizing the signal to background ratio (cf. fig. 5.7).
[13] The dead time is largely dominated by the foreseen 500 μs offline window after a muon since it could have given rise to dangerous cosmogenic backgrounds with long halflife time (see section 4.1.1).
[14] This reaction is also called inverse neutron decay.

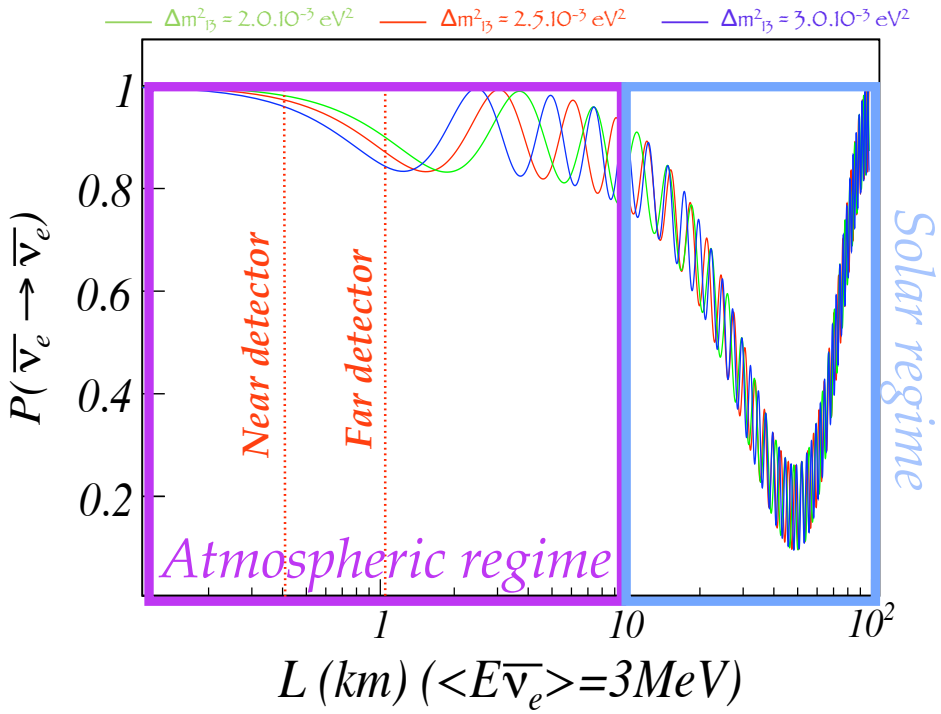

Figure 5.7: $\bar{\nu}_e$ survival probability for different Δm^2_{13} and $< E_{\bar{\nu}_e} >$=3 MeV. The atmospheric regime governed by Δm^2_{13} and the solar regime governed by Δm^2_{12} are displayed as well as the mean near and far detector positions. A value of $\theta_{13} = 12°$ has been arbitrarily chosen. For the plot, we used $\theta_{12} = 32°$, $\Delta\, m^2_{12} = 7.59 \times 10^{-5}$ eV^2 for the solar oscillations.

Neglecting the $\bar{\nu}_e$ mass and assuming a proton at rest, the squared energy in the center of mass is $s = 2E_{\bar{\nu}_e} m_p + m_p^2$. This interaction is possible only if s is sufficient to produce the e^+ and n masses. Consequently:

$$E^{thresh}_{\bar{\nu}_e} = \frac{(m_e + m_n)^2 - m_p^2}{2m_p} \simeq 1.806 \text{ MeV} \tag{5.8}$$

where m_e, m_n and m_p are respectively the positron, neutron and proton masses, and $E_{\bar{\nu}_e}$ is the $\bar{\nu}_e$ energy. This energy threshold implies that only $\sim 25\%$ of the reactor $\bar{\nu}_e$ flux is detectable. The $\bar{\nu}_e$ energy is related to the e^+ energy deposition by:

$$E_{\bar{\nu}_e} = \frac{2m_p E_e + m_n^2 - m_p^2 - m_e^2}{2(m_p - E_e + \sqrt{E_e^2 - m_e^2}\cos\theta)} \tag{5.9}$$

where E_e is the e^+ energy and θ is the angle between the $\bar{\nu}_e$ and e^+ directions. This equation is well approximated by: $E_{\bar{\nu}_e} \simeq E_e + m_n - m_p$. In a liquid scintillator detector, the e^+ annihilation with an electron of the medium is observed at the

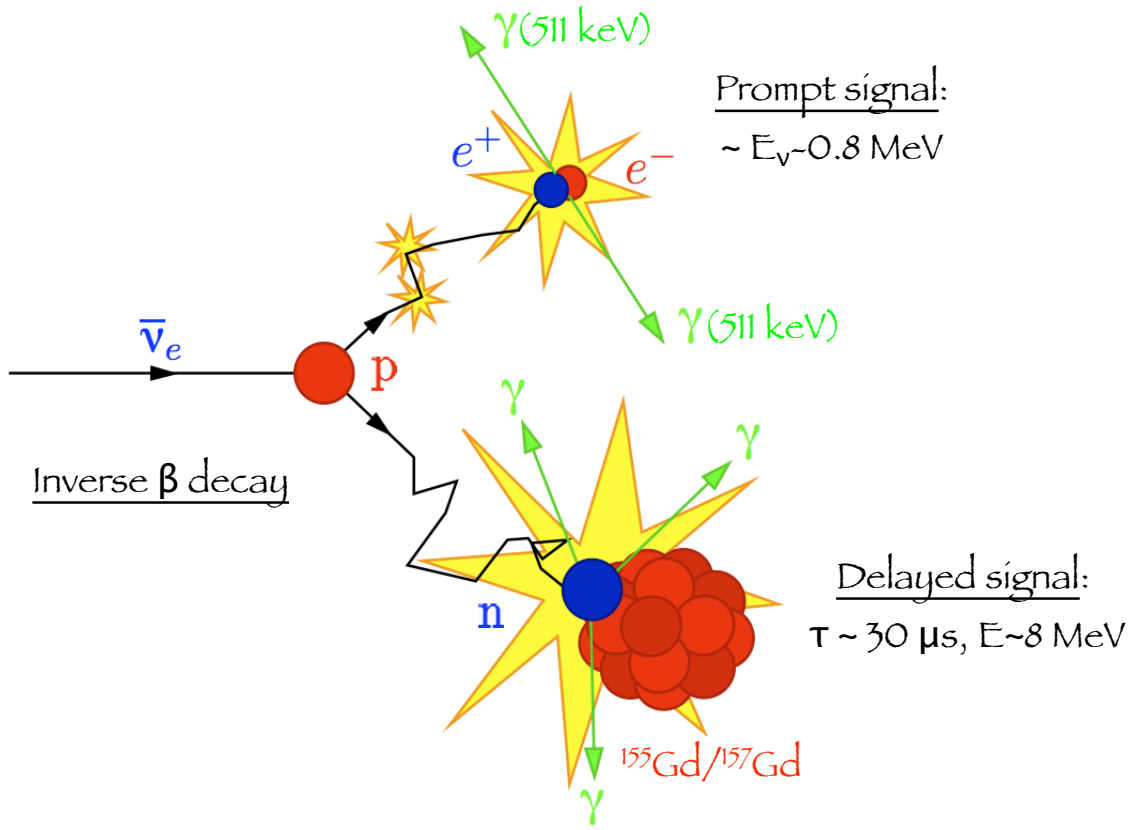

Figure 5.8: Illustration of the inverse β-decay with the neutron capture occurring of Gd [140].

same time as its kinetic energy loss and hence the visible energy E_{vis} is related to the $\bar{\nu}_e$ energy through:

$$E_{vis} = E_e + m_e = E_{\bar{\nu}_e} + m_e + m_p - m_n \simeq E_{\bar{\nu}_e} - 0.782 \text{ MeV} \tag{5.10}$$

The IBD cross section is [150]:

$$\sigma = \frac{2\pi^2\hbar^3}{m_e^5 f \tau_n} p_e E_e (1+\delta) \tag{5.11}$$

where τ_n is the neutron lifetime and f is the free neutron decay phase space factor. p_e and E_e are the e^+ momentum and energy. δ takes into account the radiative and weak magnetism corrections of the order of 1% each. It can be expressed as a function of the $\bar{\nu}_e$ energy [104]:

$$\sigma = K \times (E_{\bar{\nu}_e} + m_p - m_n)\sqrt{(E_{\bar{\nu}_e} + m_p - m_n)^2 - m_e^2} \tag{5.12}$$

with $K = (9.559 \pm 0.009) \cdot 10^{-44}$ cm^2/MeV^2.
The choice of the IBD was driven by the facts that the elastic scattering on electrons has a lower cross section ($\sim 39 \cdot 10^{-46}$ s cm^2/MeV^2 where s is the squared sum of the initial particles), because the interaction on deuteron ($^2_1$H) has a higher energy threshold (2.2 MeV) and because the interaction on a nucleus is hardly detectable (a few keV of nucleus recoil energy); besides their signature is weaker. Using a LS doped with Gd allows to have a lot of protons as target for the IBD and a strong signature. The e^+ energy is constrained as well as the energy from the neutron capture and the delay time between the two energy depositions. The e^+ looses quickly its energy in the liquid scintillator by ionizing and exciting the electron of the molecules. Then the e^+ annihilates with an electron of the medium producing two 511 keV γ. This energy deposition is called the primary energy deposition and is required to be above 1 MeV and below $\sim$ 9 MeV. Meanwhile the neutron with its small kinetic energy thermalizes by making collisions on protons ($^1_1$H nuclei) whose energy is not visible. Finally the neutron is captured in typically $\tau \sim 30$ μs on Gd what yields a mean number of three γ carrying 8 MeV due to the Gd de-excitation, this is the secondary energy deposition. The 8 MeV γ ray cascade allows to be above the radioactivity background due to γ (up to 2.6 MeV) and due to alpha (up to 7 MeV but with a quenching factor of $\sim$ 10). In order not to loose too many events and to not introduce too much of the remaining background, a 100 μs ($\sim 3\tau$) coincidence time window is used.

5.2.2 Design of the detector and integration

As highlighted in the previous section, the Double Chooz detector design has been inspired by the CHOOZ detector with optimization towards a higher neutrino rate and a higher signal to background ratio. Thus the detector components were chosen in order to have a radioactivity background level $\leq$10 Bq in the detection volumes. Besides since the far detector is located in the previous site of the CHOOZ detector, its size and shape were constrained to fit in a cylindrical pit of 7 m in height and diameter. The final detectors design consists of concentric cylinders completed by a plastic scintillator muon veto named 'outer veto'; from the center to outside we find the 'target', the 'γ-catcher', the 'buffer', the 'inner veto' and the 'shielding' (cf. fig. 5.9 and 5.10). The glovebox which is located above the outer veto will be described in the next section. Nevertheless, the near and far detectors need to be identical only up to the buffer tank to lower the detection systematic errors and

hence, better radioactivity γ and muon protections can be envisaged for the near detector which is at 120 m.w.e. At the time this thesis is being written, only the far detector integration is being done while the near detector integration start is expected for the end of 2011.

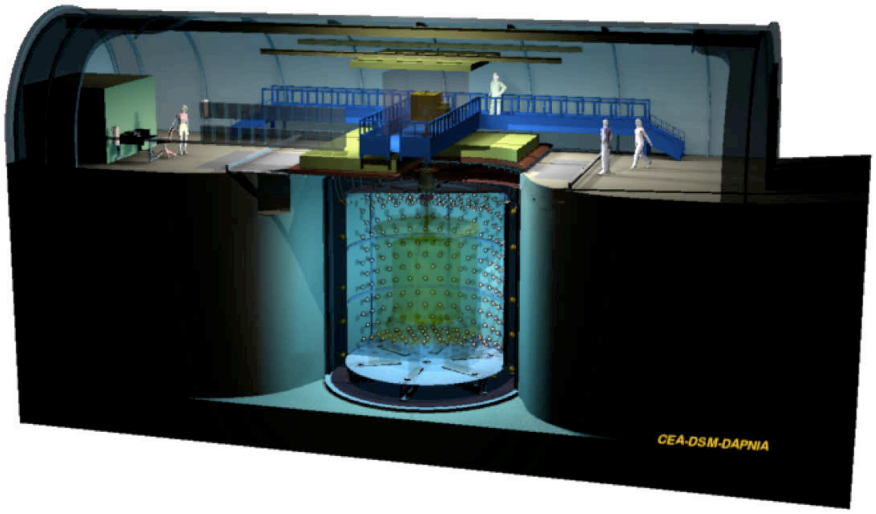

Figure 5.9: Scheme of the Double Chooz far detector lab.

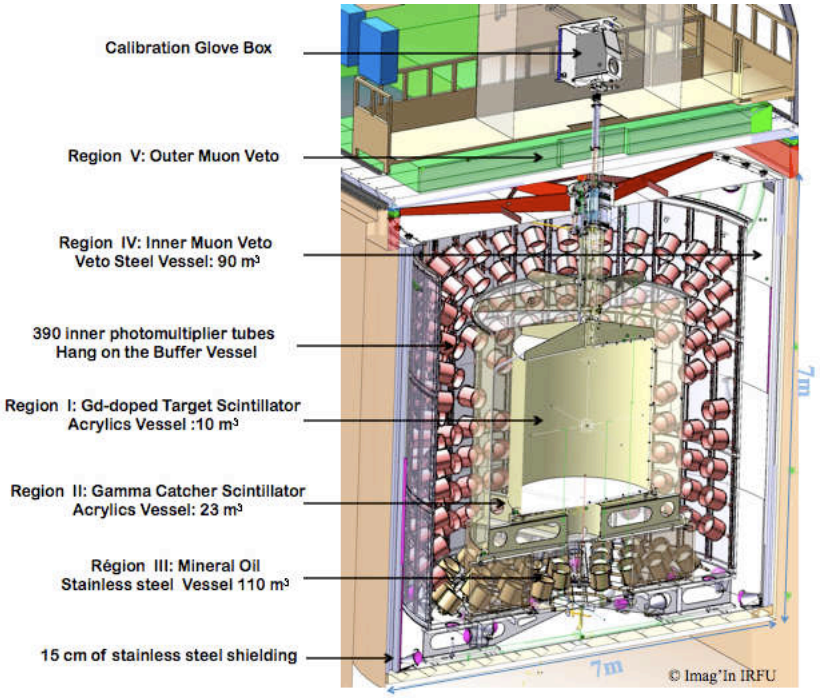

Figure 5.10: The Double Chooz detector design.

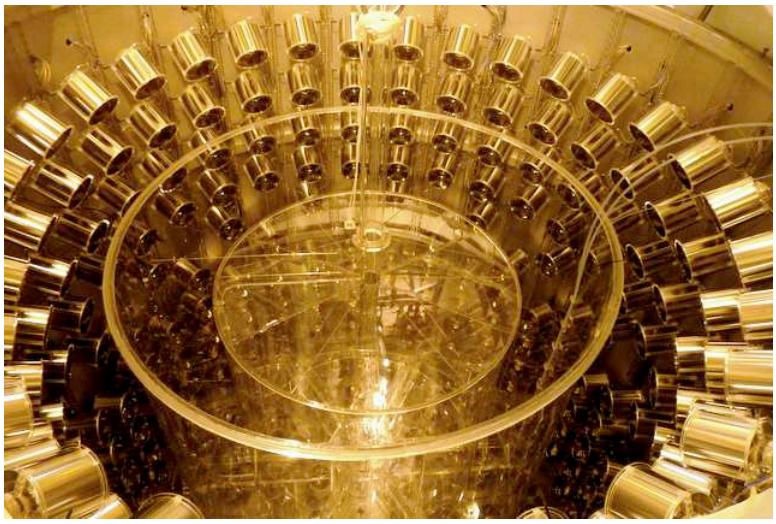

Figure 5.11: Acrylics target with its glued chimney installed in the γ-catcher acrylic vessel.

The target The target is the volume where neutrino interactions are intended to be detected with the neutron capture on Gd. Its dimensions are a radius of 1150 mm and a height of 2458 mm for a mass of 8.23 tons (10.3 m^3 with a density of 0.835 g/cm^3). It is filled with a Gd-doped liquid scintillator contained in an 8 mm thick acrylic vessel, the liquid composition is: 80% of dodecane and 20% of PXE (Phenyl-o-Xylylethan) with 7 g/L of PPO (2,5-diphenyl-oxazole), 20 mg/L of bis-MSB (1,4-bis-(2-Methylstyryl)Benzen)) and 1g/L of Gd. PXE and dodecane are aromatic molecules and thus gets easily excited or ionized by energy depositions. Then the energy is transferred non-radiatively to a PPO molecule and finally to bis-MSB that shifts the emission frequency in the PMT quantum efficiency range. Special care has been given to the development of this liquid scintillator for at least a five year stability. A method has been developed to encapsulate the Gd atom in a molecule named $Gd(dpm)_3$ for an efficient dissolving in the scintillator resulting in a durable transparency of the scintillator.
The target integration occurred during september-october 2009, a picture of the target with its calibration chimney is displayed in figure 5.11. After this operation, the γ-catcher was closed and followed by the buffer (cf. fig 5.2.2).

The γ-catcher The γ-catcher volume is a 22.3 m^3 liquid scintillator volume without Gd, designed to fully contain the γ rays from both the neutron capture and the e^+ annihilation especially those of the events happening close to the border of the target volume. This allows to have a fully active target volume at the cost of

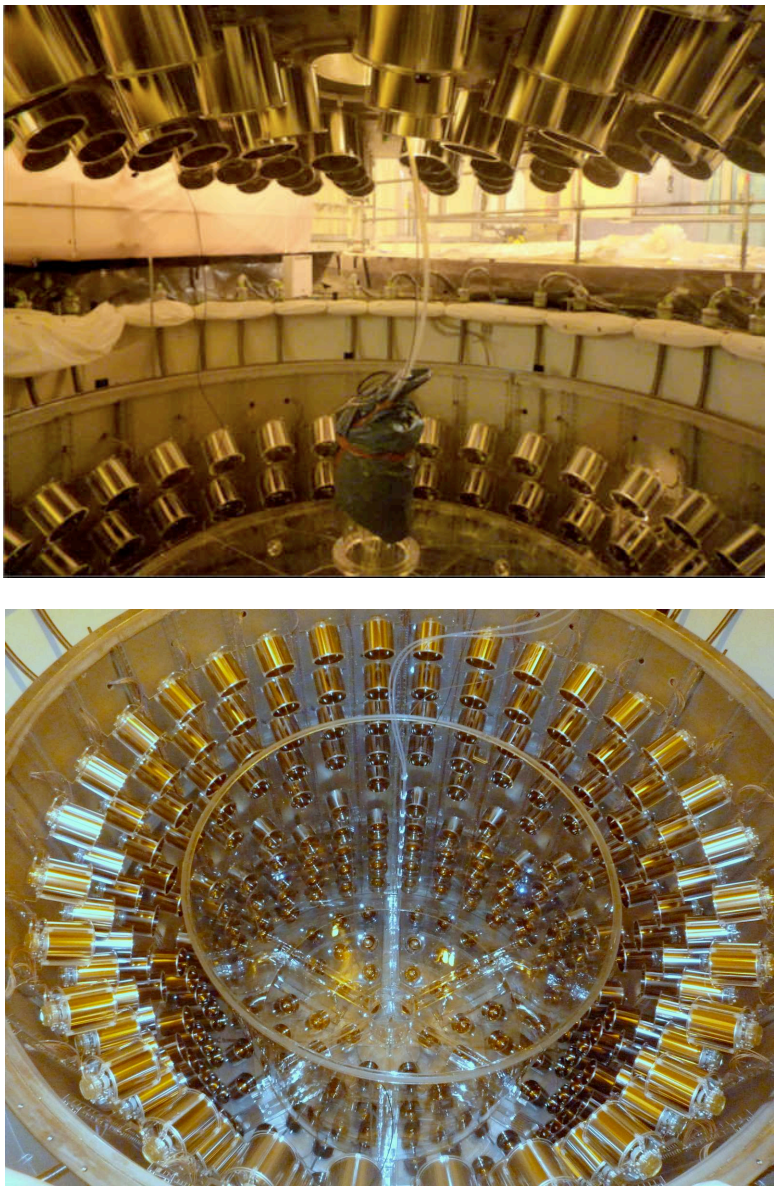

Figure 5.12: γ-catcher vessel installed in the buffer tank.

non trivial spill in/out effects. A spill out happens when the e^+ deposits its energy in the target but the neutron with its higher path length gets captured in the γ-catcher and the spill in is the opposite. The two effects do not exactly compensate but can be neglected if the two detectors are identical. This volume surrounds the target and is 55 cm thick with a 12 mm thick acrylic vessel of 1708 mm in radius and 3572 mm in height. The LS composition is 30% of dodecane, 66% of ondina 909 and 4% of PXE with 2 g/L of PPO and 20 mg/L of bis-MSB.
Work has been carried out to match the target and γ-catcher liquid scintillators light yields while maximizing the difference in their time response. It is presented

at the section 7.2.3.
The γ-catcher was integrated during the august-september 2009 (cf. fig. 5.12). It came in one piece and the difficult operation of entering in the lab and then rotating it was performed successfully to make it lie on its acrylics feet in the buffer tank.

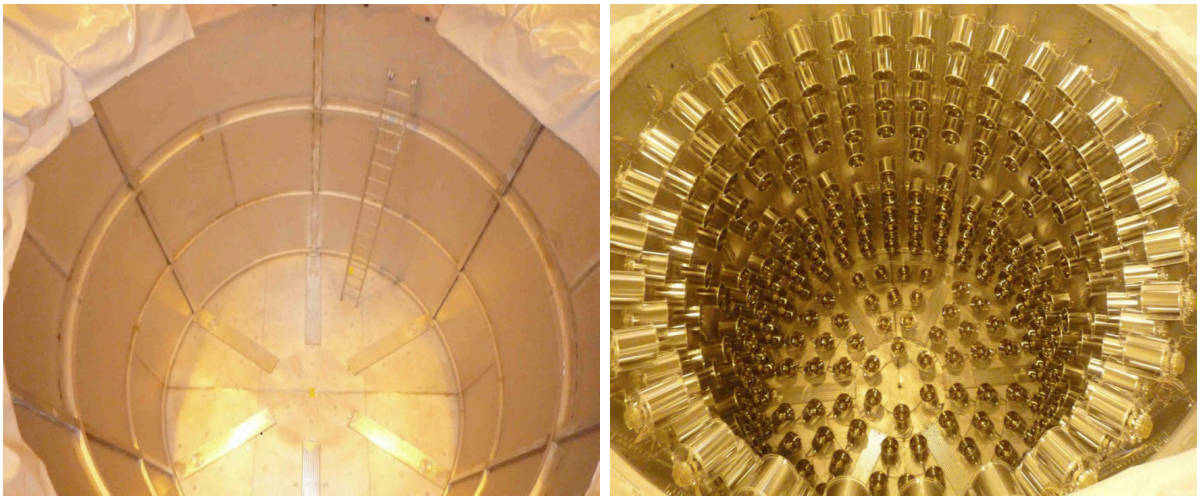

Figure 5.13: Left plot: buffer tank with its stiffeners. Right plot: buffer after the PMTs installation.

The buffer This region is one of the main improvement with respect to CHOOZ, it is meant to reduce the environmental radioactivity γ and especially those from the PMTs. It is a 114 m^3 volume of non scintillating liquid (∼50% of decane to tridecane and ∼ 50% ondina 917) contained in a 3 mm thick stainless steel tank of radius 2758 mm and height 5675 mm. This tank is the support for the 390 10 inches low radioactivity PMTs (Hamamatsu R7081MOD-ASSY[151]) giving a 13% photocathode coverage; PMTs are fixed on the top, bottom and lateral surface of the buffer tank wall. Each PMT has a mu metal protection against magnetic field and is angled in order to ensure a uniform detector response for the innermost part of the enclosed volumes. Besides the photons have to reach the PMTs and thus the enclosed materials are designed to be highly transparent to photons above 420 nm. According to simulation, the number of photoelectrons (PEs) per MeV of energy deposited is about 180 PEs/MeV and thus the energy resolution is expected to be $\sim \frac{7.5\%}{\sqrt{E(\text{ MeV})}}$. At a time, we considered to use light concentrators fixed on PMTs for a better energy resolution. Studies of their impact on the detector uniformity is presented at section 7.2.1.
The buffer tank with it stiffeners were installed during march-april 2009 and the

PMTs installation happened in may-june 2009. Pictures are displayed on figure 5.13.

Figure 5.14: Left plot: Inner veto tank with its PMTs. Right plot: Reflective white paint on the inner veto tank wall and foils on the buffer tank outer wall.

The inner veto The main purpose of this optically separated volume is to detect and track muons which are a source of background. Another goal is to detect the fast neutrons entering the detector. It is thus filled with a liquid scintillator made of $\sim 50\%$ decane to tridecane (decane, undecane, dodecane, tridecane) and $\sim 50\%$ LAB (lineares alkylbenzene) with 2g/L of PPO and 20 mg/L of bis-MSB. It is observed by 78 8 inches PMTs (Hamamatsu R1408 [151]) which were previously used in the IMB experiment [152]. PMTs are fixed on the bottom and lateral surface of the 10 mm thick inner veto tank and as well on the upper buffer lid. In order to increase the light collection (the photocathode coverage is 0.6%), reflective foils and paint have been used respectively on the outer buffer wall and on the inner veto tank wall. Due to the rather small space between these two walls, the PMTs are oriented parallel to the surface they are fixed to. The dimensions of the inner veto tank are 3250 mm in radius and 6830 in height for a volume of 90 m^3.
The inner veto (IV) integration happened between end 2008 and beginning 2009 and the PMTs installation occurred in may 2010. Pictures are displayed on figure 5.14. On these pictures we can observe the white reflective paint on the inner veto wall. At section 7.1.2, an analysis for the appropriate paint choice will be shown.

The shielding Because of the enlargement of the target and the adding of the buffer, space for the shielding against radioactivity γ was strongly reduced. Hence it was decided to enclose the detector in a 150 mm thick stainless steel volume.

Figure 5.15: Left plot: Demagnetization process of the shielding bars. The V shape of the bar can be viewed. Right plot: shielding integration during the summer 2008.

This protection is made of 66 V-shaped bars individually demagnetized, 42 for the lateral part and 12 for the upper and lower lids. The inner radius is 3300 mm and the height is 7150 mm.
The bars were individually demagnetized during may-june 2008 and the shielding was assembled in the refurbished pit during the summer 2008. Pictures are displayed on figure 5.15. For safety reasons, a sealant had to be introduced between the bars. At section 7.1.1, we report analyses that have been performed to determine the accidental background rate to expect from this component.

The outer veto The outer veto is an additional rejection tool against muons with respect to CHOOZ. It is made of plastic scintillator strips coupled to wavelength-shifting fibers surrounding the detector and extended over its diameter. The dimensions will be 6.4 $\times$ 12.8 m^2 for the far detector and possibly 11 $\times$ 12.8 m^2 for the near one. In order not to have a dead zone induced by the glove box, the latter is covered with planes. The purpose of the outer veto is to detect and track the muons with a much better precision than the inner veto thanks to the crossing of the strips (X-Y positioning). Furthermore, the extension beyond the detector diameter will allow to observe near-miss muons and thus fake $\bar{\nu}_e$ interactions due to a muon-induced fast neutrons. Besides, together with the inner veto, they provide a very good detection efficiency for muons entering the detector that can create dangerous cosmogenic isotopes. The outer veto should be installed during november/december 2010.

Near detector status The near detector location will be under a small natural hill giving 120 m.w.e. of shielding at distances of 350 and 450 m from the nuclear cores. This site has been approved by Électricité De France (EDF), the company operating the nuclear power plant (cf. fig. 5.16). 85 m of open air ramp and 155 m of tunnel will give access to the neutrino lab with a liquid storage and handling hall at its entrance. Civil engineering works have to be performed for a period of one year, from december 2010 to end 2011 according with the new schedule. An extended outer veto is already foreseen and as well as a possible larger inner veto region. It is expected to benefit from the lessons of the far detector integration to speed up the near detector one. The data taking start is expected for mid-2012.

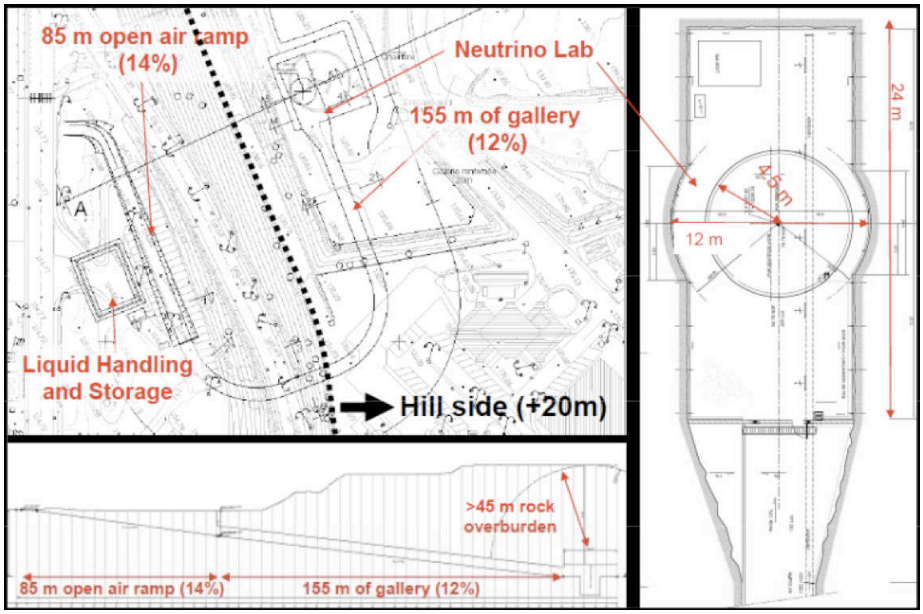

Figure 5.16: Near detector site plans.

5.2.3 Calibration systems

As pointed out in the previous section, the calibration of the detector efficiency is critical for the sensitivity of the experiment. The goal is a relative error on the detection efficiency of $\sim 0.5\%$ and an absolute one better than 1.5%. It is indeed important to determine accurately the positron and neutron energy scale for an efficient IBD event selection. The detector response depends on the type of particle which deposit energy, the energy of the particle and the position where the energy deposition occurred. It is important to determine as accurately as possible the scintillator response to β, γ and neutrons, the light transport properties (speed

of light, attenuation length) and the time offsets, gains and quantum efficiencies of PMTs.
The calibration tools can be divided into two categories:

- the cosmic muon products. They are Michel electrons, cosmogenic ^{12}B (β^- decay with 20.2 ms half-life) and neutrons.
- the γ, neutron and light sources.

The light sources will illuminate the LS to collect informations on the light transport properties and on the PMTs. The γ sources will be firstly used to derive the positron energy scale and secondly to give a cross check to the light sources. The neutron sources will be used to monitor the capture detection efficiency and to allow a correct simulation of the proton energy recoil spectrum induced by fast neutron events.
The light sources are of two types:

- the embedded ones, the Light Injection (LI) systems. They are made of light-emitting diodes (LED) light transported by optical fibers fixed on the edge of some PMTs in the Inner Detector (IDLI, $\lambda = 425$ nm or $\lambda = 475$ nm) and in the inner veto (IVLI, $\lambda = 365$ nm or $\lambda = 475$ nm).
- the intrusive one. It is light flashers: laser ball with $\lambda = 337$ nm and $\lambda = 470$ nm and a central blue LED coupled to a diffuser.

The LI systems can be used either in diffuse mode or in pencil beam and will be very useful for the detector commissioning. The light flashers are complementary to the LI systems. Their goal is to operate at different wavelength covering the LS excitation band with energies from a few to hundreds of PE per PMT (with isotropic light emission). The γ sources are ^{203}Hg: 0.289 MeV, ^{137}Cs: 0.667 MeV, ^{68}Ge: 2×0.511 MeV, ^{60}Co: 1.173 and 1.333 MeV, and finally the neutron sources are Am-Be[15] sources (tagged and untagged) and spontaneous fission neutrons from ^{252}Cf: 2.2 MeV for neutron capture on H, 8 MeV for a capture on Gd and even 4.94 MeV for a capture on C.
The calibration sources will be the same for the two detectors and will be introduced through the glovebox. This system will be located above the outer veto. The glovebox will be light tight and under a nitrogen (N_2) atmosphere at the same

[15]The americium ^{241}Am is a source of α and the beryllium ^{9}Be gives neutron by α capture. $^{241}_{95}\mathrm{Am} \rightarrow {}^{237}_{93}\mathrm{Np} + \alpha$; ${}^{9}_{4}\mathrm{Be} + \alpha \rightarrow {}^{12}_{6}\mathrm{C} + \mathrm{n}$.

pressure as inside the detector. The calibration system will be introduced through an airlock which will be purged with N_2 with constant monitoring of oxygen (dangerous for the LS) and radon (source of background), it will as well allow to look for potential leakage. The systems used to deploy the sources have been tested to ensure a compatibility with the detector liquids. For the neutron and γ sources, they are the 'buffer tube', which is a vertical tube located in the buffer, close to the γ-catcher, the 'guide tube' which is located in the γ-catcher, a part is close to the target acrylic vessel and the other part is close to the γ-catcher acrylic vessel. These two tubes are already installed in the detector. The 'articulated arm' will allow to fully calibrate the target. It is made of two parts, a straight upper part and a lower part that can be angled. The Z-axis system which is a straight tube that will be used to deploy vertically the sources. This will allow the laser ball and the central LED to be deployed.

5.3 Acquisition system

5.3.1 Read-out system

The energy depositions occurring in the LS produce scintillation light which is shifted for a good scintillator transparency and to accommodate the PMTs quantum efficiency. The signal produced in the PMTs is carried on the same cable as the high voltage (HV) and thus a 'high voltage splitter' (HV-splitter) is needed to isolate it. Then it is sent to the front end electronic (FEE) that amplify the signal to match the dynamic range of the Flash-ADCs[16] (FADC). Meanwhile the signals are summed and sent to the trigger units which after computations, send a trigger signal to the Flash-ADCs to store the event. Finally the event stored in the internal FADC memories are read out by computers and the needed online work before the analysis begins. Figure 5.17 shows the read-out scheme (excluding the outer veto read-out) that is briefly presented below together with the components of the main read-out system.

PMTs, HV and HV-splitters

Two types of PMTs are in use in the experiment:

- 10 inches PMTs, Hamamatsu R7081MOD-ASSY for the inner detector (ID)

[16] ADC= Analog to digital converter.

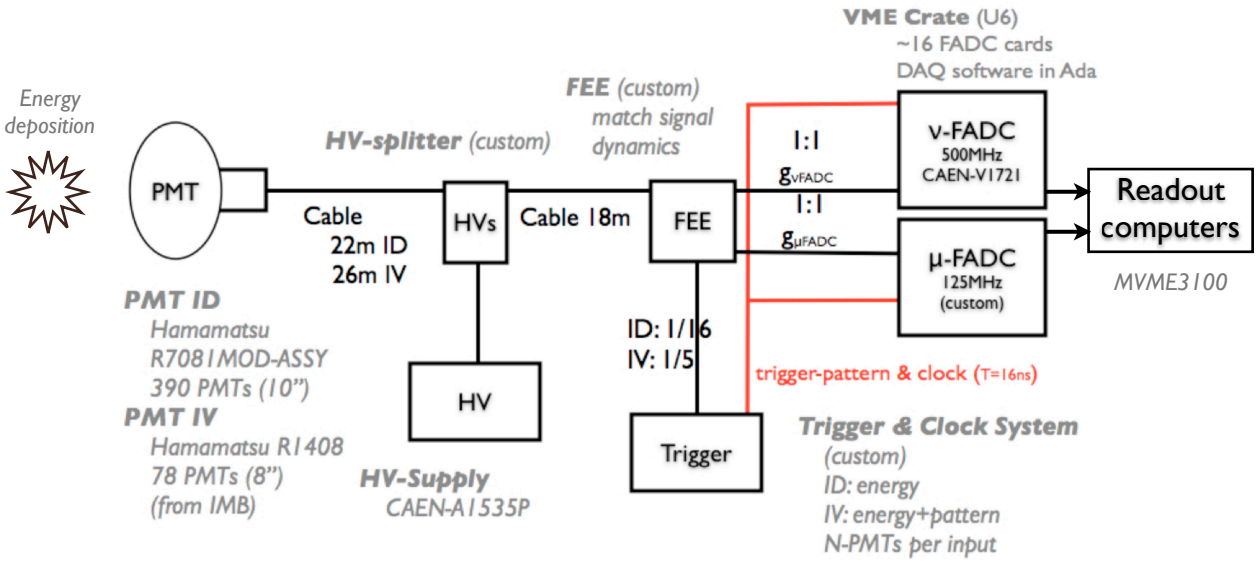

Figure 5.17: The Double Chooz read-out scheme.

- 8 inches PMTs, Hamamatsu R1408 for the IV (from the IMB experiment, see section 3.2.1).

Both are operated with a 10^7 gain what produces single photo-electron (SPE) pulses of less than 10 mV after a cable length of 40 m for the IDPMTs and 44 m for the IVPMTs. About 1.5 kV of HV is fed into these PMTs by the CAEN-A1535P power supplies. The HV-splitter which is custom made has been developed with care to well isolate the few mV AC PMT signal from the HV and its noise.

Front End Electronics and Flash-ADCs

The FEE board is custom made. Its primary goal is to match the dynamic range of the two FADC systems: the neutrino FADC system (νFADC) and the muon FADC system (μFADC). In addition, it allows to avoid distortions due to decoupling between the signal and HV, to keep the baseline stable[17] and to limit the signals voltage in order to protect electronic devices coming after it. It feeds as well summed analog signal for the trigger unit.
The two FADC systems are meant to be complementary over the experimental energy range: the νFADC system for the SPE per channel regime up to about

[17]The baseline is the default digitization value of the FADCs when no input voltage is fed into it. It is also called 'pedestal' (see chapter 6). A non stable baseline can lead to loss of energy resolution.

15 MeV and the μFADC system for higher energies like muon energy depositions where the νFADCs are saturated. Thus the signal fed into the μFADC has a gain of $\sim$0.5 while for the νFADCs, it has a gain of $\sim$7.5-8 yielding SPE pulses with a mean voltage of 50 mV. The νFADC system is optimized for the neutrino interactions, it is composed of CAEN-V1721 cards codeveloped with the APC laboratory (Paris). Their features are a 500 MHz sampling, a 8 bit resolution with 1V of reference tension, 8 channels per card and a 2 MB memory per channel. In DC, the channel memory is split into 1024 buffers of 4 μs. More details on its functioning will be given in the dedicated chapter. The μFADC system is custom 8 channels-cards composed of TDCs[18] with a time resolution of 81 ps for a dynamic range of 9.8 μs and FADCs operating at 125 MHz for a 10 bits resolution with 1.2V of reference tension. The adding of the TDC is meant to give more precision on the timing signal rising edge which is crucial for the muon tracking accuracy and therefore background studies related. Only 1/3 of wisely chosen IDPMTs will be connected into the muon electronics.

5.3.2 Trigger system

The trigger system is custom and relies on the estimation of the deposited energy in the detector based on the analog sum of the signals out of the FEE. It is composed of four units: three trigger boards and one trigger master board (TMB). Among the three boards, two are designed to trigger on the energy and multiplicity in the ID and the remaining one for the IV has rough energy determination but gives hints on the hit pattern in the IV useful for muon identification. Figure 5.18 displays the functioning of the trigger system explained below. Studies on the performances of such a trigger as a function of the energy as well as a possible new trigger based on the number of hit PMTs are presented at the section 7.2.2.

ID trigger boards The IDPMTs are divided into 12 sectors containing each 32 PMTs, 6 sectors for the upper part of the ID and 6 for the bottom part. Half of the PMTs from a given sector are connected to the first trigger board called A while the others are connected to the second one called trigger board B. The FEE sums the signals from a sector (by group of 16 PMTs) and sends it to the trigger boards. The choice of the PMTs grouping in a sector is done in order to always have a A-PMT surrounded by B-PMTs and vice-versa. Each board makes a trigger decision

[18]TDC= Time to Digital Converter.

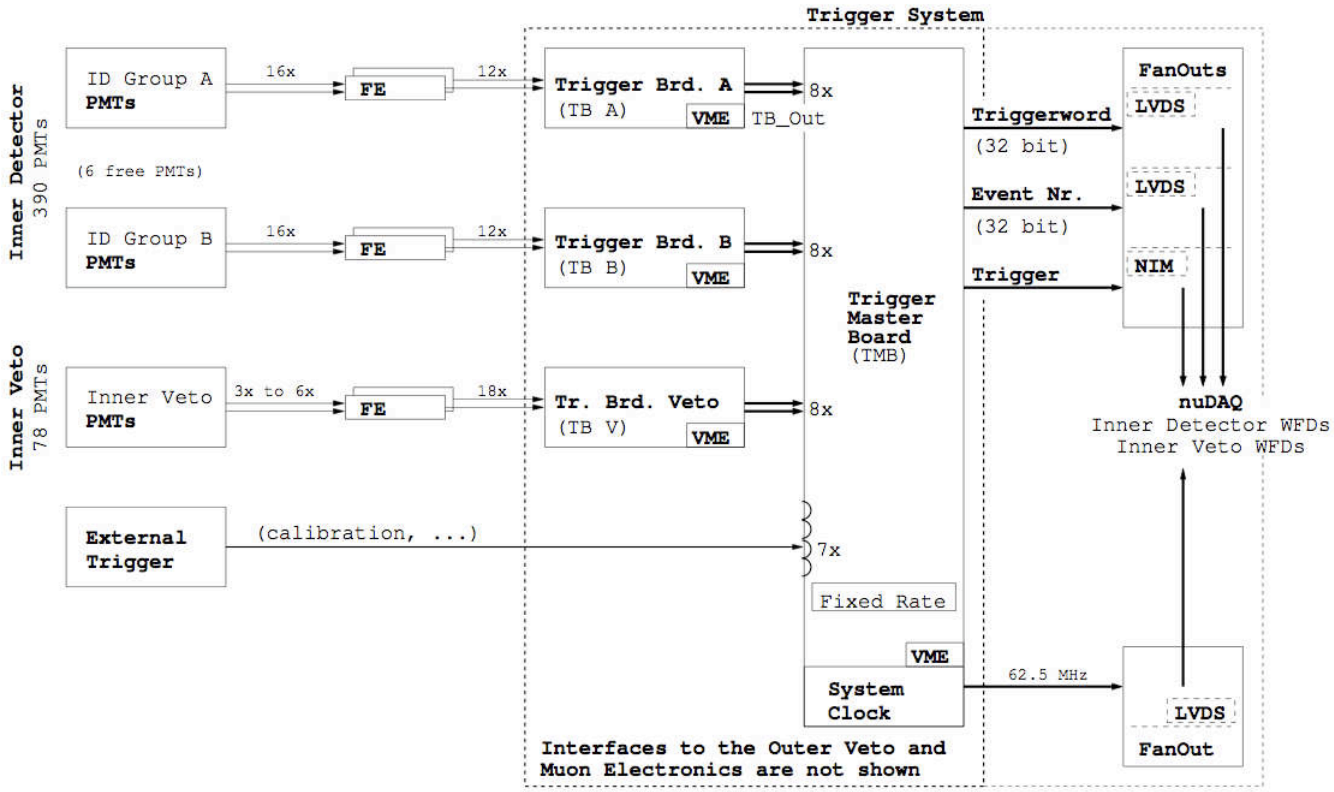

Figure 5.18: Scheme of the analog trigger system composed of three trigger boards and one trigger master board (outer veto and μFADCs systems are not displayed) [153]. The trigger decision is distributed to the Flash-ADCs for data volume reduction.

based on the analog sum on half of the IDPMTs. This technique implies that the trigger boards look in the same way at the same volume and thereby their trigger decision should be the same apart from statistical fluctuations. This allows to have an intrinsic trigger efficiency monitoring. There exists four trigger decisions that are enabled only if the multiplicity is higher than two (two sectors at least should be hit):

- very high energy deposition. Its value has still to be tuned but a default value of 50 MeV has been chosen. It allows to tag muon-like depositions (the threshold corresponds roughly to a 25 cm path length in the scintillators for a muon).
- High energy deposition. Its value is 5 MeV which allows to tag n capture-like energy depositions.
- Low energy deposition. Its value is 0.5 MeV which allows to tag e^+-like

energy depositions but also radioactivity γ and α.

- Prescaled. Its value is not yet fixed but a default value of 0.3 MeV is foreseen. The purpose is to monitor the low energy trigger efficiency and meanwhile to study the background below the possible e^+ energy analysis cut at 0.5 MeV.

An eight bit word which contains the trigger decision is sent to the TMB. The above trigger conditions are stored each on one bit put to one in case the condition is fulfilled[19].

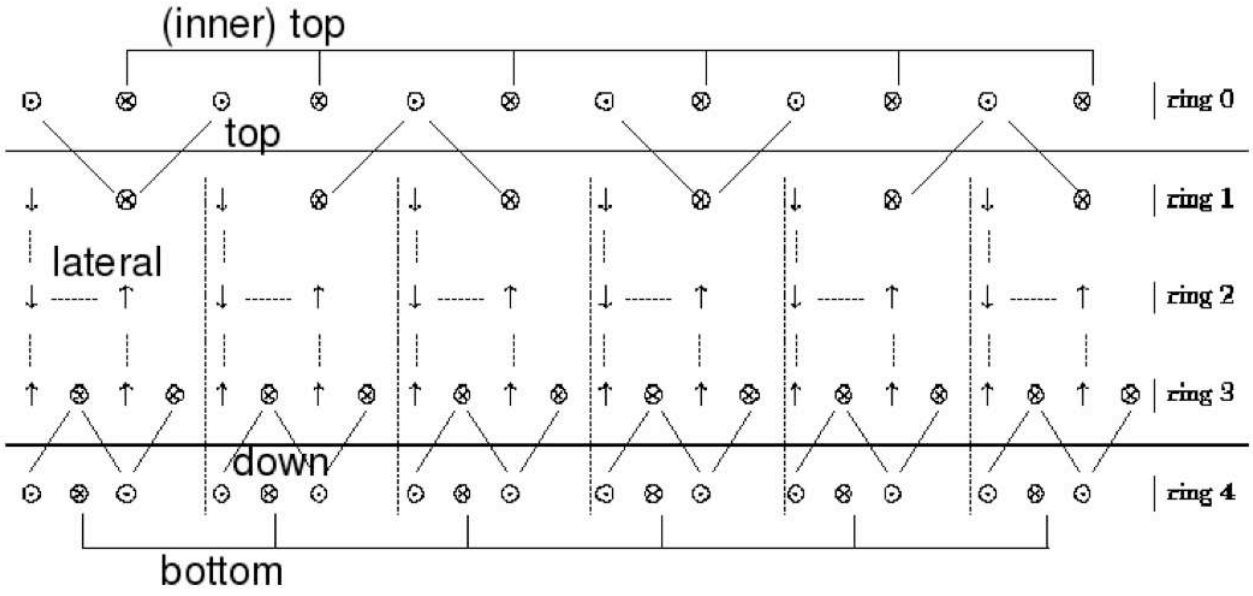

Figure 5.19: The Inner Veto is cut open and spread out such that one stands 'outside the detector'. Thus the symbol $\odot$ indicates a PMT facing outwards, away from the detectors central axis, the symbol $\otimes$ represents an inward looking PMT. Arrows also represent a PMT and point into the direction of the PMTs field of view. The 78 inner veto PMTs are lined up on five rings. For the trigger conditions they form groups between 3 and 6 PMTs, each group is assigned to a region. It can be noted, that the number of PMTs in the bottom part of the Inner Veto is higher [153].

The IV trigger board The functioning of the inner veto trigger board (IVTB) is different from the ID trigger boards. The goal of this system is to disentangle the muons that stopped in the detection volumes from those that went out of the detector and as well to distinguish a possible fast neutron interaction in correlation

[19]The other bits have been let free in case of new features in the future.

with an IBD-like signal. Thus the trigger conditions are mainly based on the hit pattern. The PMTs grouping scheme is represented in figure 5.19. Careful attention to the event topology in the bottom part of the IV allows to know if the muon stopped or not. Besides if a high enough energy deposition is detected in the IV and not in the ID, it is either a passing muon in the IV or a fast neutron candidate. Finally, it exists a prescaled trigger condition for further possible background studies.
An eight bit word which contains the trigger decision is sent to the TMB with the passing muon/fast neutron like decisions being computed by the TMB.

The TMB The TMB is the board that receives the 8 bits words on the event from the 2 IDTB and from the IVTB. 8 other bits are reserved for the external triggers from the calibration forming a final 32 bits trigger word. All the bits are kept as they are except the 'passing-muon/fast neutron' bit. The TMB follows an 'OR' logic: if a bit is at 1 then the delayed trigger signal is distributed to the FADCs to store the event in their internal memory[20]. Moreover, to ensure that the event is correctly recorded, a 62.5 MHz clock is distributed to all FADCs for synchronization. The 32 bits trigger word along with a 32 bits event number word is sent to some FADCs. It will be used by the online system to perform a needed data volume reduction (see section 5.3.4).

5.3.3 Outer veto read-out and acquisition systems

An energy deposition in the scintillator planes creates light that is shifted and transported by fibers to the Hamamatsu M64 multi-pixel-PMTs themselves connected to the MAROC2 chip [154] on a custom PMT board. All the PMTs data is collected USB card. The outer veto system is synchronized with the main read-out system thanks to the TMB clock signal. A hardware trigger named 'X-Y trigger' is computed at this level and sent to the TMB as an external trigger. It is however inhibited because the outer veto is meant to work as a tool to give complementary information on the events.

[20]The FADC memory is split into buffers. When a trigger comes, the writing changes to a new buffer. This is why the trigger signal out of the TMB is delayed by $\sim$ 200 ns (cf. chapter 6).

5.3.4 Online system

The core of the read-out system is made of the FADCs and the trigger system which are VME[21] devices. Up to 21 trigger and FADC cards can be plugged into a VME crate where one card is the master and makes the read-out of the cards through the VMEbus. In the case of the DC experiment, this is the MVME3100 also called internally to the collaboration Read-Out Processors (ROPs). 6 ROPs are needed for one detector: 4 for the νFADCs, one for the μFADCs and one for the trigger system. The main Data AcQuisition system (DAQ) collect the data from the 6 ROPs with a needed reduction of the data volume. Afterwards, the data streams from the main DAQ and the outer veto DAQ (OVDAQ) are merged and converted to ROOT format [155]. It is then passed to the 'DOGSifier' that converts the event to the DC offline analysis format named DOGS (Double chooz Offline Group Software). The Run Control (RC) system allows to control the DAQs and check their good functioning while a monitoring of the data sanity is performed after the data format conversion, this stage is called 'Pseudo-Online Monitoring' (POM). Finally, the data is sent from the detectors laboratory to the centralized CEA and CNRS computer system located at Lyon where pulse and vertex reconstructions are performed and eventually the data is made available to the whole collaboration. A scheme of the online system is displayed on figure 5.20.

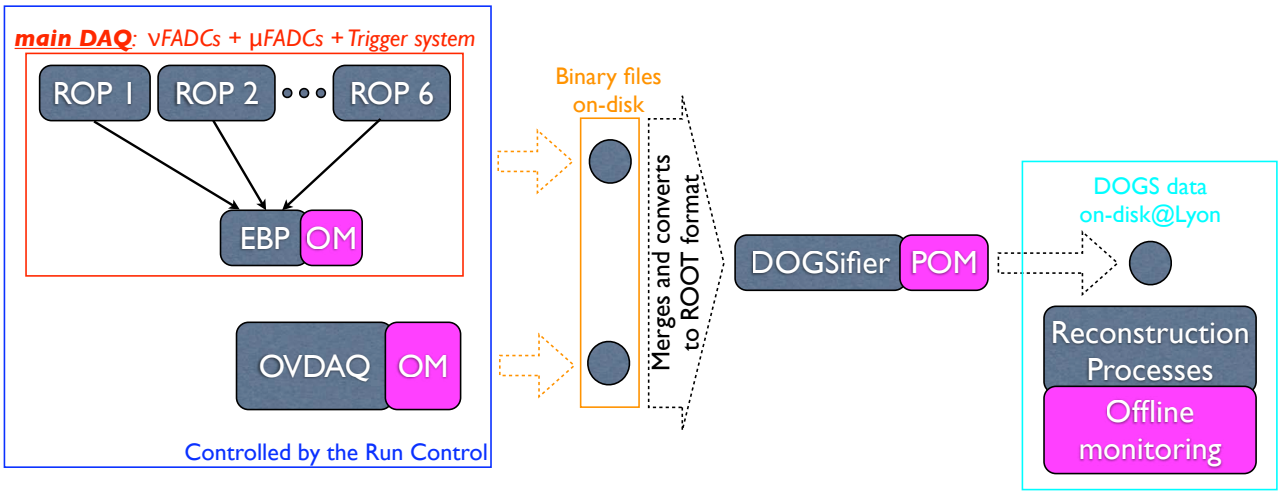

Figure 5.20: Scheme of the online system with its multi-stages monitoring. OM stands for 'online monitoring' and POM for 'pseudo online monitoring'. The two DAQs (data acquisition system), the main DAQ and the outer veto DAQ, are independent and merged after their binary data are written to disk.

[21] VERSAmodule Eurocard

Main DAQ It is composed of the 6 ROPs and the computer that collects the data from them. They are connected through TCP/IP connection to this computer named Event builder Processor (EBP) because it creates for each event a unique binary file from the data streams. The ROPs continuously read the cards to check if a trigger signal came making available an event for the read-out. Then it reads the trigger word and following this word, it performs a data reduction. In case ROPs have too much CPU being consumed, the EBP performs the job.
An online data reduction is performed since not every event has an interesting waveform pattern and because the volume of data has been limited to 10 GB per day. All the events are retained and classified into four types:

- the ν type. These are $\bar{\nu}_e$-like signal that are tagged by looking backward in the νFADCs memory. The full 4 μs of data will be taken to allow detailed background studies.

- the μ type. This is muon events that are easily tagged thanks to the large amount of energy they deposit in the detection volumes. Only time and charge are interesting for these events. However at the beginning of the experiment, the muon electronic will not be available. Hence instead of the charge, the saturation time is foreseen to be used because it should be somewhat a function of the charge.

- The light calibration type. It is light flashers calibration event. Only the charge and time are taken since the pulse shape is irrelevant.

- the default type. It is determined if none of the above type match the event features. For now, it is considered to take 256 ns of data per channel to allow detailed studies.

Besides the EBP has some special data reduction scheme for calibration runs.

Run Control The main purpose of the RC is to supervise the runs. It allows to configure the parameters of the run, to start and stop it, and finally to manage the state of the DAQs to ensure their synchronization. The communication is made through TCP/IP connection to the DAQ servers and sending of formatted ASCII texts. The RC allows as well the shifters to access the output of the monitoring stages.

Monitoring The data is monitored at different stages with thereby different capabilities. A low level of monitoring is performed on each DAQs to ensure that it is working properly or that the trigger rate is in agreement with the expectations and so on, it is called 'online monitoring'. Another monitoring stage called 'pseudo online monitoring' occurs just after the data DOGSification. The output of this stage is made available world-wide through HTTP and java-based client interfaces allowing experts not on site to early diagnosis misbehaving devices. Finally there is a monitoring stage after the reconstruction processes at Lyon computer center called 'offline monitoring'. This is the most powerful stage of monitoring with the main purpose of flagging the data and run quality, and cross check the monitoring of the previous stages.

Chapter 6

The Flash-ADC cards of the main data acquisition system

The VX1721 Flash-ADC cards codeveloped by the APC laboratory and the enterprise CAEN are the core of the Double Chooz acquisition system (see section 5.3.1). They digitize the amplified signals out of the PMTs with a good resolution and at a very high rate allowing an accurate determination of the total charge of signals and their timing characteristics (i.e. time-over-threshold, start, end and maximum). This is particularly important in order to obtain a good energy resolution and a good spatial reconstruction with the purpose of reducing the systematic error through pulse shape discrimination.
In this chapter, we first present the principle of Flash-ADCs and the advantages their use offers. Secondly, we review tests performed in order to characterize the Flash-ADC cards used for the main data acquisition system (named 'neutrino Flash-ADCs') and check if the results are in agreement with the constructor specifications. Finally, we present the results of the tests performed on the Flash-ADC cards that will be used in the phase 1 of the experiment.

6.1 Why Flash-ADCs in Double Chooz ?

In the early 1990's, the development of waveform digitizers with good resolution and high sampling rate provided a new method of recording pulses from sensors. The previous methods consisted in combining an RC circuit for the determination

of the charge[1] and a time to digital converter (TDC) for a precise determination of the pulse time. The main advantage of an ADC is that it combines the two devices and does not perform any selection at the hardware level: the signal treatment is done by software. Moreover, any improvements on the determination of pulse parameters can be re-applied to previously acquired data.
The use of Flash-ADCs (FADCs) allows to have a high sampling rate[2] giving a good time determination through a precise record of the pulse shape. In the following section, we explain how a FADC works and what are the advantages of using the VX1721 FADC card.

6.1.1 Functioning of Flash-ADCs

A Flash-ADC is a device that converts continuous analog signals into a discrete digital number with a fast sampling rate. The output is a n bits number N_D proportional to the analog signal voltage V_A. A FADC is characterized by three quantities:

- the reference voltage V_{ref}: it is the voltage range on which V_A is convertible without saturation, from 0 to V_{ref}.
- the number of bits n of N_D: it fixes the digitization resolution.
- the sampling rate S: it fixes the digitization precision on the shape of the analog signal

N_D can take 2^n values from 0 to 2^n-1 with voltage steps $q = \frac{V_{ref}}{(2^n-1)}$. It is called number of ADC counts and is related to V_A through:

$$N_D = \frac{V_A}{q} + R \quad \text{with } R < 1. \tag{6.1}$$

As can be seen on figure 6.1, Flash-ADCs are composed of 2^n-1 operational amplifiers mounted in comparators, each comparing V_A to a multiple of q up to V_{ref} thanks to resistors in series. Consequently N_d gives a voltage interval for V_A of:

$$Nq \leq V_A < (N+1)\ q \tag{6.2}$$

leading to a step function of the voltage as shown on the right panel of figure 6.1.

[1] For instance, a charge to digital converter (QDC).
[2] The resolution is currently limited to 10 bits because of the number of comparators needed that scales as $2^{\#bits}$.

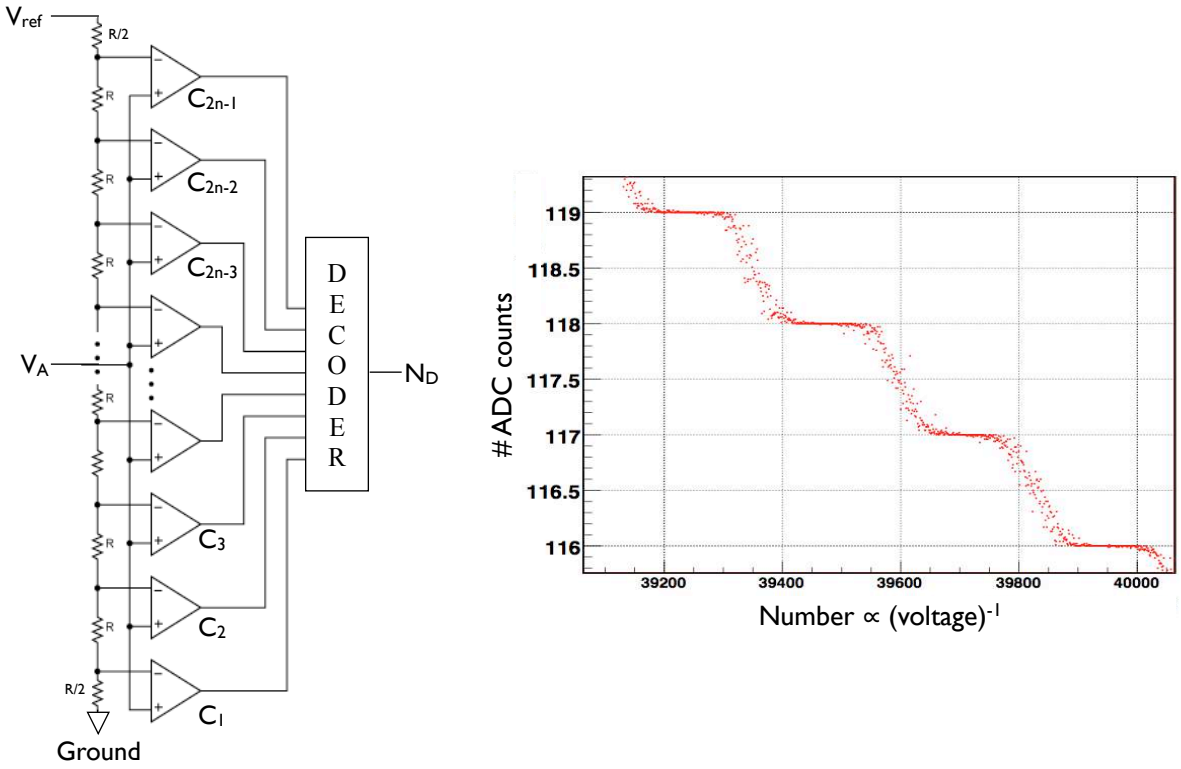

Figure 6.1: Left panel: scheme showing the functioning of Flash-ADCs with V_A the analog input voltage, V_{ref} the reference voltage and N_D the number of ADC counts in output. Right panel: Illustration of a Flash-ADC functioning with data from a DC FADC. Plotted is the mean ADC value obtained for a decreasing applied voltage, showing the step nature of the FADC.

6.1.2 Advantages

As explained in section 5.3.1, DC uses CAEN-VX1721 Flash-ADC cards of 8-bits resolution (256 ADC counts) with a reference voltage of 1V and a sampling rate of 500 MHz (a digitization sample every 2 ns). The card features 8 channels with a 2 MB internal memory that can be split. These features are at the origin of several advantages presented below.

Energy resolution and spatial reconstruction

The digitization of a single PE pulse (SPE) representing most of the signals expected on the DC PMTs for neutrino data and backgrounds from natural radioactivity, is shown on figure 6.2 where we can see the precision obtained on the shape. The energy of an event is determined through the number of PEs while a PE is recognized through the integral of the pulse called the charge. Therefore, hav-

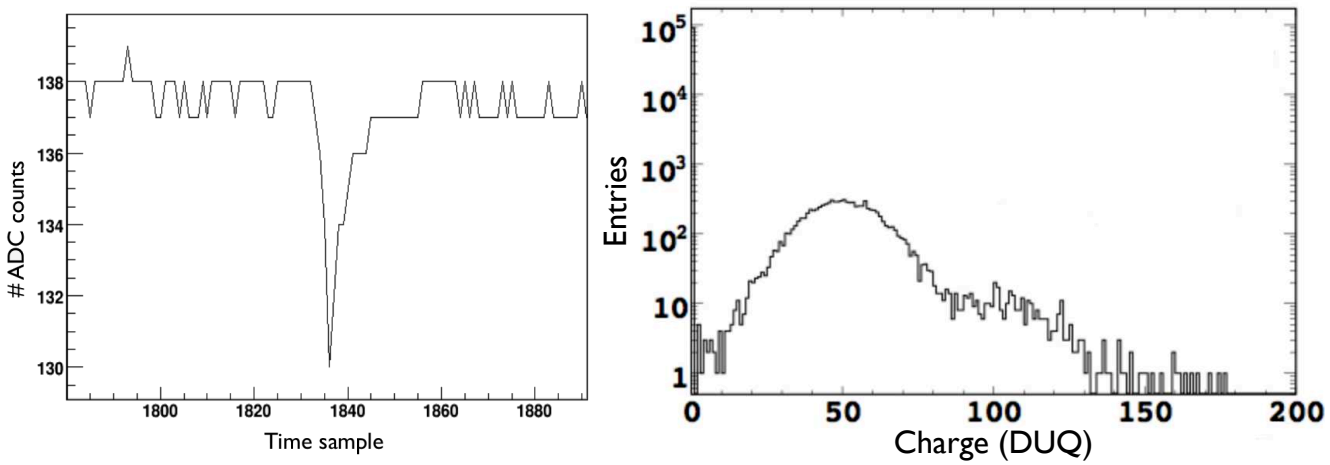

Figure 6.2: Left panel: Single PE digitized at the APC laboratory with a setup called vertical slice containing a DC's PMT, FE and FADC. Right panel: simulation of the DC PMTs charge spectrum for a 50 DUQ/PE gain where a DUQ is an ADC count times 2 ns.

ing a good digitization resolution allows for an accurate charge determination and thereby an accurate energy determination. Moreover, having a high sampling rate allows to reconstruct efficiently the signal shape resulting in an accurate time of the pulse determination. This is particularly important to obtain a good spatial reconstruction and a good reconstruction of the scintillator time response that could allow a better understanding of the background[3] (cf. chapter 8). Besides, the record of the pulse shape allow to disentangle true pulses from large charge arising from pedestal fluctuations through the pulse amplitude.

Absence of deadtime and details on the events

The 2 MB memory per channel is split into 1024 pages of 4 μs (2048 samples). The digitization process is continuous inside a page up to the 2048^{th} sample. If no trigger signal from the trigger system is sent, the first sample is overwritten by the 2049^{th} sample and so forth. The reception of a trigger signal causes the movement of the digitization process to the next page leaving the previous one available for the read-out (cf. fig. 6.3). Besides the memory can be seen as a circular FIFO (First In First Out): if a trigger occurs when writing in the 1024^{th} page with the first page already read-out, the sample writing moves to it, otherwise

[3]Most of the prompt energy backgrounds comes from outside the detection volumes. Therefore they interact mostly in the γ-catcher. A good spatial reconstruction would allow to efficiently tag them for studies (see sections (see section 7.1 & 8.1).

the trigger is disabled and hence there is dead time. In the experiment, the rate of triggers is dominated by muons with a few hundred s^{-1} and thanks to a high rate of data transfer through VME[4], the acquisition system is free of deadtime. Furthermore, the continuity between pages gives the possibility to make a 'movie' of what happened in the detector. This movie is stopped by the overwriting of a page, leaving at least 4 μs of continuous samplings. This feature is extremely important for detailed background studies, especially to look for fast neutron signature in the inner veto prior to $\bar{\nu}_e$-like signal.

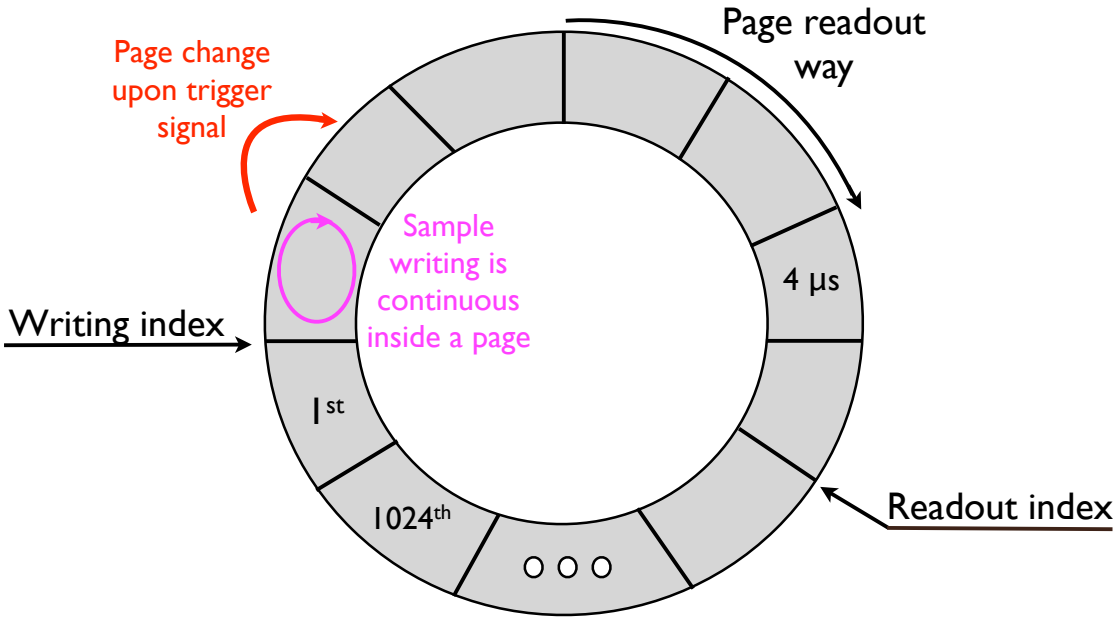

Figure 6.3: Illustration of the FADC memory split into 1024 continuous pages of 4 μs and its functioning. If the writing index never reaches the read-out index, the acquisition is free of deadtime.

6.2 Characterization of the VX1721 card

The VX1721 FADC card characterization consisted in checking that the card was fulfilling the requirement of the experiment. We first checked that the card could be configured as desired, especially the pages for the event storing and the channels pedestal. Then we checked the linearity of channels and the bandwidth. These

[4]The experiment is still in the commissioning phase but can cope with a rate of triggers of 30 Hz, taking the maximum of data per channel (2 kB from 65 cards of 8 channels). The highest rate of interactions comes from muons, while, for physics reasons, only the time and the charge are stored decreasing the amount of data to be transfered. Therefore, before optimization, the read-out system is almost ensured to be free of deadtime.

works and their motivations are described in this section. The first section is dedicated to a description of the communication with the VX1721 card.

6.2.1 VME communication

The CAEN-VX1721 FADC card (cf. fig. 6.4) uses the VME protocol to communicate [156]. It is plugged into a VME crate and communication occurs through the backplane called VMEbus for VERSAmodule Eurocard bus. The communication is initiated by a VME computer[5] that is the MVME3100 (read-out processor (ROP): see section 5.20) in our case. The ROP establishes the communication with a given device in the VME crate by its given address[6]. Inside the device, registers at specific addresses allow for instance to configure the device or read the data stored. Three types of communication are possible:

- system call. This type of communication is made of two steps: a query to the microprocessor with the instruction for the FADC (read or write of data) and then the execution of this instruction by the microprocessor through the kernel. Thus, two steps are needed while only one datum can be exchanged (with a maximum of 32 bits for our computer architecture). System calls are consequently not the most efficient way of transferring the recorded events.

- Memory mapping. For this communication, one has first to establish the projection of the FADC device into the computer memory. Subsequently, the FADC can be accessed without involving the kernel resulting in an increase of the data flow rate. Moreover, the length of bytes to read/write is variable providing a convenient way of handling a device.

- Direct memory access (DMA). A device is connected on the bus and can take temporarily its control. A query to the microprocessor is needed to initialize the DMA controller (start address, length of data and way of transfer), then data is transferred directly to the computer memory. Again, only one step is needed while a settable amount of data can be transferred.

The DMA transfer is the communication mode chosen for the experiment. It allows a bandwidth up to 320 MB/s with the 2eSST mode (two edges source synchronous

[5]The VMEbus is technically controlled by a PCI-VME bridge called Tundra Tsi148 inside the VME computer.

[6]The VMEbus uses a master-slave architecture with asynchronous data transfers. In our case, the master is the ROP and slaves are the FADCs and the trigger boards.

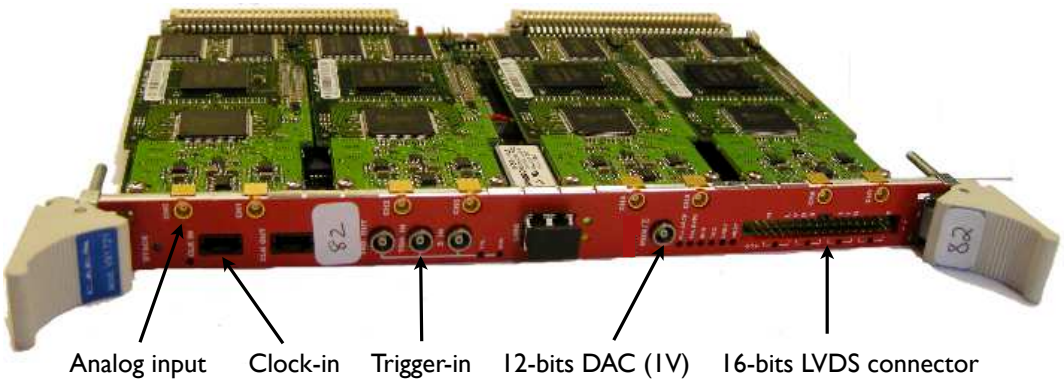

Figure 6.4: Picture of a VX1721 FADC card.

transfer) ensuring the researched data acquisition system to be free of deadtime. Furthermore, it has been chosen to use the object oriented programming language named ADA [157]. It is comparable to C++ and Java but integrates in addition the possibility to use parallel tasks. Its main advantage is the possibility to control severely the sanity of the code and to give precise diagnosis at compilation resulting in almost no errors at execution.

6.2.2 Pages

As presented in section 6.1.2, we have set the number of pages to 1024 resulting in 2048 samples (of 8 bits) per channel. We have then checked that we really have a continuity between buffers by feeding analog functions in a channel and triggering by software. Figure 6.5 displays Flash-ADC data with analog functions in input, the 1024 last samples of a page and the 1024 first samples of the following page are shown. The result confirmed the pages continuity. Besides, it allows us to check that we indeed have 2048 samples per page after setting.

6.2.3 Channels characterization

Noise level

Noise in a channel would result in a misidentification of the input voltage, hence of the charge and thereby in a misidentification of the energy (see section 6.1.2). It is important to assess it for the determination of the induced error on the energy determination.

To determine the intrinsic noise level of the card, we have filled an histogram for each channel with samples over 1024 pages with no analog input and no voltage

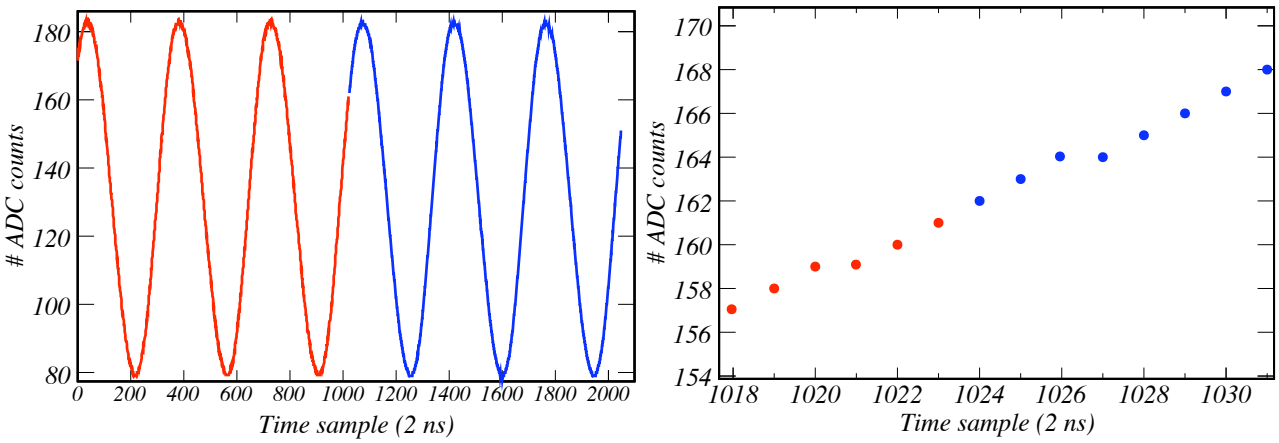

Figure 6.5: Illustration of the continuity between pages with a sinusoidal function (left panel). The right panel shows a zoom on the transition between the two buffers.

delivered by the 16 bits DAC. We have then noticed that most of the samples were distributed in one bin with a small number of entries in the adjacent bins. This was indicating a very low noise level however hard to characterize. We tried to evaluate it with a Monte Carlo method where we simulated pedestal values with assumed gaussian distributions of parameters μ and σ, which were then digitized[7]. Using MINUIT [158], a ROOT [155] fitting package, we have minimized a χ^2-like function yielding the μ and σ values reproducing the best the pedestal histogram:

$$\chi^2 = \sum_i \frac{[N^i_{ped} - N^i_g(\mu,\sigma)]^2}{max(N^i_{ped},1)} \tag{6.3}$$

where i is the index for the bins, N_{ped}, N_g are respectively the number of entries in the bin i of the pedestal histogram (data) and the digitized gaussian (MC) and the function $max(N^i_{ped},1)$ was introduced to account for N_g in a bin when there is no N_{ped}.

Figure 6.6 displays the results obtained from four measurements: one after 10 days, the other after 20 days and the last one after 60 days. We can see that the mean pedestal value μ is very stable unlike σ that remains however below 0.3 ADC count. We think that these variations can be due to temperature changes in the laboratory that was not under air conditioning at that time. The mean pedestal value is sensitive to the voltage delivered by the DAC that has 256×256 values for

[7]For instance, gaussian values between 143 and 143.5 were stored in the bin 143 while values between 143.5 and 144 were in the bin 144.

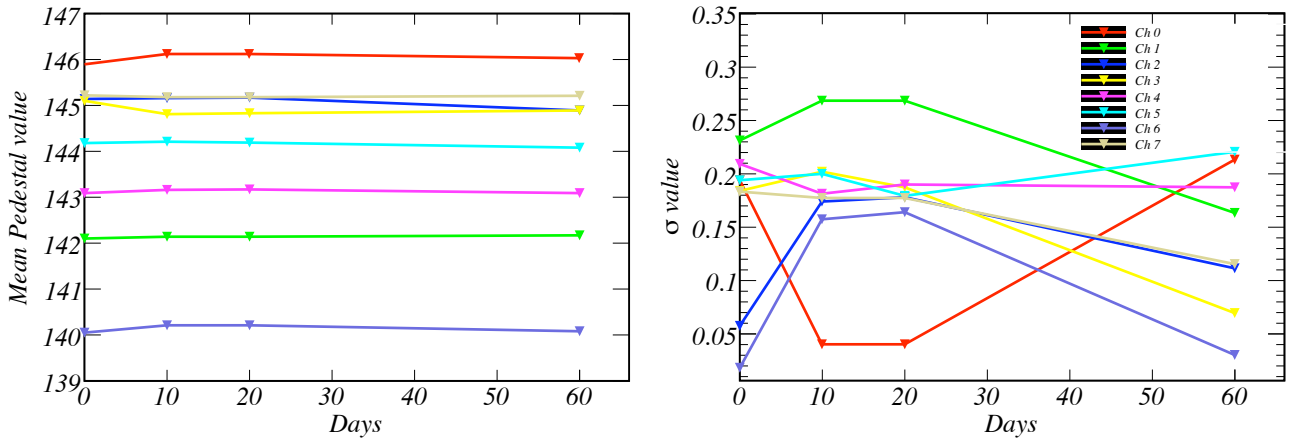

Figure 6.6: μ (left panel) and σ (right panel) parameters of the MINUIT minimization from four measurements. The mean pedestal value remains stable while there is some variations in the noise level that remains nevertheless below 0.3 ADC counts.

a precise setting of pedestals to any ADC count. The voltage was set to zero during the noise level characterization but could have been influenced by the temperature resulting in small changes on the pedestal value but larger ones on the sigma as can be seen on figure 6.7. We can see that the standard deviation value remains

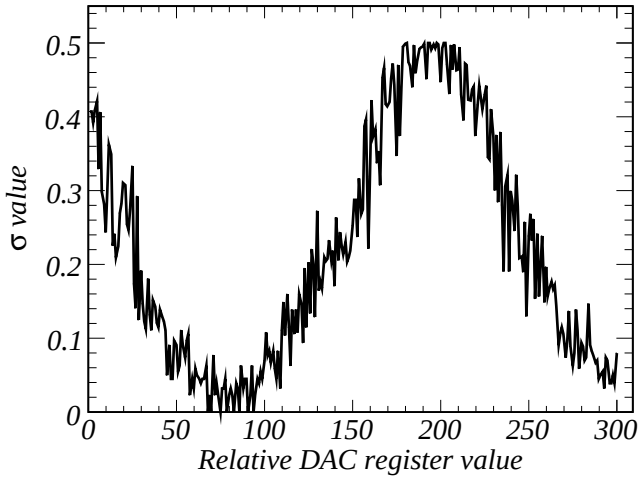

Figure 6.7: Arithmetic standard deviation as a function of the 16 bits DAC register value. One can see that the standard deviation value is strongly dependent on the DAC register value where 256 values allow to set precisely a given pedestal value. Here we allowed the DAC register value to vary upon 300 values. The 'period' seems to be different of the expected 256 values.

below 0.5 ADC counts indicating that no ADC steps are missing.

Pedestal set up

The pedestal is the number of ADC counts arising from the voltage delivered by the 16 bits DAC (Digital to Analog Converter) when no input voltage is fed into the FADC. Each channel's pedestal is thus set up thanks to this 16 bits DAC that delivers a voltage between -0.5 V and 0.5 V. A value of 0 written to this register corresponds theoretically to a voltage of 0.5 V and a number of ADC counts of 255 while a value of 2^{16} corresponds to -0.5 V and a number of ADC counts of 0. The signals out of the PMTs are negative and therefore, it is important to set the pedestals close to 255 to benefit from the full FADC dynamic for the signals digitization.
We have investigated the mean pedestal value as a function of the DAC register value with a step number of one. This allows to see the step structure of the FADC as shown on figure 6.8. The lower left plot of this figure, which is a histogram of the mean pedestal value (over 100 samples), indicates that there are regions where we can find small ADC steps like in the upper right plot compared to the upper left one. However, when filling the histogram without averaging the samples for a given DAC register value (lower right panel), we find a constant number of entries which implies at the first order that the FADC is linear. The presence of small ADC steps seems to be due to interferences at 250 MHz resulting in different odd and even samples[8]. This effect is generally small but can as well be very pronounced as can be seen on the left panel of figure 6.9, although it does not create non linearities. Nevertheless, to check this statement, we have fitted the data obtained (when averaging) on the full DAC range. We noticed a non linearity arising at small and large values of the DAC register as can be seen on figure 6.10. This effect could have been due to a non linearity induced either by the DAC or by the FADC. However after some careful linearity tests, it appeared that the DAC was responsible of this behaviour, providing nevertheless all the dynamic needed to set the pedestals to any value. We used the constant number in the lower right plot of figure 6.8 (divided by 100), about 240, to create a program setting the pedestals at about 1 ADC count after three to four loops for adjustment.

[8]The ADC digitizes at 500 MHz but has two sample outputs at 250 MHz each. The clock used to have a sample on each output at 250 MHz could be the reason why the odd and even samples have different noise levels.

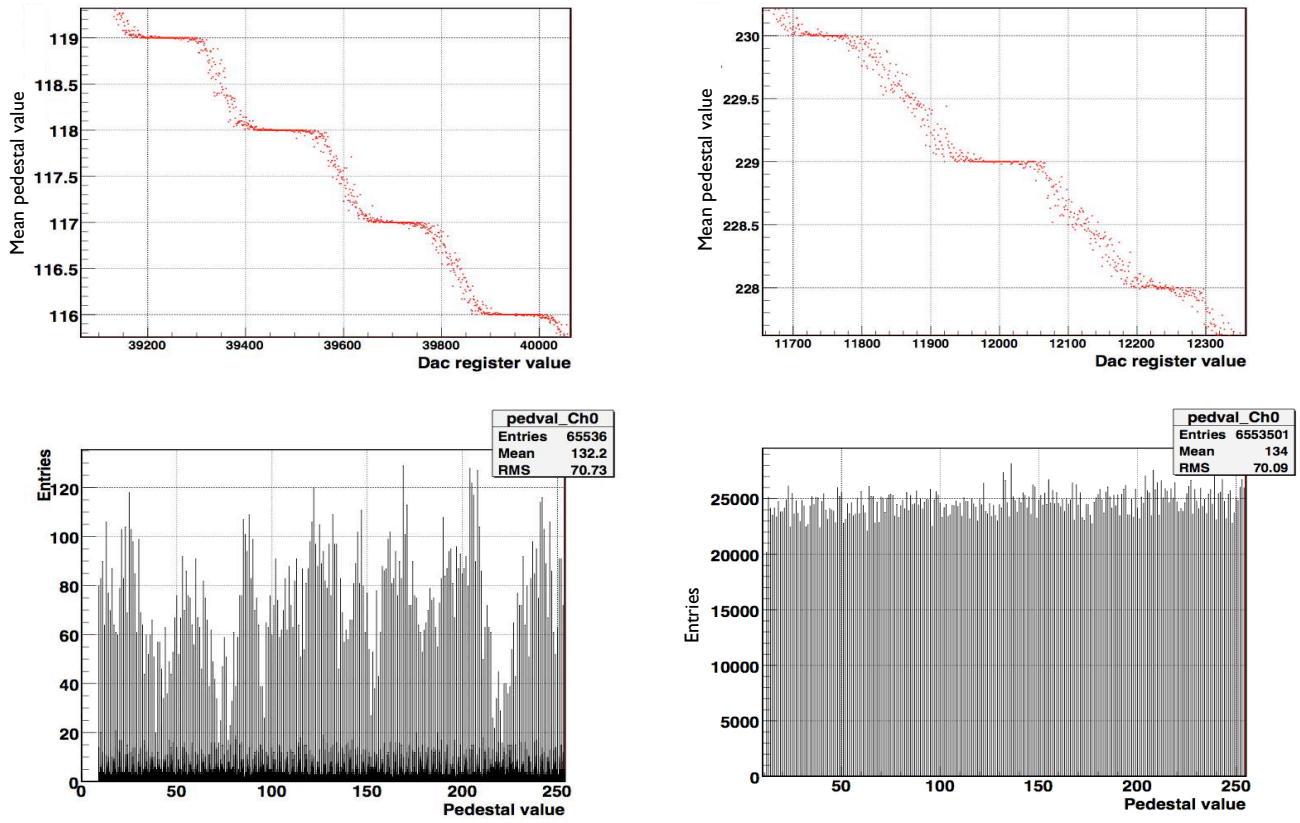

Figure 6.8: Upper plots: zoom on the mean pedestal value (over 100 samples) as a function of the 16 bit DAC register value. One can remark that the ADC steps of the left plot are of the same size whereas those of the right panel are smaller and of different sizes. Lower plots (bins of 0.02 ADC count): number of entries for the mean pedestal value as a function of ADC count value (left). The right panel shows the same as the left one but without averaging on 100 samples.

6.2.4 Linearity tests

A FADC card with a linear response ensures a simple relation between the number of ADC counts of the digitized signal and its voltage. Non linearities change this relation resulting in distortions of the input signal leading to a misdetermination of the charge and finally of the energy.

As shown in section 6.2.3, non linearities were found when characterizing the 16-bits DAC allowing the pedestal set up. In order to determine what component of the card from the 16 bits DAC and the FADC was not linear, we used a 1V 12 bits DAC available on each FADC card (see figure 6.4) providing theoretically 4096 steps of 244 μV. Using a voltmeter, we proceeded to the calibration of this

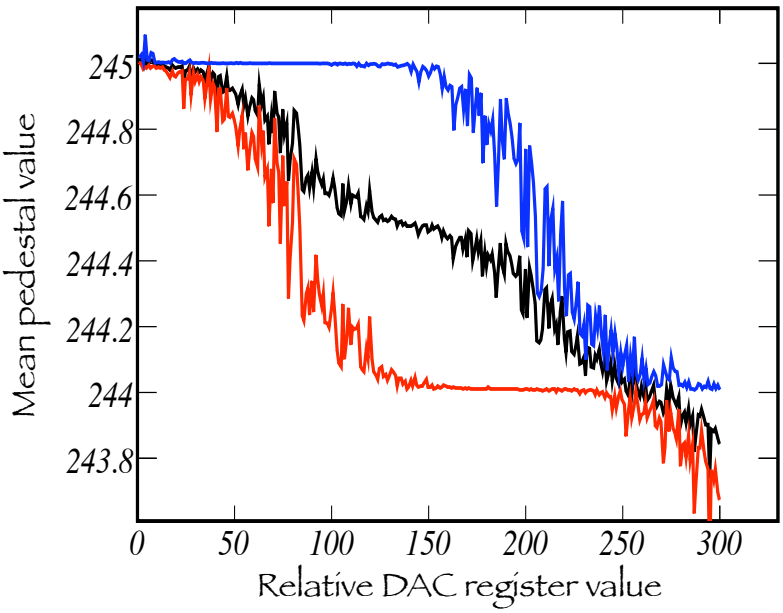

Figure 6.9: Mean pedestal value as a function of the DAC register value. The red line is for the even samples, the blue one for the odd samples and the black line is for all the samples. This shows an apparently missing ADC count that is in fact due to the interferences between the odd and even samples. Nevertheless, the linearity is preserved.

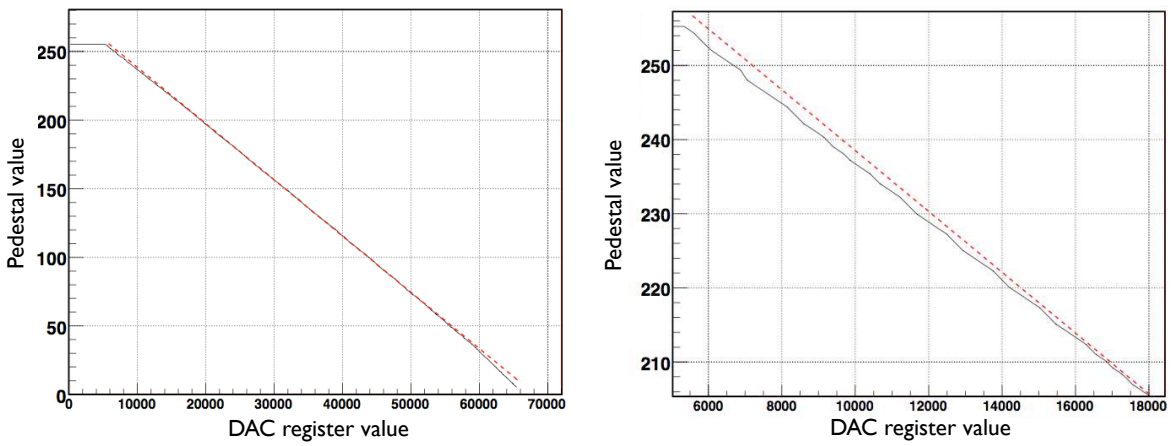

Figure 6.10: Mean pedestal value (on 100 samples) as a function of the 16 bits DAC register value. The data in black is fitted by the red dashed line. One can notice the non linearity at the extremities on small and large DAC register values. The right panel shows a zoom on the non linear region in the upper part of the left panel plot.

source on a card taken as the reference for the linearity tests of all the FADC cards presented in section 6.3.2. The results are displayed on figure 6.11. We found that

the source was linear but delivering voltages between 2 and 1017 mV. By moving

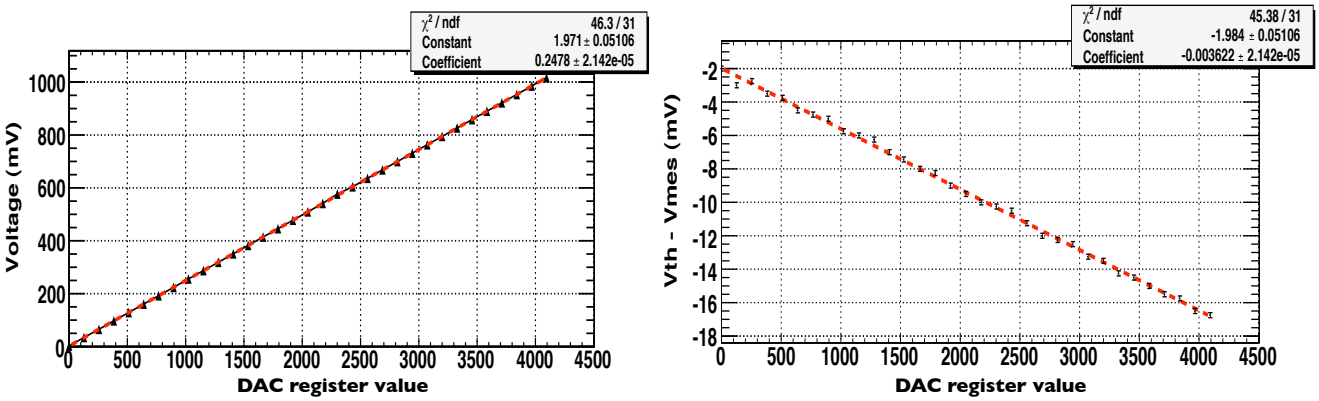

Figure 6.11: Left panel: measured voltage as a function of the 12 bits DAC register value. Right panel: residuals between the theoretical voltage and the measured voltage. Data is in black and the red dashed line is the fit. The source voltage begins at 2 mV and delivers up to ∼1.02 V.

the 12 bits DAC register value with unit steps, we carefully checked the channels linearity as can be seen on figure 6.12. The channels looked very linear as can be seen on the upper plot.

A surprise we found was that the full DAC voltage could not saturate the FADCs. 1015 mV were corresponding to about 235 ADC counts leading to ADC steps of 4.3 mV instead of the 3.9 mV of the specifications. After this plot, we performed a more careful verification of the linearity using the residuals, that are the fit value minus the data value (middle plot). It showed us that the FADC is indeed very linear with an absolute residue value below 0.6 ADC count.

Finally, we drew a histogram of the residuals (lower plot) and looked at the RMS that quantifies the differential non linearity (DNL) of a channel. Here it is ~ 0.165 ADC count, in good agreement with CAEN specifications of 0.16 ADC count.

6.2.5 Bandwidth

When performing measurements on FEE prototypes at the APC laboratory, we were concerned by the bandwidth that could distort the signals out of the PMTs. We thus checked the bandwidth of the analog part of the Flash-ADC. The constructor specifies a Flash-ADC bandwidth of 250 MHz corresponding to half the sampling frequency.

To perform this measurement, we used a high frequency generator that could deliver sinusoidal signals. The signal out of the generator was split in two thanks to a

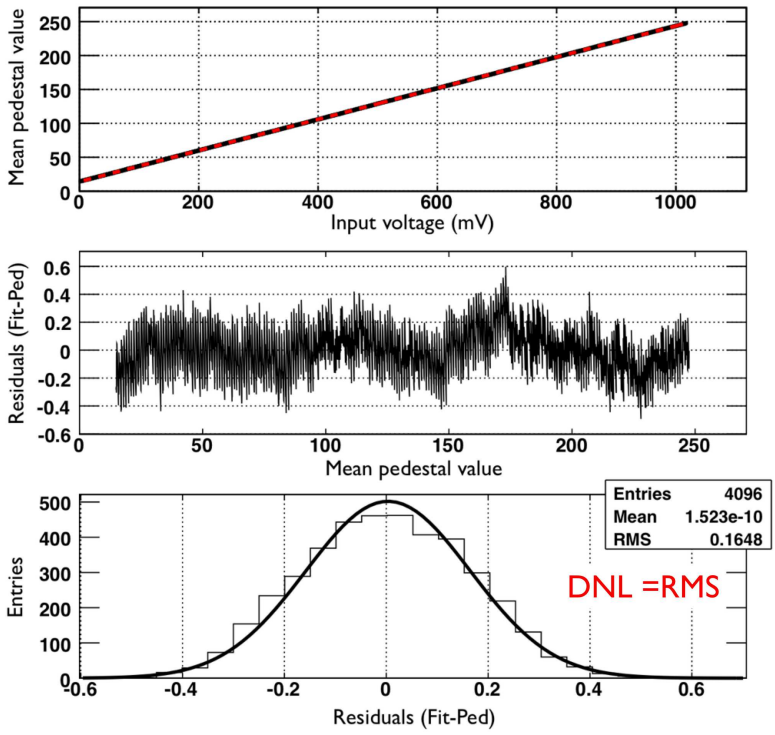

Figure 6.12: Plots showing the characterization of a channel linearity. The upper plot is the mean pedestal value obtained as a function of the input voltage with data in black and the fit in red. The middle plot is the residuals of the upper plot. The lower plot is the histogram of the middle plot allowing the determination of the channel differential non linearity (DNL) by its RMS.

high frequency splitter (using resistors) and sent to the FADC and an oscilloscope (the latter was set to the full bandwidth mode with an input impedance of 50 Ω like the FADC). The voltage measurements by the FADC and the oscilloscope were subsequently compared to determine the bandwidth. For the voltage measurement performed by the FADC, we profited from the fact that the sine function spends more time around the extreme values than between[9]. We have thus plotted a histogram of the recorded sine function digitized values, determined the number of ADC counts between the two fitted extremities with gaussian functions and converted into voltage by using the measurements of section 6.2.4 (1 ADC count = 4.3 mV). An example of the histogram together with the bandwidth measurement result are displayed on figure 6.13.

It has been found that the FADC bandwidth lies close to 300 MHz (cf. right panel of figure 6.13 and its caption), in good agreement with the CAEN specifica-

[9]For the high frequencies close to the FADC sampling rate and above, we introduced a delay between the pages to avoid the digitization of the same region of the sine function.

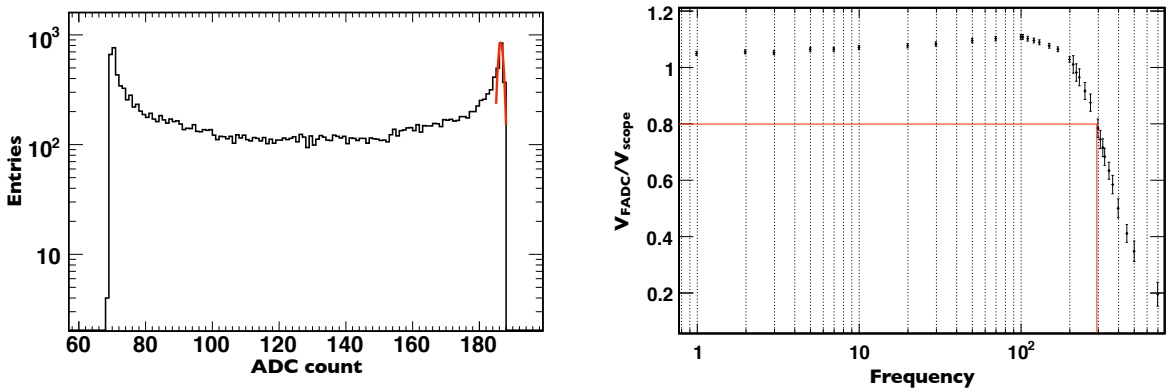

Figure 6.13: Left panel: example of an histogram of the sine function digitization with a peak fit at one extremity in red. Right panel: ratio of the voltage measured on the oscilloscope over the voltage in the FADC as a function of the sine function frequency. The bandwidth value is obtained for the maximum divided by $\sqrt{2}$ (3 dB): $\sim$ 300 MHz. This plot displays different estimated errors due to the peak determination that becomes higher with the frequency. It is not well understood why the ratio is greater than one and why it seems to increase a bit before the expected decrease due to the bandwidth.

tion. Consequently the bandwidth limitation was fixed by the FEE board with a bandwidth of about 100 MHz.

6.3 Test of the Flash-ADCs for the phase 1

In its first phase, the experiment will have to digitize the signals out of the 390 ID-PMTs plus the 78 IV-PMTs using 59 FADC cards. We thus proceeded at the APC laboratory to the test of 66 cards and only one faulty card has been found, the 16-bits DAC of one channel was not working.
The test content[10] was the following:

- Configuration of the card. It consisted in setting the card features needed for the test, such as the number of buffers, the type of triggers accepted, etc... but also a calibration procedure for the channels provided through a register (it is needed after power off or changes in temperature).

[10]The instructions to the cards were sent using system calls in order to benefit from exception handling giving precise informations in case a crash occurs unlike mapping. Besides, for each card we tested the time of reading/writing with the three communication modes. The communication time for mapping was of the order of 1-2 μs whereas it was three times more for system calls to transfer a 32 bits word. The DMA transfer was the faster as expected with about 485 μs to transfer an event (4100 words of 32 bits) giving about 120 ms for 32 bits.

- Characterization of the 16 bits DACs.
- A linearity test using the reference 12 bits DAC.
- A test of the channels pedestal set up.

In the following, we will present the three last items of the test.

6.3.1 Characterization of the 16-bits DAC

The 16-bit DAC has 65536 values from 0 to 65535 = 255 × 257, therefore we took 257 points to determine the behaviour of the DACs (the FADC is known to be linear). These data points were fitted with a simple linear function on the whole range as justified by the linearity tests described in section 6.2.4. The DAC behaviour is observed to be close to linear, with all cards DAC trends having similar slopes but different intercept. Small non-linearities arise at small and high DAC values. These non-linearities present a systematic behaviour well fitted with a

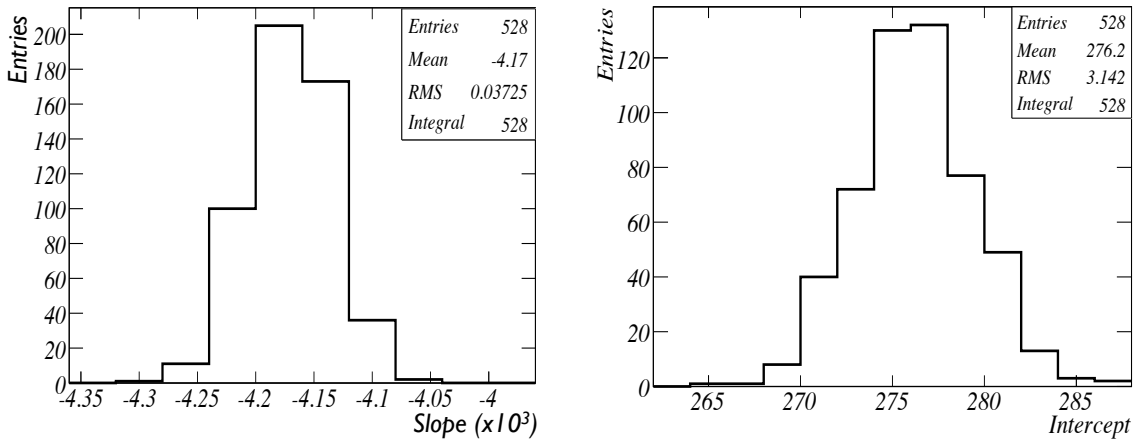

Figure 6.14: Left panel: distribution of the DACs' fit slope. Right panel: distribution of the DACs' fit intercept.

second order polynomial function as can be seen on figure 6.15. Consequently, we developed a new pedestal set up procedure requiring the read an event to determine these default pedestal values and setting the new desired pedestal value thanks to the mean of the slope distribution[11].
This new set up procedure allowed us to set the pedestals values at better than one ADC count. It is the procedure that will be used to set the pedestals to 245 ADC

[11]The number of ADC counts between the desired pedestal and the default pedestal is multiplied by the mean slope and written to the register.

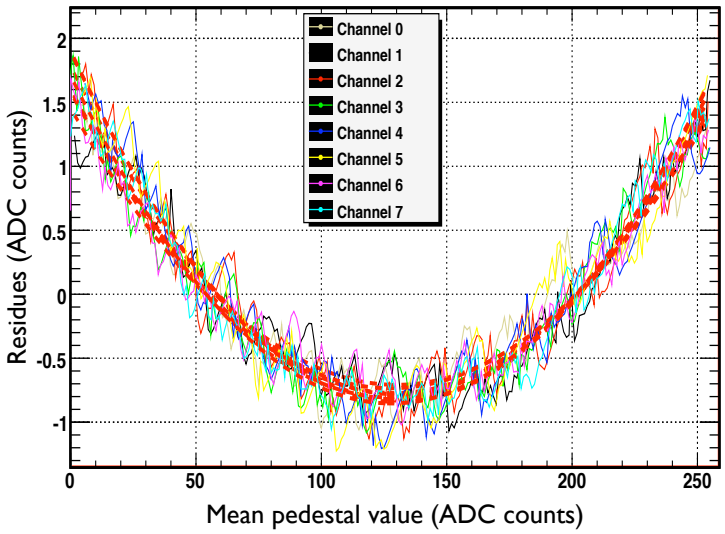

Figure 6.15: residuals (fit value minus data) as a function of the mean pedestal value (that varies because of the changes in 16-bits DAC register value) for the eight channels of a FADC card. One can see that the DACs are not linear but have a typical non-linearity less than two ADC counts astray from the fit value.

counts after two loops for adjustment[12] in order to maximize the number of ADC counts available for the signal digitization while keeping some over the baseline to digitize possible overload (and subtract it from the next signal).

6.3.2 Linearity results

Using the calibrated 12-bits DAC described in section 6.2.4, we tested the linearity of all channels. Since this reference source of voltage was covering about 235 ADC counts (from 2 to 1017 mV), we set the channels pedestal to about 15 ADC counts to test the upper part of the FADC that is relevant for the SPE digitization. To perform a careful analysis test, we have not only fitted the data on the full DAC range but also on small sections of 256 DAC values[13], the results of these two techniques are displayed on figure 6.16. We averaged the parameters found per section and compared with the parameters of the fit on the full DAC range. It allowed to detect efficiently regions where the FADC response was above or below

[12]The set up to 245 ADC counts requires two iterations because of the non-linearity. Nevertheless, since the non-linearity is the same for all channels, the second iterations is enough to have all channels set up.

[13]The 12-bits DAC have 4096 values which is equal to 16×256. This is why we choose to make 16 sections of 256 DAC values.

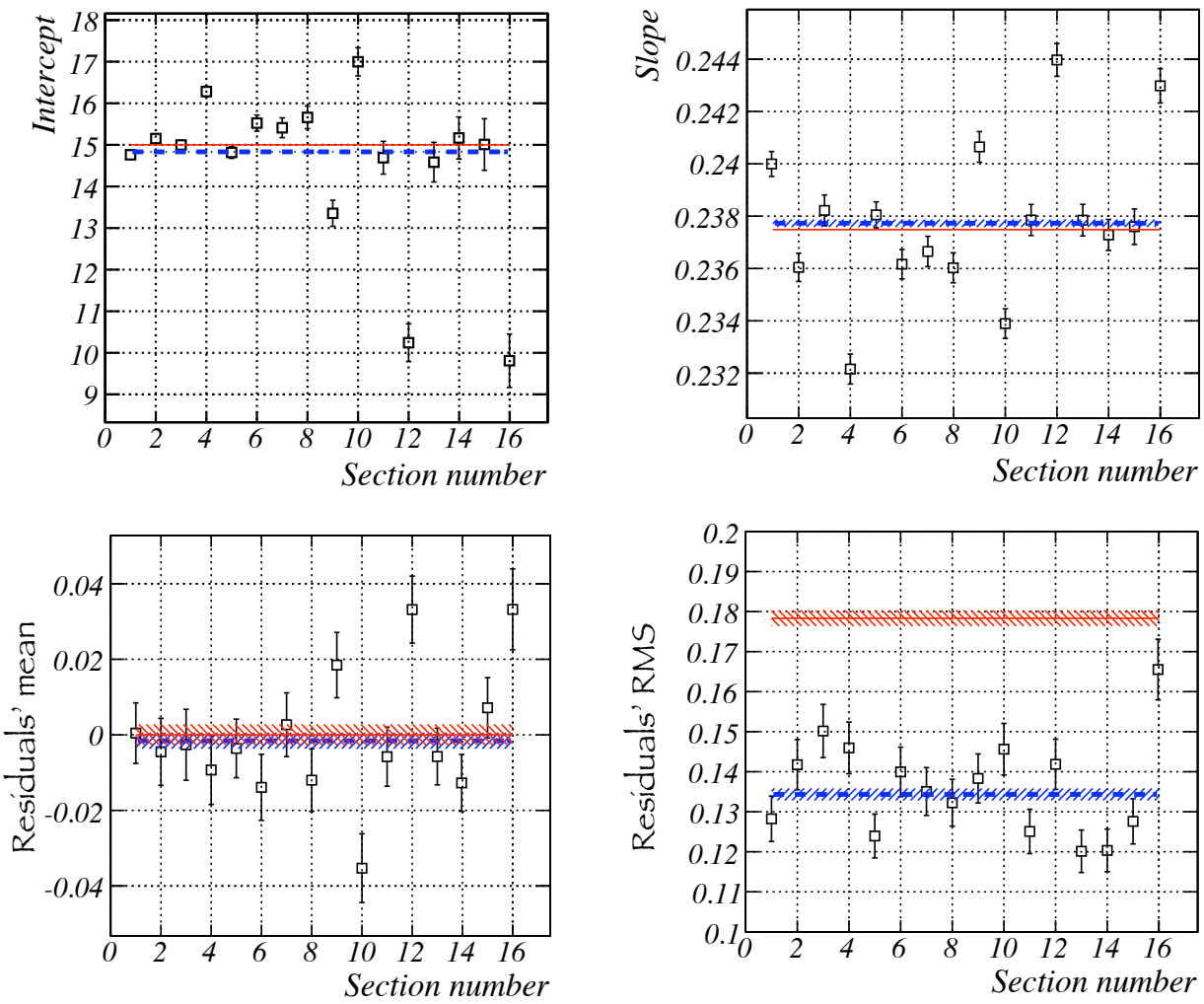

Figure 6.16: The upper plots are the intercept and the slope from the linear fit on sections of 256 DAC values. The two lower plots are the mean and the RMS of the histogram of residuals on these sections. The red line is the parameter value from the fit on the full range, the area around shows the one sigma error. The blue dashed line is the mean of the parameters per section also with its one sigma error.

the expected linear behaviour[14], as can be seen on figure 6.17. We can see that the two techniques almost yield the same slope for the fit of the data points (cf. fig. 6.18) confirming the observation of ADC steps of 4.3 mV (cf. section 6.2.4). However, the two techniques gave different DNL demonstrating the existence of substructures. The DNL histogram inform us that with the second technique, the DNL can be corrected up to a value of ∼0.14 ADC count. Without corrections,

[14] A channel with several substructures is easily detectable through the difference in the RMS (lower right plot of figure 6.16).

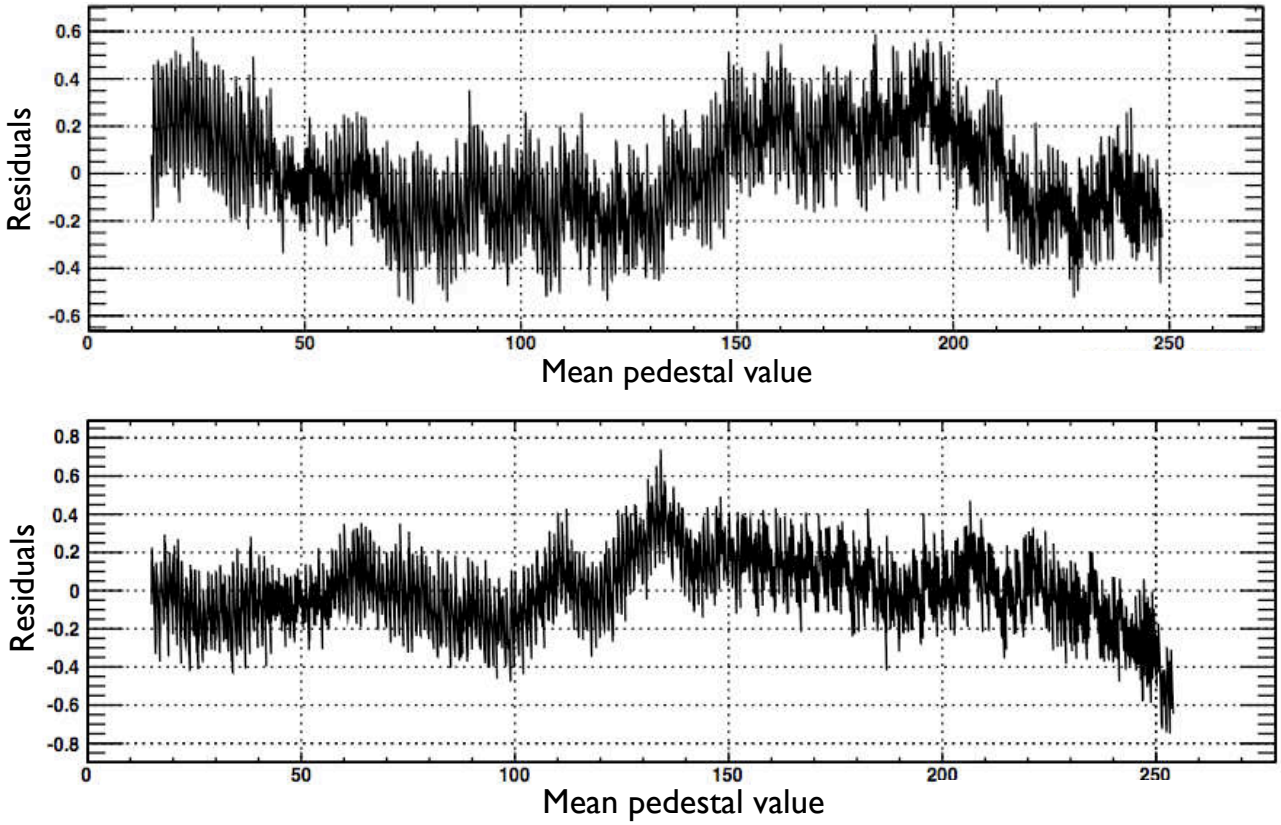

Figure 6.17: Example of channels showing substructures.

we have a DNL of about 0.17 ADC count, in good agreement with the constructor specification of typically 0.16 ADC count. At such low non-linearity values, the energy resolution will not be limited by the digitization process and thus it is not needed to correct it.

6.3.3 Conclusion

In December 2009, we proceeded with the test of 66 FADC cards. The test consisted in setting the card and testing the linearity and the set up of the channels pedestal. Only one faulty card was found while 59 are needed for the phase 1 of the experiment. After the tests at the APC laboratory, we replaced the default CAEN firmware with a customized firmware developed at APC to allow for instance to read only the wanted data in an event for the data volume reduction. The cards were transported in April 2010 to the Chooz far laboratory for installation and found to be working properly from the preliminary data of the far detector commissioning phase (cf. fig. 6.19).

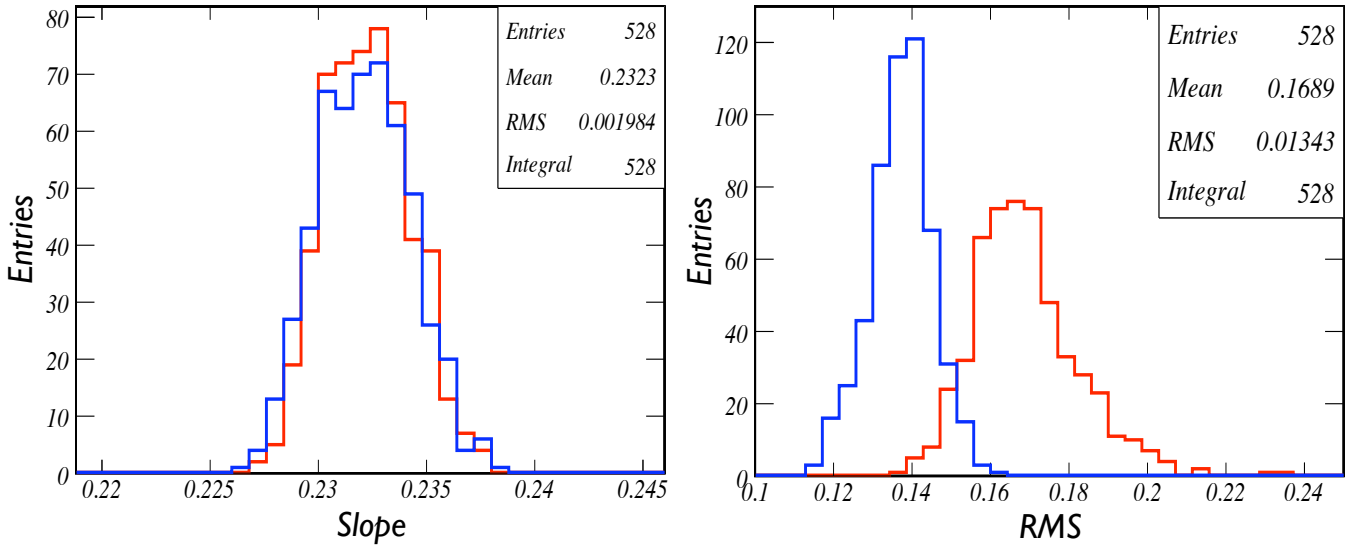

Figure 6.18: Left panel: distribution over the whole channels tested of the fit's slope. Right panel: RMS distribution of the residuals histogram. The red lines correspond to the case when we fit over the full DAC range and in blue whereas the blue lines correspond to the mean values from the fit per sections.

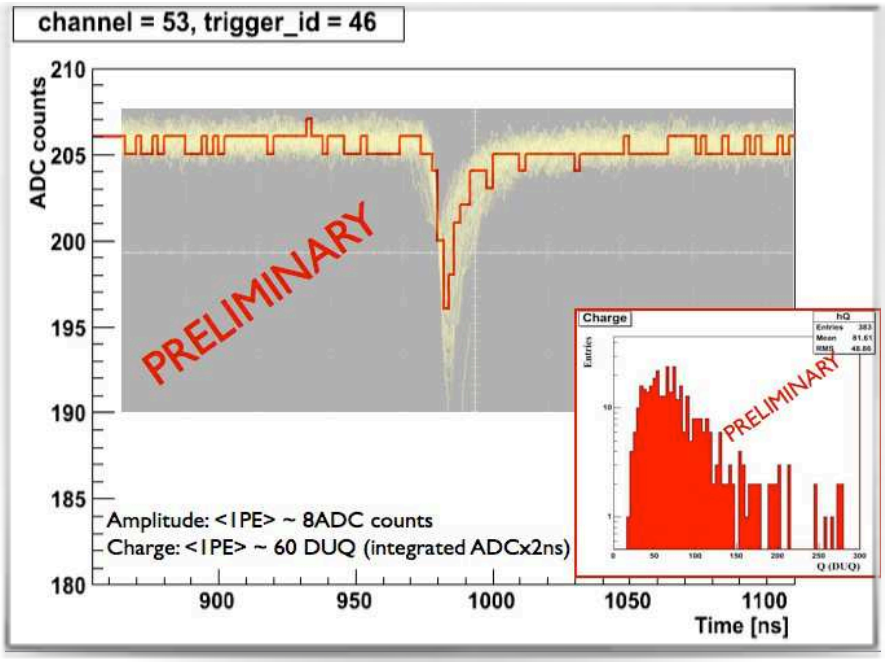

Figure 6.19: Superposition of oscilloscope and FADC commissioning data from an ID PMTs of the far detector. The small plot shows the charge spectrum obtained [112].

Chapter 7

Detector design optimization

The detector integration began in the summer 2008. Before and during the integration, several studies on the detector optimization were carried out, such as the careful choice of detector components to lower as much as possible the radioactivity background, as well as possible improvements for a better energy determination.
In this chapter, we present work on the determination of the radioactivity constraints that should be satisfied by the paint in the inner veto and a sealant between the bars of the shielding. Then we present studies on possible improvements to the energy determination with the use of light concentrators on the PMTs, with a possible digital trigger and finally with the matching of the γ-catcher and target scintillators light yield.

7.1 Radioactivity background reduction

As highlighted in section 4.1.1, the natural radioactivity is a source of background through α, β and γ radiations. The α and β particles stop quickly in materials due to their rather high dE/dx, while the γ radiation is very penetrating and has energies up to 2.6 MeV. DC will use a readout threshold of 0.5 MeV for the prompt energy deposition of the e^+ in the $\bar{\nu}_e$ signal and thus the radioactivity γ can fake it. Nevertheless, only the most abundant γ rays with large energy from ^{40}K and the ^{238}U and ^{232}Th decay chains can do so[1]. Indeed, the other γ have to cross the buffer volume, which absorbs them or let them reach the detection volumes

[1]The cobalt ^{60}Co has also to be taken into account but has a negligible impact on our studies. It has two γ rays whose energies are respectively at 1.17 and 1.33 MeV.

(target+γ-catcher) with an energy below the threshold[2]. The γ from ^{40}K have an energy of 1.46 MeV while the γ from the ^{238}U and ^{232}Th decay chains comes from respectively ^{214}Bi with γ of 1.12 and 1.76 MeV, and ^{208}Tl with γ of 2.61 MeV [160, 161, 162].
In the following studies, we decided to only consider γ's from ^{40}K and ^{208}Tl because the other γ's with an energy close to that of ^{40}K will encounter roughly the same processes. We used Monte Carlo simulation based on geant4 [163] and a DOGS package which simulates the detector and its response: DCGLG4sim.
The studies have been performed not only considering the nominal DC threshold of 0.5 MeV but also 0.7 MeV and 1 MeV (see section 5.2.1). The e^+ annihilation yields two 511 keV γ and thus a threshold of 1 MeV would be optimal. However, one of the two γ can be missed and the resolution on the measured energy is finite: for a good signal efficiency, a threshold of 0.5 MeV has to be used. As a compromise between signal efficiency and background contamination, an intermediate threshold of 0.7 MeV could be envisaged before the 0.5 MeV threshold. In the following, we will describe studies carried out to determine the radioactivity constraints that should satisfy two detector components: a sealant between the shielding bars and the paint in the inner veto (see section 5.2.2). The limit rate for their induced background have been set to $L = 0.1$ Bq in the detection volumes, 100 times less than the major contribution from the PMTs for a total accidental background of the order of 1% of the signal [104]. Knowing the component mass introduced in the detector, the purpose of the simulations was to determine the transmission factors that are the number of γ reaching the considered volume (either target or γ-catcher) and giving a detected energy above the threshold out of the whole simulated γ.

7.1.1 Shielding sealant

The liquid scintillators used in the experiment have to be contained in case of unexpected problems like scintillators leaks to the groundwater that occurred to the Borexino experiment (see section 3.1.4). The steel shielding is the outermost volume of the detector and hence it was decided to install a sealant between the bars constituting it. The shielding is made of bars with a 'V-shape' for their fitting. For the top and bottom lids, 14 bars each of different lengths are used for a total weight of 45 tons. For the lateral part, 42 bars of 4.2 tons are used (plus a closing

[2] An exception exists for the γ from the target and γ-catcher scintillators and acrylics [159].

piece). The features of the lateral bars are displayed on figure 7.1 together with an example of the shielding configuration. The sealant was introduced between the bottom lid bars and in the lower part of the lateral shielding, on a height of one meter[3]. Its contribution to the radioactivity background in the experiment was evaluated as described in the following. We present first the simulation of the

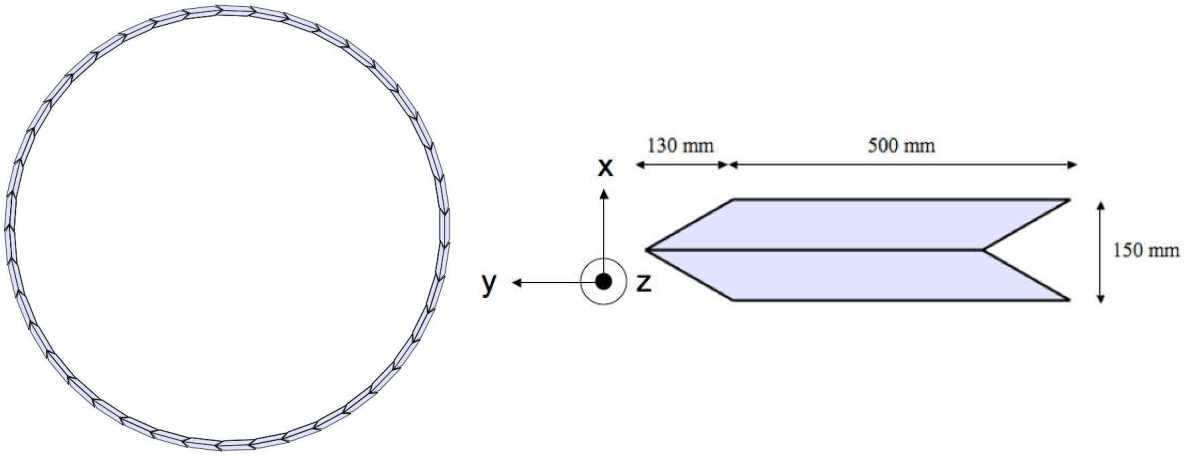

Figure 7.1: Left panel: layout of the DC steel shielding. Right panel: geant4 simulation of one bar of the shielding, it is made of two parallelepipeds. The features are a thickness of 150 mm, a width of 630 mm and a length of 6850 mm. The angle of the 'V' is here 60° while it is actually 63.5° to allow the bars rotation to form a cylinder.

shielding made for this study and then the radioactivity constraints deduced from the γ simulation.

Simulation

In the default DC simulation, the shielding was simply described by a 15 cm thick cylinder. For this study, we were led to simulate the real shielding. We made the choice to simulate only two lateral bars put straightly 1cm after the inner veto volume (in x = 3260 mm and y = $\pm$ 315 mm). The gap between the bars is constant (cf. fig. 7.2). The technical specifications were a gap of 5 mm between the bars. We have however simulated different gap values: 5, 10, 15, 20 and 50 mm to assess the impact on the background. The sealant was introduced in the detector at the level of the tip but a spread was envisaged and thus the radioactivity γ were simulated in the whole gap (cf. fig. 7.3). The next step was the determination of

[3]Some sealant was introduced in the upper part of the lateral bars to ensure a good vertical alignment.

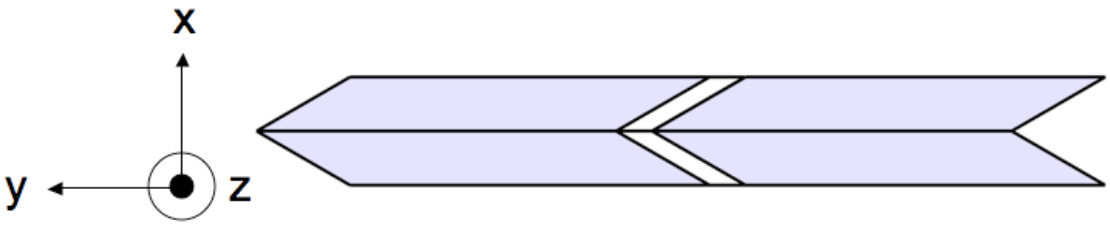

Figure 7.2: *geant*4 simulation used to determine the radioactive constraints. The gap between the bars is here 5 mm corresponding to the technical specifications.

the transmission factors from the 2.10^6 γ simulated from ^{40}K at 1.4 MeV and from ^{208}Tl at 2.6 MeV.

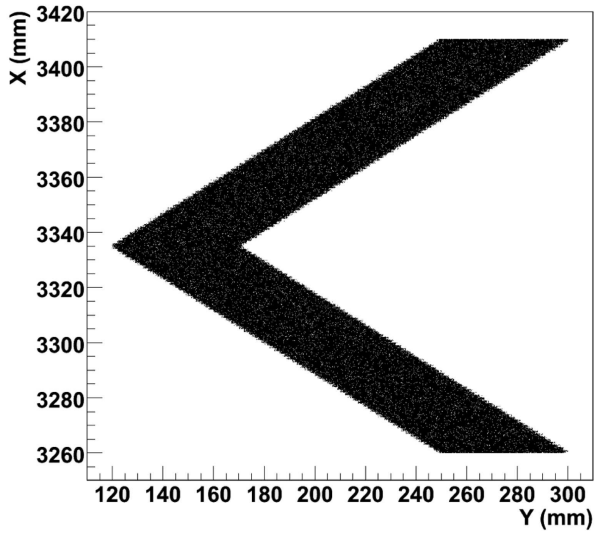

Figure 7.3: Plots showing the origin of the γ simulated. The gap is 50 mm here.

Transmission factors determination

The γ energy deposition in the target and the γ-catcher were taken into account separately for the three possible thresholds. The tables 7.1 and 7.2 summarize the results obtained for different gap and a 0.5 MeV threshold, respectively for thallium and potassium. The energy spectra can be viewed on figure 7.4.

We observe first that only 99.9% of the simulated γ manage to reach the detection volumes with an energy above the readout threshold of 0.5 MeV. Secondly, the

gap	Number of interactions out of the 2.10^6 ^{208}Tl γ simulated					
	Target			γ-catcher		
	>0.5 MeV	>0.7 MeV	>1 MeV	>0.5 MeV	>0.7 MeV	>1 MeV
5 mm	21	17	15	222	194	145
10 mm	18	17	13	211	177	136
15 mm	15	13	11	232	197	162
20 mm	25	20	16	240	200	152
50 mm	20	18	13	275	239	188

Table 7.1: Number of interactions out of the 2.10^6 ^{208}Tl γ simulated for different gap between the lateral bars of the shielding simulated.

gap	Number of interactions out of the 2.10^6 ^{40}K γ simulated					
	Target			γ-catcher		
	>0.5 MeV	>0.7 MeV	>1 MeV	>0.5 MeV	>0.7 MeV	>1 MeV
5 mm	2	1	1	22	16	5
10 mm	1	1	0	19	13	7
15 mm	0	0	0	22	14	7
20 mm	2	2	0	28	16	9
50 mm	4	4	4	41	29	18

Table 7.2: Number of interactions out of the 2.10^6 ^{40}K γ simulated for different gap between the lateral bars of the shielding simulated.

transmission factor seems to be steady for a gap value below 20 mm. Since a gap value above 15 mm is very unlikely, this result is very good for the robustness of the constraint results. This favorable situation is allowed by the V-shape of the bars[4], only a small fraction of γ ($\leq 1/1000$) can escape the shielding without interacting inside it. Considering a gap of 15 mm, the transmission factors are the following:

- $T_{^{208}Tl}(500\text{ keV}) = (1.21 \pm 0.08) \times 10^{-4}$, $T_{^{40}K}(500\text{ keV}) = (1.2 \pm 0.25) \times 10^{-5}$
- $T_{^{208}Tl}(700\text{ keV}) = (1.06 \pm 0.07) \times 10^{-4}$, $T_{^{40}K}(700\text{ keV}) = (0.85 \pm 0.21) \times 10^{-5}$
- $T_{^{208}Tl}(1\text{ MeV}) = (0.8 \pm 0.06) \times 10^{-4}$, $T_{^{40}K}(1\text{ MeV}) = (0.3 \pm 0.12) \times 10^{-5}$

Radioactivity constraints

The radioactivity constraint in Bq/kg C_X for the element X is determined through the following equation:

$$C_X = \frac{L}{M_{sealant} \times T_X} \tag{7.1}$$

[4]Most of the γ have a part of the shielding to cross which attenuate them. The γ interacting in the detection volumes come mostly from the edge the closest to the center (see section 7.1.1).

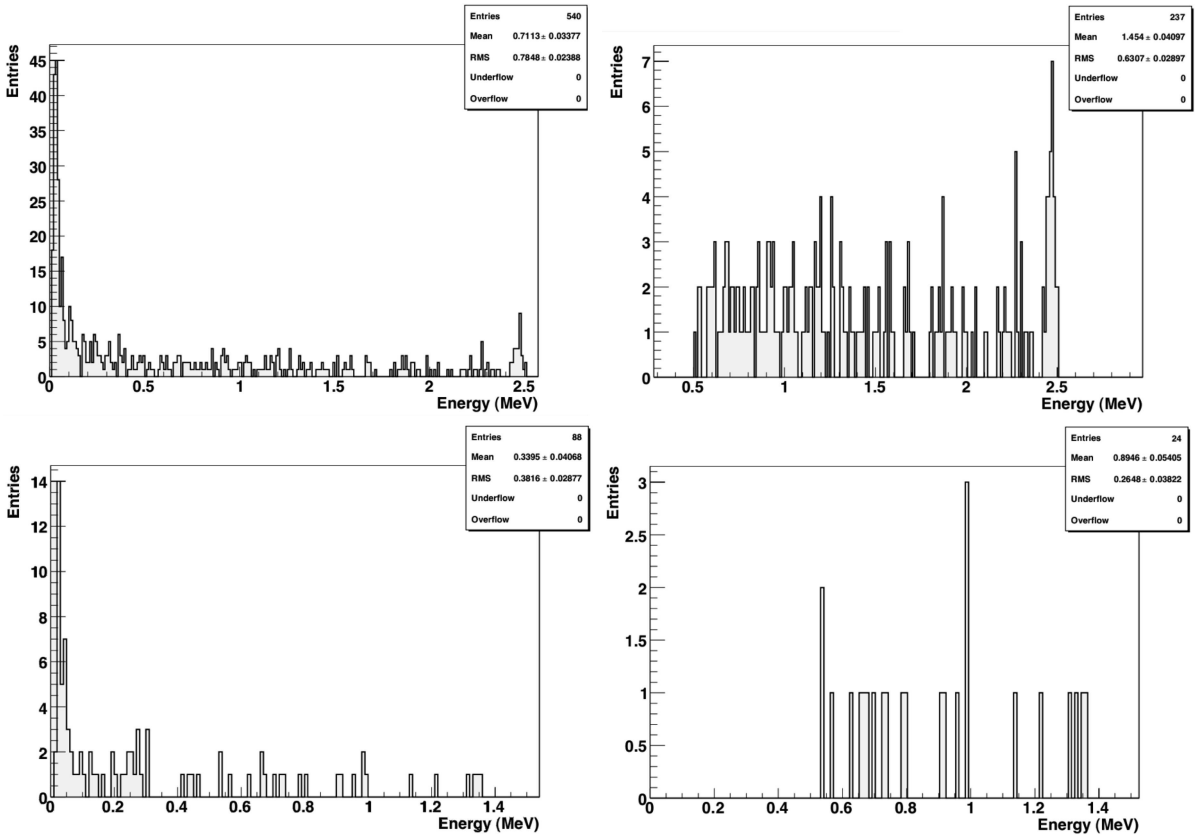

Figure 7.4: Plots showing the visible energy spectra in the target plus γ-catcher for thallium (upper plots) and potassium (lower plots) for a 5 mm gap. There is no threshold for the left plots and a 0.5 MeV threshold for the right plots.

where L is the background rate limit in Bq, $M_{sealant}$ is the introduced sealant mass in kg and T_X is the transmission factor of the element X. The sealant mass is 500 kg. Thus for a $L = 0.1$ Bq at 90% C.L., the radioactivity constraints are the following:

- $C_{^{208}\mathrm{Tl}}(500\text{ keV}) < 1.5$ Bq/kg, $C_{^{40}\mathrm{K}}(500\text{ keV}) < 13.2$ Bq/kg
- $C_{^{208}\mathrm{Tl}}(700\text{ keV}) < 1.7$ Bq/kg, $C_{^{40}\mathrm{K}}(700\text{ keV}) < 17.9$ Bq/kg
- $C_{^{208}\mathrm{Tl}}(1\text{ MeV}) < 2.3$ Bq/kg, $C_{^{40}\mathrm{K}}(1\text{ MeV}) < 43.5$ Bq/kg

These constraints hold for a sealant spread over the whole gap between the bars and put on the full height of the lateral bars. However, during the shielding integration, it was noticed that the sealant remained located at the tip of the V-shape of the bars, while as can be seen on figure 7.5, most of the γ inducing an energy deposition above the readout threshold come from the edge of the gap closest to the detector

center since the γ originating from these positions have less shield to cross. We have determined new transmission factors by selecting the γ in agreement with the diameter of the sealant[5] of the order of 20 mm allowing for 5 mm spread. Only one interaction is observed in the simulated samples above 0.7 MeV and nothing above 1 MeV for potassium. The new transmission factors are at 90% C.L.:

- $T_{^{208}Tl}(500\text{ keV}) = (7.19 \pm 1.47) \times 10^{-5}$, $T_{^{40}K}(500\text{ keV}) = (3 \pm 3) \times 10^{-6}$
- $T_{^{208}Tl}(700\text{ keV}) = (6.3 \pm 1.37) \times 10^{-5}$, $T_{^{40}K}(700\text{ keV}) = (3 \pm 3) \times 10^{-6}$
- $T_{^{208}Tl}(1\text{ MeV}) = (5.1 \pm 1.24) \times 10^{-5}$, $T_{^{40}K}(1\text{ MeV}) < 8.99 \times 10^{-6}$

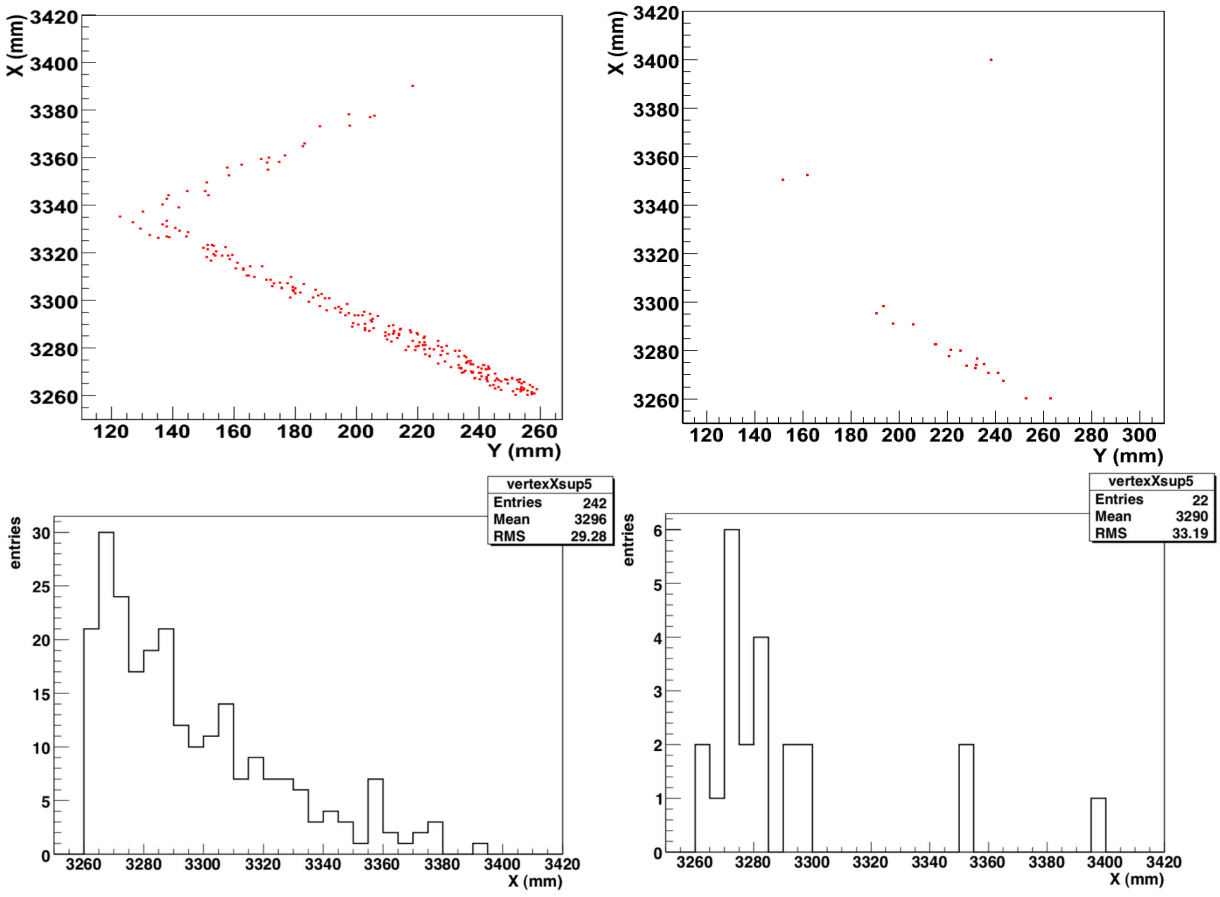

Figure 7.5: Plots showing the initial coordinates of γ that created energy depositions above 0.5 MeV in the detection volumes for thallium (left plots) and potassium (right plots). The gap between the bars is 15 mm here.

Besides, as highlighted above, the sealant was only put on a height of 1 meter in the lower part of the bars while most of the γ interactions above the readout threshold

[5]The sealant has a cylindric shape.

comes from the center in Z of the bars as can be seen on figure 7.6. Again the γ coming from the extremity of the sealant have to cross more matter (roughly a factor $\sqrt{2}$) than those coming from the center. No interactions at all are observed for potassium. The new transmission factors are at 90% C.L.:

- $T_{^{208}Tl}(500\text{ keV}) = (1.67 \pm 0.75) \times 10^{-5}$, $T_{^{40}K}(500\text{ keV}) < 9.98 \times 10^{-6}$
- $T_{^{208}Tl}(700\text{ keV}) = (1.67 \pm 0.75) \times 10^{-5}$, $T_{^{40}K}(700\text{ keV}) < 9.98 \times 10^{-6}$
- $T_{^{208}Tl}(1\text{ MeV}) = (1 \pm 0.58) \times 10^{-5}$, $T_{^{40}K}(1\text{ MeV}) < 9.98 \times 10^{-6}$

Using the most constraining transmission factors found, we calculate the following new radioactivity constraints at 90% C.L.:

- $C_{^{208}Tl}(500\text{ keV}) < 7.6$ Bq/kg, $C_{^{40}K}(500\text{ keV}) < 28.9$ Bq/kg
- $C_{^{208}Tl}(700\text{ keV}) < 7.6$ Bq/kg, $C_{^{40}K}(700\text{ keV}) < 28.9$ Bq/kg
- $C_{^{208}Tl}(1\text{ MeV}) < 11.4$ Bq/kg, $C_{^{40}K}(1\text{ MeV}) < 43.5$ Bq/kg

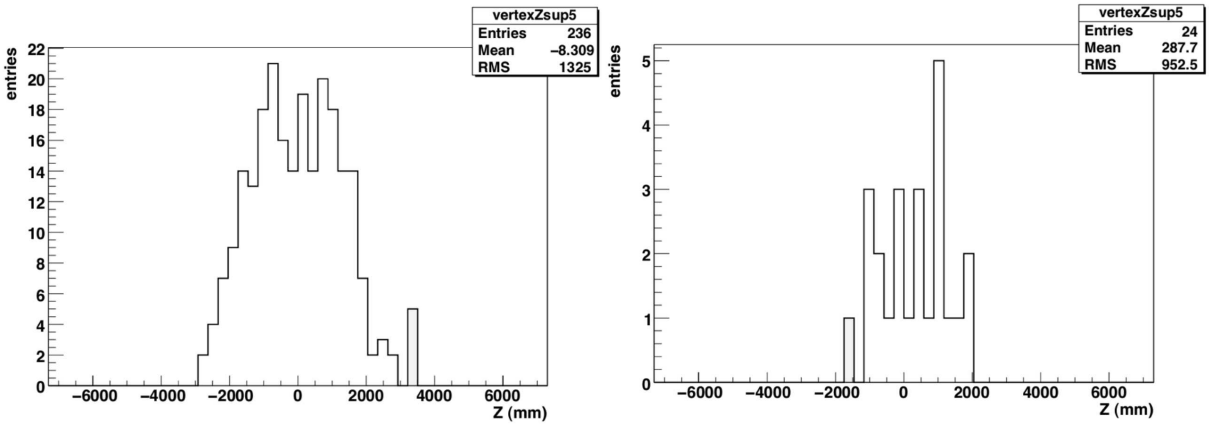

Figure 7.6: Plots showing the initial Z coordinate of the γ interacting in the detection volumes with an energy deposition above the readout threshold. The gap is 5 mm here.

Conclusion

We have determined from simulations the radioactivity constraints for the sealant that have been installed between the bars of the steel shielding. The radioactivity of several sealant candidates were measured with a germanium detector at Saclay [164]. The sealant sample that has been chosen showed the following radioactive contamination at 90% C.L.:

- thallium : 2.23 ± 0.03 Bq/kg
- bismuth : 15.1 ± 0.09 Bq/kg
- potassium : 44.8 ± 0.41 Bq/kg

These sealant candidate features are largely satisfying for the bismuth and thallium whereas it is close to the limit for potassium. However for the latter we had no interactions at all in the simulated sample after the needed selection criteria and thus the limit should be inferior. Furthermore, there is an attenuation towards the target and thus most of the interactions should be in the γ-catcher what could be identified by volume pulse shape discrimination (see section 7.2.3) and an accurate spatial reconstruction (see chapter 8). Therefore a background two times higher should not be a problem at all. The experiment will be safe with the use of this sealant. Besides to further ensure that no leak will happen a retention tank was installed outside of the shielding.

7.1.2 Inner veto paint

The inner veto (IV) photocathode coverage has a small value of 0.6%. Hence VM 2000 reflective foils were applied on the buffer tank as well as a white reflective TiO_2 paint on the interior part of the IV tank. The goal is not only to increase the light collection but also to ensure the material compatibility to prevent a degradation of the liquid scintillator. However the paint is radioactive and will therefore emit γ. For a paint with a common radioactive contamination, thanks to the presence of the buffer, the resulting background is expected to be low enough to not disturb the experiment. This statement has nevertheless to be checked for the upper part of the detector where there are the target and γ-catcher calibration chimneys filled with liquid scintillator.
We first present some results on γ transmission for different parts of the IV. For the upper part, we have investigated several horizontal positions away from the chimney. Secondly, we have determined what radioactivity constraints should be satisfied. Finally, we have double checked the results by simulating γ's uniformly on the interior part of the IV tank, including its chimney.

γ simulation and transmission factors

We have simulated 500000 γ's isotropically at the following three representative points of the IV tank and then considered the energy depositions in the detection

volumes, distinguishing target and γ-catcher depositions (the origin is the center of the detector):

- at the center of the lateral surface of the IV, which we call 'Edge', the coordinates are x = 3249 mm and y = z = 0 mm.
- 1 mm away from the chimney. This location is called 'Top' and its coordinates are x = 356mm, y = 0 mm and z = 3419 mm
- at the center of the bottom. This location is called 'Bottom' and its coordinates are x = y = 0 mm and z = -3419 mm.

The following two tables summarize the results obtained for thallium (Tab. 7.3) and potassium (Tab. 7.4). These tables indicate that the number of interactions

Name of location	Position of simulated γ's		number of interactions on 500000 γ's					
			γ-catcher (MeV)			target (MeV)		
	X(mm)	Z(mm)	> 0.5	> 0.7	> 1	> 0.5	> 0.7	> 1
Edge	3249	0	402	340	262	38	34	28
Bottom	0	−3419	401	338	243	36	35	31
Top	356	3419	1899	1579	1235	331	268	187

Table 7.3: Number of interactions out of 500000 simulated γ's from ^{208}Tl for 3 different positions (y = 0 mm).

Name of location	Position of simulated γ's		number of interactions on 500000 γ's					
			γ-catcher (MeV)			target (MeV)		
	X(mm)	Z(mm)	> 0.5	> 0.7	> 1	> 0.5	> 0.7	> 1
Edge	3249	0	37	28	11	5	3	2
Bottom	0	−3419	54	44	16	3	3	1
Top	356	3419	639	436	215	113	73	32

Table 7.4: Number of interactions out of 500000 simulated γ's from ^{40}K for 3 different positions (y = 0 mm).

due to the γ's coming from the paint at the bottom and the edge of the detector is low, as expected. The transmission factors are the following at 90% C.L. for the Edge position:

- $T_{^{208}\mathrm{Tl}}(500\ \mathrm{keV}) = (8.8\pm0.42)\times10^{-4}$, $T_{^{40}\mathrm{K}}(500\ \mathrm{keV}) = (0.84\pm0.13)\times10^{-4}$
- $T_{^{208}\mathrm{Tl}}(700\ \mathrm{keV}) = (7.48\pm0.39)\times10^{-4}$, $T_{^{40}\mathrm{K}}(700\ \mathrm{keV}) = (0.62\pm0.11)\times10^{-4}$

- $T_{^{208}Tl}(1\ \text{MeV}) = (5.8 \pm 0.34) \times 10^{-4}$, $T_{^{40}K}(1\ \text{MeV}) = (0.26 \pm 0.07) \times 10^{-4}$

and the following ones for the Bottom position:

- $T_{^{208}Tl}(500\ \text{keV}) = (8.74 \pm 0.42) \times 10^{-4}$, $T_{^{40}K}(500\ \text{keV}) = (1.14 \pm 0.15) \times 10^{-4}$
- $T_{^{208}Tl}(700\ \text{keV}) = (7.46 \pm 0.39) \times 10^{-4}$, $T_{^{40}K}(700\ \text{keV}) = (0.94 \pm 0.14) \times 10^{-4}$
- $T_{^{208}Tl}(1\ \text{MeV}) = (5.48 \pm 0.33) \times 10^{-4}$, $T_{^{40}K}(1\ \text{MeV}) = (0.34 \pm 0.08) \times 10^{-4}$

The situation is however drastically different for the γ's simulated at the Top position, we observe roughly 5 times more interactions in the detection volumes for thallium and 10 times more for potassium. The corresponding transmission factors are the following:

- $T_{^{208}Tl}(500\ \text{keV}) = (4.46 \pm 0.09) \times 10^{-3}$, $T_{^{40}K}(500\ \text{keV}) = (1.5 \pm 0.06) \times 10^{-3}$
- $T_{^{208}Tl}(700\ \text{keV}) = (3.69 \pm 0.09) \times 10^{-3}$, $T_{^{40}K}(700\ \text{keV}) = (1.02 \pm 0.05) \times 10^{-3}$
- $T_{^{208}Tl}(1\ \text{MeV})\ (2.84 \pm 0.08) \times 10^{-3}$, $T_{^{40}K}(1\ \text{MeV}) = (4.94 \pm 0.31) \times 10^{-4}$

This situation is clearly due to the presence of the calibration chimneys. The simulated γ's interact with scintillators in chimneys and part of the scintillation photons manage to reach the buffer PMTs and fake a deposited energy above the readout threshold. This is what we can see on figure 7.7 where the locations of the energy depositions above 500 keV in R and Z are plotted and shown together the corresponding energy spectra. The ^{40}K energy deposition spectrum shows an exponential behavior as does the ^{208}Tl one except from a noticeable increase at high energies. The latter exhibits the most dangerous spectrum for the oscillation analysis.

Radioactivity constraints

Most of the γ interactions in the detection volumes are due to the presence of the calibration chimneys. Since the γ's are simulated isotropically, if we move away from the IV's chimney their point of generation in R, we expect the number of interactions to decrease. We have therefore investigated several positions on the top away from the chimney whose radius is 355 mm: 1, 10, 30, 50, 100, 150, 200 and 300 mm. At each position, we have simulated isotropically 500000 γ's from thallium and potassium. This has allowed us to determine qualitatively the evolution of the number of interactions with the distance and hence, the behavior of the

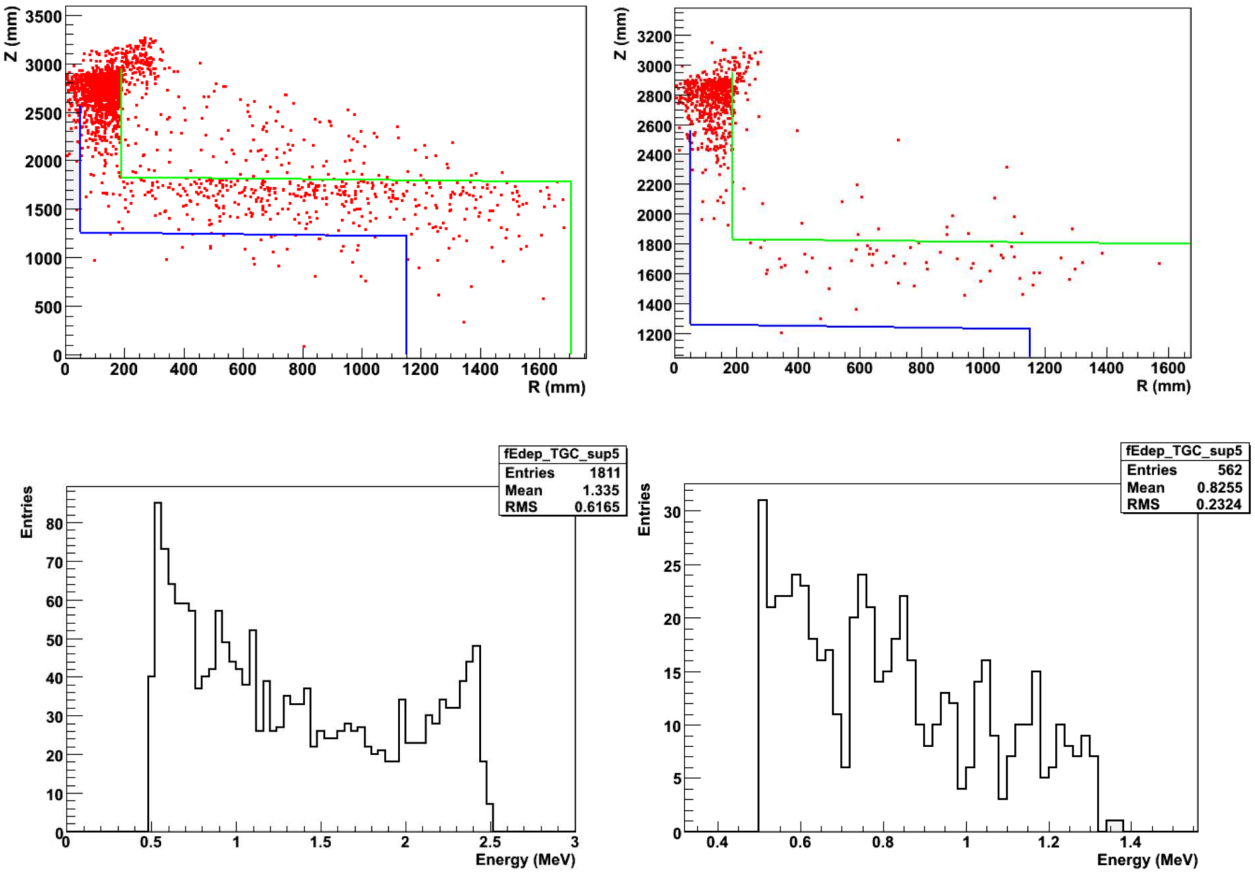

Figure 7.7: R and Z (upper plots) positions of the energy depositions higher than 0.5 MeV for the γ's of thallium (left) and potassium (right), simulated the closest to the calibration chimneys: at x=356 mm, z=3419 mm and y =0 mm. These two plots indicate that the chimneys are responsible for the high transmission factor values found previously. The two lower plots present the resulting spectra in target and γ-catcher for thallium (left) and potassium (right).

transmission factors, which have been fitted with simple exponential functions (cf. fig. 7.8) which we denote as $T(r)$.

The radioactivity constraint values are determined using the following equation:

$$C_X = \frac{L}{M_{Bottom}T^X_{Bottom} + M_{Edge}T^X_{Edge} + 2\pi e\rho_{paint}\int_{R_{IV_c}}^{R_{IV}} rT_{T+GC}(r)dr} \tag{7.2}$$

where C_X is the constraint for the element X in Bq/kg, L is the desired limit for the γ interaction rate in Bq and M is the mass of paint on the considered part of the tank. T^X is the transmission factor of the considered part and element determined previously. ρ_{paint} is the density of the paint and e its thickness. Finally the

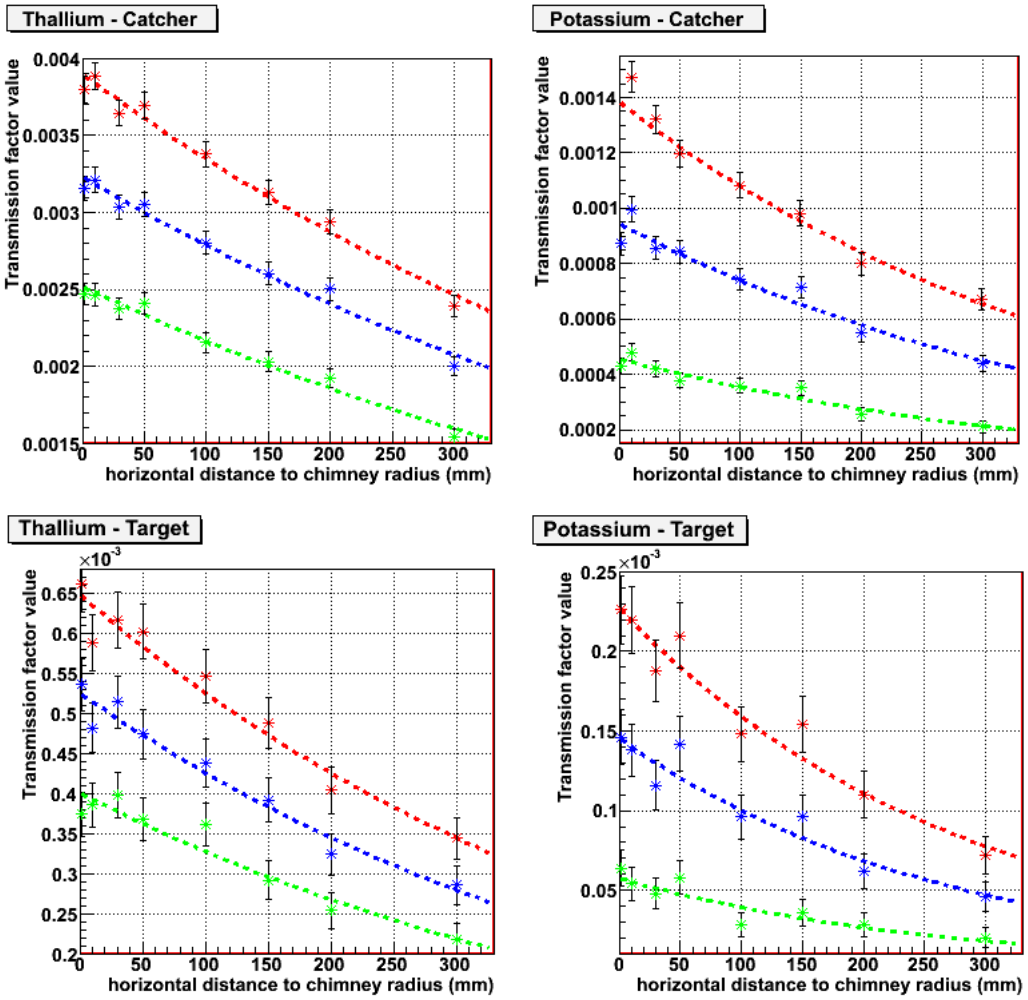

Figure 7.8: Plots showing the transmission factors as a function of the horizontal distance to the chimney. 500000 γ's were simulated at a given position on the upper interior part of the IV. The left plots are the results for thallium and the right ones are for potassium. The upper plots are the number of interactions in the γ-catcher and the lower ones correspond to the interactions in the target. The red dots are the number of interactions above the threshold of 500 keV, the blue ones are for a readout threshold of 700 keV and the green ones for 1 MeV; the error bars are statistical. These results are fitted with simple exponential functions that have been then used to determine the radioactive constraint values.

integral is the contribution of the upper part of the IV tank paint and $T(r)$ is the exponential function determined just above. R_{IV} is the radius of the IV volume and R_{IV_c} is the radius of the IV chimney.

In order to make the calculation, we assumed that ρ_{paint} is equal to 1.45 ± 0.15 g/cm^3. This assumption is needed in order to calculate the paint mass. Its value is guessed from the usual density of such paint. Another essential component for this

calculation is the paint thickness, of the order of 800 μm according to the specification the professional painters had. Finally, for the calculation, we have taken into account separately the contribution due to the Edge, the Bottom and the Top. For the Top position, we have integrated with the exponential functions determined previously while for the Edge and the Bottom positions, we have approximated the transmission factors by a constant function. The radioactivity constraints obtained are at 90% C.L.:

- $C_{^{208}Tl}(500\text{ keV}) < 0.52$ Bq/kg, $C_{^{40}K}(500\text{ keV}) < 3.09$ Bq/kg
- $C_{^{208}Tl}(700\text{ keV}) < 0.6$ Bq/kg, $C_{^{40}K}(700\text{ keV}) < 3.97$ Bq/kg
- $C_{^{208}Tl}(1\text{ MeV}) < 0.79$ Bq/kg, $C_{^{40}K}(1\text{ MeV}) < 7.89$ Bq/kg

Second analysis

To have more conclusive results, we have made a second analysis that takes into account, at the simulation level, all the IV paint. Indeed, we have simulated γ's uniformly on the interior part of the IV tank (cf. fig. 7.9), and we have then observed the number of interactions in the detection volumes. The results obtained

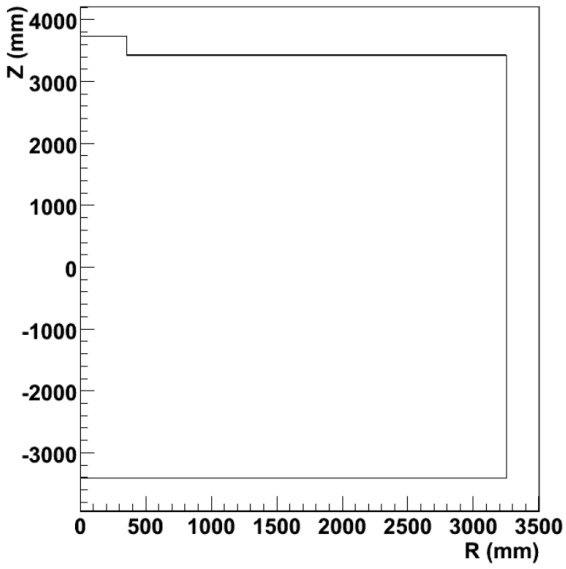

Figure 7.9: Plots showing the origin of the simulated γ's. We observe that in this simulation, γ's from the IV's chimney have as well been simulated.

for γ's originating from thallium and potassium are presented in table 7.5 and figure 7.10 presents the location in R and Z of the interactions which have deposited

Origin of γs	Number of interactions out of 2000000 γ simulated					
	γ-catcher			target		
	>0.5 MeV	>0.7 MeV	>1 MeV	>0.5 MeV	>0.7 MeV	>1 MeV
Tl	1023	871	672	83	69	49
K	124	97	56	11	7	4

Table 7.5: Number of interactions in the detection volumes on 2000000 γ's simulated uniformly on the interior part of the IV tank.

an energy higher than 500 keV for thallium and potassium; the corresponding spectra are as well presented. We observe on this figure that most of the interactions occur close to the edge of the γ-catcher and the high contribution due to the chimney observed previously is confirmed. From the values of the table 7.5, we extract the transmission factors:

- $T_{^{208}Tl}(500\text{ keV}) = (5.53\pm0.17)\times10^{-4}$, $T_{^{40}K}(500\text{ keV}) = (6.75\pm0.58)\times10^{-5}$
- $T_{^{208}Tl}(700\text{ keV}) = (4.7\pm0.15)\times10^{-4}$, $T_{^{40}K}(700\text{ keV}) = (5.2\pm0.51)\times10^{-5}$
- $T_{^{208}Tl}(1\text{ MeV}) = (3.61\pm0.13)\times10^{-4}$, $T_{^{40}K}(1\text{ MeV}) = (3\pm0.39)\times10^{-5}$

Considering a $L = 0.1$ Bq and a total paint mass of 238.8 kg, we obtain from equation 7.1 the following constraints at 90% C.L.:

- $C_{^{208}Tl}(500\text{ keV}) < 0.51$ Bq/kg, $C_{^{40}K}(500\text{ keV}) < 3.95$ Bq/kg
- $C_{^{208}Tl}(700\text{ keV}) < 0.6$ Bq/kg, $C_{^{40}K}(700\text{ keV}) < 5.03$ Bq/kg
- $C_{^{208}Tl}(1\text{ MeV}) < 0.78$ Bq/kg, $C_{^{40}K}(1\text{ MeV}) < 8.18$ Bq/kg

These results are less constraining than the first analysis. It can be explained by the fact that here we make no assumptions on a steady transmission factor for the Edge and the Bottom, which represents the largest surface.

Paint choice

The radioactivity constraints that the IV paint should satisfy have been assessed by two different methods as described above. For the first one, we have simulated radioactivity γ at some precise points and then integrated on the whole IV volume while for the second one, we have simulated the γ uniformly in the IV tank; the former being less reliable. The results obtained are compatible and of the order of 0.6 Bq/kg for the thallium and 5 Bq/kg for the potassium. The constraints for

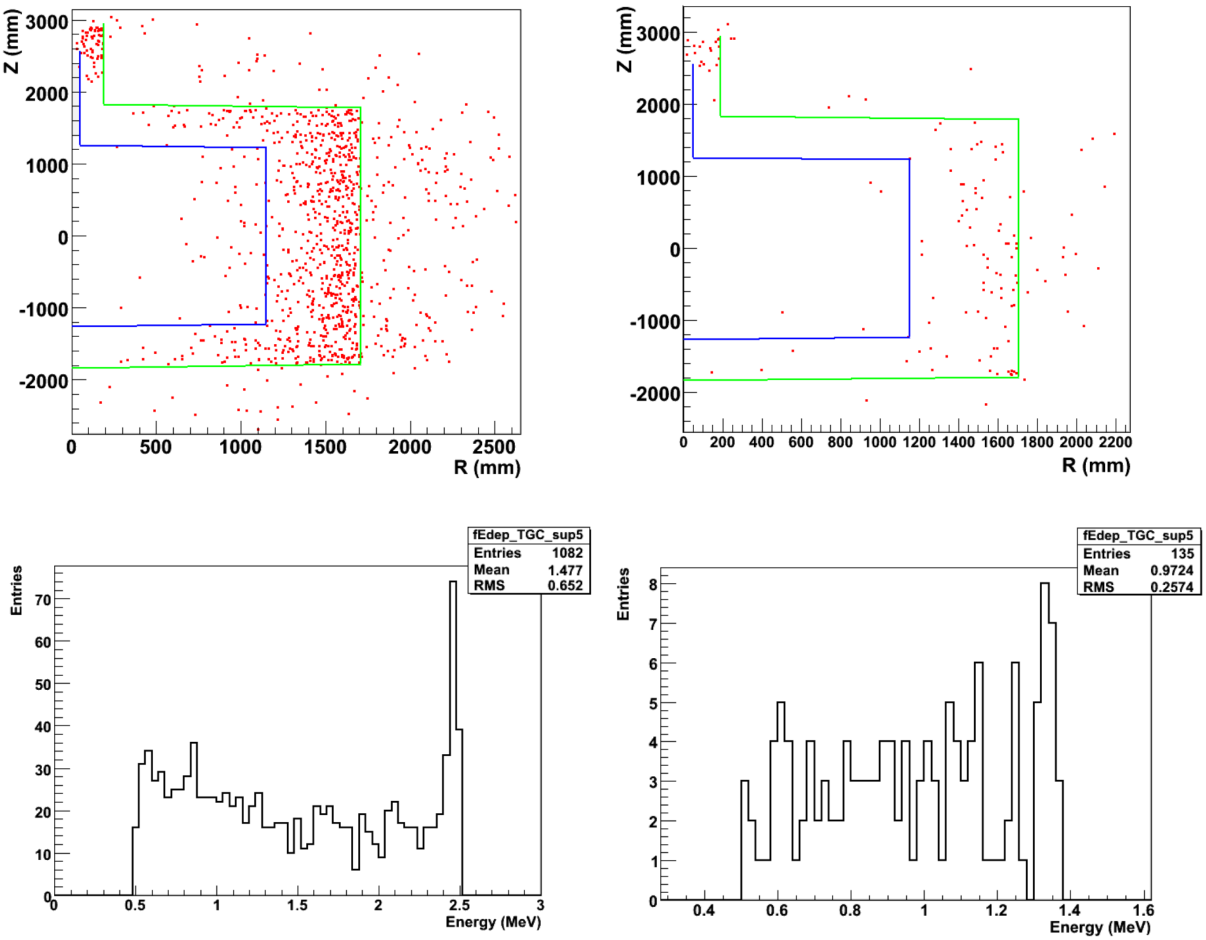

Figure 7.10: The two upper plots show the R and Z positions of the energy depositions higher than 0.5 MeV for the γ's of thallium (left) and potassium (right) . The blue line marks the target out and the green one the γ-catcher. The two lower plots show the corresponding spectra obtained in target plus γ-catcher for thallium (left) and potassium (right).

the readout thresholds of 500 keV and 700 keV are of the same extent whereas for 1 MeV, the constraint is about 2 times higher for potassium and 1.5 for thallium. Several candidate paints were measured at Saclay with a Germanium crystal and the selected paint sample has the following radioactive contamination at 90% C.L. [164, 165]:

- cobalt: < 70 mBq/kg
- thorium: 0.5 ± 0.17 Bq/kg
- uranium: 4.8 ± 1.15 Bq/kg

- potassium: 2.1 ± 2.47 Bq/kg

The Cobalt contribution can be neglected since the sample contamination is two orders of magnitude lower than potassium[6]. The corresponding activities for the three remaining elements are: Taking into account that we have two relevant γ

Element	0.5 MeV	0.7 MeV	1 MeV
Th	0.07 ± 0.02	0.06 ± 0.02	0.043 ± 0.01
U	0.08 ± 0.02	0.06 ± 0.02	0.034 ± 0.01
K	0.04 ± 0.02	0.03 ± 0.02	0.017 ± 0.01

Table 7.6: Contributions expected in Bq for the three main radioactive elements of the IV's paint

rays for the Bismuth, we expect a total background rate induced by the paint of:

- 0.25 ± 0.06 Bq for a threshold of 0.5 MeV,
- 0.2 ± 0.05 Bq for a threshold of 0.7 MeV,
- 0.13 ± 0.03 Bq for a threshold of 1 MeV.

The total rate due to the IV paint is of the order of 0.1-0.2 Bq and therefore the experiment will be easily safe with this rate of interactions. Besides, as seen in section 7.1.2, most of the interactions are located in the γ-catcher. A good spatial reconstruction (see chapter 8) possibly combined with a volume pulse shape discrimination (see section 7.2.3) would help to better understand this background and possibly leading to a cut to reject it (this has to be studied because it could also be a source of uncertainty what is definitely not wanted, see 4.1.1).

7.2 Towards a better energy determination

7.2.1 Concentrators to improve the energy resolution ?

As pointed out in section 4.1.1, efforts towards the best energy resolution are necessary to lower the systematic error induced by the energy cuts and to have an accurate $\bar{\nu}_e$ energy determination. The energy resolution σ_R is determined through the mean number of PEs μ_{PE} observed given by:

$$\frac{\sigma_E}{E} = [\mu_{PE}]^{-1/2} = (LY \times PC \times QE \times CE)^{-1/2} \tag{7.3}$$

[6]The cobalt ^{60}Co γ rays have an energy close to the potassium one and thus the corresponding transmission factors should be close but lower to the potassium one.

where LY is the number of photons produced by the scintillator in response to the considered energy deposition and PC is the photocathode coverage (ratio of the photocathode solid angle over 4π). QE and CE are the quantum and collection efficiencies of the used PMTs.
LY is a scintillator feature whose formula is fixed as well as the PMTs used. One can however try to improve the photocathode coverage. Thereby, it was envisaged to use aluminum cones plugged on PMTs, called light concentrators (an example is shown on figure 7.11), in order to direct photons through reflections to the PMTs photocathode leading to an increased effective solid angle. However the PMTs are angled towards the detector center. If an energy deposition occurs away from the

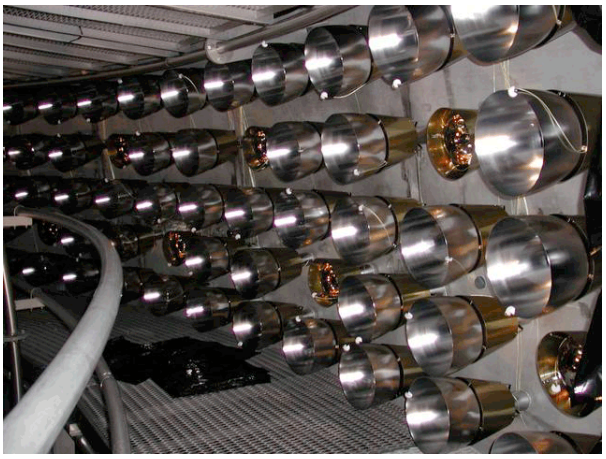

Figure 7.11: Picture of PMTs with and without the light concentrators (in grey) during their installation in the Borexino experiment [166].

center region, the light collection is not optimized and thus non-uniformity in the detector energy response will be enhanced. The non-uniformity should be more pronounced with concentrators than without [167].
We have first investigated the non-uniformities with and without concentrators by obtaining the detector response maps. Then we have made assumptions on energy calibration and developed a method to correct the non-uniformities. Finally, we have investigated the impact of the spatial resolution on the accuracy of the correction.

Evaluation of the non-uniformity

In order to obtain the detector non-uniformity, we made the choice to simulate 1 MeV electrons. This choice was driven by the fact that the electron dE/dX is similar to the positron one (but without annihilation) and because an energy of 1

MeV makes it lose its full energy in a 10 mm radius from its initial position [168] (the energy choice is a compromise between the path length and the energy resolution). We simulated 110000 electrons uniformly in the detection volumes[7] (40000 in the target and 70000 in the γ-catcher to respect the volumes ratios) and looked at the number of PEs created in each event following its simulation position. What matters here is the exact detector response and thereby the electronics read-out resolution effects have been switched off. At some approximations[8], the detector exhibits azimuthal (in R) and up/down (in Z) symmetries. Consequently, we have represented the detector response in terms of PEs on 1/4 of the detector in R and Z. We thus have constructed the so-called 'response maps' displayed on figure 7.12.

We observe that the introduction of light concentrators raises the number of PEs per MeV. In the center, it increases from $\sim$ 195 PEs/MeV to $\sim$ 300 PEs/MeV which induces an improvement in the energy resolution of $\sim$1.5%. We observe as well that the two configurations, with and without concentrators, exhibit very similar response patterns. The target seems very uniform while 'hot' and 'cold' regions appear in the γ-catcher volume: the closest to the PMTs the highest number of PEs created (this corresponds to the top/bottom and lateral parts) whereas in the corner the solid angle of the PMTs that are close is highly reduced due to the PMTs direction and thus less PEs are created. Nevertheless the non-uniformity values are very different. For the baseline case, without concentrators, in the target they go up to +5% with a mean of $\sim$2%, while for the γ-catcher they go up to +15% for the top/bottom and lateral parts and down to -8% for the corners. For the case with concentrators, the non-uniformities in the target are up to +10% with a mean of $\sim$5% and in the γ-catcher, they go from -20% for the corners to +25% for the top/bottom part.

Concentrators could be seen as a cheap solution for better detector performances but meanwhile as a potential danger since they amplify the existing non-uniformities. If the non-uniformities can be efficiently corrected, the latter problem no longer holds. In the analysis presented below, we have tried to assess how well these non-uniformities can be corrected and compared the two configurations: with (baseline configuration) and without concentrators.

[7] In figure 7.12, the statistical fluctuations are of $\sim$ 10% in the first column of bins in R and $\sim$ 2.5% in the last one.

[8] The presence of the chimneys in the upper part of the detector and the supports in the lower part are neglected.

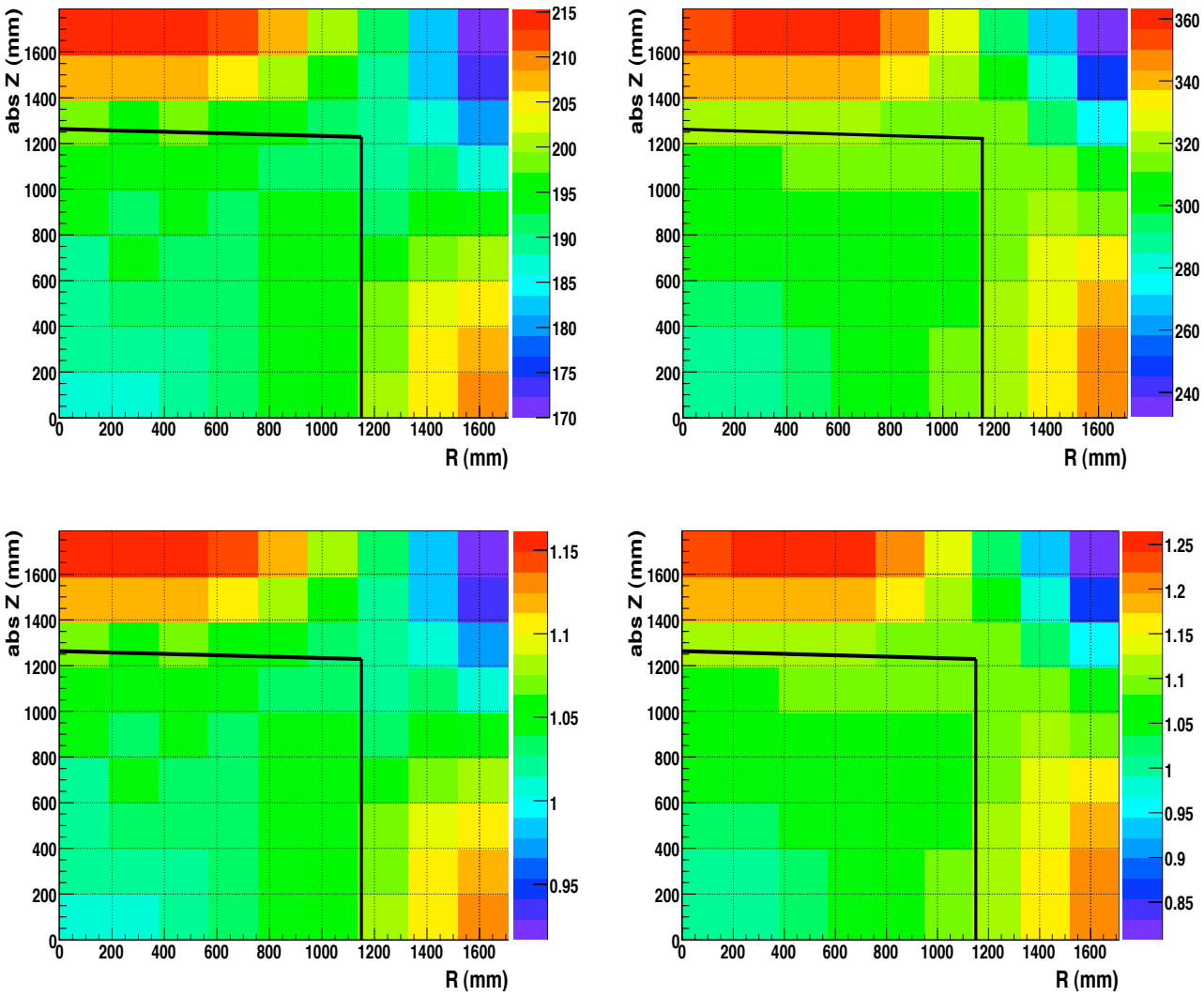

Figure 7.12: Detector response maps without concentrators (left plots) and with concentrators (right plots). The black line is the target/γ-catcher boundary. The upper plots show the detector response in terms of the mean number of PEs created in the events whereas the bottom plots show the relative response to the center. The thick black line is the target boundary.

Non-uniformities correction

The binning used in the detector response maps was chosen in order to have statistical fluctuations of the mean number of PEs below 10% using points which could correspond to possible calibration points during the experiment's functioning. The

bin dimensions are a height of 200 mm and a radius of 190 mm which lead to 9 bins in R and Z[9]. A trivial correction of the non-uniformity is to multiply the observed number of PEs for an event simulated in a given bin by the ratio of the reference number of PEs we want (here the number of PEs in the center) over the mean number of PEs in this bin. We went further by cutting a bin in four different regions and by making a linear interpolation between the mean number of PEs in the bin and the one of the closest bins in R and Z. This process leads us to have a correction coefficient for any position (cf. fig. 7.13). We have then simulated a

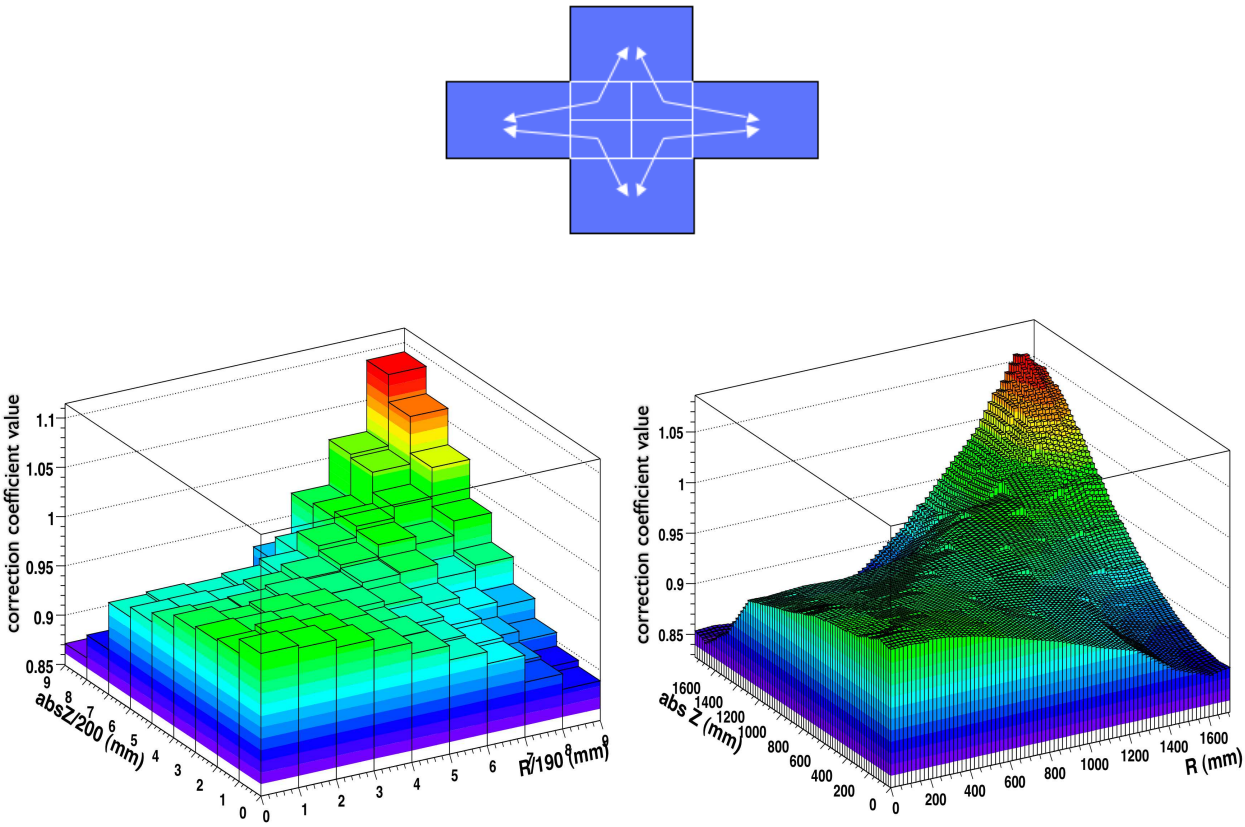

Figure 7.13: Upper plot: illustration of the correction coefficient interpolation process following the location of the energy deposition in a bin. Lower plots: correction coefficients before and after the interpolation process.

new sample of electrons and compared the effect of the correction algorithm on the two configurations assuming first that we have a perfect spatial reconstruction. We looked then at the new distribution of PEs in the detection volumes. The criteria

[9]This spacing between calibration points is feasible for the target thanks to the Z-axis and articulated arm systems. For the γ-catcher, the situation is far much harder but good calibration is expected from the guide and buffer tubes (see section 5.2.3).

used to assess the correction efficiency were the Root Mean Square (RMS) divided by the mean and the kurtosis. The first one is the resolution in terms of PEs, which is directly correlated with the energy resolution. The second criterion is complementary to the previous one, it gives hints about the shape of the distribution and the existence of residual areas with response very far from the average, rendering the resolution non-gaussian[10]. A high value of the kurtosis indicates that the distribution is more peaked than the normal distribution. The population close to the mean value is higher than for the normal distribution possibly resulting in energy cuts with a smaller systematic error. We can go further with the first criteria by subtracting its statistical part letting only the non-uniformity one:

$$\sigma_{n.s} = \sqrt{\sigma_{tot}^2 - \sigma_{stat}^2} \tag{7.4}$$

where $\sigma_{n.s}$ is the non statistical sigma with $\sigma_{stat} = \sqrt{mean}$ the statistical part and σ_{tot} the RMS. This statement is valid only if the distribution is poissonian/gaussian.

The PEs distribution before and after the application of the correction algorithm

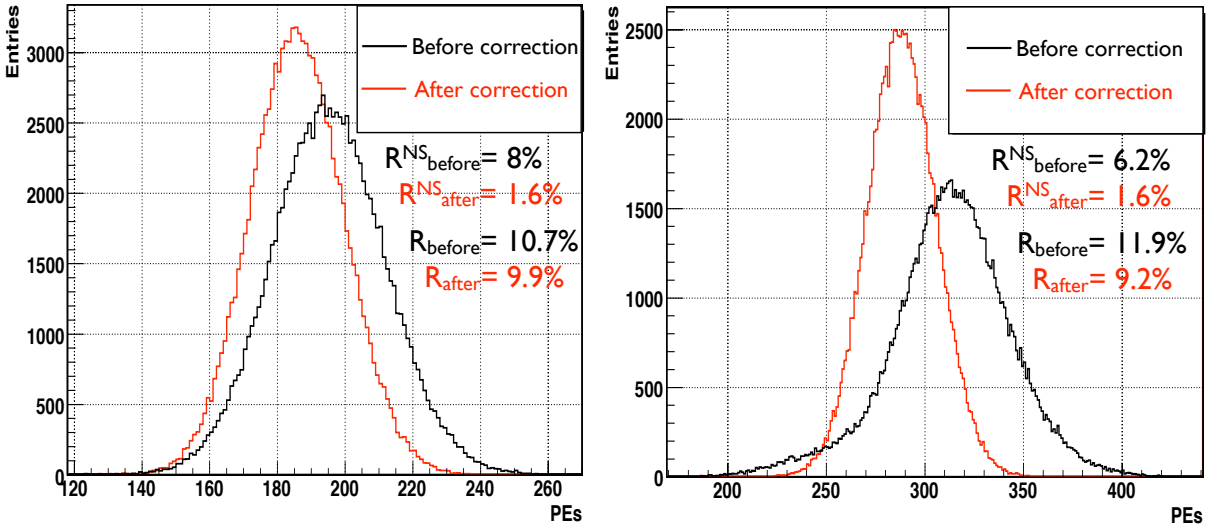

Figure 7.14: PEs distribution before and after the application of the correction algorithm without concentrators (left) and with concentrators (right). R_{NS}, R are respectively the non statistical and total energy resolutions.

are displayed on figure 7.14. For the baseline configuration, the energy resolution goes from 10.7% to 9.9% after the correction which gives in terms of non uniformity

[10] A kurtosis value of zero corresponds to a gaussian distribution, a value higher than zero indicates a distribution more peaked with longer tails than the normal distribution (this is the inverse for a value below zero).

a transition from 8% to 1.6%. The improvement is clear as well for the kurtosis criteria, it goes from a value of 18.1 to 26.9. The situation looks very similar for the configuration with concentrators apart from the presence of long tails before correction. The energy resolution goes from 11.9% to 9.2% after correction, that is to say a transition from 6.2% to 1.6% for the non-uniformities. The kurtosis confirms the improvement with a transition from 13.5 to 42.7. The level at which the non-uniformities can be corrected is the same for the two configurations assuming a perfect spatial reconstruction: 1.6%[11].

Spatial reconstruction impact

We have then investigated the influence of the spatial reconstruction accuracy on the correction efficiency. To achieve this goal, we have introduced a smearing on the particle position in x, y and z. We have tested resolutions of 100, 200, 300, 400 and 1000 mm. The PEs distributions obtained as well as a summary of the energy resolution and kurtosis for the two configurations is displayed on figures 7.15 and 7.16.

We can observe that the loss of spatial resolution has a stronger impact on

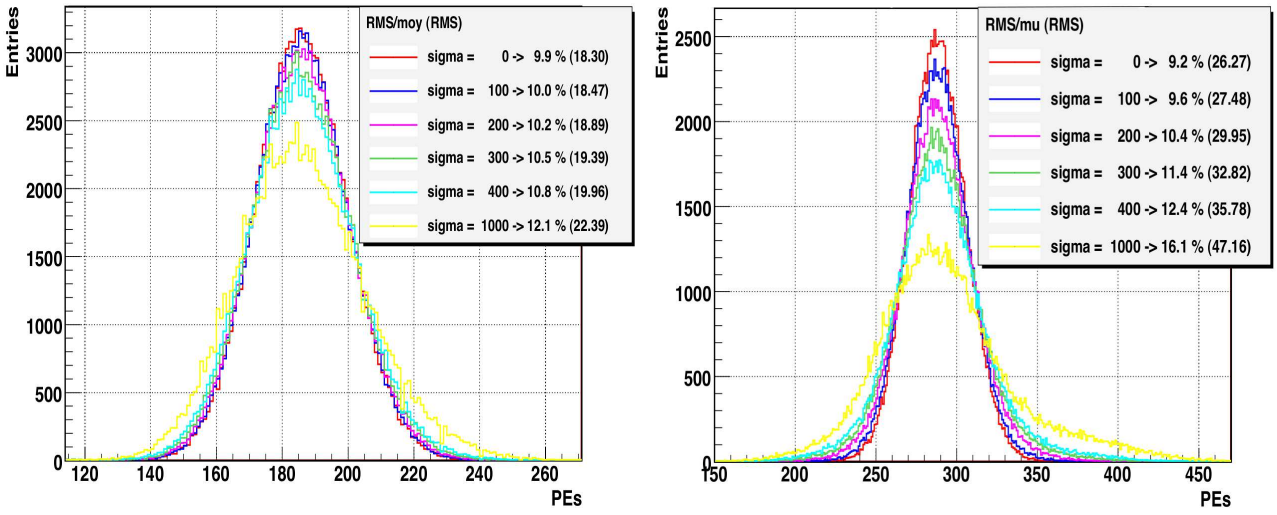

Figure 7.15: Corrected PEs distribution for several spatial resolutions, from a perfect one to 1000 mm, for 1 MeV electrons. The left plot corresponds to the baseline configuration and the right plot to the case with concentrators. The energy resolution degradation is less pronounced for the baseline configuration.

[11]This 1.6% should arise from the large binning and the fact that we don't have taken into account the diagonal bin for the linearization what should be done ideally. The latter can be seen on figure 7.13.

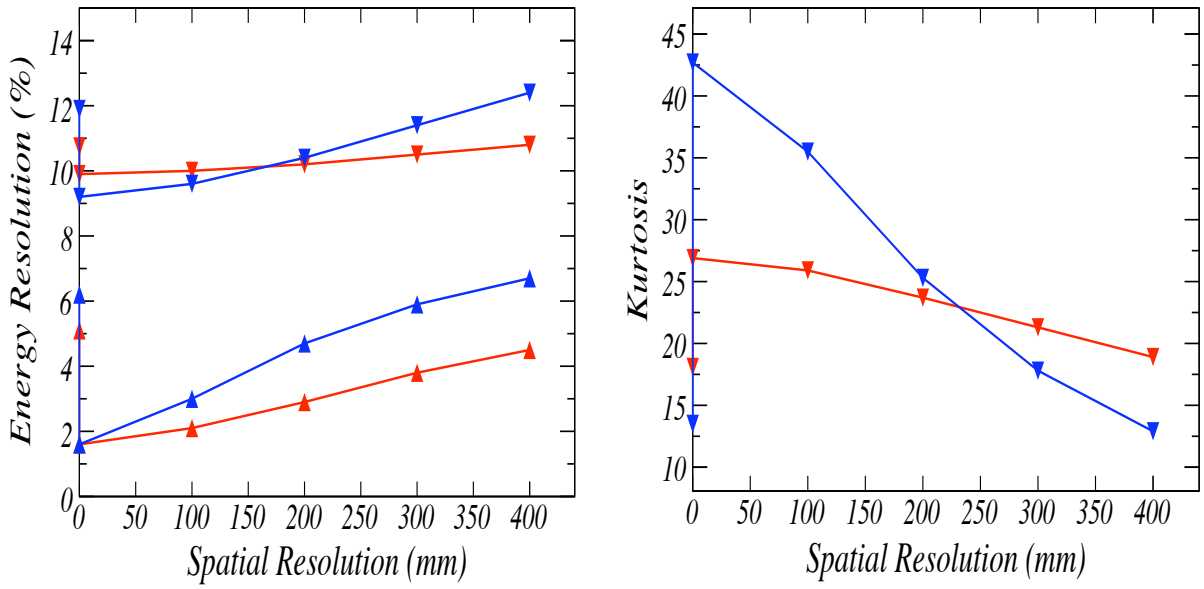

Figure 7.16: Summary and comparison of the energy resolution results with (blue) and without (red) concentrators for several spatial resolutions. The left plot corresponds to the total energy resolution ($\bigtriangledown$) and the non-statistical part ($\bigtriangleup$). The right plot shows the kurtosis value as a function of the spatial resolution. The points on the axis not connected to lines correspond to the values before correction. The configuration with concentrators seems better up to a spatial resolution of $\sim$ 200 mm thanks to the highest level of PEs.

the case with concentrators which is explained by the higher non-uniformity level highlighted previously. The same energy resolution as without corrections is found for a spatial resolution of $\sim$400 mm for the two configurations. The concentrators configuration is better than the baseline up to a spatial resolution of $\sim$200 mm. This limit stands for the two criteria, the energy resolution and the kurtosis. Above this limit, the energy resolution with concentrators degrades quickly. The favorable situation below 200 mm for the case with concentrators is entirely due to the higher number of PEs per event as can be seen by looking at the non-statistical part behaviour. Since the spatial resolution in the experiment should be of the order of 100-150 mm and because the use of concentrators improves it by $\sim$30 mm [169], it seems that this configuration is preferable. We have nevertheless checked this statement with non-localized energy depositions.

Results for a non-localized energy deposition

In this section, we have simulated e^+ of 3 MeV. Positrons are the prompt energy deposition that we will measure for the neutrino signal. The dE/dx of e^+ is roughly the same as for electrons. However, its energy deposition is followed by its annihilation resulting in two back-to-back 511 keV γ that induces a delocalization of the energy deposition. We finally choose an energy of 3 MeV for e^+ because the $\bar{\nu}_e$ induced prompt energy peak is close to 4 MeV and the e^+ kinetic energy is $T_{e^+} \simeq E_{vis} - 1$ MeV.

The results obtained before and after the correction algorithm, with and without

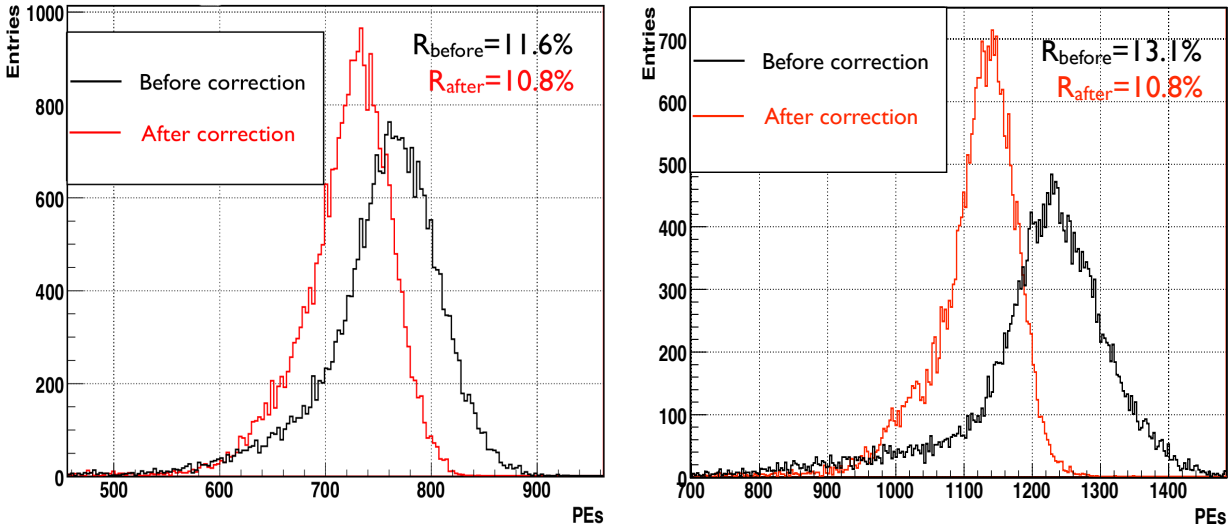

Figure 7.17: PEs distribution before and after the application of the correction algorithm without concentrators (left) and with concentrators (right).

concentrators are displayed on figure 7.17. We first observe that the distributions are no longer gaussian with a tail at lower energies (the determination of the non-statistical energy resolution can thus no more be used). This is mostly due to the fact that we can lose part of the energy of the annihilation γ. The other part due to the non-uniformities can theoretically be recovered after correction, the same energy resolution for the gaussian part of the distribution: 10.8% was found for the two configurations, assuming a perfect spatial resolution. This situation is induced by the delocalization of the deposition. Nevertheless, here again, the effect of the correction is more pronounced for the case with concentrators with a resolution of 13.1% before correction while it was initially 11.6% for the baseline configuration.

The energy resolution we had without correction is obtained for a spatial resolution of ∼400 mm for the baseline, as previously, but ∼350 mm with concentrators.

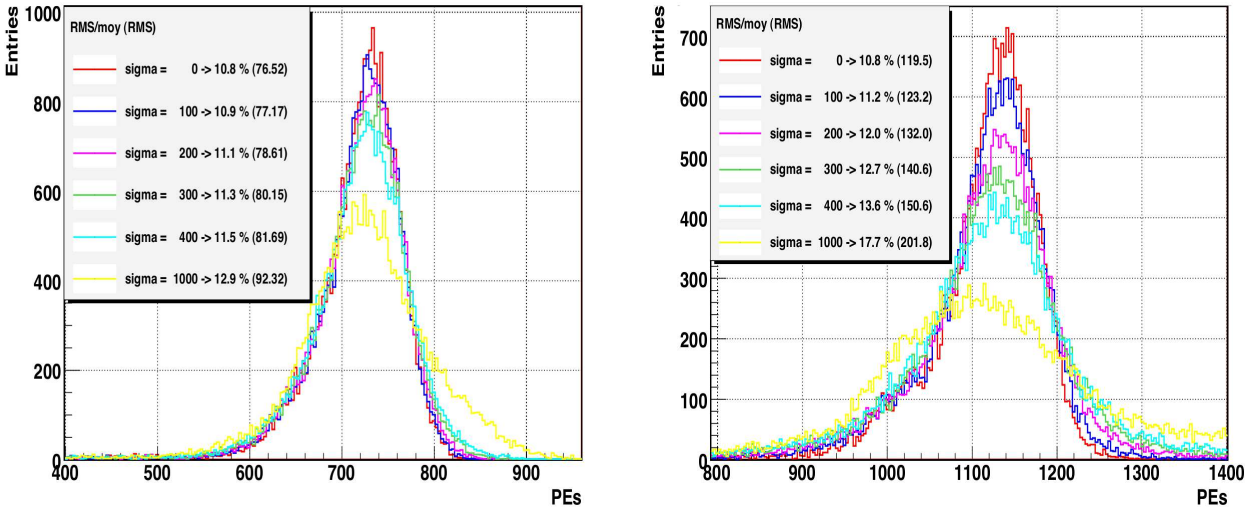

Figure 7.18: Corrected PEs distribution for several spatial resolutions, from a perfect one to 1000 mm, for 3 MeV positrons. The left plot correspond to the baseline configuration and the right plot to the case with concentrators. The energy resolution degradation is again less pronounced for the baseline configuration.

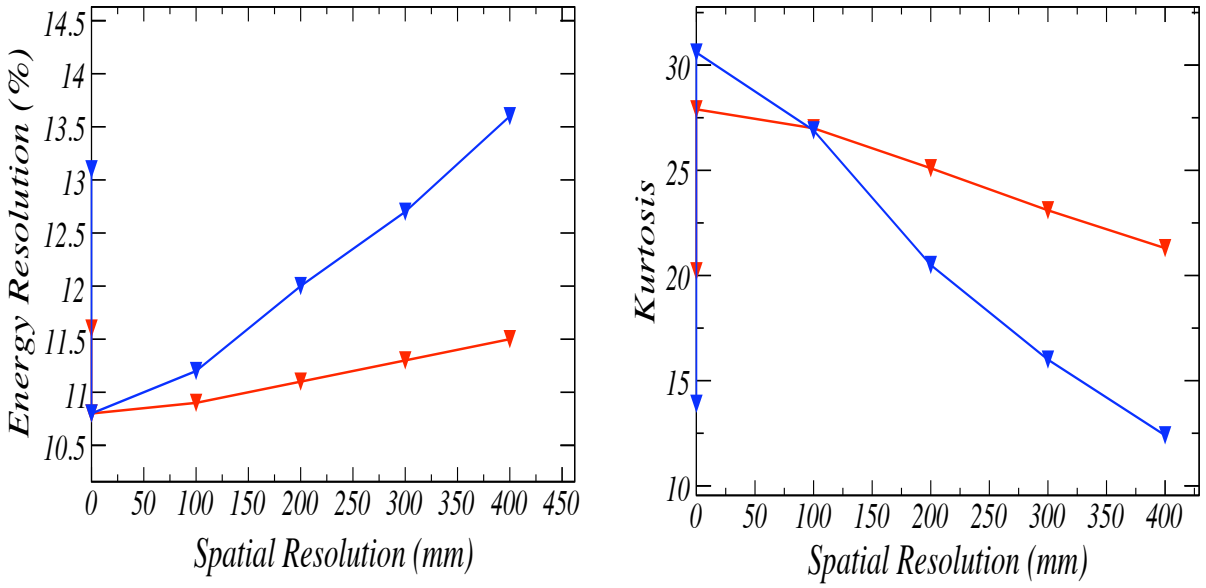

Figure 7.19: Summary and comparison of the the energy resolution results with (blue) and without (red) concentrators for several spatial resolutions. The left plot corresponds to the energy resolution. The right plot shows the kurtosis value as a function of the spatial resolution. The points on the axis not connected to lines correspond to the values before correction. The configuration without concentrators seems better.

It is approximately in agreement with the observations made for a localized energy deposition. However, the energy resolution criterion indicates that the baseline configuration is always better than the concentrator one while the kurtosis indicates rather a spatial resolution limit value of ∼100 mm above which the baseline is better. The energy resolution behaviour can be explained by the fact that at higher energies, the statistical fluctuations have a small impact and thus only the non-uniformities, that are more pronounced with concentrators, matters. It is the same behaviour as the non-statistical criterion for the localized case.

Conclusion

We have shown that with a good spatial reconstruction in complementarity with a good calibration, the developed algorithm can be used to correct the non-uniformity in the detector response. It is valid for the two configurations: with and without concentrators, up to a spatial resolution of ∼400 mm. For localized small energy deposition (1 MeV electrons), the case with concentrators seems better than without up to a spatial resolution of ∼200 mm while this holds for spatial resolution of ∼100 mm for a higher energy deposition that is non-localized such as 3 MeV positrons. By looking more closely, it appears that for the localized case, the non-statistical part of the energy resolution due to the non-uniformities in the response, is always better without concentrators. In addition, for the non-localized case, the total energy resolution is never below the one corresponding to the concentrators case. Furthermore the degradation of the energy resolution with the loss of spatial resolution is greater with concentrators. It seems thus better not to use concentrators even if they increase the light collection and improve the spatial reconstruction. At the end of the year 2008, it was decided not to use light concentrators in DC. Besides, studies have been performed to achieve the best uniformity possible in the detector response [170]. The PMTs configuration have been changed as well as their orientation. The configuration consists of 4 rings of PMTs on the top and bottom at radii 650, 1200, 1750, and 2300 mm, plus 10 rings on the sides at the following Z coordinates: ±250, ±750, ±1250, ±1750 and ±2250 mm. The PMTs on the lid and floor are pointed at the center of the target, and the PMTs on the side are pointed according to the equation $\theta = 90° + (0.0151°/\text{mm})Z$. The new detector response map for 1 MeV electrons is displayed on figure 7.20. One can see that the non-uniformities are now limited to -5%/+8% in the γ-catcher.

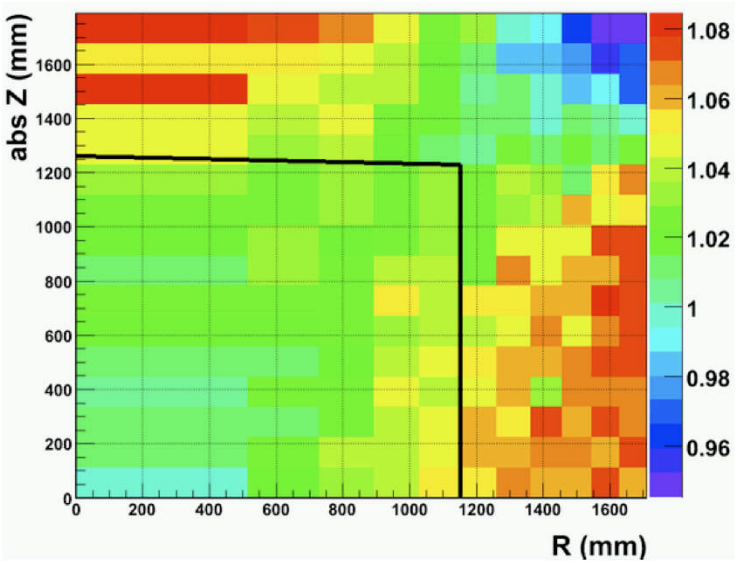

Figure 7.20: New relative detector response map to 1 MeV electrons [170]. The black line is the target/γ-catcher boundary.

7.2.2 Towards a digital trigger ?

As highlighted in section 5.2.3, the relative difference in detection efficiencies between the two Double Chooz detectors should be below $\sim 0.5\%$. Changes in the detectors response will change the ratio and affect the sensitivity (cf. section 4.1.1). It is thus of primary importance to monitor the detectors response with frequent calibrations. Another complementary solution is to monitor the individual PMT signal rate with discriminators, this system is called 'PMT rate monitor'. It would give information on changes in the PMT gain (from high voltage, magnetic field, PMT aging...) but as well on changes in the scintillator response and the electronics. The idea has been proposed to use a trigger based on the number of PMTs hit in the event, rather than on the total number of PEs. This new trigger is named 'digital trigger' while the trigger based on the number of PEs is called 'analog trigger'. Its advantage would be a monitoring of the scintillator response independent of the electronics readout[12], which would ensure the precision of the detector with an additional crosscheck.

As has been shown in the previous section, the detector response is dependent on the location of the energy deposition that has an impact on both types of trigger. As a function of the energy deposition radius, the number of PEs increases while we observe a decrease of the number of hit-PMTs. The figure 7.21 displays the

[12]This statement is valid only at low energies since the number of hit PMTs is limited to the total number of functioning PMTs.

number of hit-PMTs and the number of PEs for 0.5 and 1 MeV electrons simulated uniformly in the detection volumes (The choice of the electron energies was driven by the possible e^+-like readout threshold where 0.5 MeV is the baseline). We observe that the closer to the lateral PMTs, the higher the number of PEs be-

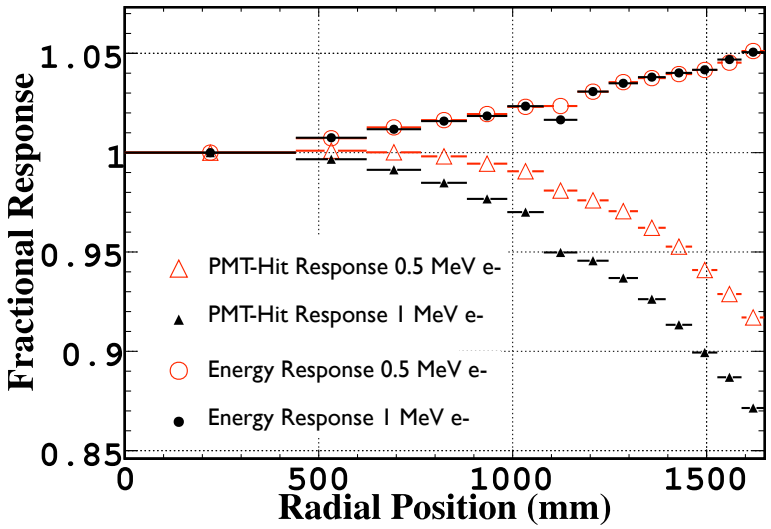

Figure 7.21: Detector response in terms of the number of PEs (analog trigger) and the number of PMT hit (digital trigger) as a function of the radial position for 0.5 and 1 MeV electrons simulated uniformly in the target plus γ-catcher according to their volumes.

come. It is due to an increasing effective photocathode coverage entirely caused by the close PMTs. This observation, together with more scintillator to cross for the photons to reach the PMTs at the opposite, explain why the number of hit-PMTs decreases. Furthermore, we observe that the energy estimation variation with the radial position is small for the analog trigger unlike the digital trigger.
In this work, we have studied the efficiency and energy spread of different types of trigger as a function of the radial position. The purpose was to assess whether the addition of a digital trigger can improve our triggering logic.

Triggers efficiencies and spreads

In this section, we have investigated the analog and digital trigger efficiencies as a function of the radial position as well as AND/OR combinations of those two triggers. In the previous section, we have shown that the number of PEs and the number of hit PMTs have antagonist behaviour as a function of the radial position: the number of PEs is increasing while the number of hit PMTs is decreasing. Thus

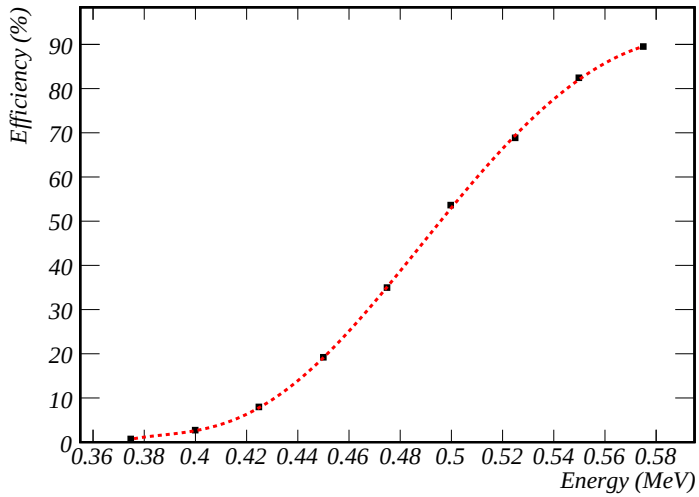

Figure 7.22: Plot showing the model with a sixth degree polynomial function of the analog trigger efficiency evolution as a function of the energy in the first bin. The non-linear parts are due to the tails of the gaussian distribution of the number of PEs.

the reference simulation location for this study was the center for the analog trigger, which is based on the number of PEs, and $\sim$ 30 mm away from the γ-catcher acrylic (x=z=0 mm, y= 1670 mm) for the digital trigger which is based on the number of hit PMTs[13]. We have simulated 0.5 MeV electrons at these locations and taken the mean number of the PEs and hit-PMTs distribution as the reference. We respectively obtain $\sim$50% triggering efficiency for a threshold of 91 PEs and 74 hit-PMTs. Then we have simulated electrons of several energies: from 375 keV to 575 keV with a 25 keV energy step. This has allowed us to model the trigger efficiency in each position bin as a function of the energy, an example is displayed on figure 7.22. Figure 7.23 displays the results obtained for a 50% efficiency in each radial position bin.

We observe that the analog trigger shows an efficiency that is the less position-dependent whereas the digital one has higher efficiency. It is in agreement with the expectations from figure 7.21. The analog AND/OR digital triggers (AND/OR) show an intermediate behaviour with the OR trigger being less position-dependent while having the lowest energy requirement.

From the model, we can extract the energy spread that corresponds to the energy interval from 25% to 75% trigger efficiency. It is plotted as a function of the

[13]In the liquid scintillators, a 1MeV electron loses its energy in roughly 10 mm [168]. By simulating at 30 mm away from the acrylic, we want to avoid the light losses due to non yet shifted light (cf. section 7.2.3).

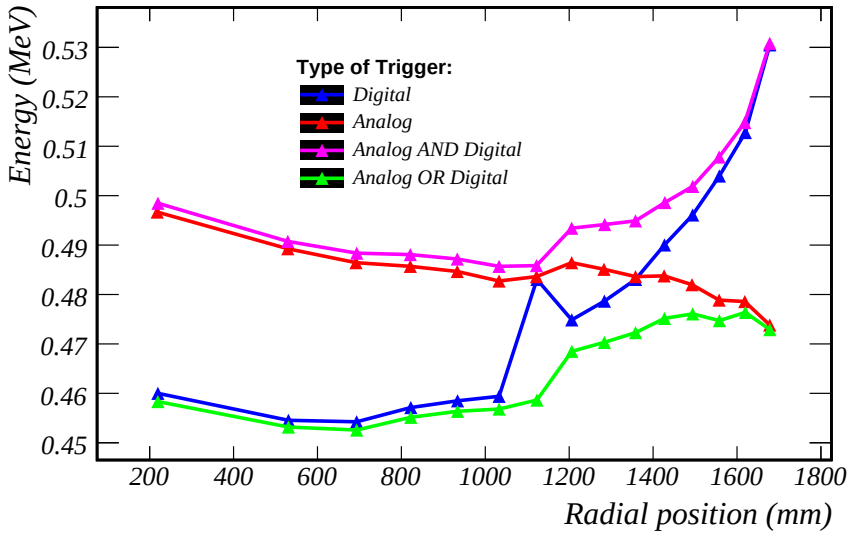

Figure 7.23: Evolution of the energy needed to have a 50% trigger efficiency as a function of the radial position for different types of trigger: digital in blue, analog in red, analog and digital in purple and analog or digital in green. The analog trigger in the first bin is below 0.5 MeV since it includes all the events with a radius below $\sim$ 360 mm with a higher number of PEs. The same stands for the digital trigger, in the last bin we have events with less hit-PMTs implying an energy above 0.5 MeV.

radial position on figure 7.24. The highest the energy spread the better for the efficiency stability. However, a position-dependent spread would imply a different efficiency following the location of the energy deposition which is not acceptable. The highest spread is for the digital trigger while the lowest is for the analog trigger explaining the small energy decrease to reach the same efficiency as in the center. The AND/OR triggers have again intermediate values. However, here the digital and AND triggers have the highest variation with the radius while it is moderate for the OR and analog triggers. The most favorable situation seems to be for an OR trigger which exhibits the highest spread and the lowest variation.

Conclusion

The analog trigger based on the number of PEs in an event is a robust way of triggering thanks to the detector design (i.e. the detector uniformity, cf. figure 7.20). The energy spread between 25% and 75% efficiency is the lowest (implying the highest dependence on the scintillator changes) but remains stable as a function of the radius providing similar efficiencies as a function of the radial position. The digital trigger based on the number of hit PMTs has an opposite behaviour with

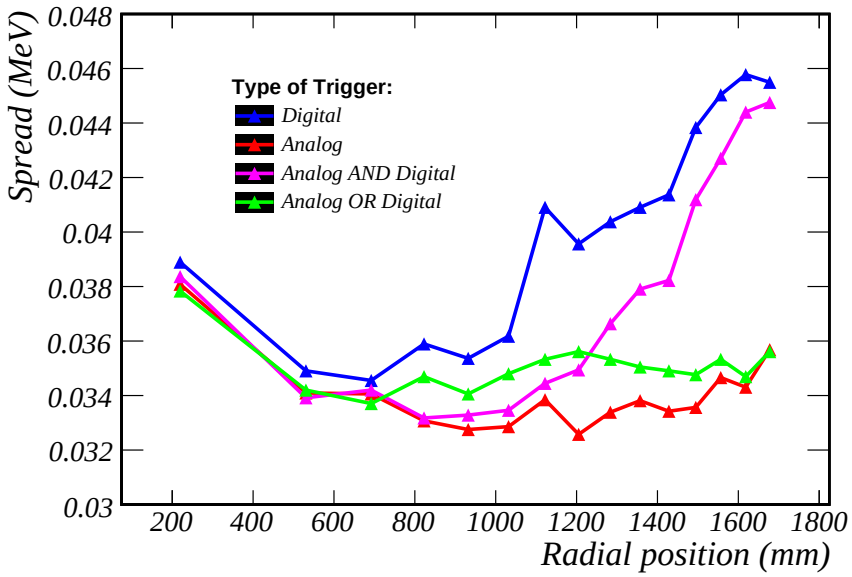

Figure 7.24: Evolution of the energy spread between 25% and 75% trigger efficiency as a function of the radial position for different types of trigger: digital in blue, analog in red, analog and digital in purple and analog or digital in green. The analog trigger shows the lowest energy spread. One looks for the highest and the most stable energy spread.

respectively a slowly changing number of hit-PMTs for a given position as a function of the energy and a strong response gradient in the γ-catcher. However, it seems that a favorable situation arises when using the analog and digital triggers with an OR logic. The efficiency is the best of the tested configurations with a small variation and moreover, the spread is the most stable with a greater value than the analog trigger. Nevertheless, it has to be noticed that the calibration needed for the digital trigger is more difficult than for the analog one.
This work was carried out when some DC colleagues were asking for a financial support and no money was given for the PMT rate monitor. However the number of PMTs hit in an event of low energy can be used for monitoring and energy determination crosschecks.

7.2.3 Light yield and different scintillator time responses

The target and γ-catcher liquid scintillators have different compositions. They were tuned in order to have the same light yields (same amount of light in response to a deposited energy), the same densities but different time responses as we will show in the next section. The background e^+-like events tend to interact more in

the outermost part of the detector while the $\bar{\nu}_e$-induced e^+ signal is uniformly distributed in the target and its boundaries. Thus different scintillator time responses in target and γ-catcher could be useful to tag and study background events for a better experimental sensitivity. I report here a work carried out with Dario Motta at CEA/Saclay in order to match the scintillator light yields while maximizing the difference in the time responses.

Light production and time response

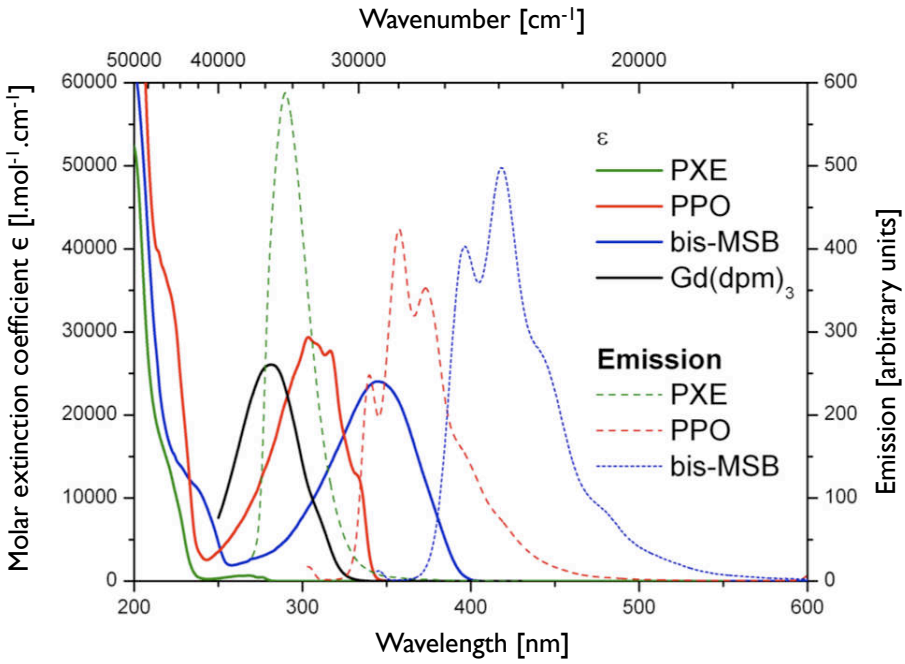

Figure 7.25: Measurements of the absorption and emission spectra of the different components of the target and γ-catcher scintillators [172].

The target and γ-catcher liquid scintillators are both composed of dodecane, PXE, PPO and bis-MSB (see section 5.2.2). The mixture of dodecane-PXE constitutes the solvent and is therefore the most abundant whereas PPO and bis-MSB are respectively the primary and secondary solutions with very small concentrations. In both liquids, the light production path following an energy deposition is (see figure 7.25):

- PXE, that is an aromatic molecule, gets excited or ionized by the energy deposition. This molecule possesses delocalized electrons that absorb energies of the order of 0.1-1 eV corresponding to an absorption spectra in the ultraviolet

radiation region. A shift between the absorption and emission spectra avoids the absorption by PXE of its own emission and allows an energy transfer to PPO (see section 8.2).

- PPO (fluor) gets energy from PXE by radiativeless processes. It is mainly a long range dipole-dipole coupling depending on the PXE emission and PPO absorption spectra.

- The energy radiated by PPO is absorbed by bis-MSB (fluor) that reemits subsequently in the wavelength corresponding to the PMTs quantum efficiency resulting in the energy deposition detection.

The Gd-complex present in the target but not in the γ-catcher is responsible of light quenching. Indeed part of the PXE energy is transmitted to Gd, being lost for detection. This would have resulted into a smaller light yield for the target if the PXE concentration had not been lowered in the γ-catcher. Meanwhile, to match the densities, a mineral oil with a higher density was used. From this configuration, it appeared that a decrease of the PPO concentration would give rise to different time responses for the two liquid scintillators. Indeed, there are fewer PXE molecules to absorb the energy deposited and moreover, there are fewer PPO molecules to which transfer the energy. At the time this work was carried out, no final scintillator formula was developed and we choose to work with a sample having 4% PXE and 2 g/L of PPO showing great differences between the target and γ-catcher scintillators time responses (cf. fig. 7.26) while having a light yield comparable to the target one. From model calculations, it was expected to have a light yield much lower (about 10%) for the γ-catcher and thus the work consisted in trying to make accurate measurements to ensure similar light yields.

Light yield measurements

The absolute light yield of scintillators is hard to obtain. Since the light is detected by the PMTs, there is actually a convolution of the scintillator response, the light propagation and detection. Consequently, we performed relative measurement of the γ-catcher sample with respect to a target sample . For the measurements, the liquid scintillators were put in a 10 cm long quartz cell coupled at the extremities with two PMTs by using silicone. Quartz is transparent and compatible with the liquid scintillators and hence no reaction will affect the scintillator properties. Furthermore, the coupling process ensures that no photons will be lost due to the

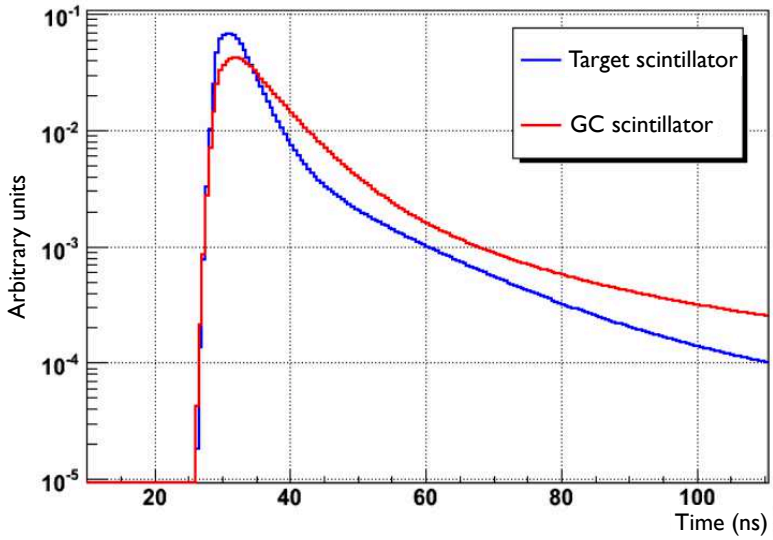

Figure 7.26: Target and γ-catcher scintillators time response [171].

passage in air that has a higher refractive index than quartz. The cell and the PMTs were mounted on a rail to align them and placed in a box for isolation from the ambient light (cf. fig 7.27).

A source of ^{22}Na which is a e^+ emitter was placed outside the box. One of the two back to back 511 keV γ resulting from the e^+ annihilation was collimated towards the center of the quartz cell while the other one was detected by a NaI inorganic scintillator coupled to a PMT. At an energy of 511 keV, the γ interacts mainly through Compton effect that exhibits an important feature. The energy of the scattered γ E_s is given by:

$$E_s = \frac{E_\gamma}{1 + \alpha(1 - \cos\theta)} \qquad \text{and} \qquad T_e = E_\gamma - E_s \tag{7.5}$$

where E_γ is the initial γ energy, θ is the angle between the initial and scattered γ directions, $\alpha = \frac{E_\gamma}{m_e} = 1$ (with m_e the electron mass) is the Lorentz factor and T_e is the electron kinetic energy.

Since T_e depends on the angle at which the γ has been scattered, another NaI detector was placed at an angle of 120° to detect the scattered γ of energy 204 keV that deposited about 307 keV in the cell[14]. The selection of the signals for the measurements were then based on a four-fold coincidence between the two PMTs

[14]The dependence on θ is through a cosine and thus one should avoid angles around 0° and 180° that have very close values resulting in a not well defined energy peak.

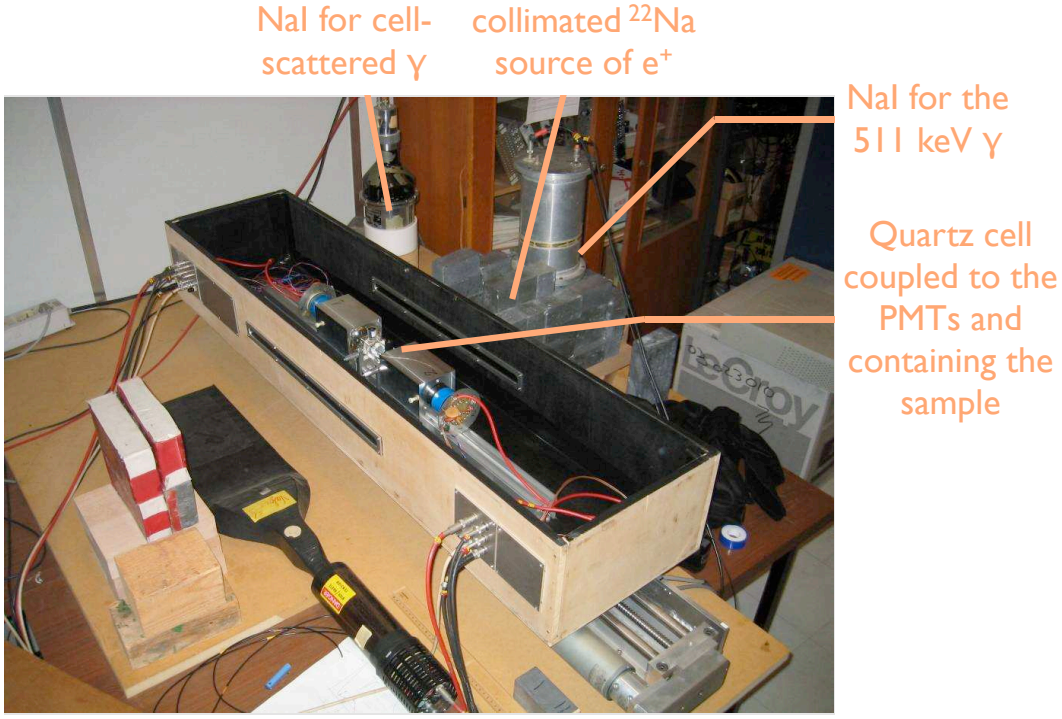

Figure 7.27: Picture of the test bench for the scintillator light yield measurements at CEA/Saclay. We see a quartz cell at the center optically coupled to two PMTs at its extremities. They are mounted on a rail to ensure their alignment. We can see slits in the box to allow the radioactivity source γ to reach the cell. The two NaI for the scattered γ and the 511 keV γ detection are also shown.

and the two NaI[15]. At each coincidence signal, the charge on the PMTs coupled to the cell were recorded to fill histograms for each run. The light yield comparison between the two scintillators was finally based on the mean of the ratio of the charge on each PMT.

First technique of measurement The first measurements were very surprising. Contrary to model predictions, they indicated a GC light yield larger than the target one:

$$\frac{LY_{GC}}{LY_{target}} \simeq 107\% \tag{7.6}$$

with nevertheless a discrepancy going up to 10%. We attributed this effect to a change in the couplings after dismounting for a new sample measurement, and also to PMT gain variations after switching off/on the high voltage (see formula

[15] A coincidence was first required for the two NaI on one hand and the two PMTs on the other hand. Then, since the scintillation times are different for the NaI (about 200 ns) and the cell scintillator (about 2 ns), the coincidence signal of the two PMTs observing the cell was delayed.

of equation 8.2.2). Thus we decided to proceed with the measurements of the two samples at once.

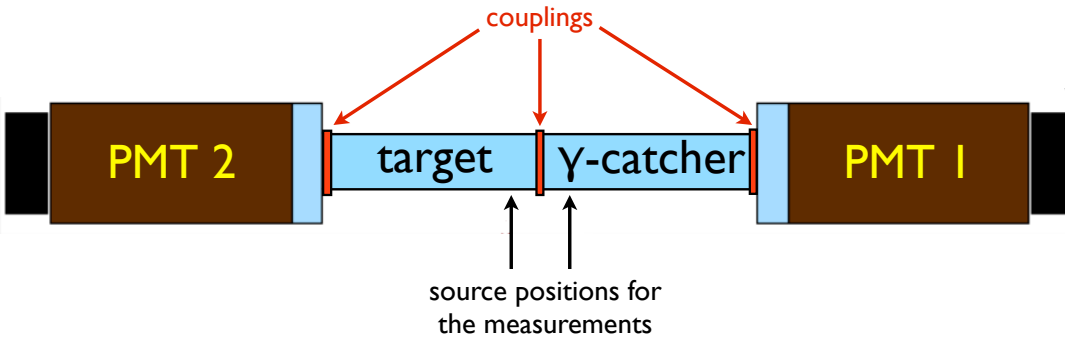

Figure 7.28: Scheme showing the samples set-up for the second measurement technique. There is more coupling but there are set once for the target and γ-catcher measurements. Moreover the PMT high voltage does not have to be switched off. The source position is close to the coupling between the two cells to diminish the solid angle difference of the two PMTs.

Second technique of measurement This technique consisted in setting the two sample cells on the rail for a given measurement as can be seen on figure 7.28. In this configuration, when collimating the source on the target we have:

$$\begin{aligned} Q_1^T &= LY_{target} \times T_1 \times QE_1 \times G_1 \\ Q_2^T &= LY_{target} \times T_2 \times QE_2 \times G_2 \end{aligned} \tag{7.7}$$

and for the collimation on the γ-catcher we have:

$$\begin{aligned} Q_1^{GC} &= LY_{GC} \times T_1' \times QE_1 \times G_1 \\ Q_2^{GC} &= LY_{GC} \times T_2' \times QE_2 \times G_2 \end{aligned} \tag{7.8}$$

where Q is the charge on a PMT, QE is the probability to obtain a PE and G is the PMT gain. LY is the number of photons produced in response to the energy deposition and T is the photon transmission factor (number of photons arriving to the considered PMT). The labels 1 and 2 stand for the PMT1 and the PMT2 from figure 7.28.

No sizable effect on the scintillation light transmission was expected between the target and GC positions since there is no absorption in wavelengths corresponding to the bis-MSB emission spectrum and the space between the two positions (about

6 cm) makes the solid angle effect negligible. Consequently, one can safely assume that $T = T'$ and obtain the light yield ratio through:

$$\frac{LY_{GC}}{LY_{target}} = \sqrt{\frac{Q_1^{GC} \times Q_2^{GC}}{Q_1^T \times Q_2^T}} \tag{7.9}$$

getting thereby rid of the systematics associated to coupling and PMTs gain. We performed two times the measurement and the results obtained were in good agreement (the errors quoted are statistical):

$$\frac{LY_{GC}}{LY_{target}} = 97 \pm 1\%, 96 \pm 1\% \tag{7.10}$$

We decided to dismount the set-up, swap the cells and redo three times the measurement giving (the errors quoted are statistical):

$$\frac{LY_{GC}}{LY_{target}} = 90 \pm 1\%, 92 \pm 1\%, 89 \pm 1\% \tag{7.11}$$

Again the individual measurements were compatible (at about 2% here). Moreover the two sets of measurements were indicating a GC light yield below the target one as predicted by the model. Nevertheless, the measurement discrepancy before and after the dismounting amounted to about 7% confirming the gain fluctuations and especially the couplings as the sources of systematic error.

Conclusion The couplings and the PMT gains were confirmed as the major difficulties towards an accurate measurement of the GC over target light yield ratio tried to be tuned to 1. The couplings of the cell between each other and with the PMTs were obtained manually. They were tightened with screws up to judging by eye that the coupling was efficient. An upgrade of the test bench was envisaged with the immersion of the two samples in a bigger open quartz cell containing a liquid whose refractive index matches the quartz one. Furthermore the PMTs high voltage was quite old and it was decided to change it. Unfortunately, D. Motta was forced to interrupt his activity and then we stopped these measurements. The same measurements were performed in another group of the collaboration. They used a ^{137}Cs source of 662 keV γ put in a box with the scintillator sample to characterize coupled to a PMT. The energy of the scattered γ was selected thanks to a PMT coupled to a NaI detector. The signal was selected by coincidence between the two

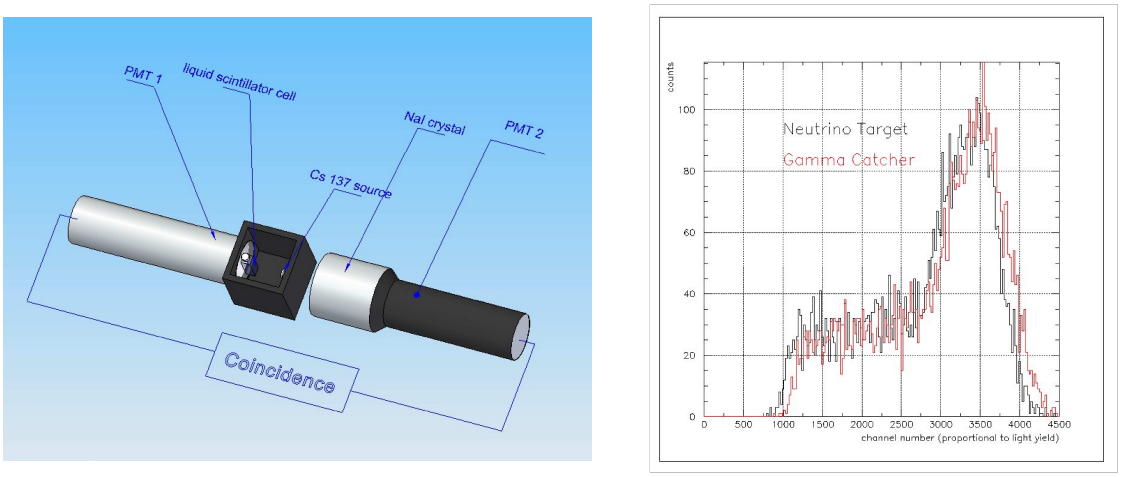

Figure 7.29: Left panel: Set-up for the light yield measurements at MPIK, Heidelberg (Germany). Right panel: example of the charge obtained on the PMT measuring the light output for the target and GC samples [172].

PMTs (see figure 7.29). They performed five measurements and the results were:

$$\frac{LY_{GC}}{LY_{target}} = 97 \pm 2\% \tag{7.12}$$

These results were in agreement with those we found and thus 4% PXE and 2 g/l PPO has been taken as the baseline for the γ-catcher scintillator.

Chapter 8

Spatial reconstruction

It was highlighted in chapter 7 that some backgrounds could be identified through the scintillator time response. The accurate reconstruction of the latter requires to know the interaction vertex of the particle and thus, the spatial reconstruction is of high importance. Furthermore, we showed in section 7.2.1, that the energy determination from the number of PEs needs as well an accurate spatial reconstruction. For these reasons, we came to be interested in spatial reconstructions and develop a new reconstruction based on the time of flight of scintillation photons.
In this chapter, we will first review the motivations for an accurate spatial reconstruction. Then we focus on the informations available to perform a spatial reconstruction and the available reconstructions in the experiment. Finally, we present the ideas on which relies the new reconstruction, the performances of the DC spatial reconstructions and a possible future criterion for the evaluation of the reconstruction accuracy.

8.1 Motivations for a spatial reconstruction

8.1.1 Energy determination

The determination of the energy is crucial in the experiment in order to lower the systematic error, since the selection of the $\bar{\nu}_e$ events relies on energy cuts (see section 4.1.1). Moreover, the primary energy deposition allows to access the neutrino energy that is mandatory to extract the oscillation parameters with the envisaged precision. For these reasons, the energy resolution is of first importance.Furthermore, as showed in section 7.2, the detector energy response depends

on the location of the interaction because of its finite size and cylindrical shape (cf. fig. 8.1) in addition to slightly different light yield for the target and γ-catcher scintillators (see section 7.2.3). It has been shown in section 7.2.1 that the non uniformities in the response can be efficiently corrected in case of an efficient spatial reconstruction leading to an improved energy resolution.

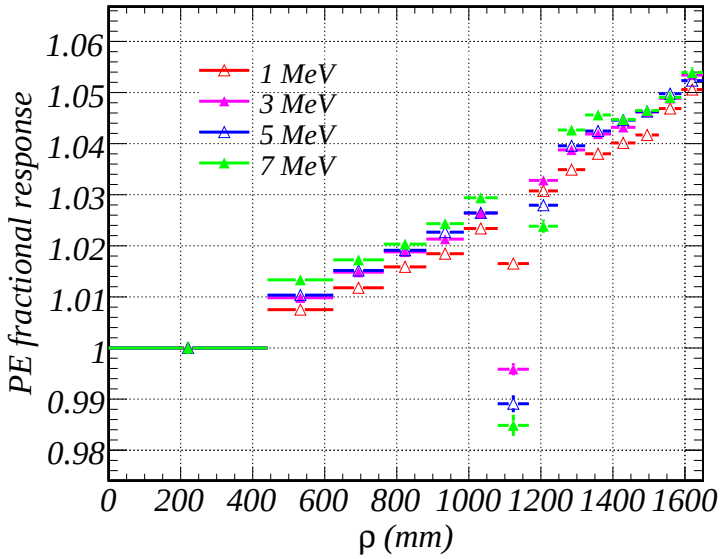

Figure 8.1: PE fractional response as a function of the distance from the detector's center for different energies. The number of PEs is normalized to the first bin value and the bin size is chosen in order to have the same number of events in each bin. One can see that the energy response is dependent on the location of the deposition and the variation is stable as a function of the energy. The drop in the response at $\rho \sim 1150$ mm is due to the target/γ-catcher boundary not allowing the photons to be shifted to the good wavelength.

8.1.2 Background identification

A good spatial reconstruction is mandatory to make background discriminations based on the shape of the scintillator response and the location of the energy deposition. We first describe the way light is emitted in organic scintillators in order to review subsequently the two possible pulse shape discriminations in the experiment. Then we show a possible background identification based on the location of the energy deposition.

Pulse shape discriminations

Scintillator luminescence Organic scintillators contain aromatic molecules that are at the origin of the luminescence. These molecules possess carbon atoms which are organized in a planar hexagonal ring structure. They have double bounds where one bound is ensured by π-electrons that are completely delocalized. These π-electrons can be easily excited leading to luminescence through their deexcitation. There exists different types of luminescence:

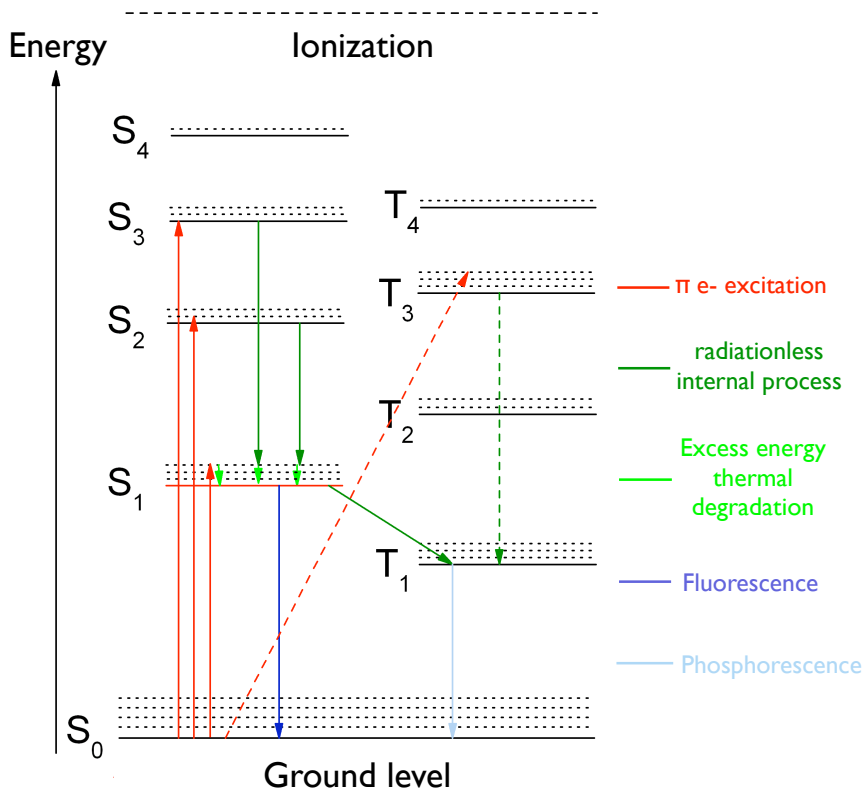

Figure 8.2: Scheme showing the luminescence path in organic scintillators. The slow fluorescence arising from $T_1 \rightarrow S_1 \rightarrow S_0$ transitions and from dimer formation is not explicitly represented.

- Fluorescence, this is the main process of luminescence which takes typically a few ns. In this case, the electron is excited from the ground state S_0 to various singlet (electrons have opposite spins) excited state (S_1, S_2, S_3, ...) and their vibrational sub-levels. By fast radiationless internal conversion and thermal degradation of the excess vibrational energy, the molecule is brought to its first excited state S_1 from which the radiative transition occurs towards any of the ground vibrational states. The fact that the absorption implies

any of the excited states but that the emission occurs only from the S_1 state ensures a small overlapping between the absorption and emission spectra[1].

- Slow fluorescence and the phosphorescence, these processes correspond to a radiativeless population of a metastable state that has an energy lower than S_1. It corresponds to a triplet state (electrons have similarly oriented spins) that can be populated through a spin reversal. This first triplet state T_1 cannot be directly populated because $S_0 \rightarrow T_1$ transitions are spin-forbidden. However, transition from T_1 to S_0 are however possible leading to phosphorescence with a decay time above hundreds of μs. Moreover, if the temperature is high enough, transitions back to S_1 are possible leading to slow fluorescence with typical time of the order of the μs.

- 'Dimer-induced fluorescence', it arises from the collisions of molecules in the excited triplet state T_1 created by recombination after an ionizing radiation. A collision gives rise to two molecules in state S_0 and S_1, the latter giving the fluorescence light. This luminescence has its own decay time determined by the life time of the T_1 state and the rate of $T_1 - T_1$ collisions that is dependent on the ionization power of the incident particle.

Particle identification By neglecting the phosphorescence that involves time responses not included in the event time window in the experiment, the scintillator time response is composed of the fast and the slow fluorescence. Since the fast component is due to π-electrons excitation and the slow component is mainly due to ion recombination in T_1 state, the scintillator time response is dependent on the ionizing power of the particle that interacts. Consequently, particles with a higher dE/dX than electrons will ionize more, resulting in a lower fast fluorescence and a larger slow fluorescence component[2]. Thereby, in an event, the ratio of the slow component over the fast component will identify the particle that has interacted. By having an accurate spatial reconstruction and by using the time of flight of photons that produced a PE in an event, the scintillator time response can be accurately reconstructed. From the probability density functions (PDFs) of the scintillator time response for the different particles: α, β and protons, the technique described above can be applied to try to identify the interacting particle. α has a high dE/dX leading to a promising tagging of the α background (cf. fig 8.3) that

[1] The same vibrational states structure explains the same shapes of the absorption and emission spectra (see figure 7.25).

[2] This effect is called 'quenching'.

will be helpful to lower the readout threshold where the energy of the radioactivity α upon quenching lies (a factor above 10 of quenching). Moreover, fast neutrons deposit energy through protons recoil and thereby it could be possible to study this critical background through protons/β discrimination since protons have as well a high dE/dX, although smaller than α. Consequently, a good spatial reconstruction allowing for a good time response reconstruction is mandatory.

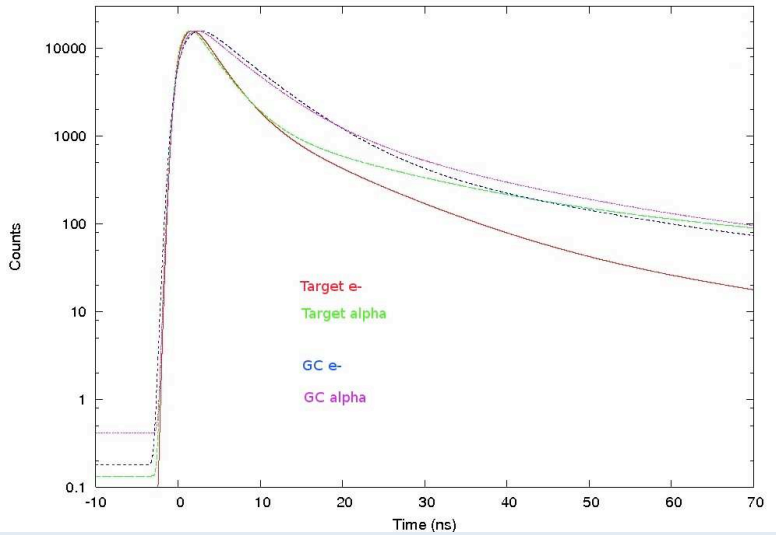

Figure 8.3: Measured scintillator time response probability density function for electrons (e^-) and alphas (α) excitations for the final target and γ-catcher scintillators [173]. One can see that the e-/α scintillator time response PDFs are very different while the difference is small in the γ-catcher due to a small concentration of PXE. However the PDF differences between e^- in the target and γ-catcher are large for the slow component indicating good possibilities in the determination of the volume of the interaction.

Volume identification As described in section 7.2.3, the target and γ-catcher scintillators have been optimized in order to obtain different scintillator response. Besides, measurements performed on the final γ-catcher and target scintillators for α and β indicate that the volume-induced difference is more pronounced than the dE/dX effect (cf. fig 8.3) and hence the two effects can be used in complementarity. Using the fast to slow component ratio of the scintillator time response, the volume of the interaction can be determined. It would possibly result in radioactivity γ background events tagging (see next paragraph). Besides, it has been presented in section 5.2.2 that there exists a spill-in/spill-out effect that does not compensate exactly and will result in a systematic error in the first phase of the experiment.

However, with the volume identification, one can determine the prompt interactions happening in the γ-catcher (spill-in) and hence study it towards an improved error.

Location of the deposition The $\bar{\nu}_e$ candidate interactions occur in the target while most of the natural radioactivity γ comes from outside the detection volumes (from the PMTs, the surrounding rock ...) and will therefore interact most of the time in the γ-catcher as observed in section 7.1.2. Figure 8.4 shows the distributions of the interaction vertex of the $\bar{\nu}_e$ signals and the main sources of natural radioactivity γ (PMTs, liquids, acrylics, the buffer tank and shielding). Using the reconstructed interaction vertex in complementarity with the reconstructed scintillator time response, a large part of the radioactivity γ could be identified. This information could then be used for background studies and/or to give a weight to events in the θ_{13} fit, although not to make event rejections since it would add a systematic error.

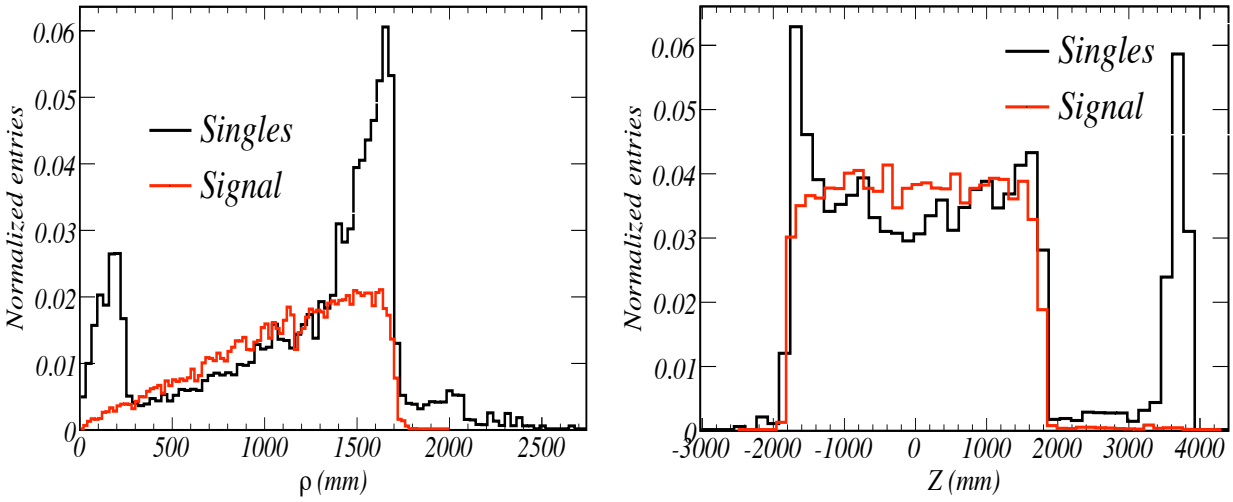

Figure 8.4: Signal ($\bar{\nu}_e$ in target and γ-catcher) and singles (radioactivity γ above 0.5 MeV) interaction point distributions as a function of the radial distance to the center of the detector (left panel) and the Z coordinates (right panel) in the DC far detector. The peaks at small radius and large Z are due to the calibration chimneys while the other one is due to the background coming from outside the detection volumes. They could allow to tag the background, especially the peaks at large radius and small Z since the corresponding $\bar{\nu}_e$ interactions would produce a neutron that could not be captured on Gd.

8.2 Principle of spatial reconstructions

The inputs available for a spatial reconstruction are the time and the charge of pulses on PMTs. To determine the location of the interaction vertex, one can use either the time information as described in section 8.2.1 or the charge information as described in section 8.2.2 or even both. The different reconstructions available in the experiment are reviewed in section 8.2.3.

8.2.1 Time information

The reconstruction of the scintillator time response requires the time of the PE pulses on PMTs and their coordinates. The time of a PE pulse could be either the start time or the end time or the time of the maximum amplitude of the pulse. The latter is the most reliable and is hence the one that is used for the scintillator time response reconstruction. It is achieved through the reconstruction of the emission time of the photons that have hit a PMT in an event through:

$$t^i_{scint} = \left(t_i - TO_i - t_{event} - \frac{d_i}{c_n} \right) \text{ with } t_{event} = t_{first} - \frac{d_{first}}{c_n} - TO_{first} \qquad (8.1)$$

where t_i and d_i (d_{first}) are respectively the time and distance to the interaction vertex of the PMT hit i (first hit PMT). TO_i (TO_{first}) is the time offset of the PMT i (first hit PMT) that is a time delay induced by the electronic and is susceptible to vary from a PMT to another PMT. It can however be accurately measured through calibration with the IDLI (see section 5.2.3). c_n is the speed of light in the scintillator and t_{event} is the time of the interaction in the detector assuming that the first hit PMT is hit by a photon emitted at the beginning of the scintillator luminescence. The distribution of t^i_{scint} represents the time response of the scintillator.
From equation 8.1, one can see that the scintillator response reconstruction has two parameters (the PMTs coordinates are known):

- c_n. The speed of light in the scintillator is a crucial parameter towards an accurate spatial reconstruction since it changes the shape of the time response to be fitted by the scintillator time response PDF. A wrong c_n value induces a bias on the vertex determination. To avoid this effect, c_n will be determined accurately and at different wavelengths[3] by the IDLI calibration devices (see

[3]A PE on a PMT can be induced by photons in a wavelength interval determined by the PMT

section 5.2.3).

- d_i. It is through this parameter that the time response reconstruction is dependent on the interaction vertex location. For a given vertex, the reconstructed time response is compared to the scintillator probability density function which can be determined through calibration.

The minimization of the log likelihood outputs the vertex that fits at best the scintillator time response PDF and the fit function value. The latter can be used to estimate the quality of the fit.

8.2.2 Charge information

The charge information can as well be used to determine the interaction vertex but requires to know the individual PMT gains for correction. The charge information can trivially be used to calculate the charge barycenter giving good indication on the vertex location. Going further requires the knowledge of the absolute light yield of the scintillator LY, the PMT quantum efficiency times the collection efficiency η and the effective attenuation length in the scintillators λ. The expected number of PEs N_i^{exp} on a PMT i is thus given by:

$$N_i^{exp} = E \times LY \times \eta \times \frac{\Omega_i}{4\pi} \times \exp\left(-\frac{d_i}{\lambda}\right) \tag{8.2}$$

where Ω_i is the solid angle of the PMT i which is dependent on the vertex position and d_i is the distance of the vertex to the PMT i.
The observed number of PEs N_i^{obs} can depart from N_i^{exp} in a poissonian distribution of mean N_i^{exp}. One is thus led to write the likelihood for the observed number of PEs in the N PMTs (L) as:

$$L = \prod_i^N \left(\frac{N_i^{exp}(\vec{x}, E)^{N_i^{obs}}}{N_i^{obs}!} e^{-N_i^{exp}(\vec{x},E)} \right) \tag{8.3}$$

The log likelihood minimization outputs in the same time the energy of the event E and the interaction vertex $\vec{x}$.

quantum efficiency. However, the refractive index and thereby the speed of light is dependent on the photon wavelength. The used speed of light is the refractive index corresponding to the integration over the PMTs quantum efficiency spectrum.

8.2.3 Existing spatial reconstructions in DC

The experiment has two spatial reconstructions at hand:

- a 'light' reconstruction called RecoMOSCOW which only uses the time information.
- a 'heavy' reconstruction called RecoBAMA that uses the charge and time informations.

Both reconstructions use only the first hit on each PMT for the scintillator time response reconstruction. The reason is that they are less susceptible of having undergone diffusion or reflection making them lose their information on the vertex and hence bias the vertex determination. These reconstructions are detailed below. During the development of our new spatial reconstruction, an energy reconstruction algorithm called 'CocoReco' has been developed at CEA/Irfu/SPP (Saclay, France) using the charge information as presented in section 8.2.2. It has therefore capabilities for the evaluation of the interaction vertex. Its performances are presented together with the other reconstructions in section 8.3.3.

RecoMOSCOW

The RecoMOSCOW[4] reconstruction uses the techniques described in section 8.2.1 where the scintillator time response PDF is modeled by a Landau function with a standard deviation value of 3.6 (cf. fig. 8.5). This function was chosen because it fits at best the real PDF when only the hits occurring in a 15 ns time window after the first hit in an event are selected. The purpose of this hit selection window is to avoid the reflection and diffusion hits while allowing photons to reach PMTs that are the most remote. The requirements of this reconstruction are only the time offsets TO_i and the speed of light that will be available at the beginning of the experiment.

RecoBAMA

The RecoBAMA[5] reconstruction uses as well the time information but compares the reconstructed scintillator time response to scintillator time response PDFs obtained from simulation and implemented as a function of charge. The hit selection is based on a selection window of 1 μs after the first hit PMT in the event with an effective

[4]This reconstruction was developed by a Double Chooz group from Moscow (Russia).
[5]This reconstruction was developed by a Double Chooz group from Alabama (U.S.A).

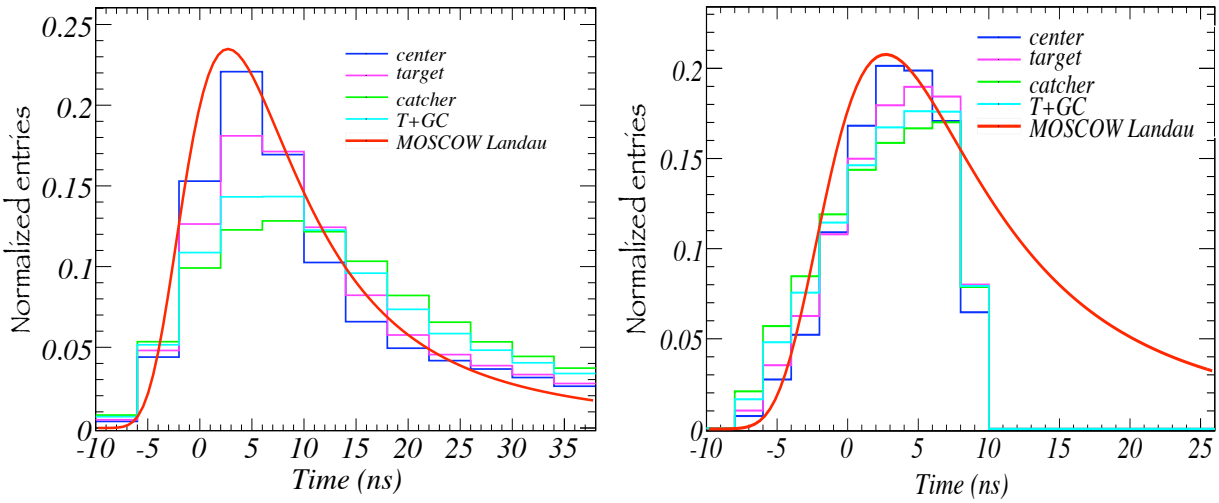

Figure 8.5: RecoMOSCOW Landau function compared to the real scintillator time response (after simulation of the detector response) for four interaction vertices location: the center of the detector, vertices uniformly distributed in the target, the γ-catcher and in both volumes. The right panel corresponds to the case with the 15 ns selection window (see text) and the left panel corresponds to the case without. One can see that the Landau function fits rather well the center and target scintillator time response PDFs but less accurately those including the γ-catcher (hits before 0 are due to the PMTs transit time spread and digitization errors plus a not perfectly adjusted refractive index of 1.48).

refractive index tuned to 1.53. As shown on the left panel of figure 8.5, the PDF can be obtained from calibration. Moreover, by reconstructing the charge on PMTs, one can implement changing PDF as a function of the charge (cf. fig 8.6) that requires nevertheless to know the PMTs individual gain as well as incorporating an accurate optical model to account for the photon propagation in the scintillators. The estimation of the charge can add a new constraint on the vertex location through the technique described in section 8.2.2. To benefit from the full capabilities of this reconstruction, one needs a detailed calibration of the detector that won't be available at the beginning (see section 5.2.3). With Monte Carlo (MC) simulations, it gives however the best performances as it is shown in section 8.3.3.

8.3 A new spatial reconstruction: RecoTOF

Working on finding quality criteria for the spatial reconstructions, we thought about a possible improvement to the RecoMOSCOW reconstruction. It consisted in extracting the most useful hits in an event thanks to the time of flight information

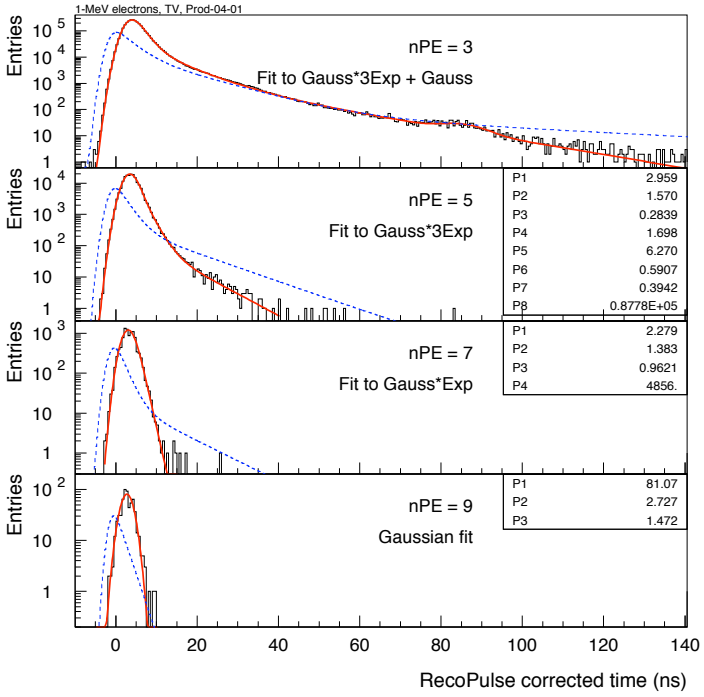

Figure 8.6: Scintillator time response to simulated 1 MeV electrons for different observed charge on PMTs: 3, 5, 7 and 9 PEs [174]. Data is in black, the red line is a polynomial fit and the dashed blue line is a combination of gaussian and exponential functions. One can see that the scintillator time response PDF changes very much as a function of charge. This effect is due to a decreasing number of hit PMTs but a larger charge on individual PMTs as a function of the radius (cf. fig. 7.21).

(TOF) and using a new fitting function for a more robust reconstruction. We developed this new reconstruction algorithm and named it RecoTOF. Afterwards, we evaluated the performances of this new reconstruction and made comparisons with the other reconstructions. Finally, we briefly discuss a possible criterion for the evaluation of the accuracy of the reconstructions and possible improvement to RecoTOF through it.

8.3.1 A better hit selection

As shown in the previous section, the two available reconstructions use a time window whose origin is the first hit PMT in the event and the first hit on each PMT in this time window is used for the fit. In the case of RecoBAMA, the time window is long enough to allow all the PMTs to be hit while it is not the case for RecoMOSCOW. Indeed, the most remote PMTs end up not contributing to the

reconstruction: besides receiving a small flux, they have a small window to account for their observed signal. One could think about enlarging the window, but this lead to more hits that have undergone diffusions and/or reflections leading to worse performances[6].

The idea we developed was a selection of hits based not on their quantity, but on their 'quality', i.e. the amount of information they actually carry for the reconstruction. This was done using the time of flight which allows to get rid of most of the diffusion and/or reflection hits while taking into account all good PMT hits, and especially those which are far from the interaction vertex and have thus a high lever arm on the fit (cf. fig 8.7). From the figure, one can notice that RecoTOF can possibly recover 'good' far PMT hits forgotten by RecoMOSCOW while decreasing the amount of used hits that most probably have undergone diffusions and/or reflections.

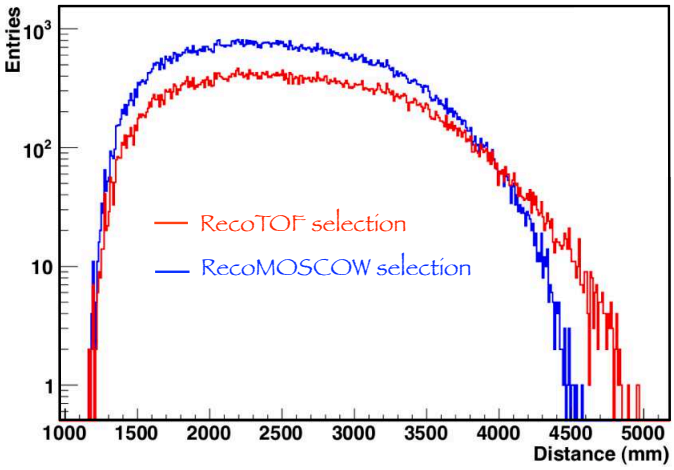

Figure 8.7: Number of selected hits as a function of the distance from the actual interaction vertex to the PMT for 1 MeV electrons simulated in the target and the γ-catcher (the electronic response is not enabled in the simulation). The RecoTOF reconstruction uses here the truth vertex to reconstruct the scintillator response and hits below 3 ns are considered.

[6]The RecoMOSCOW window has been optimized to avoid at best these hits while taking into account as much hits as possible. The RecoBAMA compute directly the PDF from measurements and is thus not concerned by this consideration.

8.3.2 Time selection

Protection against noise

From equation 8.1, it is clear that a misdetermination of the first hit PMT leads to a wrong hit selection and thus to a bad reconstruction. At the level of the detector response, several sources can induce a wrong first hit selection:

- pre-pulses that correspond to photons interacting directly with the first dynode of a PMT instead of the photocathode. They induce a lower transit time to the anode for the photoelectron not taken into account by the time offset correction. The difference in transit time between a pre-pulse and a normal pulse is characteristic of a PMT.
- Dark noise pulses that correspond to pulses induced by thermal emission of electrons of the photocathode. The rate is characteristic of the PMT.
- Pulses induced by baseline fluctuations that have a sufficient charge to be considered as a PE pulse. The rate of such pulses is characteristic of the electronic noise in the read-out electronic chain. This source of bad reconstruction was found surprisingly to be important as can be seen on figure 8.8[7].

Besides, since only the first hit on a PMT is considered for the fitting procedure, these sources of noise are also at the origin of the loss of possibly good hits.
The misidentification of the first hit has a non negligible impact on the reconstruction performances. The example of RecoMOSCOW together with the charge barycenter of all hits that is weakly sensitive to the misidentification are shown on figure 8.9. The charge barycenter is defined as:

$$\begin{pmatrix} x \\ y \\ z \end{pmatrix} = \frac{1}{Q_{tot}} \sum_i q_i \begin{pmatrix} x_i \\ y_i \\ z_i \end{pmatrix} \tag{8.4}$$

where (x, y, z) and (x_i, y_i, z_i) are respectively the reconstructed and hit PMT i coordinates. q_i is the charge of PMT i and Q_{tot} is the total charge in the event.
From these observations, we decided to use the barycenter as the first estimated vertex. Then we reconstructed the scintillator response for electrons simulated uniformly in the target and γ-catcher with and without pre-pulses, dark noise pulses

[7]This problem could be in principle resolved by using the digitization of the Flash-ADCs (also for pre-pulses). Albeit baseline fluctuations have sufficient charge, they have a small amplitude unlike real SPE pulses as can be seen on the right panel of figure 8.8.

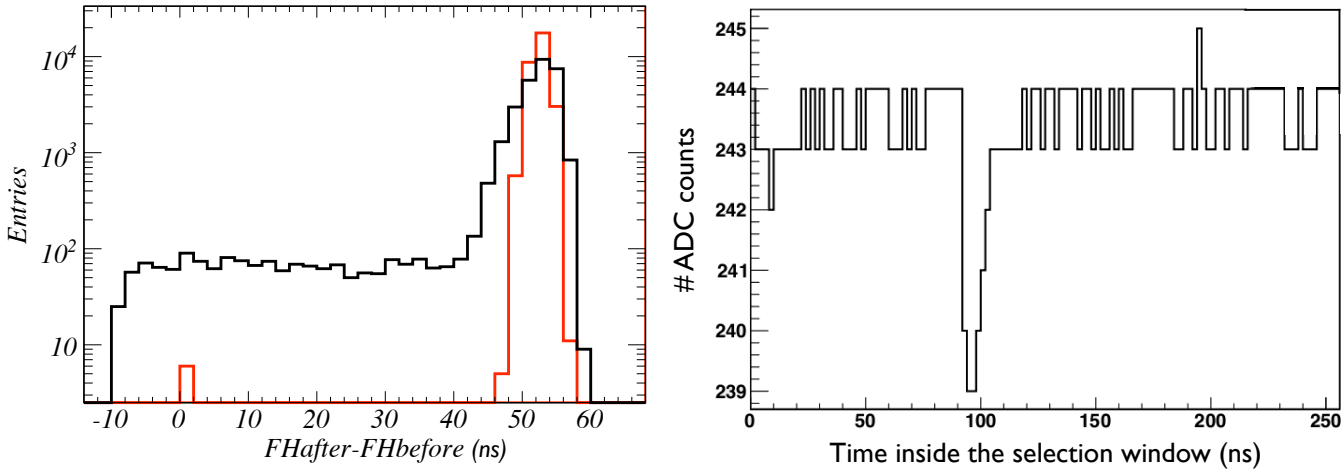

Figure 8.8: Left panel: time difference between the first hit PMT after the electronic response simulation and before. The difference should correspond to the PMT transit time with the characteristic time spread (the time before the response simulation corresponds to the time when the photon reached the photocathode). It is the case for the red histogram that corresponds to a situation with the above sources of misidentification switched on/off in the simulation whereas the black histogram with only baseline fluctuations of typically 0.5 ADC counts enabled in the simulation shows a continuous misidentification (cf. right panel of fig 8.8). Right panel: digitization of the signal on a PMT that induced a misidentification through a baseline fluctuation pulse located at 2 ns.

and baseline fluctuations pulses enabled in the simulation. They are displayed on figure 8.10 together with reconstructed scintillator response in case of a perfect spatial reconstruction. One can observe that the scintillator response is well reconstructed by the barycenter and that a minimum time value for the first hit PMT time can be used to get rid of most of the misidentified first hit PMT. Consequently, we decided to set the following criterion for the first hit PMT:

- the time of the first hit PMT should be in a T_{low} time interval before the maximum of the reconstructed scintillator response.

The default T_{low} value was chosen from the reconstructed scintillator time response with and without the sources of noise displayed on figure 8.10. The intersection of these histograms below their maximum was indicating the time when we have more probability to misidentify the first hit PMT in the event. This technique yielded a time of about 10 ns before the histogram maximum in the two detection volumes. However we actually choose a value lower of 8 ns to ensure the selection of a good first hit PMT at the cost of the loss of good hits.

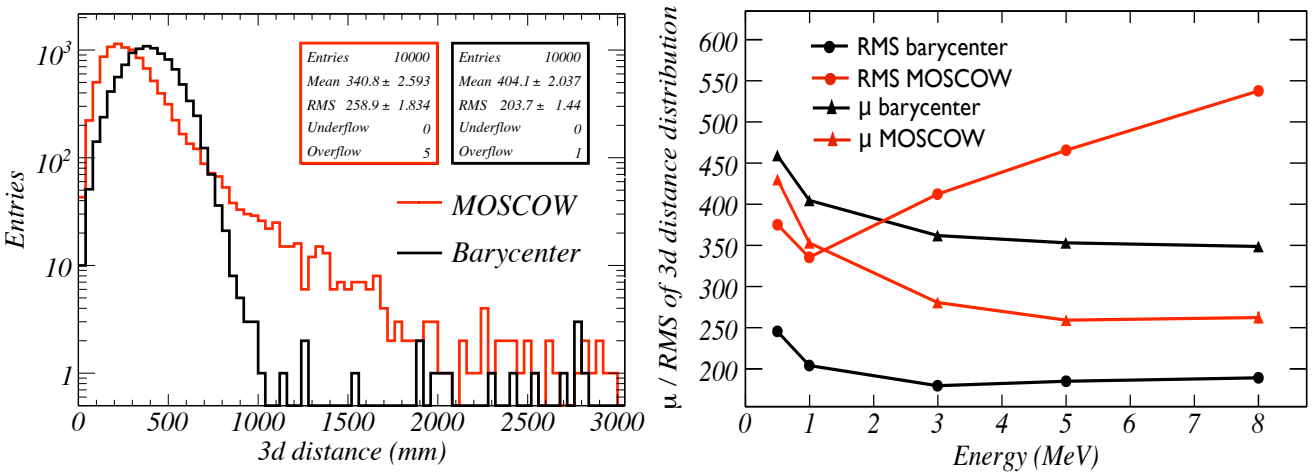

Figure 8.9: Left panel: histogram of the distance of the reconstructed to the actual vertex for 1 MeV electrons simulated uniformly in the target and for RecoMOSCOW in red and the barycenter of all charges in black. The bad reconstructions of RecoMOSCOW (with a distance above 1 m) arises from the non existence of a protection against the misdetermined first hit PMT in the event. It can be seen more clearly on the right plot showing that the mean value of the MOSCOW distribution gets better as a function of the energy while the RMS is worse, whereas it is not the case for the barycenter. It is due to a more accurate reconstruction as a function of the energy for the normal events while the events with a wrong first hit cannot be correctly fitted.

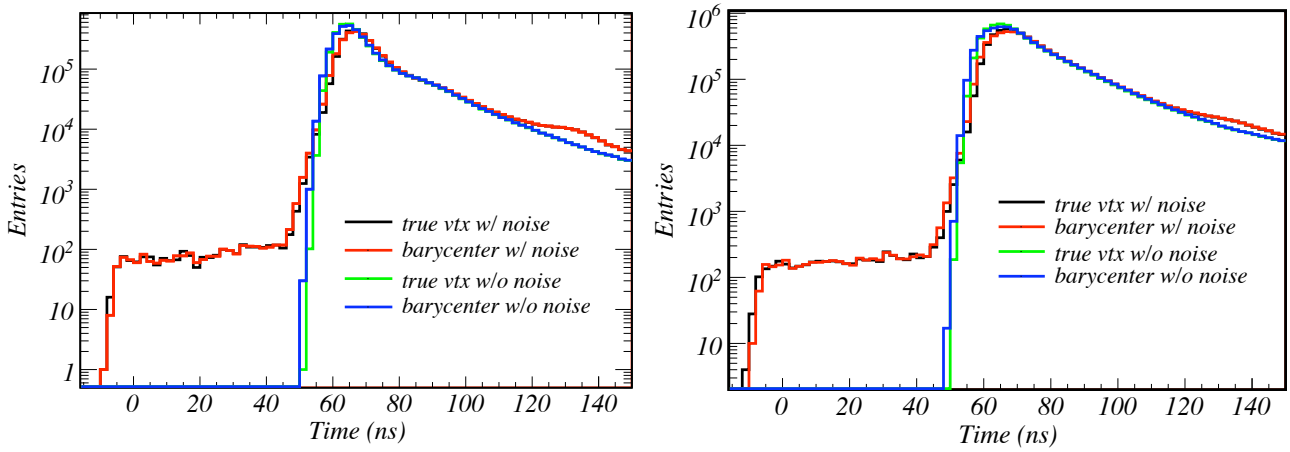

Figure 8.10: Reconstructed scintillator time response using the barycenter or the true vertex for electrons simulated uniformly in the target (left panel) and in the γ-catcher (right panel), with and without noise arising from the read-out electronic response. Even the late pulses have been switched off in the simulation as can be seen at about 130 ns. For this plot, the time offsets have not been subtracted but they all have the same value of 50 ns.

A new fitting function

As shown in section 8.1.2, the scintillator time response is composed of a fast gaussian component, corresponding to the fast fluorescence, and another one decaying with exponential functions, corresponding to slow fluorescence, being dependent on the dE/dX of the particle that interacted. Consequently, we decided to set an upper time selection for the hits in order to try to get only the fast component. The advantages being to avoid most of the diffusion and/or reflection hits, to avoid the slow component dependent on the particle and especially to fit the scintillator response with a gaussian function what requires no parameters[8]. Indeed, assuming a fixed standard deviation value for the fast component, the latter disappears from the minimization of the log likelihood function.
An upper limit on the scintillator time response T_{up} should be set to get the fast component looking like a gaussian distribution. This time is chosen in agreement with the sources of uncertainty in the scintillator response reconstruction that are:

- the use of the barycenter to estimate the true vertex. The mean distance to the interaction vertex is of the order of 400 mm in the target leading to an error of about 2 ns with an effective refractive index of 1.53 in the scintillators.
- the misidentification of the time when a PMT is hit determined from the maximum of the pulse shape. Since Flash-ADCs digitization have a sampling rate of 2 ns, the determination of the time of a PMT hit suffers from an error of 2 ns.
- the transit time spread (TTS) that corresponds to the error on the time a photoelectron takes to reach the anode. Its value is about 1.5 ns.

Theses errors add to the intrinsic standard deviation of the scintillator fast component. To evaluate the intrinsic standard deviation, we simulated 1 MeV electrons in the target and the γ-catcher with the sources of noise switched off in the simulation. We have then reconstructed the scintillator time response using the interaction vertex and fitted the gaussian of the fast response. We found standard deviation values for the fast component of 3.5 ns in the target and 4.6 ns in the γ-catcher (see figure 8.11). These values are the convolution of the scintillator intrinsic standard deviation with the digitization and TTS errors. By adding the error induced by the barycenter, we get a mean standard deviation value of $\sim$4.5

[8]The mean value of the gaussian parameter is taken into account in the fitting procedure through a global time shift to be fitted in the same time as the vertex.

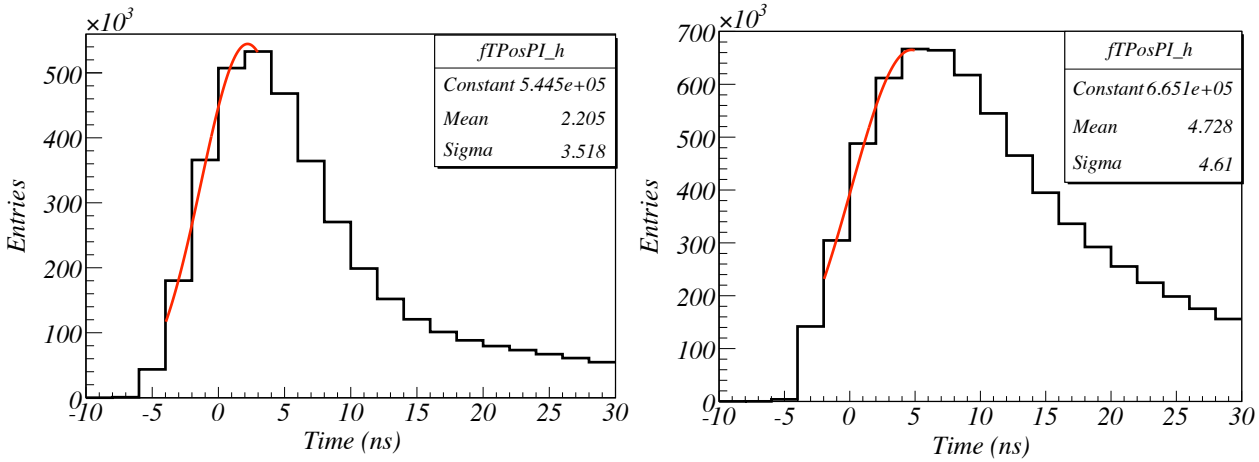

Figure 8.11: Scintillator time response reconstructed by using the actual vertex for 1 MeV electrons simulated in the target (left panel) and the γ-catcher (right panel). The fit of the fast component on the left by a gaussian gives the intrinsic standard deviation value plus the digitization and TTS errors. The first vertex error should be added in order to determine the appropriate hit time selection. It is more complicated to extract the γ-catcher standard deviation value because of the slow component that represents a higher percentage of the fast component (see section 8.1.2).

ns. With a hit selection within two standard deviations of the maximum of the scintillator response, we get a time interval in ns of [-7,11] for the target and [-5,13] for the γ-catcher that agrees well with what one would expect by eye (cf. fig. 8.11). From these observations, we took a default upper time value T_{up} of 12 ns for the hit selection.

Parameters optimization

The impact of T_{low} and T_{up} on the reconstruction performances were investigated to choose the optimal parameters value. We first investigated the T_{up} value, that has a strong impact on the shape of the scintillator response, and, after its optimization, it was the turn of the T_{low} value.

For the T_{up} optimization, we looked at the scintillator time response PDF after the hit selection for different T_{up} values and simulated 1 MeV electrons in the target (cf.fig 8.12). This verification confirmed the default 12 ns value as the good default value. Its skewness is almost equal to zero with a kurtosis close to zero while providing more entries for the fit. Besides, the 12 ns value was later confirmed by looking at the reconstruction performances for 1 MeV electrons as a function of the T_{up} value (cf. upper panel of figure 8.13).

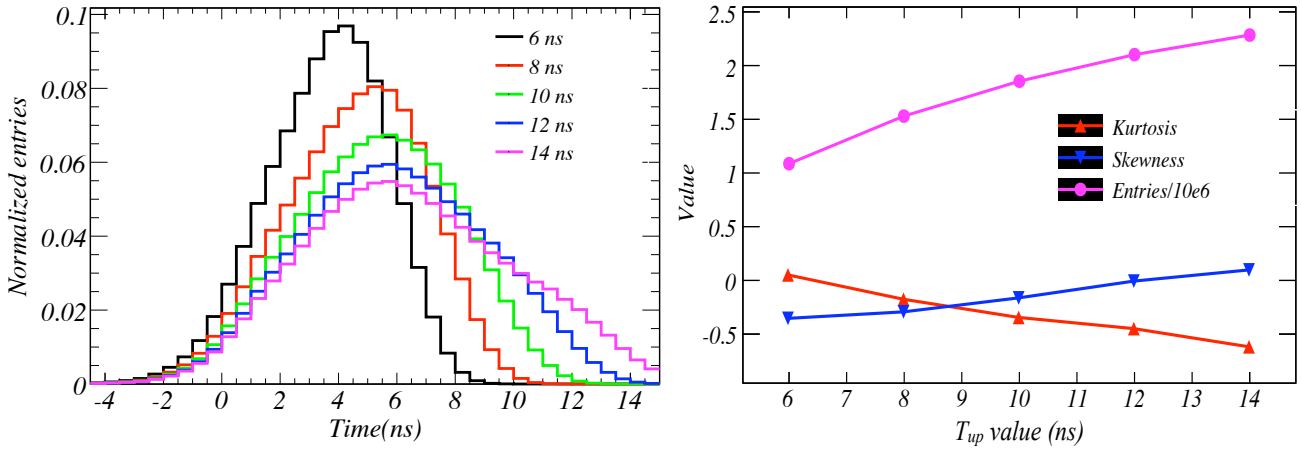

Figure 8.12: Left panel: scintillator time response PDF for different T_{up} values using the barycenter (1 MeV electrons uniformly simulated in the target). Right panel: kurtosis, skewness and number of entries divided by 1×10^6 of these distributions. The PDFs for T_{up} equal to 10 and 12 ns look like the most to gaussian distribution. It is confirmed by the kurtosis and skewness values that are close to 0.

Subsequently, we checked the distance distribution to the actual vertex as a function of the T_{low} value (cf. right panel of fig. 8.13). It showed that the value giving the best performances was 10 ns instead of 8 ns. It was then taken as the default T_{low} value.

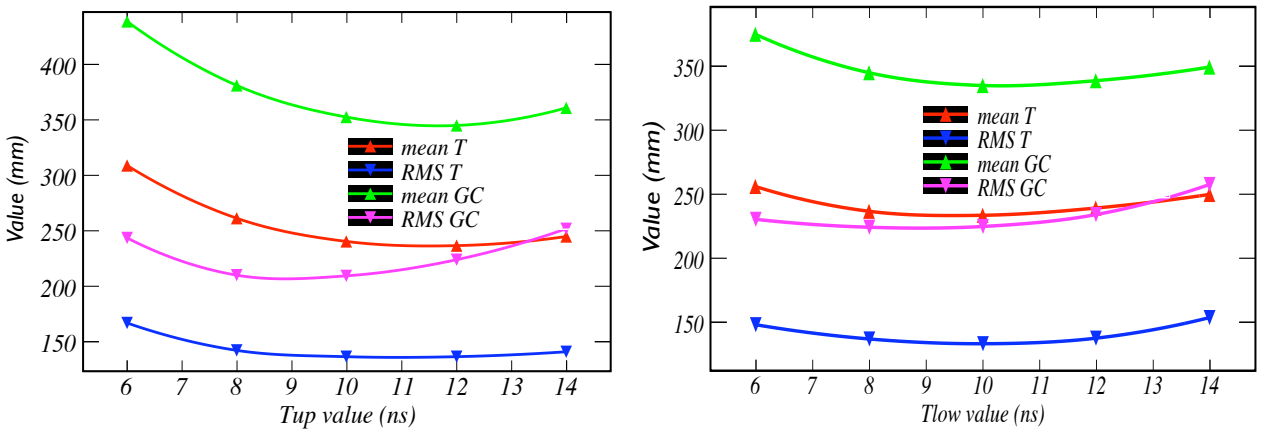

Figure 8.13: Mean and RMS of the distance to the real vertex distribution as a function of T_{up} (left panel) and T_{low} (right panel) for 1 MeV electrons simulated uniformly in the target (T) and the γ-catcher (GC). For the left plot, a T_{low} value of 8 ns is used while for the right plot a T_{up} value of 12 ns is used. The optimal T_{up} value in the target is found to be 12 ns while the results for the γ-catcher indicates that the better performances are obtained for 10 ns. The optimal T_{low} value is found to be 10 ns for both volumes.

8.3.3 Performances comparison

Performances

After the development of the RecoTOF reconstruction, we evaluated its performances in the MC simulation by looking at the mean and RMS of the distance to the actual vertex of simulated electrons as a function of the energy. The performances are displayed, together with those of the other available reconstructions, on figure 8.14.

First of all, one can observe that the performances are improving as a function

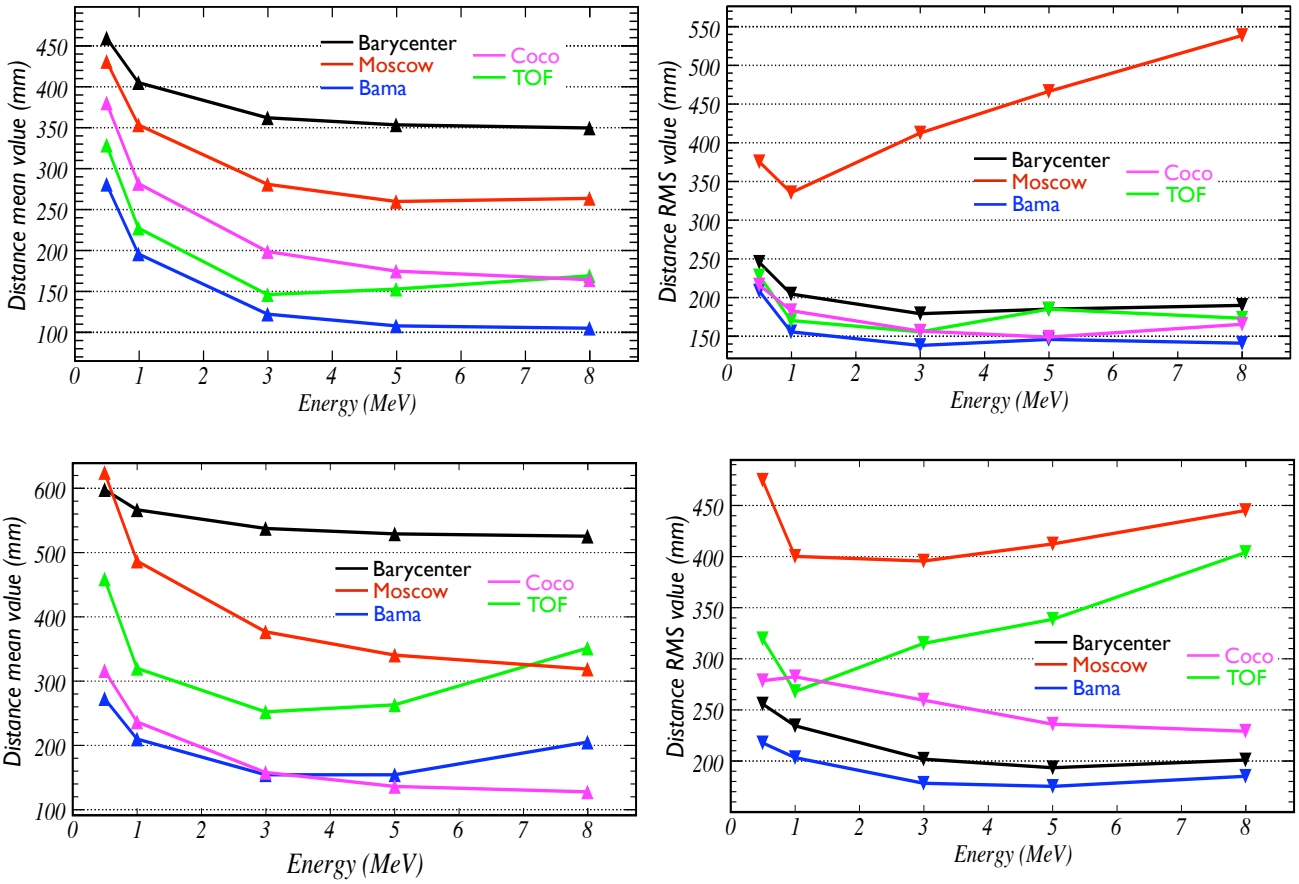

Figure 8.14: Mean (left plots) and RMS (right plots) of the distance to the actual vertex in the target (upper plots) and the γ-catcher (lower plots) for several spatial reconstructions described in the text.

of the increasing energy. It is explained by the fact that we have more hits to perform the fit and thus, we are less sensitive to statistical fluctuations. On the other hand, the reconstructions based only on the scintillator time response reconstruction show a degradation of the performances at high energy. This effect is

due to the fact that the energy deposition is no longer localized and that hence, the scintillator time response becomes the convolution of several individual time responses. It results eventually in an enlargement of the gaussian not taken into account by the fitting function for RecoMOSCOW and the hit selection for RecoTOF with T_{up}. Nevertheless, one can remark that the performances of RecoTOF are very good in the target. They are close to the best performances owned by RecoBAMA up to 3 MeV. One can also notice the good performances of CocoReco and the pathological behaviour of RecoMOSCOW that is not protected against the sources of misidentification of the first hit PMT and should moreover use a fitting function as a function of the charge.
In the γ-catcher, the situation is different from the target. As shown in section 7.2.2, the number of hit PMTs for interactions in this volume is lower than in the target for a given energy. Moreover, a high number of PEs is created on the closest PMTs. These observations result in good performances improving with the energy for the RecoBAMA and especially the CocoReco reconstructions. It has been shown in section 8.1.2 that the scintillator time responses for the target and γ-catcher are different. The fast to slow component ratio is lower in the γ-catcher. This observation in addition to the fact that fewer PMTs are hit, explains why the performances of RecoMOSCOW and RecoTOF are less good than in the target. RecoTOF has its best performances for 3 MeV like in the target, and the same behaviour is experienced by RecoBAMA. One has also to notice that the increasing energy, and thus charge on the closest PMT, allows CocoReco, which uses only the charge information, to be the most accurate.
Besides, it is interesting to look at the RMS of the distributions because, with an accurate calibration, the mean distance can be corrected and only the RMS remains. One can see that RecoBAMA and the charge barycenter have a rather low and stable RMS value as a function of the energy that is almost the same in the two volumes.

Performances with the electronics response switched off in the simulation

To better understand the behaviours of the reconstructions as a function of the energy, we evaluated their performances when the electronic response was switched off in the simulation. This can be seen on figure 8.15. In this case, the CocoReco reconstruction, which uses only the charge information, is not implemented. The RecoTOF and RecoBAMA reconstructions use the number of PEs instead for the

calculations and besides, the RecoTOF T_{up} value had to be adjusted to 6 ns.

The RecoBAMA performances are similar to the case with the electronic response,

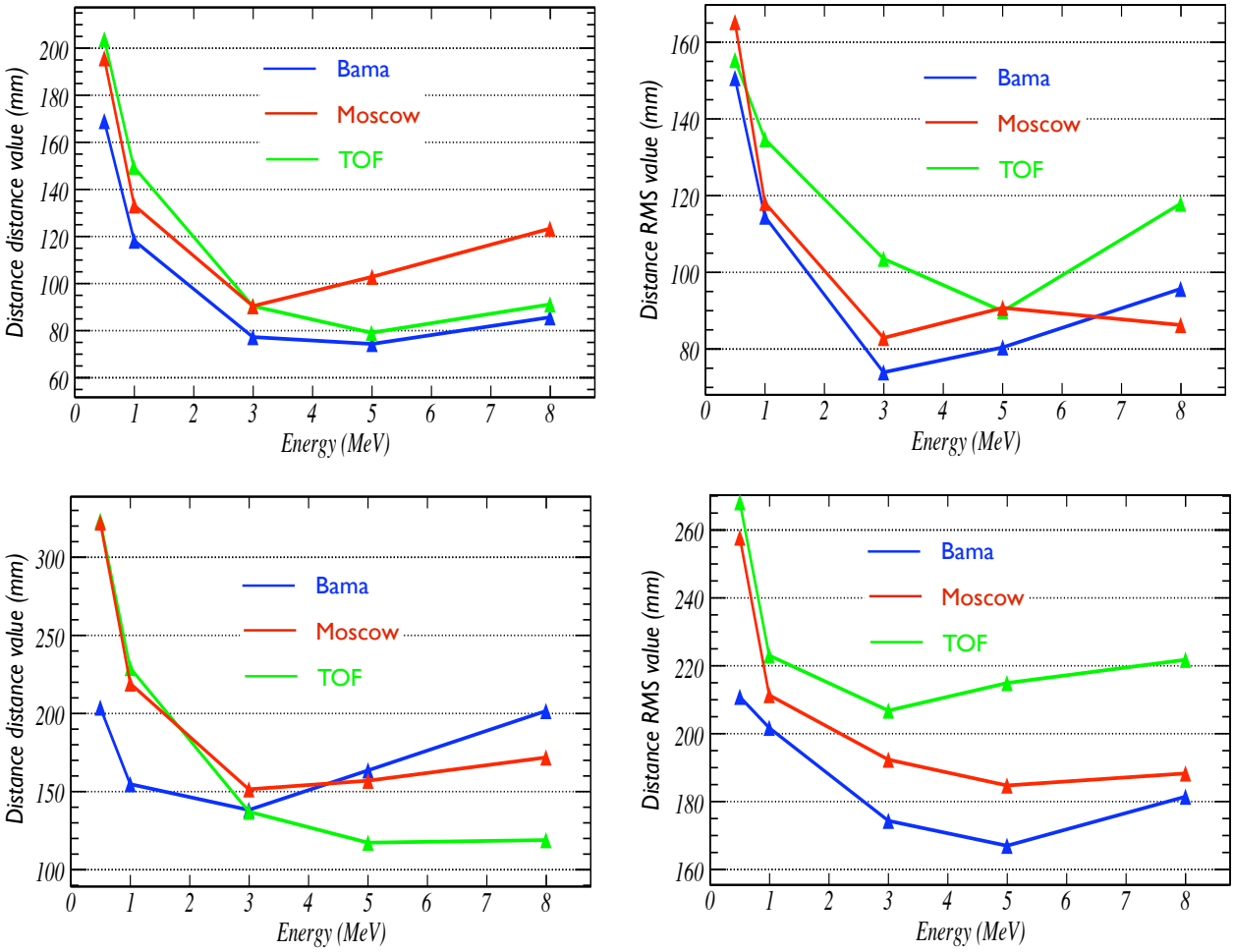

Figure 8.15: Mean (left plots) and RMS (right plots) of the distance to the actual vertex in the target (upper plots) and the γ-catcher (lower plots) for several spatial reconstructions when the electronic reponse has been switched off in the simulation.

showing its robustness and its fine tuning. On can notice also the good behaviour of RecoMOSCOW, that here does not suffer from the sources of noise. The surprise comes from the RecoTOF behaviour. The bad behaviours arising after 3 MeV in the target and especially in the γ-catcher have vanished. When the electronic response is switched off in the simulation, the time of PEs corresponds to the time when the photon reached the photocathode. One can think that the bad behaviours with the electronic response are due to pile-up signals on the PMTs resulting in a misidentification of the time of the PE that is a crucial information for the fitting procedure. It would furthermore explain why the effect is more pronounced in the

γ-catcher where the hit PMTs have a high charge. This suggests that the algorithm could be further improved.

8.3.4 Evaluation of the reconstructions accuracy

As shown in section 8.3.2, the standard deviation of the reconstructed fast component of the scintillator time response is the convolution of the intrinsic standard deviation of the time response plus the sources of error. The errors induced by the digitization of the FADCs and the transit time spread on PMTs have definite values and therefore, a departure of the standard deviation of the reconstructed response from the intrinsic standard deviation plus these two errors will indicate how accurate the reconstruction process[9] was. This statement is valid for all the available reconstructions.

As a consequence, in the RecoTOF reconstruction, one could iterate the reconstruction process with the hit selection being made with the reconstructed vertex and a T_{up} value chosen accordingly. The iteration process would finish with the measurement of a standard deviation corresponding to the intrinsic standard deviation plus the two errors or the measurement of a standard deviation higher after iteration.

The possibility to realize such a quality criteria and the possibility to use it to determine the good number of interations for RecoTOF has to be investigated.

8.3.5 Conclusions and outlook

In this chapter, we have shown that it is important to have a good spatial reconstruction for an accurate energy determination and background reduction, in order to push the sensitivity to θ_{13} to its maximum. Therefore we developed a new reconstruction with a hit selection based on the time of flight. This algorithm called RecoTOF, has been integrated into the Double Chooz software.

The best reconstruction performances are those of another existing reconstruction algorithm, called RecoBAMA, that needs however several calibrations which will not be at hand at the beginning of the experiment. The RecoTOF reconstruction has performances close to RecoBAMA, but it has the advantage of requiring inputs

[9]The standard deviation will be evaluated from a gaussian fit to the left of the maximum of the reconstructed scintillator time response since this part is not contaminated by the slow component.

that will be available at the start of the experiment. From the spatial reconstruction performance in the target at 3 MeV: 150 mm and figure 7.16, one could expect an energy resolution of the order of 10%.
Our reconstruction still has a not well understood behaviour for energy depositions above 3 MeV in both volumes: this requires investigations towards possible improvements.
For now, RecoTOF makes a hit selection using the trivial charge barycenter. Therefore, the accuracy of the latter has a strong impact on the performances. One could think about a little more elaborated first vertex guess by including the attenuation length and possibly including the probability to hit a PMT with the charge observed on it. Another complementary solution would be to make iterations of the reconstruction process with the hit selection based on the newly reconstructed vertex. In addition, it could be interesting to determine the RecoTOF performances with the first vertex being RecoBAMA. It will allow to determine if we can still improve the accuracy on the interaction vertex. Besides, we have seen that some electronics effect can spoil the reconstruction and thus, based on the FADCs capabilities, it could be envisaged to remove some, such as the baseline fluctuation pulses and the pre-pulses whose amplitude is lower than that of SPE pulses.
Furthermore, we suggested a criteria to evaluate the accuracy of the spatial reconstructions using the shape of the fast component of the scintillator time response. It should correspond to a gaussian and from its standard deviation, the inaccuracy of the reconstruction can be inferred. The feasibility has nevertheless to be proved.
Finally, we simulated in the MC only electrons while we will also detect e^+, protons, α interacting in the detector and even γ whose interaction is delocalized. Therefore, the performances of the reconstruction will eventually have to be checked with those particles. This work done, it could be interesting to try to distinguish the backgrounds using the spatial reconstruction.

Chapter 9

Conclusions

The reactor neutrino oscillation experiment Double Chooz aims at measuring the θ_{13} mixing angle with unprecedented sensitivity. Its concept relies on the use of two identical detectors with an increased target mass in order to lower both the systematic and statistical errors. The near detector should be ready for the middle of 2012 while the far detector integration in the renewed laboratory of the past CHOOZ experiment is about to be finished. At the time this thesis is being written, the experiment is in its filling phase while the commissioning has already started. The start of the experiment is expected for November 2010. The experiment will thus have two phases, the phase I when only the far detector will be running and the phase 2 when both detector will take data. The sensitivity, which is the capability to disentangle a non zero θ_{13} value from no oscillations, is $\sin^2 2\theta_{13} \leq 0.058$ for the phase I and $\sin^2 2\theta_{13} \leq 0.03$ for the phase II at 90% C.L. Double Chooz will be the first experiment to shed new lights on θ_{13} since the CHOOZ limit can be reached in less than 3 months. No data were available during my thesis and thus, all the work presented in this manuscript is based on Monte Carlo simulations except the hardware work on the neutrino Flash-ADCs.

The neutrino energy depositions in the detector are transformed into light by the scintillators and changed into electrical signal by the photomultiplicator tubes (PMTs). Their signal is subsequently digitized by the Flash-ADCs that are the core of the acquisition system. They have been chosen so that the acquisition system is free of deadtime. We first performed tests on the VX1721 Flash-ADC card used in the experiment to ensure the card features specified by the constructor. Then, we performed a global test of 66 cards of the phase I with special care given to

the response that should be linear. Eventually, only one faulty card was found and the others showed a very good linearity ensuring no limitation on the energy determination arising from the Flash-ADC cards.

Before and during the far detector integration, we performed several analyses towards improvements to the detector design. This optimization of the detector design was composed of:

- the determination of the radioactivity constraints that some minor components of the detector should satisfy: the sealant between the shielding bars and the paint in the Inner Veto. The purpose was to have a low rate of natural radioactivity γ interaction, that is a background, in the detection volumes. These analyses allowed us to make the choice of the safe components for the experiment.

- An analysis to determine if the use of light concentrators (aluminium cones) attached on PMTs is appropriate for a better energy resolution. The detector has a finite size, which results in an energy determination dependent on the location of the energy deposition (it is called non-uniformities). We found that, as expected, they increase the amount of light for a given energy deposition but at the cost of a higher gradient of non-uniformities. Thus, we developed an algorithm to correct the non-uniformities based on the reconstruction of the interaction location and found that the situation was better without concentrators in general. This effect was due to the non localization of the prompt energy deposition induced by neutrinos.

- The test of a new way of triggering the acquisition system. The original trigger was only based on the charge on the PMTs. This new method consists of triggering on the number of hit PMTs that is also dependent on the energy. The problem was that both are dependent on the location of the energy deposition but in an opposite way. Therefore, we tried combinations of these triggers to determine the best configuration against non-uniformities and possible changes in the amount of light emitted by the scintillator. The outcome was that such a combination would be interesting at low energy and that the triggering based on the charge was satisfying for the needs of our experiment. However, no funds were given for the electronic devices allowing its implementation.

- The tuning of the percentage of the scintillator components for a better back-

ground rejection. Double Chooz has two scintillating detection volumes: the target and the gamma-catcher whose chemical formula are different (the target formula is fixed by experimental needs). In order to have a uniform energy response, the amount of light for a given energy deposition should be the same in the two volumes. From these constraints, we tried to tune the composition of the gamma-catcher scintillator with the purpose of obtaining different time responses, allowing to distinguish the volume where particles interacted. This aim was achieved and now the two scintillators have different time response.

Possible discriminations between the signal and the backgrounds could be made from the location of the energy deposition and from the scintillators time responses as presented above. This will nevertheless require an accurate spatial reconstruction of the events. We worked on developing a new concept of spatial reconstruction based on the time of flight of photons from the interaction vertex and the PMTs. The idea was to try to make a better choice of the hit PMTs in an event. This reconstruction is still under development but shows already promising performances with nevertheless some strange behaviours to be understood. Furthermore, we found a possible criterion for the evaluation of the accuracy of a reconstruction process based on the shape of the reconstructed scintillator time response, whose functioning has however not yet been demonstrated.

Bibliography

[1] E. Fermi. An attempt of a theory of beta radiation. 1 (German). Z.Phys., 88, 161, 1934.

[2] C. L. Cowan *et al.* Detection of the free neutrino. Phys. Rev. Lett., 92, 830-831, 1953.
C. L. Cowan *et al.* Detection of the free neutrino: a confirmation. Science 124, 103, 1956.
C. L. Cowan *et al.* Detection of the free neutrino. Phys. Rev. Lett., 117, 159-173, 1960.

[3] T.D. Lee and C.N. Yang. Question of parity conservation in weak interactions. Phys. Rev. Lett., 1044, 254-258, 1956.

[4] C.S. Wu *et al.* Experimental test of parity conservation in beta decay. Phys. Rev. Lett., 105, 1413-1415, 1957.

[5] C.S. Wu *et al.* Further experiments on β decay of polarized nuclei. Phys. Rev. Lett., 106, 1361-1363, 1957.

[6] M. Goldhaber *et al.* Helicity of neutrinos. Phys. Rev. Lett., 109, 1015-1017, 1958.

[7] L. Grodzins. Measuring the helicity of the neutrino. Neutrino 2010, XXIV International Conference on Neutrino Physics and Astrophysics, Athens, Greece.

[8] G. Danby *et al.* Observation of high energy neutrino reactions and the existence of two kinds of neutrinos. Phys. Rev. Lett., 9, 36-44, 1962.

[9] F. J. Hasert *et al.* Search for elastic muon-neutrino electron scattering. Phys. Lett. B, 46, 121-124, 1973.

[10] F. J. Hasert *et al.* Observation of neutrino-like interactions without muon or electron in the Gargamelle neutrino experiment. Phys. Lett. B, 46, 138-140, 1973.

[11] R. Arnison *et al.* (UA1). Phys. Lett. B, 122, 103, 1983.
M. Banner *et al.* (UA2). Phys. Lett. B, 122, 476, 1983.
R. Arnison *et al.* (UA1). Phys. Lett. B, 126, 398, 1983.
P. Bagnaia *et al.* (UA2). Phys. Lett. B, 129, 130, 1983.

[12] The ALEPH, DELPHI, L3, OPAL and SLD Collaborations. Precision electroweak measurements on the Z resonance. Physics Reports, 427, 257-454, 2006.

[13] Kodama K. *et al.* Observation of tau neutrino interactions. Phys. Lett. B, 504, 218, 2001.

[14] B. Pontecorvo. Mesonium and antimesonium. Sov. Phys. JETP, 6, 429, 1957.

[15] Z. Maki, M. Nakagawa and S. Sakata. Remarks on the unified model of elementary particles. Prog. Theor. Phys., 28, 870, 1962.

[16] C. Giunti and M. Laveder. Neutrino mixing. hep-ph/0310238v2, 2003.

[17] E. Kh. Akhmedov and A. Yu. Smirnov. Paradoxes of neutrino oscillations. arXiv 0905.1903, 2009.

[18] L. Wolfenstein. Neutrino oscillations in matter. Phys. Rev. D17, 2369, 1978.

[19] S. P. Mikheev and A. Yu. Smirnov. Resonance enhancement of oscillations in matter and solar neutrino spectroscopy. Sov. J. Nucl. Phys., 42, 913-917, 1985.

[20] C. Giunti and C. W. Kim. Fundamentals of neutrino physics and astrophysics. Oxford University Press, 2007.

[21] C. Amsler et al. (Particle Data Group), Phys. Lett. B, 667, 1, 2008.

[22] A. Osipowicz *et al.* KATRIN: a next generaion tritium beta decay experment with sub-eV sensitivity for the electron neutrino mass. hep-ex/0109033, 2001.

[23] C. Kraus *et al.* Final results from phase II of the Mainz neutrino mass search in Tritium β decay. Eur. Phys. J., 40, 447, 2005.

[24] V. M. Lobashev *et al.* Direct search for mass of neutrino and anomaly in the tritium beta-spectrum. Phys. Lett. B, 460, 227-235, 1999.

[25] C. Giunti. Phenomenology of neutrino mixing and oscillations. Colloquium APC, Paris, 2009.

[26] H. V. Klapdor-Kleingrothaus *et al.* Evidence for Neutrinoless Double Beta Decay. Mod. Phys. Lett., A16, 2409, hep-ph/0201231, 2001.
H. V. Klapdor-Kleingrothaus *et al.* Data acqquisition and analysis of the ^{76}Ge double beta experiment in Gran Sasso 1990-2003. NIM A, 522, 371-406, 2004.

[27] I.V. Kirpichnikov. Klapdor's claim for the observation of the neutrinoless 2β-decay of ^{76}Ge. Analysis and corrections. arXiv 1006.2025, 2010.

[28] S. M. Bilenky. Neutrinoless double beta-decay. arXiv 1001.1946, 2010.

[29] D. N. Spergel *et al.* First year Wilkinson Microwave Anisotropy Probe (WMAP) observations: determination of cosmological parameters. Astrophys. J. Suppl., 148, 175-194, astro-ph/0302209, 2003.

[30] S. Parke. Neutrino physics, important issues and the future. Neutrino 2010, XXIV International Conference on Neutrino Physics and Astrophysics, Athens, Greece.

[31] Y. Y. Y. Wong. Precision cosmology as a neutrino laboratory. Neutrino 2010, XXIV International Conference on Neutrino Physics and Astrophysics, Athens, Greece.

[32] J.N. Bahcall *et al.* Astrophys. J., 137, 344-346, 1963.

[33] J.N. Bahcall *et al.* Solar Models: current epoch and time dependences, neutrinos, and helioseismological properties. Astrophys. J., 555, 990-1012, astro-ph/0010346, 2001.

[34] E. G. Adelberger. Solar fusion cross sections II: the pp chain and CNO cycles. arXiv 1004.2318, 2010.

[35] J. N. Bahcall. http://www.sns.ias.edu/~jnb/

[36] B. T. Cleveland *et al.* Measurement of the solar electron neutrino flux with the Homestake chlorine detector. Astrophys. J., 496, 505-526, 1998.

[37] M. Altmann *et al.* Complete results for five years of GNO solar neutrino observations. Phys. Lett. B, 616, 174, hep-ex/0504037, 2005.

[38] J. N. Abdurashitov *et al.* Measurements of the solar neutrino capture rate by the Russian-American gallium solar neutrino experiment during one half and the 22-year cycle of solar activity. J. Exp. Theor. Phys., 95, 181-193, astro-ph/0204245, 2002.

[39] Y. Fukuda *et al.* Solar neutrino data covering solar cycle 22. Phys. Rev. Lett., 77, 1683-1686, 1996.

[40] J. Hosaka *et al.* Solar neutrino measurements in SuperKamiokande I. Phys. Rev. D73, 112001, hep-ex/0508053, 2006.

[41] Q. R. Ahmad *et al.* Direct evidence for neutrino flavor transformation from neutral-current interactions in the Sudbury Neutrino Observatory. Phys. Rev. Lett. 89, 011301, nucl-ex/0204008, 2002.

[42] R. Davis *et al.* Search for neutrinos from the Sun. Phys. Rev. Lett. 20, 1205-1209, 1968.

[43] J. N. Abdurashitov *et al.* Measurements of the solar neutrino capture rate with gallium metal. III: results for the 2002-2007 data taking period. Phys. Rev. C80, 015807, arXiv 0901.2200v3, 2009.

[44] K.S. Hirata *et al*, Observation in the Kamiokande-II detector of the neutrino burst from supernova SN1987A. Phys. Rev. D38, 448, 1987.

[45] J. P. Cravens *et al.* Solar neutrino measurements in SuperKamiokande II. Phys. Rev. D78, 032002, arXiv 0803.4312v1, 2008.

[46] Q. R. Ahmad *et al.* Measurement of the rate $\nu_e + d \rightarrow p + p + e^-$ interactions produced by ^{8}B solar neutrinos at the Sudbury Neutrino Observatory. Phys. Rev. Lett., 87, 071301, nucl-ex/0106015, 2001.

[47] B. Aharmin *et al.* Electron energy spectra, fluxes, and day-night asymmetries of ^{8}B solar neutrinos from the 391-day salt phase SNO data set. Phys. Rev. C72, 055502, nucl-ex/0502021, 2005.

[48] G. Alimonti *et al.* The Borexino detector at the Laboratori Nazionali del Gran Sasso. arXiv 0806.2400, 2008.

[49] G. Bellini *et al.* Measuremnt of the solar ^{8}B neutrino rate with a liquid scintillator target and 3 MeV energy threshold in the Borexino detector. arXiv 0808.2868v3, 2008.

[50] K. S. Hirata. Experimental study of the atmospheric neutrino flux. Phys. Lett. B, 205, 416-420, 1988.

[51] K. S. Hirata. Observation of a small atmospheric ν_μ/ν_e ratio in Kamiokande. Phys. Lett. B, 280, 146-152, 1992.

[52] K. S. Hirata. Atmospheric ν_μ/ν_e ratio in the multi-GeV energy range. Phys. Lett. B, 335, 237-245, 1994.

[53] D. Casper *et al.* Measurement of atmospheric neutrino composition with the IMB-3 detector. Phys. Rev. Lett., 66, 2561-2564, 1991.

[54] R. Becker-Szendy *et al.* Search for muon neutrino oscillation with the Irvine-Michigan-Brookhaven detector. Phys. Rev. Lett., 69, 1010-1013, 1992.

[55] R. Clark *et al.* Atmospheric muon neutrino fraction above 1 GeV. Phys. Rev. Lett., 79, 345-348, 1997.

[56] Y. Ashie *et al.* A measurement of atmospheric neutrino oscillation parameters by Super-Kamiokande I. Phys. Rev. D71, 112005, hep-ex/0501064, 2005.

[57] Y. Fukuda *et al.* Evidence for oscillation of atmospheric neutrinos. Phys. Rev. Lett., 81, 1562-1567, hep-ex/9807003, 1998.

[58] Y. Ashie *et al.* Evidence for an oscillatory signature in atmospheric neutrino oscillation. Phys. Rev. Lett., 93, 101801, hep-ex/0404034, 2004.

[59] M. Sanchez *et al.* Observation of atmospheric neutrino oscillations in Soudan 2. Phys. Rev. D68, 113004, hep-ex/0304037, 2003.

[60] M. Ambrosio *et al.* Atmospheric neutrinos oscillations from upward through-going muon multiple scattering in MACRO. Phys. Lett. B, 566, 35, hep-ex/0307069, 2003.

[61] E. Kearns *et al.* Experimental measurements of atmospheric neutrinos. Nucl. Phys. Proc. Suppl. 70, 315-323, hep-ex/9803007, 1999.

[62] M . Aglietta *et al.* Experimental study of atmospheric neutrino flux in the NUSEX experiment. Europhys. Lett. 8, 611-614, 1989.
M . Aglietta *et al.* Experimental study of upward stopping muons in NUSEX. Europhys. Lett. 15, 559-564, 1991.

[63] C. Berger *et al.* A study of atmospheric neutrino oscillations in the Fréjus experiment. Phys. Lett. B, 245, 305-310, 1990.
K. Daum *et al.* Determination of the atmospheric neutrino spectra with the Fréjus detector. Z. Phys., C66, 417-428, 1995.

[64] A. Aguilar *et al.* Evidence for neutrino oscillations from the observation of electron anti-neutrinos in a muon anti-neutrino beam. Phys. Rev. D64, 112007, hep-ex/0104049, 2001.

[65] C. Athassopoulos *et al.* Evidence for $\nu_\mu \rightarrow \nu_e$ oscillations from LSND. Phys. Rev. Lett., 81, 1774, nucl-ex/9709006, 1997.

[66] B. Armbruster *et al.* Upper limits for neutrino oscillations muon-antineutrino to electron-antineutrino from muon decay at rest. Phys. Rev. D65, 112001, hep-ex/0203021, 2002.

[67] H. De kerret. New results of neutrino oscillation search at the Bugey reactor. Talk given at the 23^{rd} 'Rencontre de Moriond', 1988.

[68] A. A. Aguilar-Arevalo *et al.* A search for electron antineutrino appearance at the $\Delta m^2 \sim 1$ eV^2 scale. arXiv 0904.1958, 2009.

[69] G. Karagiorgi. Toward solution of the MiniBooNE and LSND anomalies. Neutrino 2010, XXIV International Conference on Neutrino Physics and Astrophysics, Athens, Greece.

[70] M.H. Ahn *et al.* Indication of neutrino oscillation in a 250 km long-baseline experiment. Phys. Rev. Lett., 90, 041801, hep-ex/0212007, 2002.

[71] M.H. Ahn *et al.* Measurement of neutrino oscillation by the K2K experiment. Phys. Rev. D74, 072003, hep-ex/0606032, 2006.

[72] P. Adamson *et al.* Measurement of neutrino oscillations with the MINOS detectors in the NuMI beam. arXiv 0806.2237, 2008.

[73] D. G. Michael *et al.* Observation of muon neutrino disappearance with the MINOS detectors in the NuMI neutrino beam. Phys. Rev. Lett., 97, 191801, hep-ex/0607088, 2006.

[74] F. Boehm. Studies of neutrino oscillations at reactors (from Current aspects of neutrino physics, David O. Caldwell). nucl-ex/0005002, 2000.

[75] H. Kwon *et al.* Search for neutrino oscillations at a fission reactor. Phys. Rev. D24, 1097, 1981.

[76] F. Reines *et al.* Evidence for neutrino instability, Phys. Rev. Lett. 45, 1307-1311, 1980.

[77] S. P. Riley *et al.* Neutrino-induced deuteron disintegration experiment, Phys. Rev. C59, 3, 1998.

[78] G. Zacek *et al.* Neutrino-oscillation experiments at the Gösgen nuclear power reactor. Phys. Rev. D34, 2621, 1986.

[79] J.F. Cavaignac *et al.* Indication for neutrino oscillation from a high statistics experiment at the bugey reactor, Phys. Lett. B, 148, 387, 1984.

[80] A. I. Alfonin *et al.* A study of the reaction $\bar{\nu}_e + p \rightarrow e^+ + n$ on a nuclear reactor. JETP 67, 213, 1998.

[81] G. S. Vidyakin *et al.* Limitations on the characteristics of neutrino oscillations. JETP Lett. 59, 390, 1994.

[82] B. Achkar *et al.* Comparison of antineutrino reactor spectrum models with the Bugey-3 measurements. Phys. Lett. B, 374, 243-248, 1996.

[83] K. Eguchi *et al.* First results from KamLAND: evidence for reactor anti-neutrino disappearance. Phys. Rev. Lett., 90, 021802, hep-ex/0212021, 2003.

[84] Z. D. Greenwood *et al.* Results of a two-position reactor neutrino-oscillation experiment. Phys. Rev. Lett., D53, 6054, 1996.

[85] Y. Fukuda *et al.* Atmospheric ν_μ/ν_e ratio in the multi-GeV energy range. Phys. Lett. B, 335, 237, 1994.

[86] C. Bemporad *et al.* Reactor-based neutrino oscillation experiments. Rev. Mod. Phys., 74, 297, hep-ph/0107277, 2002.

[87] M. Apollonio *et al.* Initial results from the CHOOZ long baseline reactor neutrino oscillation experiment. Phys. Lett. B, 420, 397, 1998.

[88] M. Apollonio *et al.* Limits on neutrino oscillations from the CHOOZ experiment. Phys. Lett. B, 466, 415, 1999.

[89] M. Apollonio *et al.* Search for neutrino oscillations on a long base-line at the CHOOZ nuclear power station. Eur. Phys. J., C27, 331, 2003.

[90] Y. Fukuda *et al.* Study of the atmospheric neutrino flux in the multi-GeV energy range, Phys. Rev. Lett., 81, 1562, 1998.

[91] F. Boehm *et al.* Final results from the Palo Verde neutrino oscillation experiment. Phys. Rev. D64, 112001, hep-ex/0107009, 2001.

[92] F. Boehm *et al.* Results from the Palo Verde neutrino oscillation experiment. Phys. Rev. Lett., 84, 3764-3767, hep-ex/0003022, 2000.

[93] T. Araki *et al.* Measurement of neutrino oscillation with KamLAND: evidence of spectral distortion. Phys. Rev. Lett., 94, 081801, hep-ex/0406035v3, 2005.

[94] S. Abe *et al.* Precision measurement of neutrino oscillation parameters with KamLAND. Phys. Rev. Lett., 100, 221803, arXiv 0801.4589v3, 2008.

[95] H. Murayama. http://hitoshi.berkeley.edu/neutrino

[96] O. Sato. Observation of a first ν_τ candidate event in the OPERA experiment in the CNGS beam. Neutrino 2010, XXIV International Conference on Neutrino Physics and Astrophysics, Athens, Greece.

[97] A. Guglielmi. Status and early events from ICARUS T600. Neutrino 2010, XXIV International Conference on Neutrino Physics and Astrophysics, Athens, Greece.

[98] B. Aharmin *et al.* Low energy threshold analysis of the phase I and phase II data sets of the Sudbury Neutrino observatory. Phys. Rev. C81, 055504, arXiv 0910.2984, 2009.

[99] P. Adamson *et al.* New constraints on muon-neutrino to electron-neutrino transitions in MINOS. FERMILAB-PUB-10-176-E. arXiv 1006.0996, 2010.

[100] T. Schwetz *et al.* Three-flavour neutrino oscillation update. New J. Phys., 10, 113011, arXiv 0808.2016v3, 2008.

[101] G. L. Fogli *et al.*. Hints of $\theta_{13} > 0$ from global neutrino data analysis. Phys. Rev. Lett., 101, 141801, arXiv 0806.2649, 2008.

[102] M. C. Gonzalez-Garcia *et al.* Updated global fit to three neutrino mixing: status of the hints of $\theta_{13} > 0$. JHEP, 04, 056, 2010, arXiv 1001.4524, 2010.

[103] M. Mezzetto and T. Schwetz. θ_{13}: phenomenology, present status and prospect. arXiv 1003.5800, 2010.

[104] F. Ardellier *et al.* Double Chooz: A search for the neutrino mixing angle θ_{13}. hep-ex/0606025, 2006.

[105] D. Motta. Search for the θ_{13} neutrino mixing angle using reactor anti-neutrinos. hep-ex/0702003, 2007.

[106] T. Hagner *et al.* Muon-induced production of radioactive isotopes in scintillation detectors. Astropart. Phys., 14, 33, 2000.

[107] S. Abe *et al.* Production of radioactive isotopes through cosmic muon spallation in KamLAND. Phys. Rev. C81, 025807, arXiv 0907.0066v2, 2010.

[108] P. Huber *et al.* From Double Chooz to Triple Chooz - neutrino physics at the Chooz reactor complex. JHEP, 0605, 072, hep-ph/0601266v1, 2006.

[109] P. Huber *et al.* Reactor neutrino experiments compared to superbeams. Nucl. Phys. B, 665, 487, hep-ph/0303232v3, 2003.

[110] M. Goodman. Search for the neutrino mixing angle θ_{13} at reactors. hep-ex/07060512, 2007.

[111] G. Mention *et al.* A unified analysis of the reactor neutrino program towards the measurement of the θ_{13} mixing angle. hep-ex/07040498, 2007.

[112] A. Cabrera. Double Chooz: 'the first lights'. Neutrino 2010, XXIV International Conference on Neutrino Physics and Astrophysics, Athens, Greece.

[113] Daya Bay Collaboration. Precision measurement of the neutrino mixing angle θ_{13} Using Reactor Antineutrinos At Daya Bay. hep-ex/0701029, 2006.

[114] W. Meng. Status of Daya Bay reactor neutrino experiment. Neutrino 2010, XXIV International Conference on Neutrino Physics and Astrophysics, Athens, Greece.

[115] J. K. Ahn *et al.* RENO: An experiment for neutrino oscillation parameter θ_{13} Using Reactor Neutrinos at Yonggwang. arXiv 1003.1391, 2010.

[116] K. K. Joo. Status of RENO reactor neutrino experiment. Neutrino 2010, XXIV International Conference on Neutrino Physics and Astrophysics, Athens, Greece.

[117] P. Vahle. New results from MINOS. Neutrino 2010, XXIV International Conference on Neutrino Physics and Astrophysics, Athens, Greece.

[118] M. H. Ahn *et al.* Search for electron neutrino appearance in a 250 km Long-Baseline Experiment. Phys. Rev. Lett., 93, 051801, hep-ex/0402017, 2004.

[119] P. Adamson *et al.* Search for muon-neutrino to electron-neutrino appearance transitions in MINOS. Phys. Rev. Lett., 103, 261802, arXiv 0909.4996, 2009.

[120] M. Fechner's PhD thesis. Determination of the expected performances for the research of $\nu_\mu \rightarrow \nu_e$ oscillation in the T2K experience from the study of the K2K experiment data (French), 2006.

[121] T. Kobayashi. Status of T2K. Neutrino 2010, XXIV International Conference on Neutrino Physics and Astrophysics, Athens, Greece.

[122] T. Le. Overview of the T2K long baseline neutrino oscillation experiment. Proceedings of the DPF-2009 Conference. arXiv 0910.4211, 2009.

[123] Y. Itow *et al.*. The JHK-Kamioka neutrino project. Nucl. Phys. Proc. Suppl., 111, 146. hep-ex/0106019, 2001.

[124] NOνA experiment web page. http://www-nova.fnal.gov.

[125] H. Minakata *et al.* Reactor measurement of θ_{13} and its complementarity to long-baseline experiments. Phys. Rev. D70, 059901, hep-ph/0211111v2, 2002.

[126] V.Barger *et al.* Breaking eight-fold degenereacies in neutrino CP violation, mixing and mass hierarchy. Phys. Rev. D65, 073023, hep-ph/0112119, 2002.

[127] A. Yu. Smirnov. Neutrino oscillations: what is magic about 'magic' baseline? hep-ph/0610198v2, 2006.

[128] J. C. Anjos *et al.* Angra dos Reis reactor neutrino oscillation experiment. Brazilian Journal of Physics, vol. 36, no4A, 2006

J. C. Anjos *et al.* Angra Neutrino Project: status and plans. hep-ex/0511059, 2005

[129] J. E. Campagne *et al.* Physics potential of the CERN-MEMPHYS neutrino oscillation project. hep-ph/0603172, 2007.

[130] P. Zucchelli. A novel concept for a $\bar{\nu}_e/\nu_e$ neutrino factory : the beta beam. Phys. Lett. B, 532, 166, 2002.

[131] J.L.Borne *et al.* Physics with Memphys detector. Acta Physica Polonica B, vol.41, number 7.
MEMPHYS presentation on the APC laboratory website (French) http://www.apc.univ-paris7.fr/APC_CS/experiences/memphys/

[132] M. Mezzetto. Next challenge in neutrino physics: the θ_{13} angle. hep-ph/0905.2842, 2009.

[133] E. Kh. Akhmedov *et al.* A simple analytic three-flavour descrition of the day-night effect in the solar neutrino flux. JHEP, 0405, 057, hep-ph/0404083v3, 2004.

[134] Y. Takeuchi. Results from Super-Kamiokande. Neutrino 2010, XXIV International Conference on Neutrino Physics and Astrophysics, Athens, Greece.

[135] J. Klein. Results and prospects for SNO. Neutrino 2010, XXIV International Conference on Neutrino Physics and Astrophysics, Athens, Greece.

[136] F. Calaprice. Recent solar and terrestrial neutrino results with Borexino. Neutrino 2010, XXIV International Conference on Neutrino Physics and Astrophysics, Athens, Greece.

[137] C. Lunardini and A. Yu. Smirnov. Probing the neutrino mass hierarchy and the 13-mixing with supernovae. hep-ph/0302033v3, 2003.

[138] N. S. Bowden. Reactor monitoring and safeguards using antineutrino detectors. nucl-ex/08092128, 2008.

[139] F. Ardellier *et al.* Letter of intent for Double Chooz: a search for the mixing angle θ_{13}. hep-ex/0405032, 2004.

[140] G. Mention's PhD thesis. Sensibility study and backgrounds in the Double Chooz experiment for the research of the leptonic mixing angle parameter θ_{13} (French), 2005.

[141] V. I. Kopeikin *et al.* Spectrum of electronic reactor anti-neutrinos. Phys. Atom. Nucl., 60, 172, 1997.

[142] P. Vogel *et al.* Reactor antineutrino spectra and their application to antineutrino-induced reactions. II. Phys. Rev. C24, 1543, 2004.

[143] ENSDF database: http://ie.lbl.gov/databases/ensdfserve.html
JEFF-3.1.1 database: http://www.nea.fr/dbforms/data/eva/evatapes/jeff_31/index-JEFF3.1.1.html

[144] K. Schreckenbach *et al.* Determination of the antineutrino spectrum from ^{235}U thermal neutron fission products up to 9.5 MeV. Phys. Lett. B, 160, 325, 1985.

[145] A.A. Hahn *et al.* Antineutrino spectra from ^{241}Pu and ^{239}Pu thermal neutron fission products. Phys. Lett. B, 218, 365, 1989.

[146] Th. A. Mueller's PhD thesis. Double Chooz experiment: simulation of the spectrum of antineutrinos coming from reactors (French), 2010.

[147] Description of the MURE package. http://www.nea.fr/tools/abstract/detail/nea-1845

[148] Description of the DRAGON package. http://www.polymtl.ca/nucleaire/DRAGON/en/

[149] Private communication with A. Tonazzo.

[150] P. Vogel and J. F. Beacom. The angular distribution of the reaction $\bar{\nu}_e + p \rightarrow e^+ + n$. hep-ph/9903554, 1999.

[151] Hamamatsu Corporation. http://sales.hamamatsu.com/

[152] R. M. Bionta *et al.* Search for Proton Decay into $e^+\pi^0$. Phys. Rev. Lett. 51, 27, 1983.

[153] B. Reinhold's PhD thesis. Development and implementation of a level-1 trigger and timing system for the Double Chooz reactor antineutrino experiment, 2009.

[154] A. Lucotte *et al.* A front-end read out chip for the OPERA scintillator tracker. NIM A, 521, 378-392, 2004.

[155] ROOT, a C++-based library for data analysis. http://root.cern.ch/drupal/

[156] VME bus specifications. http://www.vita.com/vme-faq/.

[157] Adahome, a website dedicated to the ADA language. http://www.adahome.com/

[158] MINUIT minimization package http://root.cern.ch/root/html/TMinuit.

[159] R. Queval's PhD thesis. Characterization, Modelization and Optimization of the Double Chooz acrylic vessels: Physics Impact, 2010.

[160] Th-232 Decay Series. http://www.csupomona.edu/\~pbsiegel/www/decaychain/Th232.html

[161] U-238 Decay Series. http://www.csupomona.edu/\~pbsiegel/www/decaychain/U238.html

[162] Interactive Chart of Nuclides. http://www.nndc.bnl.gov/nudat2/

[163] Geant4. http://geant4.web.cern.ch. NIM A, 506, (2003) 250-303; IEEE TNS 53 No.1 (2006) 270-278.

[164] C. N. Henson. UCD Counting Facility at Saclay. Double Chooz collaboration meeting, June 2008.
M. Fechner *et al.* To be published.

[165] Private communications with H. De Kerret, M. Fechner and T. Lasserre. August 2009.

[166] A. Brigatti. http://pcbrigatti.mi.infn.it/Borexino_images/Borexino_images_in_the_sphere/in_the_sphere_main.htm

[167] D. Motta. Report of a study on light collection in Double Chooz. Internal note, June 2007.

[168] J. B. Birks. The theory and practice of scintillation counting. Pergamon Press, 1964.

[169] I. Stancu. DC Reconstruction Studies. Double Chooz collaboration meeting, june 2007.

[170] D. Shrestha et G. Horton-Smith. http://neutrino.phys.ksu.edu/~gahs/doublechooz/geometry/pointing/
D. Shrestha et G. Horton-Smith. http://neutrino.phys.ksu.edu/~dchooz/private/pmtpointing/

[171] D. Motta. Scintillator timing and implication for a novel PSD^2. Double Chooz collaboration meeting, Oxford, september 2007.

[172] C. Aberle. Optimization of the fluorescence features of Double Chooz reactor neutrino experiment liquid scintillators (German). Diplomarbeit, 2008.

[173] C. Aberle. Scintillator pulse shape with e^- and α excitation. Double Chooz internal presentation.

[174] I. Stancu. Reconstruction possibilities as calibration constants availability. Double Chooz collaboration meeting, Reims, october 24^{th}, France.